A Nonlocal Operator Method for Quasi-static and Dynamic Fracture Modeling

(Eine nichtlokale Operatormethode zur Modellierung quasistatischen und dynamischen Materialversagens)

DISSERTATION

Zur Erlangung des akademischen Grades eines

Doktor-Ingenieur

an der Fakultät Bauingenieurwesen

der Bauhaus-Universität Weimar

vorgelegt von

M.Eng. Yongzheng Zhang

(interner Doktorand)

Aus der Provinz Shandong, China

Betreuer:

Prof. Dr.-Ing. Timon Rabczuk

Gutachter:

Prof. Dr. Erkan Oterkus

Prof. Dr. Mehmet Dorduncu

Prof. Dr. rer. nat. Björn Rüffer

Weimar, Oktober 2022

"This dissertation is dedicated to: My beloved parents,

who love me, believe in me, inspire me and have supported me every step of the way.

My dear girlfriend for her patience and encouragement throughout this work.

My whole family."

Acknowledgements

This dissertation marks the end of my journey to obtain a doctorate title. I am grateful to all the people who have contributed to shaping this dissertation. First and foremost, the individual to whom I am most indebted is Prof. Timon Rabczuk for his sustained guidance, his support, and his inspiration throughout all my Ph.D. studies. I wish to express my deep gratitude and appreciation to him. His great patience and encouragement enabled me to make continuous progress in my research. I also would like to thank Prof. Xiaoying Zhuang for her sustained guidance and his inspiration during my Ph.D. studies.

My sincere thanks also go to the members of my dissertation referees: Prof. Erkan Oterkus, Prof. Mehmet Dorduncu, and Prof. Björn Rüffer for their patience in reading this dissertation and for the comments they provided to improve it.

I would like to express my special thanks to Dr. Huilong Ren for his insightful ideas, comments, and encouragement. My best harvest in obtaining the degree was his measureless mentoring. Thank you for correcting me every time.

I am grateful to Ms. Ines Meisner, Ms. Rosemarie Mayer, Ms. Judith Brömel, Ms. Elisa Kolling, and Ms. Sarah Grosch for their willingness to help me whenever needed and for supporting me in the process of my Ph.D. study and Ph.D. defense. I also would like to thank my colleagues at the Institute of Structural Mechanics for their help and friendly support.

Furthermore, I gratefully acknowledge the China Scholarship Council (CSC) for financially supporting me during my Ph.D. studies.

Last but not least, I would like to express my deepest gratitude to my family, especially my parents, for their unchanging love, support, and encouragement in the pursuit of my doctoral goal.

Weimar, November 2021

Yongzheng Zhang

Ehrenwörtliche Erklärung

Ich erkläre hiermit ehrenwörtlich, dass ich die vorliegende Arbeit ohne unzulässige Hilfe Dritter und ohne Benutzung anderer als der angegebenen Hilfsmittel angefertigt habe. Die aus anderen Quellen direkt oder indirekt übernommenen Daten und Konzepte sind unter Angabe der Quelle gekennzeichnet.

Insbesondere habe ich hierfür nicht die entgeltliche Hilfe von Vermittlungs-bzw. Beratungsdiensten (Promotionsberater oder anderer Personen) in Anspruch genommen. Niemand hat von mir unmittelbar oder mittelbar geldwerte Leistungen für Arbeiten erhalten, die im Zusammenhang mit dem Inhalt der vorgelegten Dissertation stehen. Die Arbeit wurde bisher weder im In-noch im Ausland in gleicher oder ähnlicher Form einer anderen Prüfungsbehörde vorgelegt. Ich versichere ehrenwörtlich, dass ich nach bestem Wissen die reine Wahrheit gesagt und nichts verschwiegen habe.

Ort, datum: Weimar, November 2021

Unterschrift:

Abstract

Material failure can be tackled by so-called nonlocal models, which introduce an intrinsic length scale into the formulation and, in the case of material failure, restore the well-posedness of the underlying boundary value problem or initial boundary value problem. Among nonlocal models, peridynamics (PD) has attracted a lot of attention as it allows the natural transition from continuum to discontinue and thus allows modeling of discrete cracks without the need to describe and track the crack topology, which has been a major obstacle in traditional discrete crack approaches. This is achieved by replacing the divergence of the Cauchy stress tensor through an integral over so-called bond forces, which account for the interaction of particles. A quasi-continuum approach is then used to calibrate the material parameters of the bond forces, i.e., equating the PD energy with the energy of a continuum. One major issue for the application of PD to general complex problems is that they are limited to fairly simple material behavior and pure mechanical problems based on explicit time integration. PD has been extended to other applications but losing simultaneously its simplicity and ease in modeling material failure. Furthermore, conventional PD suffers from instability and hourglass modes that require stabilization. It also requires the use of constant horizon sizes, which drastically reduces its computational efficiency. The latter issue was resolved by the so-called dual-horizon peridynamics (DH-PD) formulation and the introduction of the duality of horizons.

Within the nonlocal operator method (NOM), the concept of nonlocality is further extended and can be considered a generalization of DH-PD. Combined with the energy functionals of various physical models, the nonlocal forms based on the dual-support concept can be derived. In addition, the variation of the energy functional allows implicit formulations of the nonlocal theory. While traditional integral equations are formulated in an integral domain, the dual-support approaches are based on dual integral domains. One prominent feature of NOM is its compatibility with variational and weighted residual methods. The NOM yields a direct numerical implementation based on the weighted residual method for many physical problems without the need for shape functions. Only the definition of the energy or boundary value problem is needed to drastically facilitate the implementation. The nonlocal operator plays an equivalent role to the derivatives of the shape functions in meshless methods and finite element methods (FEM). Based on the variational principle, the residual and the tangent stiffness matrix can be obtained with ease by a series of matrix multiplications. In addition, NOM can be used to derive many nonlocal models in strong form.

The principal contributions of this dissertation are the implementation and application of NOM, and also the development of approaches for dealing with fractures within the NOM, mostly for dynamic fractures. The primary coverage and results of the dissertation are as follows:

- The first/higher-order implicit NOM and explicit NOM, including a detailed description of the implementation, are presented. The NOM is based on so-called support, dual-support, nonlocal operators, and an operate energy functional ensuring stability. The nonlocal operator is a generalization of the conventional differential operators. Combining with the method of weighted residuals and variational principles, NOM establishes the residual and tangent stiffness matrix of operate energy functional through some simple matrix without the need of shape functions as in other classical computational methods such as FEM. NOM only requires the definition of the energy drastically simplifying its implementation. For the sake of conciseness, the implementation in this chapter is focused on linear elastic solids only, though the NOM can handle more complex nonlinear problems. An explicit nonlocal operator method for the dynamic analysis of elasticity solid problems is also presented. The explicit NOM avoids the calculation of the tangent stiffness matrix as in the implicit NOM model. The explicit scheme comprises the Verlet-velocity algorithm. The NOM can be very flexible and efficient for solving partial differential equations (PDEs). It's also quite easy for readers to use the NOM and extend it to solve other complicated physical phenomena described by one or a set of PDEs. Several numerical examples are presented to show the capabilities of this method.

- A nonlocal operator method for the dynamic analysis of (thin) Kirchhoff plates is proposed. The nonlocal Hessian operator is derived from a second-order Taylor series expansion. NOM is higher-order continuous, which is exploited for thin plate analysis that requires C^1 continuity. The nonlocal dynamic governing formulation and operator energy functional for Kirchhoff plates are derived from a variational principle. The Verlet-velocity algorithm is used for time discretization. After confirming the accuracy of the nonlocal Hessian operator, several numerical examples are simulated by the nonlocal dynamic Kirchhoff plate formulation.

- A nonlocal fracture modeling is developed and applied to the simulation of quasi-static and dynamic fractures using the NOM. The phase field's nonlocal weak and associated strong forms are derived from a variational principle. The NOM requires only the definition of energy. We present both a nonlocal implicit phase field model and a nonlocal explicit phase field model for fracture; the first approach is better suited for quasi-static fracture problems, while the key application of the latter one is dynamic fracture. To demonstrate the performance of the underlying approach, several benchmark examples for quasi-static and dynamic fracture are solved.

Contents

List of Figures

List of Tables

Nomenclature

Symbols and abbreviations regularly used in the dissertation are listed. Symbols less frequently used, or having different meanings in different contexts, are defined where they are used.

Symbols	**Description**
$\boldsymbol{x}_i$	spatial coordinates in domain Ω
$\boldsymbol{u}$	displacement field
$\boldsymbol{\xi}_{ij}$	relative position vector
$\mathbb{w}\left(\boldsymbol{\xi}_{ij}\right)$	the weight function
$\mathcal{S}_i$	the support of particle $\boldsymbol{x}_i$
$\mathcal{S}_i'$	the dual-support of particle $\boldsymbol{x}_i$
$\tilde{\nabla}\boldsymbol{u}_i$	nonlocal gradient operator of point $\boldsymbol{x}_i$
$\mathcal{F}_i^{hg}$	operator energy functional of point $\boldsymbol{x}_i$
$\mathbf{K}_i$	the shape tensor
$\partial\Omega$	the boundary of domain Ω
$\boldsymbol{\sigma}$	Cauchy stress tensor
$L(\dot{\boldsymbol{u}}, \boldsymbol{u})$	Lagrange energy functional
$\psi(\boldsymbol{\sigma}, \boldsymbol{\varepsilon}(\nabla\boldsymbol{u}))$	strain energy density
ρ	the density of the material
$\mathbf{b}$	the body force density
$\mathbf{f}$	the external traction force
N	the number of points in solid domain Ω
ΔV_i	the volume associated with point $\boldsymbol{x}_i$
$u_i(t)$	the ensemble of the position vector of point $\boldsymbol{x}_i$
$\boldsymbol{P}_i$	the internal force vector of point $\boldsymbol{x}_i$
$\mathbb{M}_i$	the mass of point $\boldsymbol{x}_i$
$\mathbf{F}_i$	the deformation tensor of point $\boldsymbol{x}_i$
$\ddot{\boldsymbol{u}}_i$	the acceleration of point $\boldsymbol{x}_i$
$\boldsymbol{p}_j$	the flattened polynomials
$\partial_\alpha^{\mathbb{1}}\mathbf{u}_i$	scaled partial derivatives
$\partial_\alpha\mathbf{u}_i$	partial derivatives
$\alpha_{\mathrm{r}}^{\mathrm{n}}$	multi-index notation

$\mathbf{B}_{\alpha i}$	the nonlocal operator coefficient matrix of point $\mathbf{x}_i$
$\mathbf{P}$	the first Piola-Kirchhoff stress
$\mathbf{D}_4$	the fourth order elastic tensor
$\boldsymbol{n}^*$	the outward-pointing normal vector for boundary $\partial\Omega_f$
$H(\boldsymbol{x}, t)$	the local history field of strain

Abbreviations	**Description**
PDEs	Partial Differential Equations
NOM	Nonlocal Operator Method
FEM	Finite Element Method
XFEM	Extended Finite-Element Method
PG DEM	Petrov-Galerkin Diffuse Element Method
EFG	Element-Free Galerkin
RKPM	Reproducing Kernel Particle Method
RKCM	Reproducing Kernel Collocation Method
PUM	Partition of Unity Methods
IGA	Isogeometric Analysis
GFDM	Generalized Finite Difference Method
SPH	Smoothed Particle Hydrodynamics
PD	Peridynamics
TSE	Taylor Series Expansion
CAD	Computer Aided Design
CPM	Cracking Particles Method

Chapter 1

Introduction

1.1 Background and Motivation

Numerous physical problems can be modeled with the help of partial differential equations (PDEs). Since the solution of PDEs is not possible analytically for complex geometries and with increasing complexity, the development of numerical methods for obtaining approximate solutions to these PDEs is a critical challenge in computational mechanics. Over the last several decades, various numerical methods categorized into mesh-based and mesh-free ones, have been proposed and developed so far to solve PDEs based on the classical local and nonlocal continuum mechanics theory. For mesh-based methods, which include FEM [Zienkiewicz et al., 1977, Larsson and Thomée, 2003, Jiang and Ma, 2011, Grande and Reusken, 2016, Feng et al., 2017], extended finite-element method (XFEM) [Hossain et al., 2013], Generalized Finite Difference Method (GFDM) [Liszka, 1984, Gavete et al., 2017, Ureña et al., 2020],Petrov-Galerkin Diffuse Element Method (PG DEM) [Nayroles et al., 1992, Krongauz and Belytschko, 1997], Element-Free Galerkin (EFG) method [Deb et al., 2001, Babuska et al., 2004, Antonietti et al., 2016], Reproducing Kernel Particle Method (RKPM) [Liu et al., 1995, Chen et al., 2017, Huang et al., 2020], Partition of Unity Methods (PUM)[Babuška and Melenk, 1997, Safdari-Vaighani et al., 2015, Larsson et al., 2017], isogeometric analysis (IGA)[De Falco et al., 2011, Tagliabue et al., 2014, Dalcin et al., 2016, Garotta et al., 2020], the reproducing kernel collocation method [Aluru, 2000, Hu et al., 2011, Cialenco et al., 2012, Fasshauer and Ye, 2013, Mohammadi and Mokhtari, 2014, Mohammadi et al., 2018, Mahdavi et al., 2019, 2020], etc. Among mesh-free methods, *hp*-Meshless clouds (HPC) [Duarte and Oden, 1996], Smoothed Particle Hydrodynamics (SPH) [Lucy, 1977, Liu and Liu, 2003, 2006], for example, have been proposed and developed to solve PDEs. Among these numerical methods, in FEM, the computational domain is discretized by elements, and the shape functions are defined within an element to interpolate the primary variable for each el-

ement. The most common element formulations are based on Lagrange polynomials. These do not allow the formulation of discontinuities such as cracks within an element. Also, higher-order PDEs are not easy to model with the FEM due to their C^0 continuity. The XFEM allows the modeling of discontinuities - like cracks - within an element. For this purpose, the approximation space of the primary variable is modified using a so-called partition-of-one concept and a corresponding enrichment function. However, crack imaging still requires techniques to capture the crack topology. Likewise, crack tracking algorithms are needed, which makes the implementation of XFEM extremely difficult, especially for problems with complex crack geometries (crack branches or crack interactions). Mesh-free methods avoid elements, which facilitates the modeling of large deformations. In principle, discontinuities in mesh-free methods can be realized with the same concepts as in FEM. Due to their higher-order continuity, they also simplify the solution of higher-order PDEs. The main disadvantage of mesh-free methods is the high computation time. The GFDM is an alternative to FEM and mesh-free methods. In contrast to the FEM and most mesh-free methods, the GFDM is based on a strong form, which makes it difficult to apply natural boundary conditions. Compared to the FEM, the GFDM is not robust and stable. Crack propagation requires natural boundary conditions on the crack surfaces, which cannot be effectively modeled with GFDM. The so-called IGA is based on CAD shape functions, which are characterized by their higher-order continuity. Thus, IGA is suitable for higher-order PDEs. For complex geometries, which are composed of so-called 'patches', the IGA is only C^0 continuous at the transitions, which requires additional effort. Likewise, the IGA is not very suitable for modeling crack propagation.

In summary, most numerical methods are based on so-called shape functions for field interpolation, where the derivatives of the shape function represent differential operators. For higher-order PDEs, there are correspondingly high requirements on the differentiability of the shape functions. Furthermore, the differential operators are so-called 'local' operators, which are specified at a point. Such numerical methods have difficulties in numerically solving problems with moving boundaries/edges or discontinuities within the domain. A classic example is crack propagation problems. When there is no definition for problems involving strong or weak discontinuities, the conventional local differential operator encounters difficulties. To address this issue, meshless methods or FEMs employ a particular treatment or an extra kinematics model to build the shape function and compute its derivatives. However, this unique technique causes numerical instabilities, such as improper stiffness matrix conditioning. Furthermore, the implementation of 3D challenges becomes difficult and time-consuming.

To overcome these challenges, so-called nonlocal theories have been developed, in which no particular handling of discontinuities is required, such as nonlocal linear elasticity[Emmrich and Weckner, 2007, Bertoldi et al., 2007, Weckner et al., 2009, Di Paola et al., 2009, 2010], nonlocal fluid dynamics [Eringen, 1972b, Caffarelli and Vasseur, 2012,

El-Nabulsi, 2018], nonlocal electromagnetic theory [Eringen, 1973, Mikki, 2020a,b], nonlocal continuum field theories [Eringen, 1992, 2002, Eringen and Wegner, 2003, Rafii-Tabar et al., 2016], nonlocal damage mechanics [Bažant and Jirásek, 2002, Borino et al., 2003, Jirásek, 2007, Samal et al., 2008], nonlocal calculus [Gunzburger and Lehoucq, 2010, Du et al., 2013]. The nonlocal theory is founded on an integral form with a limited intrinsic length scale, whereas the definition of a local differential operator is founded on an intrinsic length scale approaching infinitesimal. And it provides an improved predictive capability to capture effects that classical differential equations fail to capture. In comparison to the local theory, the nonlocal theory not only has a greater numerical well-posedness, but also resembles the real physical process better due to its inherent length scale. [Silling, 2000, Eringen, 2002, Bažant and Jirásek, 2002]. A recently emerged and developed approach based on nonlocal theory, peridynamics (PD) [Silling, 2000, Silling and Askari, 2005, Silling and Bobaru, 2005, Silling et al., 2007, Silling and Lehoucq, 2008, 2010, Silling et al., 2010], has received a great deal of interest because to its comparatively simple numerical implementation for fracture. To account for long-range forces, PD reformulates the elasticity theory in integral form, overcoming the challenge of defining the local derivatives for fractures. In PD theories, integrodifferential equations without displacement derivatives perform as the governing equations of motion, in contrast to numerical models based on classical local continuum mechanics, which enables the occurrence of discontinuities in deformation fields. PD theory provides the following benefits over classical continuum mechanics (CCM): PD theory allows for the handling of discontinuous problems and the removal of spatial derivatives of displacements, and it also allows for both meshless and mesh-based discretization; In addition, numerical models based on PD theory can easily simulate complicated fracturing processes, such as crack branching and coalescence. Various PD models, including bond-based peridynamics (BB-PD) models [Ballarini et al., 2018, Gu et al., 2019, Wang et al., 2019b, Han et al., 2019, Yu et al., 2020], state-based peridynamic (SB-PD) models[Amani et al., 2016, Zhou and Wang, 2016, Wang et al., 2016, Gu et al., 2018, Madenci et al., 2019b, Hashim et al., 2020], and hybrid models coupled classical continuum mechanics and PD [Macek and Silling, 2007, Lubineau et al., 2012, Azdoud et al., 2013, 2014, Yaghoobi and Chorzepa, 2018, Wang et al., 2019a, Bode et al., 2020] have been developed during the last two decades. In the idea of nonlocality, PD has been expanded in a variety of ways, including dual-horizon PD [Ren et al., 2016, 2017, Rabczuk and Ren, 2017], peridynamic plate/shell theory [O'Grady and Foster, 2014, Chowdhury et al., 2016, Dorduncu et al., 2020, Zhang et al., 2021], mixed peridynamic Petrov-Galerkin method [Bode et al., 2020], phase-field based peridynamic damage model [Roy et al., 2017, Mehrmashhadi et al., 2020, Roy et al., 2021], wave dispersion analysis of PD [Wildman and Gazonas, 2014, Bažant et al., 2016, Butt et al., 2017, Mutnuri and Gopalakrishnan, 2020, Chan and Chen, 2021], higher-order PD models [Yaghoobi and Chorzepa, 2017, Chen and Chan, 2020, Yang et al., 2021], to name a few. In general, PD is an elegant mesh-free numerical method to solve crack propagation problems. PD is based on so-called non-locality. This non-locality

makes PD fundamentally different from most "ordinary" local methods, i.e., FEM. Both FEM and many mesh-free methods are based on a variational principle and the weighted residuals method. The usage of the variational principle would also be advantageous for the aforementioned nonlocal theories mentioned above - such as PD - as it greatly expands the scope of application. PD replaces the divergence term in the equation of motion with an integrated form that is related to a bond force. Hence, it can treat the continuum in the same way as a discontinued. One issue is the integration of complex constitutive models, especially for coupled problems. However, PD is based on explicit time integration, which limits its applicability to quasi-static/static problems.

In recent years, several numerical approaches based on peridynamic differential operator (PDDO) [Madenci et al., 2016, 2017, Bazazzadeh et al., 2018, Madenci et al., 2019a, Dorduncu, 2019, Gao and Oterkus, 2019, Dorduncu, 2020, Dorduncu and Apalak, 2020, Haghighat et al., 2021, Kan et al., 2021] have been proposed, which can be viewed as an interesting extension to PD. The PDDO employs the concept of PD interactions, in addition, it is based on the TSE of multi-variable scalar functions and the orthogonality property of PD functions. The PDDO provides any order of derivatives to be derived directly from the orthogonality requirement of the PD functions without any differentiation. It does not use a kernel function or repeatability criteria for different derivative orders. It permits the precise calculation of any arbitrary order of partial derivatives of spatial and temporal functions. Directly determining the PD functions for the derivatives is done by making them orthogonal to each term in the Taylor series expansion. When finding the PD functions in the presence of a nonsymmetric family, both the lower and higher-order derivatives affect each other. The PDDO is exempt from the symmetric requirement. This feature eliminates the need for ghost points at the boundary. However, while the partial derivatives in PDDO rely on the orthogonality property of the PD function, which requires some extra steps in their computation. Furthermore, PDDO is only used to solve physical problems based on the strong form.

In this dissertation, the nonlocal theory is adopted for developing computationally efficient numerical approaches to solve the PDEs and phase field based quasi-static and dynamic fracture problems.

1.2 Objectives and Methodologies

The primary objective of this dissertation was devoted to the implementation, development, and application of the nonlocal operator method (NOM), which is based on the method of weighted residuals and variational principles. NOM enables the solution of static and quasi-static problems, especially for problems with material failure. For this purpose, the following techniques are used:

- The NOM is continuous in any order and provides for a straightforward description of material failures. It does not require any shape functions, only the definition of potential energy (or boundary value problem), and using the methods of weighted residuals or variational principle, the inner and outer force vectors, as well as the consistent tangent stiffness matrix, obtain automatically, which drastically simplifies the implementation.
- The first and higher-order nonlocal operations are computed through a Taylor series expansion. Within the support of a particle/node, the NOM achieves nonlocal operations through a weighted sum of the Taylor series expansion.
- The NOM is implemented using the Mathematica platform.
- A second-order phase field model is utilized to model material failure within the NOM.

1.3 Research Contribution

The contribution of this dissertation is summarized as follows:

- Conducting a comprehensive literature review of numerical methods for solving PDEs, the difficulties and challenges of using traditional numerical methods to solve PDEs are also analyzed in detail.
- Development and implementation of the implicit first-order and higher-order NOM to solve different orders of PDEs in different dimensions (2D and 3D).
- Implementation of explicit particle-based NOM for dynamic problems.
- Extension of the NOM formulation for Kirchhoff (thin) plates using the higher-order particle-based NOM.
- Application of NOM to quasi-static and dynamic fracture problems to demonstrate the efficiency and accuracy of the method.

1.4 Organization

The dissertation is presented in six chapters, including this introductory chapter. The principal goal is identified and the objectives and methodologies of this study are clarified in this chapter. The remaining chapters of the dissertation are organized as follows:

Chapter 2 presents the open-source code for the first/higher-order implicit NOM, including a detailed description of the implementation. Combined with the method of weighted

residuals and variational principles, we establish the residual and tangent stiffness matrix of operate energy functional through some simple matrix without the need of shape functions as in other classical computational methods such as FEM. This chapter's implementation focuses on linear elastic solids for the sake of conciseness, though the NOM can handle more complex nonlinear problems. Finally, several numerical examples are presented to show the capabilities of this implicit method.

Chapter 3 elaborates on the implementation progress of explicit NOM in detail, and a nonlocal dynamic elasticity solid formulation based on explicit NOM is also proposed. Combined with the variational principle, the nonlocal governing equations and nonlocal operator energy functional for linear elasticity solid are derived. The nonlocal governing equations and nonlocal operator energy functionals are expressed as the integral forms of support and dual-support. A detailed description of the explicit implementation is presented. Finally, several numerical examples are presented to show the capabilities of this explicit method.

Chapter 4 establishes a nonlocal dynamic Kirchhoff (thin) plate formulation based on NOM. The nonlocal Hessian operator is derived from a second-order Taylor series expansion. The nonlocal dynamic governing formulation and operator energy functional for Kirchhoff plates are derived from a variational principle. After confirming the accuracy of the nonlocal Hessian operator, several numerical examples are simulated by the nonlocal dynamic Kirchhoff plate formulation.

Chapter 5 develops the quasi-static and dynamic fracture modeling using the NOM. The phase field's nonlocal weak and associated strong forms are derived from a variational principle. We present both a nonlocal implicit phase-field model and a nonlocal explicit phase-field model for fracture; the first approach is better suited for quasi-static fracture problems, while the key application of the latter one is dynamic fracture. To demonstrate the performance of the underlying approach, several benchmark examples for quasi-static and dynamic fracture are solved.

Chapter 6 summarizes the research that has been presented in this dissertation. The main contributions of this research are outlined. Finally, some possibilities for future work are suggested.

Chapter 2

Implicit implementation of nonlocal operator method

This chapter is based on the journal paper 'Implicit implementation of the nonlocal operator method: an open source code' published in EWCO by my first author. The contribution of this paper is summarized as follows:

Yongzheng Zhang

- Conceptualization
- Research state of the art
- Investigation
- Formal analysis
- Methodology
- Software/Programming
- Data curation
- Data analysis
- Validation
- Visualization
- Writing original manuscript draft

Huilong Ren

- Conceptualization
- Methodology

- Programming
- Writing review and editing

Timon Rabczuk

- Conceptualization
- Mentoring the research progress

2.1 General

The nonlocal theory of elasticity [Eringen, 1972a, Rogula, 1982, Eringen, 1984, Povstenko, 1999, Faghidian, 2018] primarily considers distant action forces between objects. Different from the concept of local theory, an object can interact without physical interaction with a different object. The theory is of great significance to solve many physical problems, such as the law of universal gravitation. Some notable nonlocal numerical methods were proposed according to nonlocal interaction in nonlocal continuum field theories.

PD[Silling, 2000, Silling et al., 2007, Silling, 2010] is a formulation of continuum mechanics on the basis of the concept of nonlocal integration, PD avoids the singularity of the traditional local differential equations when solving discontinuous problems. One key application of PD is fracture. It shares the same advantages as the Cracking Particles Method (CPM) presented in [Rabczuk and Belytschko, 2004, 2007, Rabczuk et al., 2010]. In contrast to many other discrete crack approaches as presented in [Areias and Rabczuk, 2013, Areias et al., 2013, 2014, Amiri et al., 2014, Ghorashi et al., 2015, Areias et al., 2016a,b, Areias and Rabczuk, 2017, Areias et al., 2018], PD does not require the representation of the discrete crack surface and associated crack tracking algorithms. PD also has been successfully applied to rock fracture and soil damage analysis, such as impact fracture [Gerstle et al., 2007, Yin and Hai, 2013], composite material separation [Oterkus et al., 2012, Shen et al., 2013] and beam and plate structures [Lindsay et al., 2016]. However, to eliminate erroneous wave reflection and ghost force among particles, all traditional PD formulas must use the same horizon size. In many applications, to enhance calculating performance, its necessary to use different horizon sizes for the calculation of particles with non-uniform spatial distribution, such as adaptive encryption, multi-scale simulation, and multi-body analysis. In other words, in order to balance the calculation efficiency and calculation accuracy, we hope that PD can be based on the distribution characteristics of the particles, but if the size of the near field is used, it will result in the generation of false stress waves and the problem cannot be solved correctly. To address the aforementioned issue, dual-horizon PD [Ren et al., 2016, 2017] was developed to improve computing efficiency and to allow for varying horizon sizes. The dual-horizon is the dual term of the horizon when variable horizons are used in the inhomogeneous

discretization. It separates the horizon that exerts forces and counter forces between the particles, thereby solving the problem of false stress caused by the horizons. In addition, other nonlocal models mainly include nonlocal linear elasticity [Emmrich and Weckner, 2007, Di Paola et al., 2009, 2010], dynamics of nonlocal fluid [El-Nabulsi, 2018, Lee and Chang, 2008], electromagnetic nonlocal theory [Eringen, 1973, Van Mechelen and Jacob, 2019], nonlocal damage model [Pijaudier-Cabot and Bažant, 1987, Pijaudier-Cabot et al., 2004, Lorentz, 2017] and nonlocal calculus [Du et al., 2013, Alali et al., 2015].

In recent years, several numerical approaches based on peridynamics operators have been proposed, see e.g. the contributions in [Breitenfeld et al., 2014, Madenci et al., 2019a,b]. A new computational method based on nonlocal operators is the NOM first proposed in [Rabczuk et al., 2019] for electromagnetic problems. The approach has been later on extended to mechanical problems in [Ren et al., 2020a,b]. The NOM can be considered as a generalization of non-ordinary state-based PD. It has been applied to numerous challenging problems in solid mechanics and can be a viable alternative to FEM or meshless methods. In order to acquire the differential operators, FEM and meshless methods are required to establish the shape functions as well as compute their derivatives, however, NOM can acquire the differential operators easily without the use of shape functions. The tangent stiffness is obtained naturally by simply defining an energy function thus drastically simplifying its implementation. In combination with the weighted residual method and variational principle, the residual and the tangent stiffness matrix can be established by NOM with ease. NOM is enhanced here also with operator energy functional to achieve the linear consistency of the field and avoid instabilities. Although the theoretical framework of the NOM has been proposed, other benefits of this numerical method have not been thoroughly discussed. Furthermore, the details of the derivation of the first/higher-order nonlocal differential operators, construction of the first/higher-order operator energy functional, the derivation of the residual and tangent stiffness matrix of operate energy functional and the detailed implementation procedure of first/higher-order NOM has not been shown before.

The purpose of this chapter is to describe in detail the method of implicitly implementing for first/higher-order NOM, which mainly including the derivation of the first/higher-order nonlocal differential operates, the detailed form of first/higher-order tangent stiffness matrix for operate energy functional and elastic material constitutions in different conditions. The Mathematica code of first/higher-order NOM is presented and explained in detail, and it will be an effective tool for studying complicated physical problems.

The remainder of this chapter is outlined as follows: In Section 2.2, we briefly reviewed the NOM and elaborated on the fundamental concept of support and dual-support. In Section 2.3, we derived the first/higher-order implicit nonlocal differential operators based on the Taylor series expansion. Hereafter, to remove the zero energy mode, the first/higher-order operator energy functional by the nonlocal operator is constructed, combined with

the method of weighed residuals and variational principles, residual and tangent stiffness matrix of operate energy functional are established. At the end of this section, we present the detailed steps of the first/higher-order NOM implementation process. To demonstrate the capabilities of NOM, several numerical examples are presented in Section 2.4. Finally, we conclude in Section 2.5.

2.2 Nonlocal operator method (NOM)

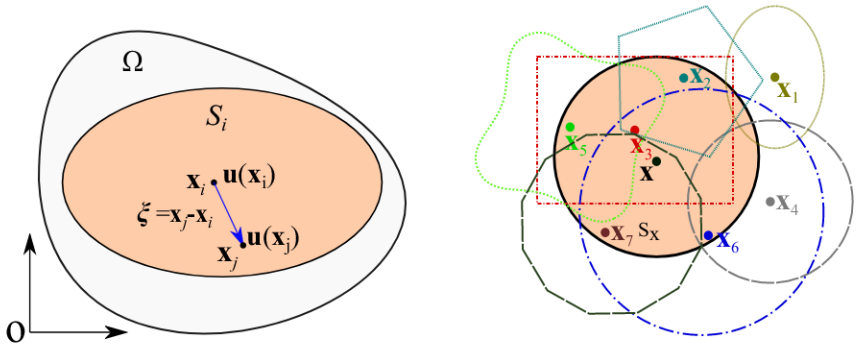

(a) (b)

Figure 2.1: (a) The deformed body's configuration. (b) Schematic diagram for NOM, $\mathcal{S}_\mathbf{x} = \{\mathbf{x}_2, \mathbf{x}_3, \mathbf{x}_5, \mathbf{x}_6, \mathbf{x}_7\}$, $\mathcal{S}'_\mathbf{x} = \{\mathbf{x}_2, \mathbf{x}_3, \mathbf{x}_6, \mathbf{x}_7\}$.

We consider a body occupying the domain $\boldsymbol{\Omega}$ as illustrated in Fig.2.1(a). Let $\mathbf{x}_i$ be the spatial coordinates, $\boldsymbol{\xi}_{ij} := \mathbf{x}_j - \mathbf{x}_i$ is a vector containing the spatial displacement from $\mathbf{x}_i$ to $\mathbf{x}_j$; $\mathbf{u}_i := \mathbf{u}(\mathbf{x}_i, t)$ and $\mathbf{u}_j := \mathbf{u}(\mathbf{x}_j, t)$ are the displacement values for $\mathbf{x}_i$ and $\mathbf{x}_j$, respectively; the relative displacements of spatial vector $\boldsymbol{\xi}_{ij}$ are given by $\mathbf{u}_{ij} := \mathbf{u}_j - \mathbf{u}_i$.

The support $\mathcal{S}_i$ of point $\mathbf{x}_i$ is the domain where any spatial point $\mathbf{x}_j$ forms a spatial vector $\boldsymbol{\xi}_{ij} (= \mathbf{x}_j - \mathbf{x}_i)$ from $\mathbf{x}_i$ to $\mathbf{x}_j$. The support is the foundation for the nonlocal operators. Note that there are no restrictions on the shape of the support. The dual-support is defined as the union of points whose supports include $\mathbf{x}$:

$$\mathcal{S}'_i = \{\mathbf{x}_j | \mathbf{x}_i \in \mathcal{S}_j\}. \tag{2.1}$$

Point $\mathbf{x}_j$ forms the dual-vector $\boldsymbol{\xi}'_{ij} (= \mathbf{x}_i - \mathbf{x}_j = -\boldsymbol{\xi}_{ij})$ in $\mathcal{S}'_i$. On the other hand, $\boldsymbol{\xi}'_{ij}$ is the spatial vector formed in $\mathcal{S}_j$. Fig.2.1(b) visualizes the concept of support and dual-support.

The nonlocal operator method is based on nonlocal operators that replace the local operators in calculus. Thus, the functional designed to construct a residual and tangent stiffness matrix is formulated in terms of the nonlocal differential operator.

The nonlocal gradient approximation [Yang and Chen, 2020, Yang and Lin, 2020] of a vector field $\mathbf{u}$ for a point $\mathbf{x}_i$ in support $\mathcal{S}_i$ is defined by

$$\tilde{\nabla}\mathbf{u}_i := \int_{\mathcal{S}_i} \mathbb{w}(\boldsymbol{\xi}_{ij})\mathbf{u}_{ij} \otimes \boldsymbol{\xi}_{ij} \mathrm{d}V_j \cdot \Big(\int_{\mathcal{S}_i} \mathbb{w}(\boldsymbol{\xi}_{ij})\boldsymbol{\xi}_{ij} \otimes \boldsymbol{\xi}_{ij} \mathrm{d}V_j \Big)^{-1}. \tag{2.2}$$

where $\mathbb{w}(\boldsymbol{\xi}_{ij})$ is the weight function for vector $\boldsymbol{\xi}_{ij}$ in support $\mathcal{S}_i$. It can be shown [Ren et al., 2020b] that the nonlocal gradient operator and it's variation in discrete form is given by

$$\tilde{\nabla}\mathbf{u}_i = \sum_{j\in\mathcal{S}_i} \mathbb{w}(\boldsymbol{\xi}_{ij})\mathbf{u}_{ij} \otimes \boldsymbol{\xi}_{ij} \Delta V_j \cdot \Big(\sum_{j\in\mathcal{S}_i} \mathbb{w}(\boldsymbol{\xi}_{ij})\boldsymbol{\xi}_{ij} \otimes \boldsymbol{\xi}_{ij} \Delta V_j \Big)^{-1}, \tag{2.3}$$

$$\tilde{\nabla}\delta\mathbf{u}_i = \sum_{j\in\mathcal{S}_i} \mathbb{w}(\boldsymbol{\xi}_{ij})\delta\mathbf{u}_{ij} \otimes \boldsymbol{\xi}_{ij} \Delta V_j \cdot \Big(\sum_{j\in\mathcal{S}_i} \mathbb{w}(\boldsymbol{\xi}_{ij})\boldsymbol{\xi}_{ij} \otimes \boldsymbol{\xi}_{ij} \Delta V_j \Big)^{-1}. \tag{2.4}$$

In order to remove the zero-energy mode, a operator energy functional to achieve the linear field of the vector field is proposed [Ren et al., 2020b]. The vector field's operator energy functional for a point is defined as

$$\mathcal{F}_i^{hg} = \frac{p^{hg}}{2m_{\mathbf{K}_i}} \int_{\mathcal{S}_i} \mathbb{w}(\boldsymbol{\xi}_{ij})(\tilde{\nabla}\mathbf{u}_i \cdot \boldsymbol{\xi}_{ij} - \mathbf{u}_{ij})^T(\tilde{\nabla}\mathbf{u}_i \cdot \boldsymbol{\xi}_{ij} - \mathbf{u}_{ij}) \mathrm{d}V_j \tag{2.5}$$

where $\frac{p^{hg}}{2m_{\mathbf{K}_i}}$ is the operator energy functional coefficient, $m_{\mathbf{K}_i} = \mathrm{tr}[\mathbf{K}_i]$, p^{hg} is the penalty coefficient. The shape tensor $\mathbf{K}_i$ is defined as

$$\mathbf{K}_i = \int_{\mathcal{S}_i} \mathbb{w}(\boldsymbol{\xi}_{ij})\boldsymbol{\xi}_{ij} \otimes \boldsymbol{\xi}_{ij} \mathrm{d}V_j \tag{2.6}$$

2.3 Implementation

2.3.1 Derivation of the first-order implicit nonlocal differential operators

The displacement field at any point in the elastic body can be represented by three displacement components u, v, w along the rectangular coordinate axis, and it's three dimension vector form is

$$\mathbf{u} = (u, v, w)^T \tag{2.7}$$

The first-order Taylor series expansion at origin point for a displacement field $\mathbf{u}$ is given as

$$\mathbf{u}' = \mathbf{u} + \nabla\mathbf{u} \cdot \boldsymbol{\xi} + O(\boldsymbol{\xi}^2) \tag{2.8}$$

where $\nabla := (\frac{\partial}{\partial x}, \frac{\partial}{\partial y}, \frac{\partial}{\partial z})$; $\boldsymbol{\xi} := (x, y, z)^T$ denotes the initial bond vector, $O(\boldsymbol{\xi}^2)$ represents higher-order terms, and for linear field $O(\boldsymbol{\xi}^2) = 0$. $(\mathbf{u}' - \mathbf{u}) \otimes \boldsymbol{\xi}$ can be obtained from Eq.2.8 and can be shown as

$$(\mathbf{u}' - \mathbf{u}) \otimes \boldsymbol{\xi} = \nabla \mathbf{u} \cdot \boldsymbol{\xi} \otimes \boldsymbol{\xi}$$

Integrate $(\mathbf{u}' - \mathbf{u}) \otimes \boldsymbol{\xi}$ in the domain $\mathcal{S}_i$, one will obtain

$$\int_{\mathcal{S}_i} \mathbb{w}(\boldsymbol{\xi}) (\mathbf{u}' - \mathbf{u}) \otimes \boldsymbol{\xi} \mathrm{d}V = \nabla \mathbf{u} \int_{\mathcal{S}_i} \mathbb{w}(\boldsymbol{\xi}) \boldsymbol{\xi} \otimes \boldsymbol{\xi} \mathrm{d}V \tag{2.9}$$

The gradient operate $\nabla \mathbf{u}$ can be expressed as

$$\nabla \mathbf{u} = \int_{\mathcal{S}_i} \mathbb{w}(\boldsymbol{\xi}) (\mathbf{u}' - \mathbf{u}) \otimes \boldsymbol{\xi} \mathrm{d}V \cdot \left[\int_{\mathcal{S}_i} \mathbb{w}(\boldsymbol{\xi}) \boldsymbol{\xi} \otimes \boldsymbol{\xi} \mathrm{d}V \right]^{-1} \tag{2.10}$$

The discrete form of Eq.2.10 at point $\mathbf{x}_i$ can be shown as

$$\nabla \mathbf{u}_i = \sum_{j \in \mathcal{S}_i} \mathbb{w}\left(\boldsymbol{\xi}_{ij}\right) (\mathbf{u}_j - \mathbf{u}_i) \otimes \boldsymbol{\xi}_{ij} \Delta V_j \cdot \left[\sum\nolimits_j \mathbb{w}\left(\boldsymbol{\xi}_{ij}\right) \boldsymbol{\xi}_{ij} \otimes \boldsymbol{\xi}_{ij} \Delta V_j \right]^{-1} \tag{2.11}$$

To simplify the equation more conveniently, in this section, letting $\mathbf{R}_j = \mathbb{w}\left(\boldsymbol{\xi}_{ij}\right) \boldsymbol{\xi}_{ij}^T V_j \cdot \left[\sum_{j \in \mathcal{S}_i} \mathbb{w}\left(\boldsymbol{\xi}_{ij}\right) \boldsymbol{\xi}_{ij} \otimes \boldsymbol{\xi}_{ij} \Delta V_j \right]^{-1} = (\xi_{x_j}, \xi_{y_j}, \xi_{z_j})$, $\mathcal{S}_i = \left[j_1, j_2, j_3, \cdots, j_n \right]$. The nonlocal gradient operator $\tilde{\nabla} \mathbf{u}$ at point $\mathbf{x}_i$ can be rewritten as

$$\tilde{\nabla} \mathbf{u}_i = \sum_{j \in \mathcal{S}_i} (\mathbf{u}_j - \mathbf{u}_i) \left[\xi_{x_j}, \xi_{y_j}, \xi_{z_j} \right] \tag{2.12}$$

According to Eq.2.12, the matrix form of nonlocal gradient operator $\tilde{\nabla} \mathbf{u}$ at point $\mathbf{x}_i$ for vector field can be expressed as

$$\tilde{\nabla} \mathbf{u}_i = \begin{bmatrix} \frac{\partial u_i}{\partial x} & \frac{\partial u_i}{\partial y} & \frac{\partial u_i}{\partial z} \\ \frac{\partial v_i}{\partial x} & \frac{\partial v_i}{\partial y} & \frac{\partial v_i}{\partial z} \\ \frac{\partial w_i}{\partial x} & \frac{\partial w_i}{\partial y} & \frac{\partial w_i}{\partial z} \end{bmatrix} = \begin{bmatrix} -\sum_{j \in \mathcal{S}_i} \xi_{x_j} & \xi_{x_{j1}} & \cdots & \xi_{x_{jn}} \\ -\sum_{j \in \mathcal{S}_i} \xi_{y_j} & \xi_{y_{j1}} & \cdots & \xi_{y_{jn}} \\ -\sum_{j \in \mathcal{S}_i} \xi_{z_j} & \xi_{z_{j1}} & \cdots & \xi_{z_{jn}} \end{bmatrix} \begin{bmatrix} u_i & v_i & w_i \\ u_{j1} & v_{j1} & w_{j1} \\ \cdots & \cdots & \cdots \\ u_{jn} & v_{jn} & w_{jn} \end{bmatrix} \tag{2.13}$$

For the convenience of calculations, we transform the matrix form of nonlocal gradient

operator $\tilde{\nabla}\mathbf{u}_i$ for vector field into vector form and it can be rewritten as

$$\begin{aligned}\tilde{\nabla}\mathbf{u}_i &= \left[\frac{\partial u_i}{\partial x}, \frac{\partial u_i}{\partial y}, \frac{\partial u_i}{\partial z}, \frac{\partial v_i}{\partial x}, \frac{\partial v_i}{\partial y}, \frac{\partial v_i}{\partial z}, \frac{\partial w_i}{\partial x}, \frac{\partial w_i}{\partial y}, \frac{\partial w_i}{\partial z}\right]^T \\ &= \begin{bmatrix} -\sum_{j\in\mathcal{S}_i}\xi_{x_j} & 0 & 0 & \xi_{x_{j1}} & 0 & 0 & \cdots & \xi_{x_{jn}} & 0 & 0 \\ 0 & -\sum_{j\in\mathcal{S}_i}\xi_{y_j} & 0 & 0 & \xi_{y_{j1}} & 0 & \cdots & 0 & \xi_{y_{jn}} & 0 \\ 0 & 0 & -\sum_{j\in\mathcal{S}_i}\xi_{z_j} & 0 & 0 & \xi_{z_{j1}} & \cdots & 0 & 0 & \xi_{z_{jn}} \\ -\sum_{j\in\mathcal{S}_i}\xi_{x_j} & 0 & 0 & \xi_{x_{j1}} & 0 & 0 & \cdots & \xi_{x_{jn}} & 0 & 0 \\ 0 & -\sum_{j\in\mathcal{S}_i}\xi_{y_j} & 0 & 0 & \xi_{y_{j1}} & 0 & \cdots & 0 & \xi_{y_{jn}} & 0 \\ 0 & 0 & -\sum_{j\in\mathcal{S}_i}\xi_{z_j} & 0 & 0 & \xi_{z_{j1}} & \cdots & 0 & 0 & \xi_{z_{jn}} \\ -\sum_{j\in\mathcal{S}_i}\xi_{x_j} & 0 & 0 & \xi_{x_{j1}} & 0 & 0 & \cdots & \xi_{x_{jn}} & 0 & 0 \\ 0 & -\sum_{j\in\mathcal{S}_i}\xi_{y_j} & 0 & 0 & \xi_{y_{j1}} & 0 & \cdots & 0 & \xi_{y_{jn}} & 0 \\ 0 & 0 & -\sum_{j\in\mathcal{S}_i}\xi_{z_j} & 0 & 0 & \xi_{z_{j1}} & \cdots & 0 & 0 & \xi_{z_{jn}} \end{bmatrix} \begin{bmatrix} u_i \\ v_i \\ w_i \\ u_{j1} \\ v_{j1} \\ w_{j1} \\ \cdots \\ u_{jn} \\ v_{jn} \\ w_{jn} \end{bmatrix} \\ &= \mathscr{B}_i\mathscr{U}_i \end{aligned} \tag{2.14}$$

Similarly, the nonlocal gradient operator $\tilde{\nabla}u$ at point $\mathbf{x}_i$ for scalar field is written as

$$\tilde{\nabla}u_i = \begin{bmatrix} \frac{\partial u_i}{\partial x} \\ \frac{\partial u_i}{\partial y} \\ \frac{\partial u_i}{\partial z} \end{bmatrix} = \begin{bmatrix} -\sum_{j\in\mathcal{S}_i}\xi_{x_j} & \xi_{x_{j1}} & \cdots & \xi_{x_{jn}} \\ -\sum_{j\in\mathcal{S}_i}\xi_{y_j} & \xi_{y_{j1}} & \cdots & \xi_{y_{jn}} \\ -\sum_{j\in\mathcal{S}_i}\xi_{z_j} & \xi_{z_{j1}} & \cdots & \xi_{z_{jn}} \end{bmatrix} \begin{bmatrix} u_i \\ u_{j1} \\ \cdots \\ u_{jn} \end{bmatrix} = \mathscr{B}_i\mathscr{U}_i \tag{2.15}$$

2.3.2 Derivation of the higher-order implicit nonlocal differential operators

The higher-order NOM is based on higher-order Taylor series expansion of a multi-variable function. Consider a vector field $\mathbf{u}$ at point $\mathbf{x}_j$ ($\mathbf{x}_j \in \mathcal{S}_i$). For convenience, we shorthand $\mathbf{u}(\mathbf{x}_j)$ by $\mathbf{u}_j$, which can be estimated via a Taylor expansion based on $\mathbf{u}_i$ in $\mathbb{r}$ dimensions with the highest order of derivatives as $\mathbb{n}$:

$$\mathbf{u}_j = \mathbf{u}_i + \sum_{(\mathbb{n}_1,\ldots,\mathbb{n}_\mathbb{r})\in\alpha_\mathbb{r}^\mathbb{n}} \frac{\boldsymbol{\xi}_1^{\mathbb{n}_1}\ldots\boldsymbol{\xi}_\mathbb{r}^{\mathbb{n}_\mathbb{r}}}{\mathbb{n}_1!\ldots\mathbb{n}_\mathbb{r}!}\mathbf{u}_{i,\mathbb{n}_1\ldots\mathbb{n}_\mathbb{r}} + O(\boldsymbol{\xi}^{|\alpha|+1}) \tag{2.16}$$

where

$$\boldsymbol{\xi}_{ij} = (\mathbf{x}_{j1} - \mathbf{x}_{i1}, \ldots, \mathbf{x}_{jd} - \mathbf{x}_{id}) \tag{2.17}$$

$$\mathbf{u}_{i,\mathbb{n}_1\ldots\mathbb{n}_\mathbb{r}} = \frac{\partial^{\mathbb{n}_1+\ldots+\mathbb{n}_\mathbb{r}}\mathbf{u}_i}{\partial\mathbf{x}_{i1}^{\mathbb{n}_1}\ldots\partial\mathbf{x}_{id}^{\mathbb{n}_\mathbb{r}}} \tag{2.18}$$

$$|\alpha| = \max(\mathbb{n}_1 + \ldots + \mathbb{n}_\mathbb{r}) \tag{2.19}$$

where $\mathbb{r}$ represents the dimension and $\mathbb{n}$ denotes the highest order of derivatives. $\alpha_{\mathbb{r}}^{\mathbb{n}}$ is a compilation of multi-indexes that have been flattened and it can be written as

$$\alpha_{\mathbb{r}}^{\mathbb{n}} = \{(\mathbb{n}_1, ..., \mathbb{n}_{\mathbb{r}}) | 1 \leq \sum_{i=1}^{\mathbb{r}} \mathbb{n}_i \leq \mathbb{n},\ \mathbb{n}_i \in \mathbb{N}^0, 1 \leq i \leq \mathbb{r}\} \tag{2.20}$$

where $\mathbb{N}^0 = \{0, 1, 2, ...\}$.

Note that Eq.2.16 is very sensitive to the round-off error, we here include the characteristic length scale $\mathbb{l}_i$ of support $\mathcal{S}_i$, and the modified Taylor series expansion can be rewritten as

$$\begin{aligned} \mathbf{u}_j &= \mathbf{u}_i + \sum_{(\mathbb{n}_1,...,\mathbb{n}_{\mathbb{r}}) \in \alpha_{\mathbb{r}}^{\mathbb{n}}} \frac{\boldsymbol{\xi}_1^{\mathbb{n}_1} ... \boldsymbol{\xi}_{\mathbb{r}}^{\mathbb{n}_{\mathbb{r}}}}{\mathbb{l}_i^{\mathbb{n}_1+...+\mathbb{n}_{\mathbb{r}}}} \Big(\frac{\mathbb{l}_i^{\mathbb{n}_1+...+\mathbb{n}_{\mathbb{r}}}}{\mathbb{n}_1!...\mathbb{n}_{\mathbb{r}}!} \mathbf{u}_{i,\mathbb{n}_1...\mathbb{n}_{\mathbb{r}}} \Big) + O(\boldsymbol{\xi}^{\mathbb{n}+1}) \\ &= \mathbf{u}_i + \sum_{(\mathbb{n}_1,...,\mathbb{n}_{\mathbb{r}}) \in \alpha_{\mathbb{r}}^{\mathbb{n}}} \frac{\boldsymbol{\xi}_1^{\mathbb{n}_1} ... \boldsymbol{\xi}_{\mathbb{r}}^{\mathbb{n}_{\mathbb{r}}}}{\mathbb{l}_i^{\mathbb{n}_1+...+\mathbb{n}_{\mathbb{r}}}}\ \mathbf{u}^{\mathbb{l}}_{i,\mathbb{n}_1...\mathbb{n}_{\mathbb{r}}} + O(\boldsymbol{\xi}^{\mathbb{n}+1}) \end{aligned} \tag{2.21}$$

For any multi-index $(\mathbb{n}_1, ..., \mathbb{n}_{\mathbb{r}}) \in \alpha_{\mathbb{r}}^{\mathbb{n}}$, $\mathbf{u}^{\mathbb{l}}_{i,\mathbb{n}_1...\mathbb{n}_{\mathbb{r}}} = \frac{\mathbb{l}_i^{\mathbb{n}_1+...+\mathbb{n}_{\mathbb{r}}}}{\mathbb{n}_1!...\mathbb{n}_{\mathbb{r}}!} \mathbf{u}_{i,\mathbb{n}_1...\mathbb{n}_{\mathbb{r}}}, \forall (\mathbb{n}_1, ..., \mathbb{n}_{\mathbb{r}}) \in \alpha_{\mathbb{r}}^{\mathbb{n}}$. We let $\boldsymbol{p}_j^{\mathbb{l}}$, $\partial_\alpha^{\mathbb{l}} \mathbf{u}_i$ and $\partial_\alpha \mathbf{u}_i$ denotes the flattened polynomials, scaled partial derivatives, partial derivatives, respectively, according to multi-index notation $\alpha_{\mathbb{r}}^{\mathbb{n}}$ and they can be shown as

$$\begin{aligned} \boldsymbol{p}_j^{\mathbb{l}} &= (\frac{\boldsymbol{\xi}_{\mathbb{r}}}{\mathbb{l}}, ..., \frac{\boldsymbol{\xi}_1^{\mathbb{n}_1} ... \boldsymbol{\xi}_{\mathbb{r}}^{\mathbb{n}_{\mathbb{r}}}}{\mathbb{l}^{\mathbb{n}_1+...+\mathbb{n}_{\mathbb{r}}}}, ..., \frac{\boldsymbol{\xi}_1^{\mathbb{n}}}{\mathbb{l}^{\mathbb{n}}})^T \\ \partial_\alpha^{\mathbb{l}} \mathbf{u}_i &= (\mathbf{u}^{\mathbb{l}}_{i,0...1}, ..., \mathbf{u}^{\mathbb{l}}_{i,\mathbb{n}_1...\mathbb{n}_{\mathbb{r}}}, ..., \mathbf{u}^{\mathbb{l}}_{i,\mathbb{n}...0})^T \\ \partial_\alpha \mathbf{u}_i &= (\mathbf{u}_{i,0...1}, ..., \mathbf{u}_{i,\mathbb{n}_1...\mathbb{n}_{\mathbb{r}}}, ..., \mathbf{u}_{i,\mathbb{n}...0})^T \end{aligned} \tag{2.22}$$

The $\mathbb{l}$ in the Eq.2.22 allows the terms of the same characteristic scale for length. The current partial derivatives can be recovered by

$$\partial_\alpha \mathbf{u}_i = \mathrm{diag}\big[\mathbb{l}_i, ..., \frac{\mathbb{l}_i^{\mathbb{n}_1+...+\mathbb{n}_{\mathbb{r}}}}{\mathbb{n}_1!...\mathbb{n}_{\mathbb{r}}!}, ..., \frac{\mathbb{l}_i^{\mathbb{n}}}{\mathbb{n}!}\big]^{-1} \partial_\alpha^{\mathbb{l}} \mathbf{u}_i \tag{2.23}$$

In which diag $[\mathcal{X}_1, ..., \mathcal{X}_{\mathbb{n}}]$ signifies a diagonal matrix of $\mathcal{X}_1, ..., \mathcal{X}_{\mathbb{n}}$, whose diagonal entries begin from the upper left corner. Hence, the expansion of the Taylor series with $\mathbf{u}_i$ to the left of the Eq.2.21 can be rewritten as

$$\mathbf{u}_{ij} = (\partial_\alpha^{\mathbb{l}} \mathbf{u}_i)^T \boldsymbol{p}_j^{\mathbb{l}}, \forall j \in \mathcal{S}_i \tag{2.24}$$

where $\mathbf{u}_{ij} = \mathbf{u}_j - \mathbf{u}_i$.

Integrate $\mathbf{u}_{ij}$ with weighted coefficient $\mathbb{w}(\boldsymbol{\xi}_{ij})(\boldsymbol{p}_j^{\mathbb{l}})^T$ in support $\mathcal{S}_i$, we obtain

$$\begin{aligned} \int_{\mathcal{S}_i} \mathbb{w}(\boldsymbol{\xi}_{ij}) \mathbf{u}_{ij} (\boldsymbol{p}_j^{\mathbb{l}})^T \mathrm{d}V_j &= (\partial_\alpha^{\mathbb{l}} \mathbf{u}_i)^T \int_{\mathcal{S}_i} \mathbb{w}(\boldsymbol{\xi}_{ij}) \boldsymbol{p}_j^{\mathbb{l}} \otimes (\boldsymbol{p}_j^{\mathbb{l}})^T \mathrm{d}V_j \\ &= (\partial_\alpha \mathbf{u}_i)^T \mathbb{L}_i \int_{\mathcal{S}_i} \mathbb{w}(\boldsymbol{\xi}_{ij}) \boldsymbol{p}_j^{\mathbb{l}} \otimes (\boldsymbol{p}_j^{\mathbb{l}})^T \mathrm{d}V_j \end{aligned} \tag{2.25}$$

where

$$\mathbb{L}_i = \mathrm{diag}\big[\mathbb{I}_i, ..., \frac{\mathbb{I}_i^{\mathbb{n}_1+...+\mathbb{n}_\mathbb{r}}}{\mathbb{n}_1!...\mathbb{n}_\mathbb{r}!}, ..., \frac{\mathbb{I}_i^{\mathbb{n}}}{\mathbb{n}!}\big] \tag{2.26}$$

Therefore, the nonlocal operator $\tilde{\partial}_\alpha \mathbf{u}_i$ and its variation can be obtained as

$$\begin{cases} \tilde{\partial}_\alpha \mathbf{u}_i = \mathbf{K}_{\alpha i} \cdot \int_{\mathcal{S}_i} \mathbb{w}(\boldsymbol{\xi}_{ij}) \boldsymbol{p}_j^{\mathbb{I}} \mathbf{u}_{ij} \mathrm{d}V_j \\ \tilde{\partial}_\alpha \delta\mathbf{u}_i = \mathbf{K}_{\alpha i} \cdot \int_{\mathcal{S}_i} \mathbb{w}(\boldsymbol{\xi}_{ij}) \boldsymbol{p}_j^{\mathbb{I}} (\delta\mathbf{u}_j - \delta\mathbf{u}_i) \mathrm{d}V_j \end{cases} \tag{2.27}$$

where

$$\mathbf{K}_{\alpha i} = \mathbb{L}_i^{-1} \Big(\int_{\mathcal{S}_i} \mathbb{w}(\boldsymbol{\xi}_{ij}) \boldsymbol{p}_j^{\mathbb{I}} \otimes (\boldsymbol{p}_j^{\mathbb{I}})^T \mathrm{d}V_j \Big)^{-1} \tag{2.28}$$

In this section, points of the domain Ω in $\mathcal{S}_i$ be symbolized as

$$\mathcal{S}_i = \{j_1, ..., j_k, ..., j_n\} \tag{2.29}$$

where $j_1, ..., j_k, ..., j_n$ denote the global indices of neighbors for point $\mathbf{x}_i$, and n denotes the quantity of i's neighbors in $\mathcal{S}_i$.

The discrete form of Eq.2.27 can be shown as

$$\tilde{\partial}_\alpha \mathbf{u}_i = \mathbf{K}_{\alpha i} \cdot \sum_{j \in \mathcal{S}_i} \mathbf{u}_{ij} \mathbb{w}(\boldsymbol{\xi}_{ij}) \boldsymbol{p}_j^{\mathbb{I}} \Delta V_j = \mathbf{K}_{\alpha i} \boldsymbol{p}_{\mathbb{w}i}^{\mathbb{I}} \Delta \mathbf{u}_i \tag{2.30}$$

$$\tilde{\partial}_\alpha \delta\mathbf{u}_i = \mathbf{K}_{\alpha i} \cdot \sum_{j \in \mathcal{S}_i} \delta\mathbf{u}_{ij} \mathbb{w}(\boldsymbol{\xi}_{ij}) \boldsymbol{p}_j^{\mathbb{I}} \Delta V_j = \mathbf{K}_{\alpha i} \boldsymbol{p}_{\mathbb{w}i}^{\mathbb{I}} \delta\Delta \mathbf{u}_i \tag{2.31}$$

where

$$\begin{aligned} \mathbf{K}_{\alpha i} &= \mathbb{L}_i^{-1} \Big(\sum_{j \in \mathcal{S}_i} \mathbb{w}(\boldsymbol{\xi}_{ij}) \boldsymbol{p}_j^{\mathbb{I}} \otimes (\boldsymbol{p}_j^{\mathbb{I}})^T \Delta V_j \Big)^{-1} \\ \boldsymbol{p}_{\mathbb{w}i}^{\mathbb{I}} &= \Big(\mathbb{w}(\boldsymbol{\xi}_{ij_1}) \boldsymbol{p}_{j_1}^{\mathbb{I}} \Delta V_{j_1}, ..., \mathbb{w}(\boldsymbol{\xi}_{ij_{n_i}}) \boldsymbol{p}_{j_{n_i}}^{\mathbb{I}} \Delta V_{j_{n_i}} \Big) \\ \Delta \mathbf{u}_i &= (\mathbf{u}_{ij_1}, ..., \mathbf{u}_{ij_k}, ..., \mathbf{u}_{ij_n})^T \end{aligned} \tag{2.32}$$

The nonlocal operator gives all partial derivatives with the highest order up to $\mathbb{n}$. In PDEs, the group of derivatives is a subgroup of the nonlocal operator. Each term in $\tilde{\partial}_\alpha \mathbf{u}_i$ corresponds to a row of $\mathbf{K}_{\alpha i} \boldsymbol{p}_{\mathbb{w}i}^{\mathbb{I}}$ multiplied by $\Delta \mathbf{u}_i$. Eq.2.30 can be used to substitute the differential operators in PDEs to generate a strong form of algebraic equations. Meanwhile, we can solve the linear (nonlinear) weak formulations using the weighted residual

methodology and the variational principle, hence the variation of $\partial_\alpha \mathbf{u}_i$ in Eq.2.31 is required in these circumstances. Eq.2.30 can also be shown more succinctly as

$$\tilde{\partial}_\alpha \mathbf{u}_i = \mathbf{K}_{\alpha i} \boldsymbol{p}^{\mathbb{l}}_{\mathrm{w}i} \Delta \mathbf{u}_i = \left[-(1, \cdots, 1)_n \mathbf{K}_{\alpha i} \mathbf{p}^{\mathbb{l}}_{\mathrm{w}i}, \mathbf{K}_{\alpha i} \mathbf{p}^{\mathbb{l}}_{\mathrm{w}i} \right] \begin{bmatrix} \mathbf{u}_i \\ \mathbf{u}_{j_1} \\ \mathbf{u}_{j_2} \\ \cdots \\ \mathbf{u}_{j_n} \end{bmatrix} = \mathbf{B}_{\alpha i} \mathbf{U}_i \tag{2.33}$$

where $\mathbf{B}_{\alpha i}$ is the nonlocal operator coefficient matrix of point $\mathbf{x}_i$, $(1, \cdots, 1)_{n_p} \mathbf{K}_{\alpha i} \mathbf{p}^{\mathbb{l}}_{\mathrm{w}i}$ is the column sum of $\mathbf{K}_{\alpha i} \mathbf{p}^{\mathbb{l}}_{\mathrm{w}i}$. Using the nodal values in support, the operator matrix generates all partial derivatives of maximal order smaller than $|\alpha| + 1$.

2.3.3 Elastic material constitution

For elastic material, the strain energy functional ψ is a function of the deformation gradient $\boldsymbol{F}$. According to the principles of traditional solid mechanics, the deformation gradient $\boldsymbol{F}$ in 3D form expressed as

$$\boldsymbol{F} = \nabla \mathbf{u} + \mathbf{I}_{3\times 3} = \begin{bmatrix} \frac{\partial u}{\partial x} + 1 & \frac{\partial u}{\partial y} & \frac{\partial u}{\partial z} \\ \frac{\partial v}{\partial x} & \frac{\partial v}{\partial y} + 1 & \frac{\partial v}{\partial z} \\ \frac{\partial w}{\partial x} & \frac{\partial w}{\partial y} & \frac{\partial w}{\partial z} + 1 \end{bmatrix} \tag{2.34}$$

where $\mathbf{I}_{3\times 3}$ denotes the identity tensor.

The first Piola-Kirchhoff stress $\mathbf{P}$ can be derived from the directly derivative of strain energy $\psi(\boldsymbol{F})$ in the context of total Lagrangian formulation, and it can be derived as

$$\mathbf{P} = \frac{\partial \psi(\boldsymbol{F})}{\partial \boldsymbol{F}} = \begin{bmatrix} \mathbb{P}_{11} & \mathbb{P}_{12} & \mathbb{P}_{13} \\ \mathbb{P}_{21} & \mathbb{P}_{22} & \mathbb{P}_{23} \\ \mathbb{P}_{31} & \mathbb{P}_{32} & \mathbb{P}_{33} \end{bmatrix} \tag{2.35}$$

In addition, the fourth order elastic tensor $\mathbf{D}_4$ can be obtained using derivation of the first Piola-Kirchhoff stress

$$\mathbf{D}_4 = \frac{\partial \mathbf{P}}{\partial \boldsymbol{F}} = \frac{\partial^2 \psi(\boldsymbol{F})}{\partial \boldsymbol{F}^T \partial \boldsymbol{F}} \tag{2.36}$$

To obtain the elasticity matrix, based on the Voigt notation, $\mathbf{D}_4$ can be written as a matrix form $\mathscr{D}_{9\times 9}$

$$\mathscr{D}_{9\times 9} = \begin{bmatrix} \frac{\partial \mathbb{P}_{11}}{\partial \mathbb{F}_{11}} & \frac{\partial \mathbb{P}_{11}}{\partial \mathbb{F}_{12}} & \cdots & \frac{\partial \mathbb{P}_{11}}{\partial \mathbb{F}_{33}} \\ \frac{\partial \mathbb{P}_{12}}{\partial \mathbb{F}_{11}} & \frac{\partial \mathbb{P}_{12}}{\partial \mathbb{F}_{12}} & \cdots & \frac{\partial \mathbb{P}_{12}}{\partial \mathbb{F}_{33}} \\ \vdots & \vdots & \ddots & \vdots \\ \frac{\partial \mathbb{P}_{33}}{\partial \mathbb{F}_{11}} & \frac{\partial \mathbb{P}_{33}}{\partial \mathbb{F}_{12}} & \cdots & \frac{\partial \mathbb{P}_{33}}{\partial \mathbb{F}_{33}} \end{bmatrix} = \begin{bmatrix} \frac{\partial^2 \psi(\mathbb{F})}{\partial \mathbb{F}_{11}^2} & \frac{\partial^2 \psi(\mathbb{F})}{\partial \mathbb{F}_{11} \partial \mathbb{F}_{12}} & \cdots & \frac{\partial^2 \psi(\mathbb{F})}{\partial \mathbb{F}_{11} \partial \mathbb{F}_{33}} \\ \frac{\partial^2 \psi(\mathbb{F})}{\partial \mathbb{F}_{12} \partial \mathbb{F}_{11}} & \frac{\partial^2 \psi(\mathbb{F})}{\partial \mathbb{F}_{22}^2} & \cdots & \frac{\partial^2 \psi(\mathbb{F})}{\partial \mathbb{F}_{12} \partial \mathbb{F}_{33}} \\ \vdots & \vdots & \ddots & \vdots \\ \frac{\partial^2 \psi(\mathbb{F})}{\partial \mathbb{F}_{33} \partial \mathbb{F}_{11}} & \frac{\partial^2 \psi(\mathbb{F})}{\partial \mathbb{F}_{33} \partial \mathbb{F}_{12}} & \cdots & \frac{\partial^2 \psi(\mathbb{F})}{\partial \mathbb{F}_{33}^2} \end{bmatrix}, \tag{2.37}$$

where $\mathbb{F}(=\mathbb{F}_{11},\mathbb{F}_{12},\cdots,\mathbb{F}_{33}),\mathbb{P}(=\frac{\partial\psi(\mathbb{F})}{\partial\mathbb{F}_{11}},\frac{\partial\psi(\mathbb{F})}{\partial\mathbb{F}_{12}},\cdots,\frac{\partial\psi(\mathbb{F})}{\partial\mathbb{F}_{33}})$ donates the flattened deformation gradient and flattened first Piola-Kirchhoff stress.

In particular, for isotropic linear elastic material, regarding infinitesimal deformations of a continuous linear elastic material with a tiny displacement gradient relative to unity (i.e.$\nabla\mathbf{u}\ll 1$), any of the strain tensors utilized in finite strain theory (such as the Lagrangian strain tensor) may be geometrically linearized. The non-linear or second-order elements of the finite strain tensor are ignored in this linearization. Hence, we can obtain the Lagrangian strain tensor $\boldsymbol{\varepsilon}=\frac{1}{2}(\boldsymbol{F}+\boldsymbol{F}^T)-\mathbf{I}$ and stress tensor $\boldsymbol{\sigma}=\mathbf{D}:\boldsymbol{\varepsilon}$.

The internal functional energy for 3D linear elastic material can be expressed as

$$\psi(\boldsymbol{\varepsilon})_{3d}=\frac{1}{2}\boldsymbol{\sigma}:\boldsymbol{\varepsilon}=\frac{1}{2}\boldsymbol{\varepsilon}:\mathbf{D}:\boldsymbol{\varepsilon}=\frac{1}{2}\mathrm{d}\mathscr{U}_{3d}^T\mathscr{D}_{3d}\mathrm{d}\mathscr{U}_{3d} \tag{2.38}$$

Likewise, the internal energy functional for plane stress and plane strain conditions can be shown as follows

$$\begin{aligned}\psi(\boldsymbol{\varepsilon})_{\text{plane stress}}&=\frac{1}{2}\mathrm{d}\mathscr{U}_{2d}^T\mathscr{D}_{\text{plane stress}}\mathrm{d}\mathscr{U}_{2d}\\ \psi(\boldsymbol{\varepsilon})_{\text{plane strain}}&=\frac{1}{2}\mathrm{d}\mathscr{U}_{2d}^T\mathscr{D}_{\text{plane strain}}\mathrm{d}\mathscr{U}_{2d}\end{aligned} \tag{2.39}$$

where

$$\mathrm{d}\mathscr{U}_{2d}=\left(\frac{\partial u}{\partial x},\frac{\partial u}{\partial y},\frac{\partial v}{\partial x},\frac{\partial v}{\partial y}\right)^T \tag{2.40}$$

$$\mathrm{d}\mathscr{U}_{3d}=\left(\frac{\partial u}{\partial x},\frac{\partial u}{\partial y},\frac{\partial u}{\partial z},\frac{\partial v}{\partial x},\frac{\partial v}{\partial y},\frac{\partial v}{\partial z},\frac{\partial w}{\partial x},\frac{\partial w}{\partial y},\frac{\partial w}{\partial z}\right)^T \tag{2.41}$$

For linear elastic material, the elastic matrix $\mathscr{D}$ in plane stress, plane strain and 3D conditions can be expressed as

$$\mathscr{D}_{\text{plane stress}}=\frac{E}{1-\nu^2}\begin{bmatrix}1&0&0&\nu\\0&\frac{1-\nu}{2}&\frac{1-\nu}{2}&0\\0&\frac{1-\nu}{2}&\frac{1-\nu}{2}&0\\\nu&0&0&1\end{bmatrix} \tag{2.42}$$

$$\mathscr{D}_{\text{plane strain}}=\frac{E}{(1-2\nu)(1+\nu)}\begin{bmatrix}1-\nu&0&0&\nu\\0&1/2-\nu&1/2-\nu&0\\0&1/2-\nu&1/2-\nu&0\\\nu&0&0&1-\nu\end{bmatrix} \tag{2.43}$$

$$\mathscr{D}_{3D} = \begin{bmatrix} \lambda+2\mu & 0 & 0 & 0 & \lambda & 0 & 0 & 0 & \lambda \\ 0 & \mu & 0 & \mu & 0 & 0 & 0 & 0 & 0 \\ 0 & 0 & \mu & 0 & 0 & 0 & \mu & 0 & 0 \\ 0 & \mu & 0 & \mu & 0 & 0 & 0 & 0 & 0 \\ \lambda & 0 & 0 & 0 & \lambda+2\mu & 0 & 0 & 0 & \lambda \\ 0 & 0 & 0 & 0 & 0 & \mu & 0 & \mu & 0 \\ 0 & 0 & \mu & 0 & 0 & 0 & \mu & 0 & 0 \\ 0 & 0 & 0 & 0 & 0 & \mu & 0 & \mu & 0 \\ \lambda & 0 & 0 & 0 & \lambda & 0 & 0 & 0 & \lambda+2\mu \end{bmatrix} \tag{2.44}$$

where λ, μ represent the Lamé constants, which are related to the Young's modulus E and Poisson's ratio ν:

$$\begin{cases} \lambda = \dfrac{E\nu}{(1+\nu)(1-2\nu)} \\ \mu = \dfrac{E}{2(1+\nu)} \end{cases} \tag{2.45}$$

2.3.4 Construction of the first/higher-order operator energy functional

As a particle-based method, when using node integration the first/higher-order NOM suffer from a zero energy mode [Pian and Chen, 1983, Vignjevic et al., 2000], which results in numerical instability. To eliminate the effect of the zero energy mode, traditional PD and SPH introduce a penalty term to the force state [Breitenfeld et al., 2014]. Nevertheless, the approach described above is only applicable in the explicit time integration formulation. NOM employs operator energy functional for nonlocal gradients to achieve the linear field of the field and avoid numerical instabilities.

In first-order NOM, the operator energy functional at point $\mathbf{x}_i$ can be construct according to the first-order nonlocal operator $\nabla \otimes \mathbf{u}_i$, it can be expressed in discretization form as

$$\begin{aligned} \mathcal{F}_i^{hg} &= \frac{p^{hg}}{2m_{\mathbf{K}_i}} \int_{\mathcal{S}_i} \mathbb{w}(\boldsymbol{\xi}_{ij}) \Big([(u_j - u_i) - \nabla u_i \cdot \boldsymbol{\xi}_{ij}]^2 + [(v_j - v_i) - \nabla v_i \cdot \boldsymbol{\xi}_{ij}]^2 + \\ &[(w_j - w_i) - \nabla w_i \cdot \boldsymbol{\xi}_{ij}]^2 \Big) \mathrm{d}V_j \\ &= \frac{p^{hg}}{2m_{\mathbf{K}_i}} \sum_{j \in \mathcal{S}_i} \mathbb{w}(\boldsymbol{\xi}_{ij}) \Big([(u_j - u_i) - \nabla u_i \cdot \boldsymbol{\xi}_{ij}]^2 + [(v_j - v_i) - \nabla v_i \cdot \boldsymbol{\xi}_{ij}]^2 + \\ &[(w_j - w_i) - \nabla w_i \cdot \boldsymbol{\xi}_{ij}]^2 \Big) \Delta V_j \\ &= \frac{p^{hg}}{2m_{\mathbf{K}_i}} \left(\sum_{j \in \mathcal{S}_i} \mathbb{w}(\boldsymbol{\xi}_{ij}) \Big((u_j - u_i)^2 + (v_j - v_i)^2 + (w_j - w_i)^2 \Big) \Delta V_j - \nabla \otimes \mathbf{u}_i : \nabla \otimes \mathbf{u}_i \cdot \mathbf{K}_i \right) \end{aligned} \tag{2.46}$$

where $\nabla u_i = [\frac{\partial u_i}{\partial x}, \frac{\partial u_i}{\partial y}, \frac{\partial u_i}{\partial z}]^T$, $\nabla \otimes \mathbf{u}_i = \begin{bmatrix} \frac{\partial u_i}{\partial x} & \frac{\partial u_i}{\partial y} & \frac{\partial u_i}{\partial z} \\ \frac{\partial v_i}{\partial x} & \frac{\partial v_i}{\partial y} & \frac{\partial v_i}{\partial z} \\ \frac{\partial w_i}{\partial x} & \frac{\partial w_i}{\partial y} & \frac{\partial w_i}{\partial z} \end{bmatrix}$, $\mathbf{K}_i = \begin{bmatrix} k_{11} & k_{12} & k_{13} \\ k_{12} & k_{22} & k_{23} \\ k_{13} & k_{23} & k_{33} \end{bmatrix}$.

It should be noted that the shape tensor $\mathbf{K}_i$ is involved in $\nabla \otimes \mathbf{u}_i : \nabla \otimes \mathbf{u}_i \cdot \mathbf{K}_i$ and the operator energy functional is valid in any dimension.

For convenience, we let $\Theta = \frac{1}{2}\nabla \otimes \mathbf{u}_i : \nabla \otimes \mathbf{u}_i \cdot \mathbf{K}_i$, $\Upsilon_{3d} = \frac{1}{2}[(u_j - u_i)^2 + (v_j - v_i)^2 + (w_j - w_i)^2]$.

$$
\begin{aligned}
\Theta_{3d} =& \frac{1}{2} \begin{bmatrix} \frac{\partial u_i}{\partial x} & \frac{\partial u_i}{\partial y} & \frac{\partial u_i}{\partial z} \\ \frac{\partial v_i}{\partial x} & \frac{\partial v_i}{\partial y} & \frac{\partial v_i}{\partial z} \\ \frac{\partial w_i}{\partial x} & \frac{\partial w_i}{\partial y} & \frac{\partial w_i}{\partial z} \end{bmatrix} \left(\begin{bmatrix} \frac{\partial u_i}{\partial x} & \frac{\partial u_i}{\partial y} & \frac{\partial u_i}{\partial z} \\ \frac{\partial v_i}{\partial x} & \frac{\partial v_i}{\partial y} & \frac{\partial v_i}{\partial z} \\ \frac{\partial w_i}{\partial x} & \frac{\partial w_i}{\partial y} & \frac{\partial w_i}{\partial z} \end{bmatrix} \begin{bmatrix} k_{11} & k_{12} & k_{13} \\ k_{21} & k_{22} & k_{23} \\ k_{31} & k_{32} & k_{33} \end{bmatrix} \right) \\
=& \frac{1}{2} \Bigg(\frac{\partial u_i}{\partial x}[k_{11}\frac{\partial u_i}{\partial x} + k_{12}\frac{\partial u_i}{\partial y} + k_{13}\frac{\partial u_i}{\partial z}] + \frac{\partial u_i}{\partial y}[k_{12}\frac{\partial u_i}{\partial x} + k_{22}\frac{\partial u_i}{\partial y} + k_{23}\frac{\partial u_i}{\partial z}] + \\
& \frac{\partial u_i}{\partial z}[k_{13}\frac{\partial u_i}{\partial x} + k_{23}\frac{\partial u_i}{\partial y} + k_{33}\frac{\partial v_i}{\partial z}] + \frac{\partial v_i}{\partial x}[k_{11}\frac{\partial v_i}{\partial x} + k_{12}\frac{\partial v_i}{\partial y} + k_{13}\frac{\partial v_i}{\partial z}] + \\
& \frac{\partial v_i}{\partial y}[k_{12}\frac{\partial v_i}{\partial x} + k_{22}\frac{\partial v_i}{\partial y} + k_{23}\frac{\partial v_i}{\partial z}] + \frac{\partial v_i}{\partial z}[k_{13}\frac{\partial v_i}{\partial x} + k_{23}\frac{\partial v_i}{\partial y} + k_{33}\frac{\partial v_i}{\partial z}] + \\
& \frac{\partial w_i}{\partial x}[k_{11}\frac{\partial w_i}{\partial x} + k_{12}\frac{\partial w_i}{\partial y} + k_{13}\frac{\partial w_i}{\partial z}] + \frac{\partial w_i}{\partial y}[k_{12}\frac{\partial w_i}{\partial x} + k_{22}\frac{\partial w_i}{\partial y} + k_{23} \cdot \frac{\partial w_i}{\partial z}] + \\
& \frac{\partial w_i}{\partial z}[k_{13}\frac{\partial w_i}{\partial x} + k_{23}\frac{\partial w_i}{\partial y} + k_{33}\frac{\partial w_i}{\partial z}] \Bigg)
\end{aligned} \tag{2.47}
$$

To facilitate numerical implementation, we transform Eq.2.46 into a detailed form and the point $\mathbf{x}_i$ displacement vector and first-order differential of displacement vector in 3D can be shown as

$$
\begin{aligned}
\mathscr{U}_i &= (u_i, v_i, w_i, u_{j1}, v_{j1}, w_{j1} \cdots u_{jn}, v_{jn}, w_{jn})^T \\
\mathrm{d}\mathscr{U}_i &= (\frac{\partial u_i}{\partial x}, \frac{\partial u_i}{\partial y}, \frac{\partial u_i}{\partial z}, \frac{\partial v_i}{\partial x}, \frac{\partial v_i}{\partial y}, \frac{\partial v_i}{\partial z}, \frac{\partial w_i}{\partial x}, \frac{\partial w_i}{\partial y}, \frac{\partial w_i}{\partial z})^T
\end{aligned} \tag{2.48}
$$

In this chapter, the special variation $\bar{\delta}\mathcal{F}$, $\bar{\delta}^2\mathcal{F}$ and $\delta\mathcal{F}$, $\delta^2\mathcal{F}$ are defined as

$$
\bar{\delta}\mathcal{F} := \partial_{\mathrm{d}\mathscr{U}}\mathcal{F}, \bar{\delta}^2\mathcal{F} := \partial_{\mathrm{d}\mathscr{U}\,\mathrm{d}\mathscr{U}}\mathcal{F} \tag{2.49}
$$

$$
\delta\mathcal{F} := \partial_{\mathscr{U}}\mathcal{F}, \delta^2\mathcal{F} := \partial_{\mathscr{U}\,\mathscr{U}}\mathcal{F} \tag{2.50}
$$

Hence, the following relationships can be derived as

$$\begin{aligned}\bar{\delta}\Theta_{3d} =& \partial_{\mathrm{d}\mathscr{U}_{3d}}\Theta_{3d} \\ =& \begin{bmatrix} [k_{11}\frac{\partial u_i}{\partial x}+k_{12}\frac{\partial u_i}{\partial y}+k_{13}\frac{\partial u_i}{\partial z}] & [k_{12}\frac{\partial u_i}{\partial x}+k_{22}\frac{\partial u_i}{\partial y}+k_{23}\frac{\partial u_i}{\partial z}] & [k_{13}\frac{\partial u_i}{\partial x}+k_{23}\frac{\partial u_i}{\partial y}+k_{33}\frac{\partial v_i}{\partial z}] \\ [k_{11}\frac{\partial v_i}{\partial x}+k_{12}\frac{\partial v_i}{\partial y}+k_{13}\frac{\partial v_i}{\partial z}] & [k_{12}\frac{\partial v_i}{\partial x}+k_{22}\frac{\partial v_i}{\partial y}+k_{23}\frac{\partial v_i}{\partial z}] & [k_{13}\frac{\partial v_i}{\partial x}+k_{23}\frac{\partial v_i}{\partial y}+k_{33}\frac{\partial v_i}{\partial z}] \\ [k_{11}\frac{\partial w_i}{\partial x}+k_{12}\frac{\partial w_i}{\partial y}+k_{13}\frac{\partial w_i}{\partial z}] & [k_{12}\frac{\partial w_i}{\partial x}+k_{22}\frac{\partial w_i}{\partial y}+k_{23}\frac{\partial w_i}{\partial z}] & [k_{13}\frac{\partial w_i}{\partial x}+k_{23}\frac{\partial w_i}{\partial y}+k_{33}\frac{\partial w_i}{\partial z}] \end{bmatrix}\end{aligned} \tag{2.51}$$

$$\begin{aligned}\bar{\delta}^2\Theta_{3d} =& \partial_{\mathrm{d}\mathscr{U}_{3d}\mathrm{d}\mathscr{U}_{3d}}\Theta_{3d} \\ =& \partial_{\mathrm{d}\mathscr{U}_{3d}}\bar{\delta}\Theta_{3d} \\ =& \begin{bmatrix} k_{11} & k_{12} & k_{13} & 0 & 0 & 0 & 0 & 0 & 0 \\ k_{12} & k_{22} & k_{23} & 0 & 0 & 0 & 0 & 0 & 0 \\ k_{13} & k_{23} & k_{33} & 0 & 0 & 0 & 0 & 0 & 0 \\ 0 & 0 & 0 & k_{11} & k_{12} & k_{13} & 0 & 0 & 0 \\ 0 & 0 & 0 & k_{12} & k_{22} & k_{23} & 0 & 0 & 0 \\ 0 & 0 & 0 & k_{13} & k_{23} & k_{33} & 0 & 0 & 0 \\ 0 & 0 & 0 & 0 & 0 & 0 & k_{11} & k_{12} & k_{13} \\ 0 & 0 & 0 & 0 & 0 & 0 & k_{12} & k_{22} & k_{23} \\ 0 & 0 & 0 & 0 & 0 & 0 & k_{13} & k_{23} & k_{33} \end{bmatrix}\end{aligned} \tag{2.52}$$

$$\begin{aligned}\delta\Upsilon_{3d} =& \partial_{\mathscr{U}_{3d}}\Upsilon_{3d} \\ =& \partial_{\mathscr{U}_{3d}}\{\frac{1}{2}[(u_j-u_i)^2+(v_j-v_i)^2+(w_j-w_i)^2]\} \\ =& \left[(u_i-u_j),(v_i-v_j),(w_i-w_j),(-u_i+u_j),(-v_i+v_j),(-w_i+w_j)\right]\end{aligned} \tag{2.53}$$

$$\begin{aligned}\delta^2\Upsilon_{3d} =& \partial_{\mathscr{U}_{3d}\mathscr{U}_{3d}}\Upsilon_{3d} \\ =& \partial_{\mathscr{U}_{3d}}\{(u_i-u_j),(v_i-v_j),(w_i-w_j),(-u_i+u_j),(-v_i+v_j),(-w_i+w_j)\} \\ =& \begin{bmatrix} 1 & 0 & 0 & -1 & 0 & 0 \\ 0 & 1 & 0 & 0 & -1 & 0 \\ 0 & 0 & 1 & 0 & 0 & -1 \\ -1 & 0 & 0 & 1 & 0 & 0 \\ 0 & -1 & 0 & 0 & 1 & 0 \\ 0 & 0 & -1 & 0 & 0 & 1 \end{bmatrix}\end{aligned} \tag{2.54}$$

According to Eqs.2.52 and 2.54, Eq.2.46 can be rewritten as

$$\begin{aligned}
\mathcal{F}_i^{hg} &= \frac{p^{hg}}{2m_{\mathbf{K}_i}}\Bigg(\sum_{j\in\mathcal{S}_i}\mathbb{w}(\boldsymbol{\xi}_{ij})\Big((u_j-u_i)^2+(v_j-v_i)^2+(w_j-w_i)^2\Big)\Delta V_j \\
&\quad -\nabla\otimes\mathbf{u}_i:\nabla\otimes\mathbf{u}_i\cdot\mathbf{K}_i\Bigg) \\
&= \frac{p^{hg}}{2m_{\mathbf{K}_i}}\Big(\mathscr{U}_i{}^T\begin{bmatrix}\sum_{j\in\mathcal{S}_i}\mathbf{I}_j & -\mathbf{I}_{j1} & \cdots & -\mathbf{I}_{j_n}\\ -\mathbf{I}_{j1} & \mathbf{I}_{j1} & \mathbf{0} & \mathbf{0}\\ \vdots & \mathbf{0} & \ddots & \mathbf{0}\\ -\mathbf{I}_{j_n} & \mathbf{0} & \mathbf{0} & \mathbf{I}_{j_n}\end{bmatrix}\mathscr{U}_i-\mathrm{d}\mathscr{U}_i{}^T\begin{bmatrix}\mathbf{K}_i & 0 & 0\\ 0 & \mathbf{K}_i & 0\\ 0 & 0 & \mathbf{K}_i\end{bmatrix}\mathrm{d}\mathscr{U}_i\Big) \\
&= \frac{p^{hg}}{2m_{\mathbf{K}_i}}\Big(\mathscr{U}_i{}^T\begin{bmatrix}\sum_{j\in\mathcal{S}_i}\mathbf{I}_j & -\mathbf{I}_{j1} & \cdots & -\mathbf{I}_{j_n}\\ -\mathbf{I}_{j1} & \mathbf{I}_{j1} & \mathbf{0} & \mathbf{0}\\ \vdots & \mathbf{0} & \ddots & \mathbf{0}\\ -\mathbf{I}_{j_n} & \mathbf{0} & \mathbf{0} & \mathbf{I}_{j_n}\end{bmatrix}\mathscr{U}_i-\mathscr{U}_i{}^T\mathscr{B}_i{}^T\begin{bmatrix}\mathbf{K}_i & 0 & 0\\ 0 & \mathbf{K}_i & 0\\ 0 & 0 & \mathbf{K}_i\end{bmatrix}\mathscr{B}_i\mathscr{U}_i\Big) \\
&= \frac{p^{hg}}{2m_{\mathbf{K}_i}}\mathscr{U}_i{}^T\Big(\begin{bmatrix}\sum_{j\in\mathcal{S}_i}\mathbf{I}_j & -\mathbf{I}_{j1} & \cdots & -\mathbf{I}_{j_n}\\ -\mathbf{I}_{j1} & \mathbf{I}_{j1} & \mathbf{0} & \mathbf{0}\\ \vdots & \mathbf{0} & \ddots & \mathbf{0}\\ -\mathbf{I}_{j_n} & \mathbf{0} & \mathbf{0} & \mathbf{I}_{j_n}\end{bmatrix}-\mathscr{B}_i{}^T\begin{bmatrix}\mathbf{K}_i & 0 & 0\\ 0 & \mathbf{K}_i & 0\\ 0 & 0 & \mathbf{K}_i\end{bmatrix}\mathscr{B}_i\Big)\mathscr{U}_i
\end{aligned}\tag{2.55}$$

where $\mathbf{I}_j=\mathbb{w}(\boldsymbol{\xi}_{ij})\Delta V_j(1,1,1)\otimes(1,1,1)^T$.

$$\mathscr{K}_i^{hg}=\partial_{\mathscr{U}_i\mathscr{U}_i}\mathcal{F}_i^{hg}=\frac{p^{hg}}{m_{\mathbf{K}_i}}\Bigg(\begin{bmatrix}\sum_{j\in\mathcal{S}_i}\mathbf{I}_j & -\mathbf{I}_{j1} & \cdots & -\mathbf{I}_{j_n}\\ -\mathbf{I}_{j1} & \mathbf{I}_{j1} & \mathbf{0} & \mathbf{0}\\ \vdots & \mathbf{0} & \ddots & \mathbf{0}\\ -\mathbf{I}_{j_n} & \mathbf{0} & \mathbf{0} & \mathbf{I}_{j_n}\end{bmatrix}-\mathscr{B}_i{}^T\begin{bmatrix}\mathbf{K}_i & 0 & 0\\ 0 & \mathbf{K}_i & 0\\ 0 & 0 & \mathbf{K}_i\end{bmatrix}\mathscr{B}_i\Bigg)\tag{2.56}$$

The global tangent stiffness matrix of operate energy functional, internal residual and tangent stiffness matrix of physical energy functional in support $\mathcal{S}_i$ can be obtained by

$$\overset{hg}{\mathscr{K}}_i=\sum_{j\in\mathcal{S}_i}\partial_{\mathscr{U}_i\mathscr{U}_i}\mathcal{F}_i^{hg}\Delta V_j=\sum_{j\in\mathcal{S}_i}\mathscr{K}_i^{hg}\Delta V_j\tag{2.57}$$

$$\mathscr{R}_i=\sum_{j\in\mathcal{S}_i}\partial_{\mathscr{U}_i}\psi(\boldsymbol{\varepsilon})_i\Delta V_j=\sum_{j\in\mathcal{S}_i}\mathscr{B}_i{}^T\cdot\mathscr{D}\cdot\Delta\mathscr{U}_i\Delta V_j\tag{2.58}$$

$$\mathscr{K}_i=\sum_{j\in\mathcal{S}_i}\partial_{\mathscr{U}_i}\mathscr{R}_i\Delta V_j=\sum_{j\in\mathcal{S}_i}\mathscr{B}_i{}^T\cdot\mathscr{D}\cdot\mathscr{B}_i\Delta V_j\tag{2.59}$$

Finally, the summation of 3D form for the first-order global tangent stiffness matrix and

hourglass tangent stiffness matrix in support $\mathcal{S}_i$ can be obtained

$$
\begin{aligned}
\mathbb{K}_i &= \mathscr{K}_i + \overset{hg}{\mathscr{K}_i} \\
&= \sum_{j\in\mathcal{S}_i} \Delta V_j \Bigg(\mathscr{B}_i{}^T \cdot \mathscr{D} \cdot \mathscr{B}_i + \frac{p^{hg}}{m_{\mathbf{K}_i}} \Big(\begin{bmatrix} \sum_{j\in\mathcal{S}_i} \mathbf{I}_j & -\mathbf{I}_{j1} & \cdots & -\mathbf{I}_{j_n} \\ -\mathbf{I}_{j1} & \mathbf{I}_{j1} & \mathbf{0} & \mathbf{0} \\ \vdots & \mathbf{0} & \ddots & \mathbf{0} \\ -\mathbf{I}_{j_n} & \mathbf{0} & \mathbf{0} & \mathbf{I}_{j_n} \end{bmatrix} \\
&\quad - \mathscr{B}_i{}^T \begin{bmatrix} \mathbf{K}_i & 0 & 0 \\ 0 & \mathbf{K}_i & 0 \\ 0 & 0 & \mathbf{K}_i \end{bmatrix} \mathscr{B}_i \Big) \Bigg) \\
&= \sum_{j\in\mathcal{S}_i} \Delta V_j \Bigg(\mathscr{B}_i{}^T \Big(\mathscr{D} - \frac{p^{hg}}{m_{\mathbf{K}_i}} \begin{bmatrix} \mathbf{K}_i & 0 & 0 \\ 0 & \mathbf{K}_i & 0 \\ 0 & 0 & \mathbf{K}_i \end{bmatrix} \Big) \mathscr{B}_i + \frac{p^{hg}}{m_{\mathbf{K}_i}} \begin{bmatrix} \sum_{j\in\mathcal{S}_i} \mathbf{I}_j & -\mathbf{I}_{j1} & \cdots & -\mathbf{I}_{j_n} \\ -\mathbf{I}_{j1} & \mathbf{I}_{j1} & \mathbf{0} & \mathbf{0} \\ \vdots & \mathbf{0} & \ddots & \mathbf{0} \\ -\mathbf{I}_{j_n} & \mathbf{0} & \mathbf{0} & \mathbf{I}_{j_n} \end{bmatrix} \Bigg)
\end{aligned}
\tag{2.60}
$$

The operator energy functional for higher-order NOM at point $\mathbf{x}_i$ can be construct according to the higher-order nonlocal operator $\partial^{\mathbb{l}}_{\alpha}\mathbf{u}_i$, it can be expressed as

$$
\begin{aligned}
\mathcal{F}^{hg}_{\alpha i} =& \frac{p^{hg}}{2m_{\mathbf{K}_i}} \sum_{j\in\mathcal{S}_i} \mathbb{w}(\boldsymbol{\xi}_{ij}) \big(\mathbf{u}_{ij} - (\boldsymbol{p}^{\mathbb{l}}_j)^T \tilde{\partial}^{\mathbb{l}}_{\alpha} \mathbf{u}_i \big)^2 \Delta V_j \\
=& \frac{p^{hg}}{2m_{\mathbf{K}_i}} \sum_{j\in\mathcal{S}_i} \mathbb{w}(\boldsymbol{\xi}_{ij}) \big(\mathbf{u}^2_{ij} + \partial^{\mathbb{l}}_{\alpha}\mathbf{u}_i^T \boldsymbol{p}^{\mathbb{l}}_j \otimes (\boldsymbol{p}^{\mathbb{l}}_j)^T \partial^{\mathbb{l}}_{\alpha}\mathbf{u}_i - 2\mathbf{u}_{ij} (\boldsymbol{p}^{\mathbb{l}}_j)^T \partial^{\mathbb{l}}_{\alpha}\mathbf{u}_i \big) \Delta V_j \\
=& \frac{p^{hg}}{2m_{\mathbf{K}_i}} \Big(\sum_{j\in\mathcal{S}_i} \mathbb{w}(\boldsymbol{\xi}_{ij}) \mathbf{u}^2_{ij} \Delta V_j + \partial^{\mathbb{l}}_{\alpha}\mathbf{u}_i^T \sum_{j\in\mathcal{S}_i} \mathbb{w}(\boldsymbol{\xi}_{ij}) \boldsymbol{p}^{\mathbb{l}}_j \otimes (\boldsymbol{p}^{\mathbb{l}}_j)^T \Delta V_j \; \partial^{\mathbb{l}}_{\alpha}\mathbf{u}_i - 2\Delta \mathbf{u}_i^T \boldsymbol{p}^T_{\mathbb{w}i} \partial^{\mathbb{l}}_{\alpha}\mathbf{u}_i \Big) \\
=& \frac{p^{hg}}{2m_{\mathbf{K}_i}} \Big(\sum_{j\in\mathcal{S}_i} \mathbb{w}(\boldsymbol{\xi}_{ij}) \mathbf{u}^2_{ij} \Delta V_j + \tilde{\partial}_{\alpha}\mathbf{u}_i^T \mathbb{L}_i \sum_{j\in\mathcal{S}_i} \mathbb{w}(\boldsymbol{\xi}_{ij}) \boldsymbol{p}^{\mathbb{l}}_j \otimes (\boldsymbol{p}^{\mathbb{l}}_j)^T \Delta V_j \; \mathbb{L}_i \partial^{\mathbb{l}}_{\alpha}\mathbf{u}_i \\
& - 2\Delta \mathbf{u}_i^T (\boldsymbol{p}^{\mathbb{l}}_{\mathbb{w}i})^T \mathbb{L}_i \tilde{\partial}_{\alpha}\mathbf{u}_i \Big)
\end{aligned}
\tag{2.61}
$$

By submitting the Eq.2.33 into the below Eq.2.61 and it can be rewritten as

$$\begin{aligned}
\mathcal{F}_{\alpha i}^{hg} =& \frac{p^{hg}}{2m_{\mathbf{K}_i}}\Big(\sum_{j\in\mathcal{S}_i}\mathbb{w}(\boldsymbol{\xi}_{ij})\mathbf{u}_{ij}^2\Delta V_j - \Delta\mathbf{u}_i^T(\boldsymbol{p}_{\mathbb{w}i}^{\mathbb{I}})^T\big(\sum_{j\in\mathcal{S}_i}\mathbb{w}(\boldsymbol{\xi}_{ij})\boldsymbol{p}_j^{\mathbb{I}}\otimes(\boldsymbol{p}_j^{\mathbb{I}})^T\Delta V_j\big)^{-1}\boldsymbol{p}_{\mathbb{w}i}^{\mathbb{I}}\Delta\mathbf{u}_i\Big)\\
=& \frac{p^{hg}}{2m_{\mathbf{K}_i}}\Big(\Delta\mathbf{u}_i^T\mathrm{diag}\big[\mathbb{w}(\boldsymbol{\xi}_{j_1})\Delta V_{j_1},...,\mathbb{w}(\boldsymbol{\xi}_{j_{n_i}})\Delta V_{j_{n_i}}\big]\Delta\mathbf{u}_i - \Delta\mathbf{u}_i^T(\boldsymbol{p}_{\mathbb{w}i}^{\mathbb{I}})^T\mathbf{K}_{\alpha i}\mathbb{L}_i\boldsymbol{p}_{\mathbb{w}i}^{\mathbb{I}}\Delta\mathbf{u}_i\Big)\\
=& \frac{p^{hg}}{2m_{\mathbf{K}_i}}\Delta\mathbf{u}_i^T\Big(\begin{bmatrix}\mathbf{I}_{j1} & \mathbf{0} & \mathbf{0}\\ \mathbf{0} & \ddots & \mathbf{0}\\ \mathbf{0} & \mathbf{0} & \mathbf{I}_{j_n}\end{bmatrix} - (\boldsymbol{p}_{\mathbb{w}i}^{\mathbb{I}})^T\mathbf{K}_{\alpha i}\mathbb{L}_i\boldsymbol{p}_{\mathbb{w}i}^{\mathbb{I}}\Big)\Delta\mathbf{u}_i\\
=& \frac{p^{hg}}{2m_{\mathbf{K}_i}}(\mathbf{K}_{\alpha i}^{-1}\mathbf{p}_{\mathbb{w}i}^{\mathbb{I}}\mathbf{B}_{\alpha i}\mathbf{U}_i)^T\Big(\begin{bmatrix}\mathbf{I}_{j1} & \mathbf{0} & \mathbf{0}\\ \mathbf{0} & \ddots & \mathbf{0}\\ \mathbf{0} & \mathbf{0} & \mathbf{I}_{j_n}\end{bmatrix} - (\boldsymbol{p}_{\mathbb{w}i}^{\mathbb{I}})^T\mathbf{K}_i\mathbb{L}_i\boldsymbol{p}_{\mathbb{w}i}^{\mathbb{I}}\Big)\mathbf{K}_{\alpha i}^{-1}\mathbf{p}_{\mathbb{w}i}^{\mathbb{I}}\mathbf{B}_{\alpha i}\mathbf{U}_i \quad (2.62)
\end{aligned}$$

where $\mathbf{I}_j = \mathbb{w}(\boldsymbol{\xi}_{ij})\Delta V_j(1,1,1)\otimes(1,1,1)^T$.

The first and second derivative $\mathcal{F}_{\alpha i}^{hg}$ yield the higher-order residual and the tangent stiffness matrix of operator energy functional and can be expressed as

$$\begin{aligned}
\mathscr{R}_{\alpha i}^{hg} &= \frac{\partial\mathcal{F}_{\alpha i}^{hg}}{\partial\mathbf{U}_i}\\
&= \frac{p^{hg}}{m_{\mathbf{K}_i}}(\mathbf{K}_{\alpha i}^{-1}\mathbf{p}_{\mathbb{w}i}^{\mathbb{I}}\mathbf{B}_{\alpha i})^T\Big(\begin{bmatrix}\mathbf{I}_{j1} & \mathbf{0} & \mathbf{0}\\ \mathbf{0} & \ddots & \mathbf{0}\\ \mathbf{0} & \mathbf{0} & \mathbf{I}_{j_n}\end{bmatrix} - (\boldsymbol{p}_{\mathbb{w}i}^{\mathbb{I}})^T\mathbf{K}_{\alpha i}\mathbb{L}_i\boldsymbol{p}_{\mathbb{w}i}^{\mathbb{I}}\Big)\mathbf{K}_{\alpha i}^{-1}\mathbf{p}_{\mathbb{w}i}^{\mathbb{I}}\mathbf{B}_{\alpha i}\mathbf{U}_i \quad (2.63)
\end{aligned}$$

$$\begin{aligned}
\mathscr{K}_{\alpha i}^{hg} &= \frac{\partial\mathscr{R}_{\alpha i}^{hg}}{\partial\mathbf{U}_i^T} = \frac{\partial^2\mathcal{F}_{\alpha i}^{hg}}{\partial\mathbf{U}_i\partial\mathbf{U}_i^T}\\
&= \frac{p^{hg}}{m_{\mathbf{K}_i}}(\mathbf{K}_{\alpha i}^{-1}\mathbf{p}_{\mathbb{w}i}^{\mathbb{I}}\mathbf{B}_{\alpha i})^T\Big(\begin{bmatrix}\mathbf{I}_{j1} & \mathbf{0} & \mathbf{0}\\ \mathbf{0} & \ddots & \mathbf{0}\\ \mathbf{0} & \mathbf{0} & \mathbf{I}_{j_n}\end{bmatrix} - (\boldsymbol{p}_{\mathbb{w}i}^{\mathbb{I}})^T\mathbf{K}_{\alpha i}\mathbb{L}_i\boldsymbol{p}_{\mathbb{w}i}^{\mathbb{I}}\Big)\mathbf{K}_{\alpha i}^{-1}\mathbf{p}_{\mathbb{w}i}^{\mathbb{I}}\mathbf{B}_{\alpha i} \quad (2.64)
\end{aligned}$$

The higher-order global tangent stiffness matrix of operator energy functional in support $\mathcal{S}_i$ can be computed by

$$\overset{hg}{\mathscr{K}}_{\alpha i} = \sum_{j\in\mathcal{S}_i}\partial_{\mathbf{U}_i\mathbf{U}_i}\mathcal{F}_{\alpha i}^{hg}\Delta V_j = \sum_{j\in\mathcal{S}_i}\mathscr{K}_{\alpha i}^{hg}\Delta V_j \quad (2.65)$$

Finally, the summation of the higher-order global tangent stiffness matrix and hourglass tangent stiffness matrix in support $\mathcal{S}_i$ can be obtained

$$\begin{aligned}\mathbb{K}_{\alpha i} &= \mathscr{K}_{\alpha i} + \overset{hg}{\mathscr{K}}_{\alpha i} \\ &= \sum_{j\in\mathcal{S}_i}\Bigg(\mathbf{B}_{\alpha i}{}^T\cdot\mathscr{D}\cdot\mathbf{B}_{\alpha i} + \frac{p^{hg}}{m_{\mathbf{K}_i}}(\mathbf{K}_{\alpha i}^{-1}\mathbf{p}_{\mathrm{w}i}^{\mathbb{I}}\mathbf{B}_{\alpha i})^T\Big(\begin{bmatrix}\mathbf{I}_{j1} & \mathbf{0} & \mathbf{0}\\ \mathbf{0} & \ddots & \mathbf{0}\\ \mathbf{0} & \mathbf{0} & \mathbf{I}_{j_n}\end{bmatrix} \\ &- (\boldsymbol{p}_{\mathrm{w}i}^{\mathbb{I}})^T\mathbf{K}_{\alpha i}\mathbb{L}_i\boldsymbol{p}_{\mathrm{w}i}^{\mathbb{I}}\Big)\mathbf{K}_{\alpha i}^{-1}\mathbf{p}_{\mathrm{w}i}^{\mathbb{I}}\mathbf{B}_{\alpha i}\Bigg)\Delta V_j\end{aligned} \tag{2.66}$$

2.3.5 Numerical implementation with an open-source code

The numerical implementation of the first/higher-order NOM are summarized as the following steps, and a flow chart of the NOM implementation procedure is depicted in Fig.2.2.

Step 1. Discretization of the solution domain.

Consider the solution domain to be a discrete domain consisting of discrete points of varying sizes and shapes that are linked to one another. There are two methods to achieve the discretization of the solution domain. For the first method, a user-defined subroutine ***GridDomain*** is customized, which can discretize the solution domain evenly. This method is mainly used for the discretization of the rule solution domain. The second method can be achieved as follows: initially, the model is created using finite element software (such as ABAQUS), then the model is divided into grids of different sizes according to the characteristics of the model and export the model information into a ***inp*** format file. The model mesh and node information can be read through a user-defined subroutine ***ParseAbaqusFile***, therefore the discrete solution domain with different densities can be achieved.

The Mathematica code for discretization of the solution domain is shown below. In the user-defined subroutine ***GridDomain***, where ***xmin***, ***xmax*** are the minimum and maximum values of solution domain and ***dx*** is the spacing between points.

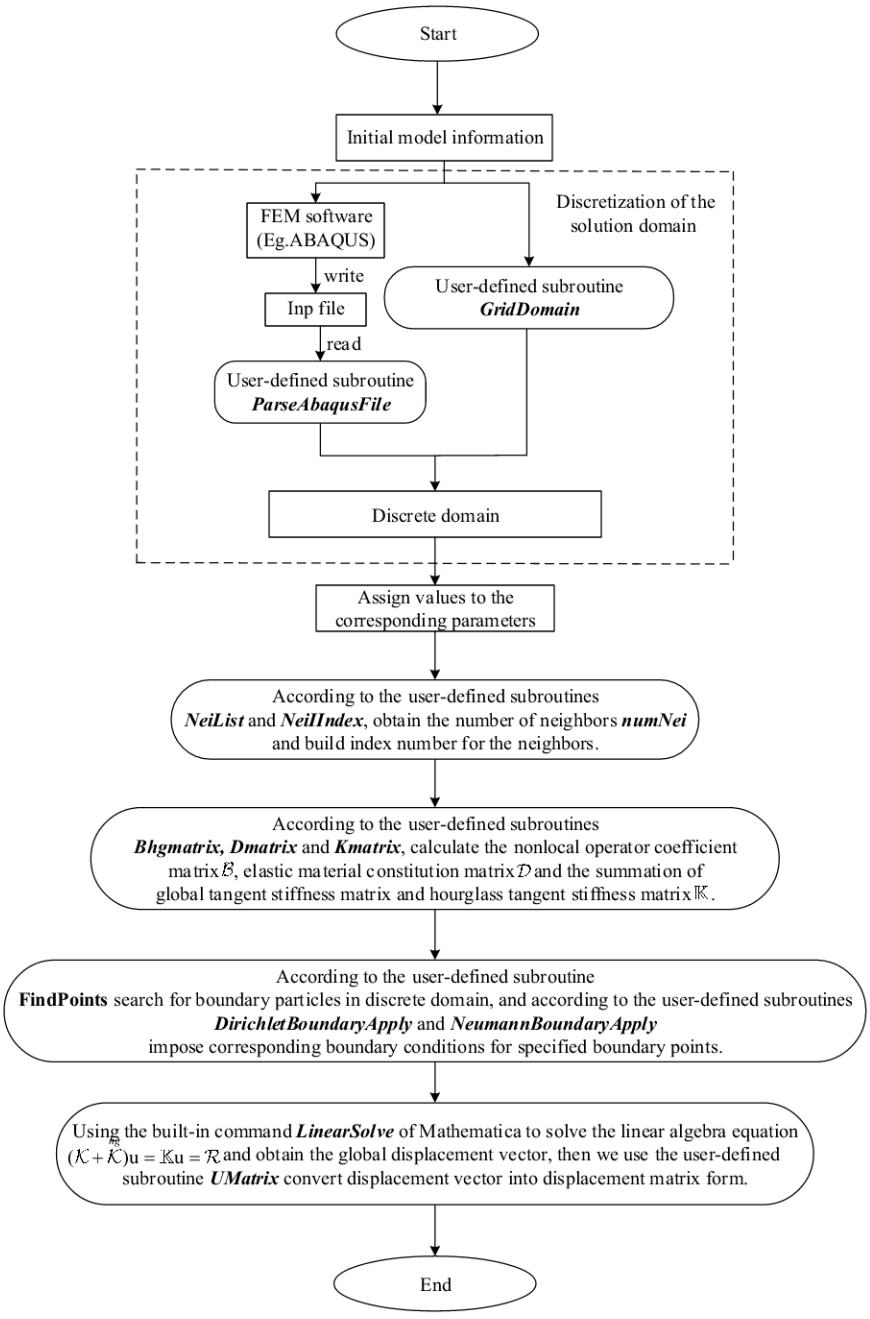

Figure 2.2: NOM implementation procedure.

```
GridDomain[xmin_, xmax_, dx_] := Block[{ndim = Length[xmin], nx = Ceiling[(xmax - xmin) / dx], dx2, res},
   dx2 = (xmax - xmin) / nx;
   If[ndim == 2, res = Table[{i, j}, {i, 0, nx[[1]]}, {j, 0, nx[[2]]}]];
   If[ndim == 3, res = Table[{i, j, k}, {i, 0, nx[[1]]}, {j, 0, nx[[2]]}, {k, 0, nx[[3]]}]];
   res = Flatten[res];
   res = ArrayReshape[res, {Length[res] / ndim, ndim}];
   Do[res[[All, i]] *= dx2[[i]], {i, ndim}]; Do[res[[i]] += xmin, {i, Length[res]}]; res];
ParseAbaqusFile[file_String] :=
  Module[{i, j, k, node, element, setList, oneSet, starList, starLine, tlineStart, tlineEnd, tline,
    strings, String2List, i1, i2, len, pair, ei, j1},
   If[FileExtension[file] ≠ "inp", Print["Error,the file should be Abaqus keyword file .inp"]; Return[];];
   strings = ReadList[file, String];
   If[strings == $Failed, Print["Error,file not found"];
    Return[]];
   i = Dimensions[strings][[1]];
   node = {};
   element = {};
   setList = {};
   starList = {};
   Do[If[StringStartsQ[strings[[j]], "*"] && ! StringStartsQ[strings[[j]], {"**", "$"}], AppendTo[starList, j]],
    {j, i}];
   String2List[str_String] := Module[{sl, s2}, s2 = StringReplace[str, {"E", "e"} → "*^"];
     sl = StringSplit[s2, {",", " "}];
     DeleteCases[ToExpression[sl], Null]];
   Do[starLine = ToLowerCase[strings[[starList[[j]]]]];
    tlineStart = starList[[j]] + 1; tlineEnd = starList[[j + 1]] - 1;
    Which[StringStartsQ[starLine, "*node"], Do[tline = strings[[k]];
      If[! StringStartsQ[tline, "*"], AppendTo[node, String2List[tline]]];, {k, tlineStart, tlineEnd}]
      (**), StringStartsQ[starLine, "*element"], Do[tline = strings[[k]];
      If[! StringStartsQ[tline, "*"], AppendTo[element, String2List[tline]]];, {k, tlineStart, tlineEnd}]
      (**), StringStartsQ[starLine, "*set"], oneSet = {};
     Do[tline = strings[[k]];
      If[! StringStartsQ[tline, "*"], AppendTo[oneSet, String2List[tline]]];, {k, tlineStart, tlineEnd}];
     AppendTo[setList, Flatten[oneSet]] (**)];, {j, 1, Length[starList] - 1}];
   len = Length[node]; i1 = node[[1, 1]]; i2 = node[[len, 1]];
   If[i1 == 1 && i2 == len, Return[{node[[All, 2 ;; -1]], element[[All, 2 ;; -1]], setList}]];
   pair = ConstantArray[0, i2];
   Do[pair[[node[[i, 1]]]] = i, {i, len}];
   len = Length[element];
   Do[ei = element[[i]];
    Do[j1 = ei[[j]];
     ei[[j]] = pair[[j1]];, {j, 2, Length[ei]}];
    element[[i]] = ei;, {i, len}];
   {node[[All, 2 ;; -1]], element[[All, 2 ;; -1]], setList}];
```

Step 2. Definition of the problem and solution domain.

Determine the overall attributes and geometric boundary conditions of the solution domain based on the real case, and assign values to the corresponding parameters.

Step 3. Specify and search for the number of neighbors for each point in support and build index numbers for the specified neighbors.

In this step, a user-defined subroutine ***NeiList*** is customized by the built-in command ***Nearest*** of Mathematica to find the required number of neighbors, and the process of building index number for the specified neighbor points can be achieved by the user-defined subroutine ***NeiIIndex***. The Mathematica code for finding the specified area points and specified number neighbor points in the solution domain is shown below, where ***coord*** is the coordinate of the points, ***numNei*** represents the number of specified neighbors and ***ndim*** denotes the dimension of coordinate.

```
NeiList = Nearest[coord → Automatic, coord, numNei + 1];
NeiIIndex[NeiList_, ndim_] := Module[{n2, n3}, n2 = ConstantArray[0, ndim Length[NeiList]];
   n3 = ndim (NeiList - 1);
   Do[n2[[i ;; -1 ;; ndim]] = n3 + i, {i, ndim}];
   n2];
```

Step 4. Establish the nonlocal operator coefficient matrix, hourglass tangent stiffness matrix, and the summation of global tangent stiffness matrix and hourglass tangent stiffness matrix in first/higher-order form.

① First-order nonlocal operator method.

As shown in below Mathematica code, three user-defined subroutines ***BHgmatrix***, ***Dmatrix*** and ***Kmatrix*** are customized to calculate the nonlocal operator coefficient matrix $\mathscr{B}$, hourglass tangent stiffness matrix $\overset{hg}{\mathscr{K}}$, elastic material constitution matrix $\mathscr{D}$ and the summation of hourglass tangent stiffness matrix and tangent stiffness matrix $\mathbb{K}$. In the user-defined subroutine ***BHgmatrix***, initially the basic forms $\mathscr{B}_i$, $\overset{hg}{\mathscr{K}_i}$ and shape tensor $\mathbf{K}_i$ at point $\mathbf{x}_i$ are constructed, which are named as ***bmatrix***, ***hgmatrix*** and ***kmatrix***, respectively. Subsequently by Eq.2.6, shape tensor can be calculated; by the equation $\mathbf{I}_j = \mathbb{w}(\boldsymbol{\xi}_{ij})V_j(1,1,1)\otimes(1,1,1)^T$ and Eq.2.55, the matrix $\mathbf{I}_j$ can be calculated and the $\overset{hg}{\mathscr{K}_i}$ matrix can be assembled. Similarly, by equation $\mathbf{R}_j = \mathbb{w}\left(\boldsymbol{\xi}_{ij}\right)\boldsymbol{\xi}_{ij}^T V_j \cdot \left[\sum_{j\in\mathcal{S}_i}\mathbb{w}\left(\boldsymbol{\xi}_{ij}\right)\boldsymbol{\xi}_{ij}\otimes\boldsymbol{\xi}_{ij}\Delta V_j\right]^{-1}$ and Eq.2.14, the intermediate variables $\mathbf{R}_j$ can be obtained and the $\mathscr{B}_i$ matrix is assembled. In the user-defined subroutine ***Dmatrix***, by Eqs.2.42, 2.43 and 2.44, the linear elastic solid elastic matrix $\mathscr{D}$ for plane stress, plane strain and 3D conditions can be obtained. Where type=1,2,3 represent the three constitutive models mentioned above. In the user-defined subroutine ***Kmatrix***, by Eq.2.66, the summation of global tangent stiffness matrix and hourglass tangent stiffness matrix $\mathbb{K}$ can be established. In the below Mathematica code, where ***WeiF*** represents the weight function, ***voli*** represents the volume of each point, ***Es, mu*** represents the Young's Modulus and Poisson's ratio, respectively.

```
BHgmatrix[coord_List, WeiF_, voli_List] := Block[{num = Length[coord],
    ndim = Length[coord[[1]]], bmatrix, kmatrix, hgmatrix, invk, xi, vw, ri, Rj, i1, i2, I1, I2},
   bmatrix = ConstantArray[0., {ndim ndim, ndim num}];
   hgmatrix = ConstantArray[0., {ndim num, ndim num}];
   kmatrix = ConstantArray[0., {ndim, ndim}];
   I2 = ConstantArray[0., {ndim ndim, ndim ndim}];
   Do[xi = coord[[j]] - coord[[1]];
    ri = Sqrt[xi.xi];
    vw = voli[[j]] × WeiF[ri];
    kmatrix += vw TensorProduct[xi, xi];
    i1 = ndim (j - 1) + 1; i2 = ndim j;
    I1 = vw IdentityMatrix[ndim];
    hgmatrix[[1 ;; ndim, 1 ;; ndim]] += I1; hgmatrix[[1 ;; ndim, i1 ;; i2]] = -I1;
    hgmatrix[[i1 ;; i2, 1 ;; ndim]] = -I1;
    hgmatrix[[i1 ;; i2, i1 ;; i2]] = I1, {j, 2, num}];
   invk = Inverse[kmatrix];
   Do[xi = coord[[j]] - coord[[1]]; ri = Sqrt[xi.xi]; Rj = voli[[j]] × WeiF[ri] invk.xi;
    Do[bmatrix[[ndim (k - 1) + 1 ;; k ndim, k]] -= Rj;
     bmatrix[[ndim (k - 1) + 1 ;; k ndim, ndim (j - 1) + k]] = Rj, {k, ndim}];
    , {j, 2, num}];
   Do[I2[[j ndim + 1 ;; (j + 1) ndim, j ndim + 1 ;; (j + 1) ndim]] = kmatrix, {j, 0, ndim - 1}];
   hgmatrix -= bmatrix^T.I2.bmatrix;
   hgmatrix /= Tr[kmatrix];
   {bmatrix, hgmatrix}
  ];
Dmatrix[Es_, mu_, type_: 3] :=
  Block[{DMatrix, ndim, l1, l2},
   If[type == 1,
    Return[Es / (1. - mu^2) {{1., 0., 0., mu}, {0., (1. - mu) / 2, (1. - mu) / 2, 0.}, {0., (1. - mu) / 2,
       {mu, 0., 0., 1.}}]];
   If[type == 2,
    Return[Es / (1. - 2 mu) / (1. + mu) {{1. - mu, 0., 0., mu}, {0., 0.5 - mu, 0.5 - mu, 0.}, {0., 0.5 - mu
       {mu, 0., 0., 1. - mu}}]];
   l1 = Es mu / ((1. + mu) (1. - 2 mu)); l2 = Es / 2. / (1. + mu);
   {{l1 + 2 l2, 0., 0., 0., l1, 0., 0., 0., l1}, {0., l2, 0., l2, 0., 0., 0., 0., 0.}, {0., 0., l2, 0., 0
    {0., l2, 0., l2, 0., 0., 0., 0., 0.}, {l1, 0., 0., 0., l1 + 2 l2, 0., 0., 0., l1}, {0., 0., 0., 0., 0
    {0., 0., l2, 0., 0., 0., l2, 0., 0.}, {0., 0., 0., 0., 0., l2, 0., l2, 0.}, {l1, 0., 0., 0., l1, 0.,
  ];
Kmatrix[voli_, bmatrix_, hgmatrix_, Es_, mu_, etype_: 3, pen_: 0.2] :=
  voli (pen Es hgmatrix + bmatrix^T.Dmatrix[Es, mu, etype].bmatrix);
```

② Higher order nonlocal operator method.

The main codes for higher-order NOM are presented in AppendixA, which includes constructing the global higher-order nonlocal operator coefficient matrix $\mathbf{B}_\alpha$, global hourglass tangent stiffness matrix $\overset{hg}{\mathscr{K}}_\alpha$ and the summation of global tangent stiffness matrix and hourglass tangent stiffness matrix $\mathbb{K}_\alpha$. Initially, a user-defined subroutine ***MultiIndex*** is customized to construct multi-index notation in Eq.2.20. where $\boldsymbol{d}$ denotes the dimension,

sum denotes the maximal order of derivatives. Then, the customized user-defined subroutine ***GFD0CoeffHalf*** can obtain the factors of multi-index, polynomials and partial derivatives in designated dimensions with maximal higher-order derivatives in Eq.2.22. For constructing the elastic material constitution matrix, according to Eqs.2.35-2.37, the user-defined subroutine ***FuncRK*** is compiled to obtain elastic matrix $\mathscr{D}$. For higher-order global hourglass tangent stiffness matrix $\overset{hg}{\mathscr{K}}_{\alpha}$ and the summation of global tangent stiffness matrix and hourglass tangent stiffness matrix $\mathbb{K}_{\alpha}$, according to Eqs.2.32, 2.33 and 2.66, two main user-defined subroutines ***NOMPwKhg*** and ***NOMRK*** are customized to achieve the establishment of corresponding matrix.

Step 5. Search boundary points in discrete domain and impose corresponding boundary conditions based on actual problems.

A user-defined subroutine ***FindPoints*** is customize for searching boundary points. When using user-defined subroutine ***FindPoints***, it's need to call another customized subroutine ***LessThancoord*** at the same time. Subsequently, to employ Dirichlet and Neumann boundary conditions to the boundary points, two user-defined subroutines ***DirichletBoundaryApply*** and ***NeumannBoundaryApply*** are customized. Where the penalty method is used in the user-defined subroutine ***DirichletBoundaryApply***. The related Mathematica codes are shown as below, where ***Ksp*** represents the summation of global tangent stiffness matrix and hourglass tangent stiffness matrix $\mathbb{K}$, ***Rsp*** represents the global internal residual, ***pd*** represents the index of the points of application of specified displacement, ***pc*** represents the penalty coefficient and ***pf*** represents the index of the points of application of specified force.

```
FindPoints[coord_List, xmin_List, xmax_List, show_: False] :=
  Module[{ilist = {}, y, r, ndim = Length[coord[[1]]], len = Length[coord]},
   Do[If[LessThancoord[coord[[i]], xmax] && LessThancoord[xmin, coord[[i]]], AppendTo[ilist, i]], {i, len}];
   If[show, If[ Length[coord[[1]]] == 2, Print[ListPlot[coord[[ilist]], DataRange → Automatic]]];
    If[ Length[coord[[1]]] == 3, Print[ListPointPlot3D[coord[[ilist]]], DataRange → Full]]];
   ilist];
LessThancoord[coord1_List, coord2_List] := Module[{p = True}, Do[If[coord1[[i]] > coord2[[i]], p = False;
     Break[]], {i, Length[coord]}];
   Return[p]];
DirichletBoundaryApply[Ksp_, Rsp_, pd_, pc_, scale_: 1.0] := Module[{pi, tk, tk2}, tk = Diagonal[Ksp] // Normal;
   tk2 = tk;
   tk2[[pd[[1]]]] *= (pc + 1.);
   tk2 -= tk;
   Ksp += SparseDiag[tk2];
   Do[pi = pd[[i, 1]]; Rsp[[pi]] = tk2[[pi]] pd[[i, 2]] scale, {i, Length[pd[[1]]]}];];
SparseDiag[a_List] := SparseArray[{{i_, i_} :→ a[[i]]}, Length[a]];
NeumannBoundaryApply[Rsp_, pf_, scale_: 1.0] := Module[{}, Rsp[[pf[[1]]]] += pf[[2]] scale;];
```

Step 6. Solve the global displacement in the discrete domain.

According to step 1 to step 5, the summation of global tangent stiffness matrix and hourglass tangent stiffness matrix $\mathbb{K}$ and global residual vector $\mathscr{R}$ can be calculated. And

the global displacement matrix can be calculated by solving the following linear algebra Eq.2.67.

$$(\mathscr{K} + \overset{hg}{\mathscr{K}})\mathbf{u} = \mathbb{K}\mathbf{u} = \mathscr{R} \tag{2.67}$$

we employ the built-in command ***LinearSolve*** of Mathematica to solve the global displacement vector, then we use the user-defined subroutine ***UMatrix*** convert displacement vector into displacement matrix form. The related Mathematica codes are shown below.

```
u = LinearSolve[Ksp, Rsp];
um = UMatrix[u, ndim];
UMatrix[u_List, udim_Integer] := Module[{m}, If[udim == 1, m = u;
    Return[m]];
   m = ConstantArray[0., {Length[u] / udim, udim}];
   Do[m[[i]] = u[[udim (i - 1) + 1 ;; udim i]], {i, Length[m]}]; m];
```

2.4 Numerical examples

Several numerical examples in 2D or 3D are presented to validate the first/higher-order NOM in this section. The numerical results are compared with the analytical solution or that by FEM software to verify the feasibility.

2.4.1 A cantilever beam under shear load

In this section, a 2D cantilever beam loaded at the end with shear load is considered. The beam with $\mathcal{H} = 3$m in height, $\mathcal{L} = 8$m in length. The cantilever beam parameters are: $E = 6 \times 10^3$MPa, $\nu = 0.33$. The shear load is parabolic distributed. The beam is discretized into 308,1155,2511,4428,6885 points respectively, which corresponding to $\Delta x \in \{\mathcal{H}/10, \mathcal{H}/20, \mathcal{H}/30, \mathcal{H}/40, \mathcal{H}/50\}$. Where Δx denotes the spacing of the points. Plane stress conditions are considered in this section. The analytical solution refers to literature [Timoshenko and Goodier, 1970, Zhuang and Augarde, 2010].

$$u_x = \frac{\mathcal{P}(y-\mathcal{H}/2)}{6E\mathcal{I}}\big[(6\mathcal{L}-3x)x+(2+\nu)((y-\mathcal{H}/2)^2-\frac{\mathcal{H}^2}{4})\big] \tag{2.68}$$

$$u_y = -\frac{\mathcal{P}}{6E\mathcal{I}}\big[3\nu(y-\mathcal{H}/2)^2(\mathcal{L}-x)+(4+5\nu)\frac{\mathcal{H}^2x}{4}+(3\mathcal{L}-x)x^2\big] \tag{2.69}$$

$$\sigma_{xx}(x,y) = \frac{\mathcal{P}(\mathcal{L}-x)(y-\mathcal{H}/2)}{\mathcal{I}}, \sigma_{yy}(x,y)=0, \tau_{xy}(x,y) = -\frac{\mathcal{P}}{2\mathcal{I}}\big(\frac{\mathcal{H}^2}{4}-(y-\mathcal{H}/2)^2\big), \tag{2.70}$$

where $x \in [0,\mathcal{L}], y \in [0,\mathcal{H}]$, $\mathcal{P}$=-5 kN, $\mathcal{I} = \frac{\mathcal{H}^3}{12}$. The discretized cantilever beam on displacement boundary are constrained using the accurate displacements according to Eqs.2.68 and 2.69, as well as the force boundary according to Eq.2.70.

To obtain the displacement of each point, we need to solve the Eq.2.67, which can be shown in detail as Eq.2.71. In this work, we use the penalty approach to apply Dirichlet boundary conditions. This method can be achieved through the following steps:

$$\begin{bmatrix} k_{11} & k_{12} & \cdots & \cdots & \cdots & k_{1n} \\ k_{21} & k_{22} & \cdots & \cdots & \cdots & k_{2n} \\ \cdots & \cdots & \cdots & \cdots & \cdots & \cdots \\ k_{i1} & k_{i2} & \cdots & k_{ii} & \cdots & k_{in} \\ \cdots & \cdots & \cdots & \cdots & \cdots & \cdots \\ k_{n1} & k_{n2} & \cdots & \cdots & \cdots & k_{nn} \end{bmatrix} \begin{bmatrix} u_1 \\ u_2 \\ \vdots \\ u_i \\ \vdots \\ u_n \end{bmatrix} = \begin{bmatrix} R_1 \\ R_2 \\ \vdots \\ R_i \\ \vdots \\ R_n \end{bmatrix} \tag{2.71}$$

When the displacement of point i $u_i = \overline{u_i}$, we modify the i-th equation as follows, multiply it's diagonal element K_{ii} by a penalty factor η (In computations, η is set to 10^{10}) and replace R_i with $\eta k_{ii}\overline{u_i}$ to obtain:

$$\begin{bmatrix} k_{11} & k_{12} & \cdots & \cdots & \cdots & k_{1n} \\ k_{21} & k_{22} & \cdots & \cdots & \cdots & k_{2n} \\ \cdots & \cdots & \cdots & \cdots & \cdots & \cdots \\ k_{i1} & k_{i2} & \cdots & \eta k_{ii} & \cdots & k_{in} \\ \cdots & \cdots & \cdots & \cdots & \cdots & \cdots \\ k_{n1} & k_{n2} & \cdots & \cdots & \cdots & k_{nn} \end{bmatrix} \begin{bmatrix} u_1 \\ u_2 \\ \vdots \\ u_i \\ \vdots \\ u_n \end{bmatrix} = \begin{bmatrix} R_1 \\ R_2 \\ \vdots \\ \eta k_{ii}\overline{u_i} \\ \vdots \\ R_n \end{bmatrix} \tag{2.72}$$

The modified i-th equation can be expressed as:

$$k_{i1}u_1 + k_{i2}u_2 + \cdots + \eta k_{ii}u_i + \cdots + k_{in}u_n = \eta k_{ii}\overline{u_i} \tag{2.73}$$

Since $\eta k_{ii} \gg k_{ij}(i \neq j)$, the $\eta k_{ii}u_i$ term at the left end of the equation is much larger than the other terms, so it can be approximated $\eta k_{ii}u_i \approx \eta k_{ii}\overline{u_i}$. Then we can obtain

$u_i \approx \overline{u_i}$. According to the Eq.2.72, we can obtain the displacement of each point. It should be noted that this method is suitable for any given displacement of points, as the order of the formula and the displacement order of the points remain unchanged during the solution process.

The number of target point's neighbors and the radius of support size in NOM can be very flexible and unlimited. However, a large number of neighbors is expensive in the k-nearest neighbor's search. Based on our numerical experience, eight points closest to the target point are selected to construct the target point's support domain. The difference between the numerical result and analytical solution is measured by the L2-norm, which is calculated by

$$\|\mathbf{u}\|_{L2} = \sqrt{\frac{\sum_j (\mathbf{u}_j - \mathbf{u}_j^{exact}) \cdot (\mathbf{u}_j - \mathbf{u}_j^{exact}) \Delta V_j}{\sum_j \mathbf{u}_j^{exact} \cdot \mathbf{u}_j^{exact} \Delta V_j}}. \tag{2.74}$$

Table.2.1 shows the statistical results of the L2-norm for displacement at various discretizations, Fig.2.3 depicts the displacement for discretization at $\Delta x = \mathcal{H}/50$. The displacement cloud diagram of the cantilever beam for discretization at $\Delta x = \mathcal{H}/50$ using first-order NOM numerical results and analytical results can be seen in Fig.2.4. As shown in Table 2.1, Figs.2.3 and 2.4, good agreements can be seen between the first-order NOM numerical results and analytical results. It shows very close variations in L2-norm and the displacement errors in different directions.

Table 2.1: The statistical results of L2-norm and error for $u_{x_{max}}$ and $u_{y_{max}}$ at different discretizations.

Npoint	Δx	L2-norm	$\frac{u_{x_{max}}^{NOM}}{u_{x_{max}}^{exact}} - 1$	$\frac{u_{y_{max}}^{NOM}}{u_{y_{max}}^{exact}} - 1$
308	$\mathcal{H}/10$	0.0118	-0.2738	-0.2679
1155	$\mathcal{H}/20$	0.0096	-0.0731	-0.0779
2511	$\mathcal{H}/30$	0.0082	-0.0289	-0.0308
4428	$\mathcal{H}/40$	0.0073	-0.0209	-0.0245
6885	$\mathcal{H}/50$	0.0068	0.0150	0.0128

2.4.2 Problem of an infinite plate with a hole in tension

Consider a 2D infinite plate with a circular hole, as shown in Fig.2.5. The plate's length is $\mathcal{L}$ and there is a small circular hole with a radius of $\rho = \mathrm{a}$ in the plate. Because the plate's thickness is substantially smaller than its length, it can be considered a plane

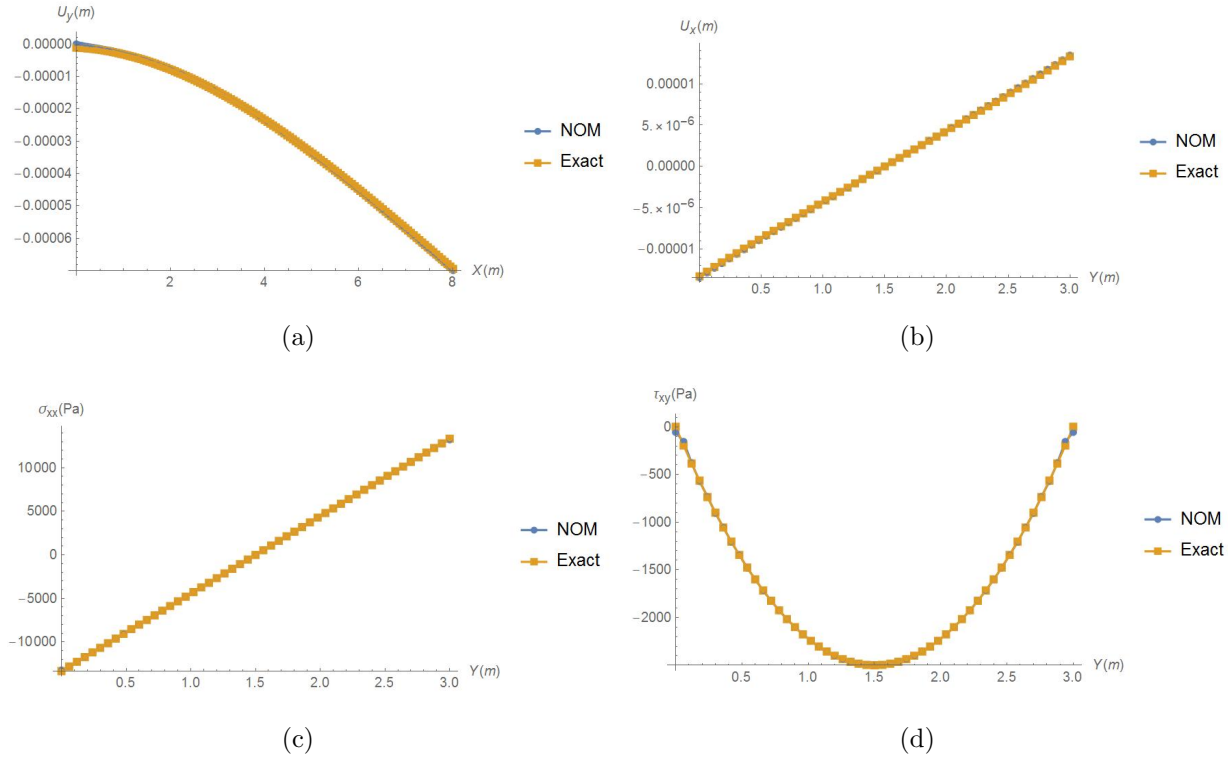

Figure 2.3: The displacement and stress for discretization at $\Delta x = \mathcal{H}/50$. (a) Displacement of points y=$\mathcal{H}/2$ in the x direction; (b) Displacement of points x=$\mathcal{L}/2$ in the y direction; (c) Stress of points x=$\mathcal{L}/2$ in the y direction; (d) Stress of points x=$\mathcal{L}/2$ in the y direction.

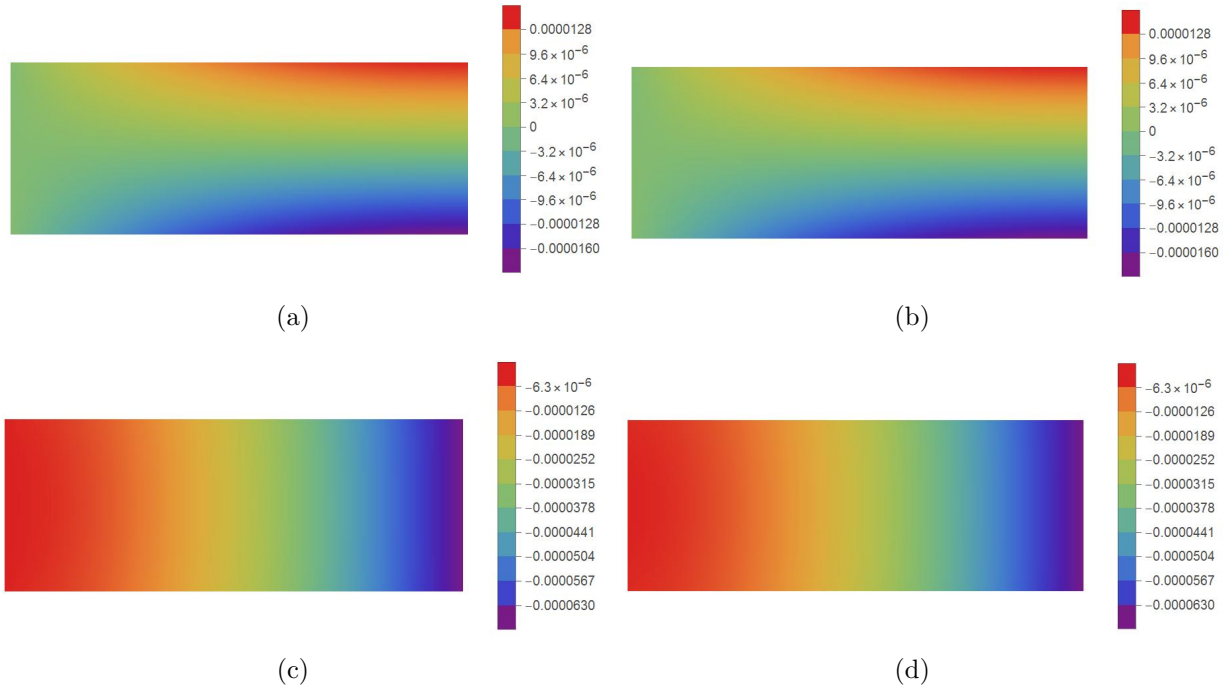

Figure 2.4: The displacement cloud diagram of the cantilever beam for discretization at $\Delta x = \mathcal{H}/50$. (a) Displacement in y direction by first-order NOM numerical results;(b) Displacement in y direction analytical results;(c) Displacement in x direction by first-order NOM numerical results;(d) Displacement in x direction analytical results.

stress problem. The force boundary condition of $\mathcal{P} = 1$ MPa. Based on the symmetry of the structure and load, one-quarter of the model is used for analysis.

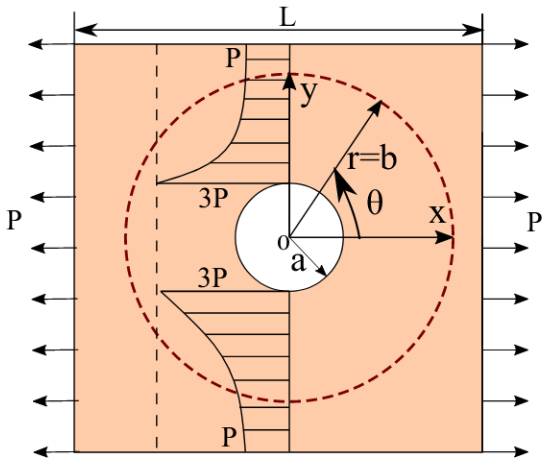

Figure 2.5: Setup of infinite plate with a circular hole.

When the plate's width is substantially more than the radius of the small hole, we can obtain the stresses analytical solution [Boresi et al., 2010] in polar coordinate system according to classical elasticity theory, and it can be expressed as

$$\begin{aligned}
\sigma_\rho &= \frac{\mathcal{P}}{2}\left(1-\frac{\mathrm{a}^2}{\rho^2}\right)+\frac{\mathcal{P}}{2}\cos 2\theta\left(1-\frac{\mathrm{a}^2}{\rho^2}\right)\left(1-3\frac{\mathrm{a}^2}{\rho^2}\right)\\
\sigma_\theta &= \frac{\mathcal{P}}{2}\left(1+\frac{\mathrm{a}^2}{\rho^2}\right)-\frac{\mathcal{P}}{2}\cos 2\theta\left(1+3\frac{\mathrm{a}^4}{\rho^4}\right)\\
\tau_{\rho\theta} &= \tau_{\theta\rho} = -\frac{\mathcal{P}}{2}\sin 2\theta\left(1-\frac{\mathrm{a}^2}{\rho^2}\right)\left(1+3\frac{\mathrm{a}^2}{\rho^2}\right)
\end{aligned} \tag{2.75}$$

The highest hoop normal stress is achieved at the hole's edge, as illustrated in Fig.2.5. When $\rho = \mathrm{a}$, $\theta = \frac{\pi}{2}(\frac{3\pi}{2})$, σ_θ attains the maximum value of three times the uniformly distributed stress $\mathcal{P}$, $(\sigma_\theta)_{\max} = 3\mathcal{P}$, and σ_θ sharply approaches to $\mathcal{P}$ as it moves away to the edge. We characterize the stress concentration phenomena using the stress concentration factor K in this case. We solve stress concentration problems by the first-order NOM, plane stress condition is considered. The numerical results were compared with ABAQUS standard and analytical solutions. The parameters for the plate include $E = 3\times10^4$MPa, $\nu = 0.3$, and the radius of the hole is ρ=1m. To facilitate the application of force boundary conditions, we converted the Eq.2.75 from polar coordinate system to

Cartesian coordinate system, it can be shown as

$$\begin{aligned}
\sigma_{xx}(\rho,\theta) &= \mathcal{P} - \mathcal{P}\frac{\mathrm{a}^2}{\rho^2}\left(\frac{3\cos 2\theta}{2} + \cos 4\theta\right) + \mathcal{P}\frac{3\mathrm{a}^4}{2\rho^4}\cos 4\theta \\
\sigma_{yy}(\rho,\theta) &= -\mathcal{P}\frac{\mathrm{a}^2}{\rho^2}\left(\frac{\cos 2\theta}{2} - \cos 4\theta\right) - \mathcal{P}\frac{3\mathrm{a}^4}{2\rho^4}\cos 4\theta \\
\tau_{xy}(\rho,\theta) &= -\mathcal{P}\frac{\mathrm{a}^2}{\rho^2}\left(\frac{\sin 2\theta}{2} + \sin 4\theta\right) + \mathcal{P}\frac{3\mathrm{a}^4}{2\rho^4}\sin 4\theta
\end{aligned} \tag{2.76}$$

To validate the feasibility of the first-order NOM, we compare the numerical simulation results with the analytical solutions. The analytical solution of the displacement under plane stress conditions can be expressed as

$$\begin{aligned}
u_x(\rho,\theta) &= \frac{\mathcal{P}\mathrm{a}}{8\mu}\left(\frac{\rho}{\mathrm{a}}(\kappa+1)\cos\theta + \frac{2\mathrm{a}}{\rho}((1+\kappa)\cos\theta + \cos 3\theta) - \frac{2\mathrm{a}^3}{\rho^3}\cos 3\theta\right) \\
u_y(\rho,\theta) &= \frac{\mathcal{P}\mathrm{a}}{8\mu}\left(\frac{\rho}{\mathrm{a}}(\kappa-3)\sin\theta + \frac{2\mathrm{a}}{\rho}((1-\kappa)\sin\theta + \sin 3\theta) - \frac{2\mathrm{a}^3}{\rho^3}\sin 3\theta\right)
\end{aligned} \tag{2.77}$$

where $\mu = \frac{E}{2(1+\nu)}$, and $\kappa = \frac{3-\nu}{1+\nu}$.

For the displacement boundary conditions, we set $u_x = 0, u_y = 0$ at left and bottom boundaries by penalty method, meanwhile, for the force boundary conditions, we applied the traction force at right and top boundaries computed by Eq.2.76.

To obtain a good discrete result, initially, we build the model and meshes in ABAQUS, then export it as an "model.inp" file, which includes the element and point coordinate information. We read the exported "model.inp" file in the environment of Mathematica. We can calculate the coordinates of each point in the model, the area of each element, and assign parameters such as area and force to the relevant points of the element according to the core principle. So as to realize the discreteness of the unit in the environment of Mathematica. It should be noted that only the nodes are used and no interaction between elements. The Mathematica software reads the "model.inp" model ($\mathcal{L}/\mathrm{a} = 5$) and discretization of the model as shown in Fig.2.6. In this study, we use the built-in command ***Nearest*** of Mathematica to find the required number of neighbor points, and eight neighbors are selected.

We fix the diameter of the hole to 2m and change the $\mathcal{L}$. Four cases of relative size of plate width and hole radius with $\mathcal{L}/\mathrm{a}$=5,7,9,11 and four cases with total 525,2050,4575,8100 nodes are investigated. The plate is discretized according to ABAQUS mesh elements and CPS3 elements are adopted in ABAQUS[Hibbett et al., 1998] to calculate the reference results. At first we test the maximum value of stress in the x-direction $(\sigma_{xx})_{max}$, according to the formulation $K = \frac{(\sigma_{xx})_{max}}{\mathcal{P}}$, we can obtain the corresponding K and compared it to the analytic solutions. According to the first-order NOM, ABAQUS standard, and

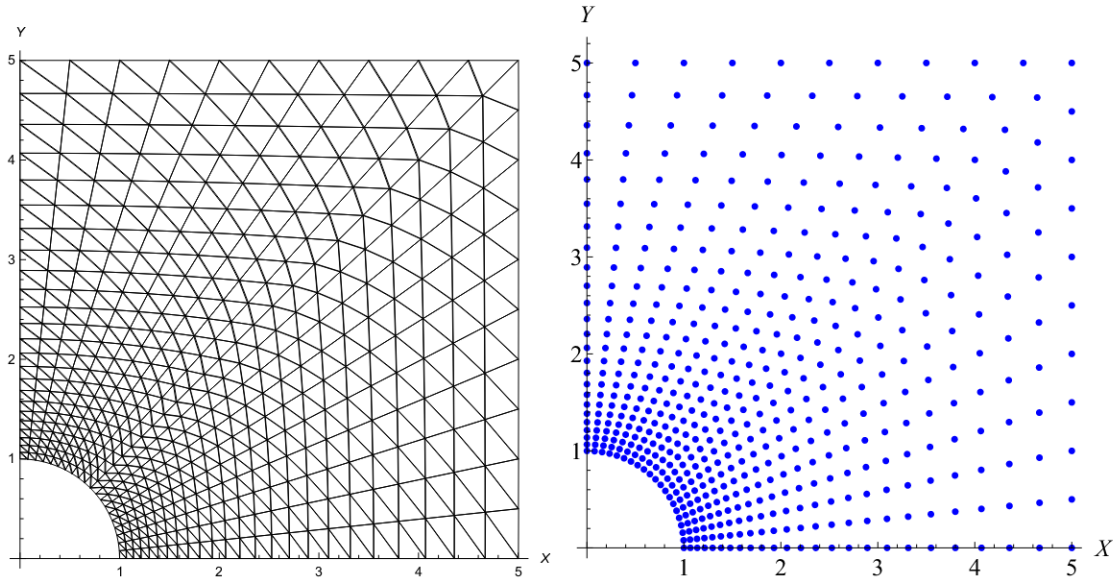

Figure 2.6: (a) The "model.inp" model shown in Mathematica;(b) Discretization of the model.

Table 2.2: The statistical results of the stress concentration factor K at different $\mathcal{L}/a$ ratios, where 525 and 2050 denotes the total number of points in the model.

$\mathcal{L}/\mathbb{a}$	Analytical solution	ABAQUS(525)	NOM (525)	ABAQUS(2050)	NOM(2050)
5	3.000	3.330	3.361	3.350	3.371
7	3.000	3.164	3.176	3.178	3.203
9	3.000	3.100	3.109	3.115	3.126
11	3.000	3.064	3.078	3.087	3.096

analytical solution, the statistical results of the stress concentration factor K, as shown in Table 2.2.

The displacement and stress distribution of the model($\mathcal{L}/\mathbb{a} = 5$) on polar coordinate system $\rho = 2$ at the case of with total 4575 and 8100 nodes using first-order NOM are compared to the analytic solutions, as seen in Figs.2.7 and 2.8. The displacement's L2 norm computed by Eq.2.74 and stress field at four different discretization cases are shown in Table 2.3. These characteristics agree well with the theoretical analysis of this problem mentioned above, and it proved that the first-order NOM established in this chapter has good applicability.

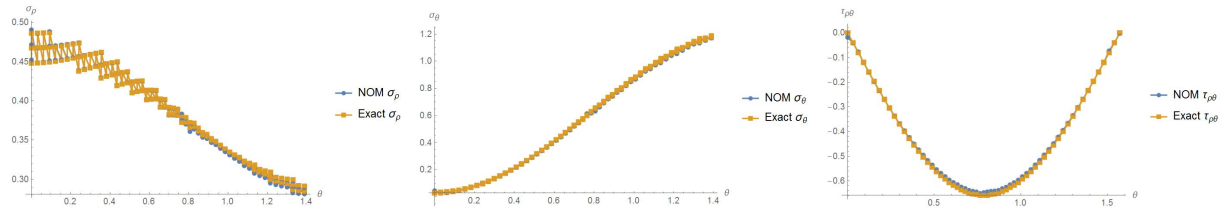

(a)

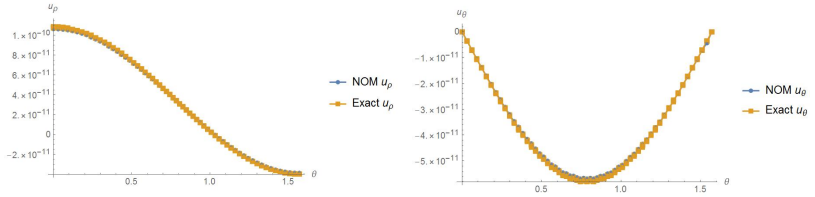

(b)

Figure 2.7: Analytical and numerical results of the stress and displacement. (a) The results of the stress (Nnodes=4575);(b) The results of the displacement (Nnodes=4575).

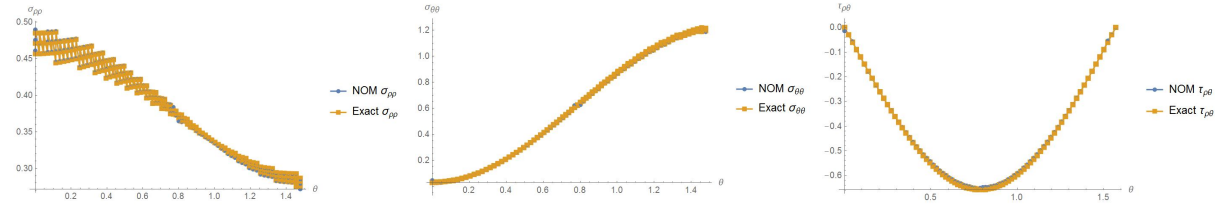

(a)

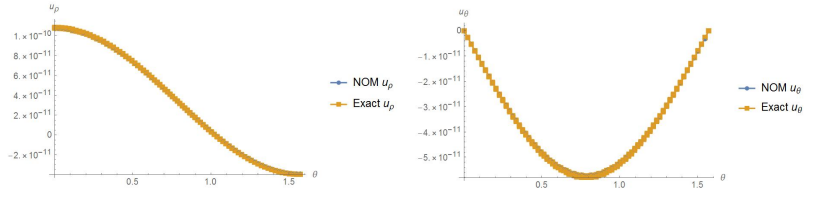

(b)

Figure 2.8: Analytical and numerical results of the stress and displacement. (a) The results of the stress (Nnodes=8100);(b) The results of the displacement (Nnodes=8100).

Table 2.3: The L2 norm of the displacement and stress at four different discretization cases.

Nnodes	L2 norm of displacement	L2 norm of stress
525	0.0581	0.0908
2050	0.0276	0.0478
4575	0.0163	0.0428
8100	0.0118	0.0376

2.4.3 3D gradient elasticity cantilever beam under shear load

To illustrate the feasibility of higher-order NOM, we expand it to handle the gradient elasticity beam issue. A 3D gradient elasticity cantilever beam under uniform shear load is considered. The cantilever beam with dimensions of $25 \times 10 \times 3$ m^3. The material parameters are considered: $E = 6 \times 10^4$ MPa, $\nu = 0.33$. The uniform shear force $P_y = -1.0 \times 10^{-3}$ MPa. The higher-order NOM based on numerical integration [Ren et al., 2020c] is employed to investigate the effectiveness of the current method for gradient elasticity cantilever beam. The cantilever beam is discretized into 3744 points and hexahedral background meshes are generated for the numerical integration. We employ 40 Gauss neighbor points in the numerical test. For separate variables (u, v, w) in 3D cantilever beam, the isotropic elasticity gradient material's energy functional include the differential operators $\nabla u,\ \nabla v, \nabla w, \nabla^2 u, \nabla^2 v, \nabla^2 w, \nabla^3 u, \nabla^3 v, \nabla^3 w$. The maximal order of partial derivatives is three, hence we select the third order of nonlocal operators in Eq.2.30. In addition, various gradient coefficients $\ell = 0, 1.5, 3.0, 4.5$ are studied by current method and the displacement field for various gradient coefficients is given in Fig.2.9. Fig.2.10 presents the displacement for points on the line $(y = 10, z = 0)$. The results obtained by higher-order NOM correspond well with those obtained by ABAQUS and with the gradient coefficient raising, the deform of the beam become more uniformly.

2.5 Conclusions

In this chapter, we presented the implementation procedure of first/higher-order NOM, and an open-source Mathematica code is presented and explained in detail. The performance of first-order NOM and higher-order NOM results are demonstrated compared with the corresponding analytical solutions or the results of the FEM commercial software. Concluding remarks can be stated as follows:

Similar to the FEM and meshless method, NOM can establish the operator energy functional and tangent stiffness matrix by some matrix multiplications. However, unlike FEM

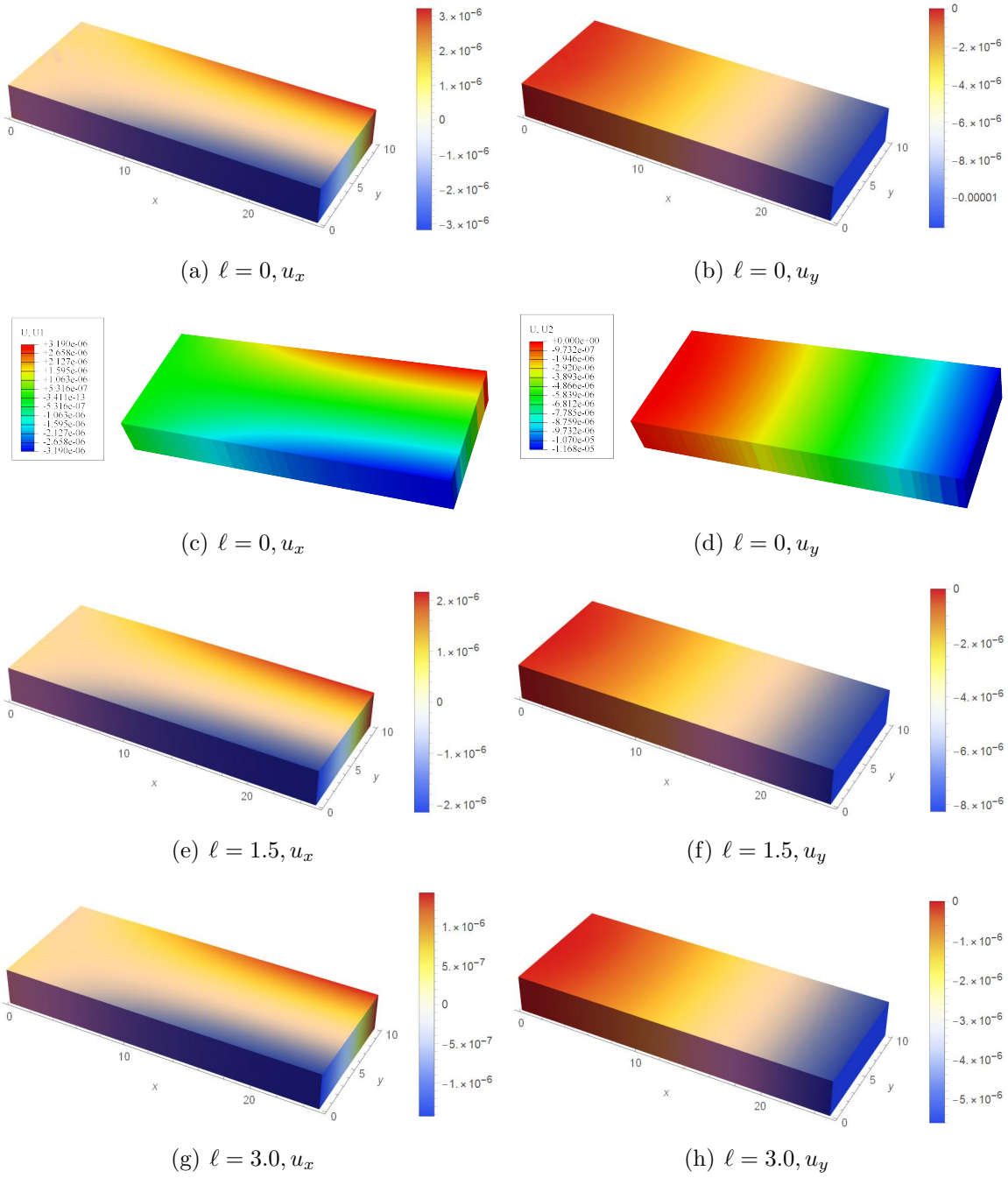

(a) $\ell = 0, u_x$ (b) $\ell = 0, u_y$

(c) $\ell = 0, u_x$ (d) $\ell = 0, u_y$

(e) $\ell = 1.5, u_x$ (f) $\ell = 1.5, u_y$

(g) $\ell = 3.0, u_x$ (h) $\ell = 3.0, u_y$

Figure 2.9: Displacement for various different gradient coefficients.

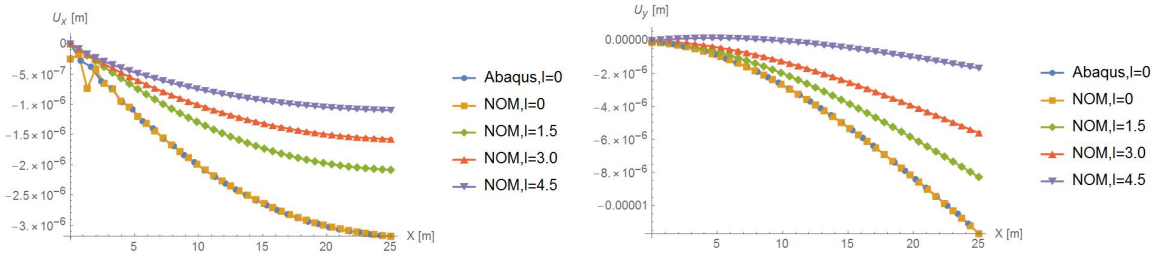

(a) (b)

Figure 2.10: Displacement for points on the line $(y = 10, z = 0)$.

and the meshless method, NOM can derive differential operators directly without employing shape functions. Hence, the complexity of the NOM is significantly reduced. The NOM requires only the definition of the energy, for a given energy functional, the nonlocal operators can be established automatically by the highest order of partial derivative and dimensions. Support, dual-support, nonlocal differential operators, and operator energy functional are the fundamental components of NOM. Several numerical examples illustrate the method's high performance and capabilities. In conclusion, NOM is an easy-to-use, flexible, and efficient numerical method.

Chapter 3

Explicit implementation of the nonlocal operator method

This chapter is based on the journal paper 'Explicit implementation of the nonlocal operator method: A nonlocal dynamic formulation for elasticity solid' published in IJHM by my first author. The contribution of this paper is summarized as follows:

Yongzheng Zhang

- Conceptualization
- Research state of the art
- Investigation
- Formal analysis
- Methodology
- Software/Programming
- Data curation
- Data analysis
- Validation
- Visualization
- Writing original manuscript draft

Huilong Ren

- Conceptualization
- Methodology

Timon Rabczuk

- Conceptualization
- Mentoring the research progress

3.1 General

The purpose of this chapter is to describe the method of explicitly implementing NOM for elasticity solid in detail and develop a nonlocal dynamic formulation for linear elasticity solid by using the explicit NOM. The remainder of the chapter is arranged as follows: In Section 3.2, based on the variational principle, the nonlocal dynamic governing equation of linear elasticity solid is derived. In Section 3.3, the operator energy functional of linear elasticity solid has been derived. Section 3.4 presents the numerical implementation of the explicit NOM. In Section 3.5, several numerical examples are presented to demonstrate the capabilities of this method. Finally, conclusions are drawn in Section 3.6.

3.2 Nonlocal dynamic governing equation of linear elasticity solid by NOM

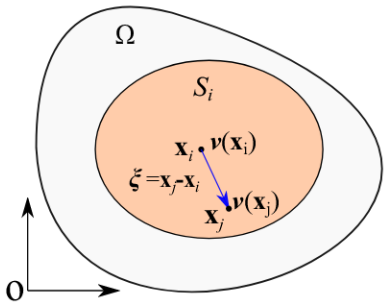

Figure 3.1: Domain and notation

Consider a solid occupying a domain $\boldsymbol{\Omega}$ consisting of material points that with mass and volume, as shown in Fig.3.1, let $\mathbf{x}_i$ represent spatial coordinates in the domain $\boldsymbol{\Omega}$; $\boldsymbol{\xi}_{ij} := \mathbf{x}_j - \mathbf{x}_i$ is a relative position vector starts from $\mathbf{x}_i$ to $\mathbf{x}_j$; $\boldsymbol{v}_i := \boldsymbol{v}(\mathbf{x}_i, t)$ and $\boldsymbol{v}_j := \boldsymbol{v}(\mathbf{x}_j, t)$ are the displacement value for $\mathbf{x}_i$ and $\mathbf{x}_j$, respectively; $\boldsymbol{v}_{ij} := \boldsymbol{v}_j - \boldsymbol{v}_i$ is the corresponding displacement field vector for spatial vector $\boldsymbol{\xi}_{ij}$.

The nonlocal gradient for vector field $\boldsymbol{v}$ at point $\mathbf{x}_i$ is defined in the support $\mathcal{S}_i$ as

$$\tilde{\nabla}\boldsymbol{v}_i := \int_{\mathcal{S}_i} \mathrm{w}(\boldsymbol{\xi}_{ij})\boldsymbol{v}_{ij} \otimes \boldsymbol{\xi}_{ij} \mathrm{d}V_j \cdot \Big(\int_{\mathcal{S}_i} \mathrm{w}(\boldsymbol{\xi}_{ij})\boldsymbol{v}_{ij} \otimes \boldsymbol{\xi}_{ij} \mathrm{d}V_j \Big)^{-1} \tag{3.1}$$

The nonlocal gradient operator and it's variation at point $\mathbf{x}_i$ in discrete form are

$$\tilde{\nabla}\boldsymbol{v}_i = \sum_{j\in\mathcal{S}_i} \mathrm{w}(\boldsymbol{\xi}_{ij})\boldsymbol{v}_{ij}\otimes\boldsymbol{\xi}_{ij}\Delta V_j \cdot \Big(\sum_{j\in\mathcal{S}_i} \mathrm{w}(\boldsymbol{\xi}_{ij})\boldsymbol{\xi}_{ij}\otimes\boldsymbol{\xi}_{ij}\Delta V_j\Big)^{-1} \tag{3.2}$$

$$\tilde{\nabla}\delta\boldsymbol{v}_i = \sum_{j\in\mathcal{S}_i} \mathrm{w}(\boldsymbol{\xi}_{ij})\delta\boldsymbol{v}_{ij}\otimes\boldsymbol{\xi}_{ij}\Delta V_j \cdot \Big(\sum_{j\in\mathcal{S}_i} \mathrm{w}(\boldsymbol{\xi}_{ij})\boldsymbol{\xi}_{ij}\otimes\boldsymbol{\xi}_{ij}\Delta V_j\Big)^{-1} \tag{3.3}$$

For vector field $\boldsymbol{v}$ with nonlocal gradient defined by Eq.3.1, we formulate a quadratic functional to eliminated the inconsistency between the $\boldsymbol{v}_{ij}$ and $\tilde{\nabla}\boldsymbol{v}_i\boldsymbol{\xi}_{ij}$, and the operator energy functional for vector field $\boldsymbol{v}$ at a point can be shown as

$$\mathcal{F}_i^{hg} = \frac{p^{hg}}{2m_{\mathbf{K}_i}}\int_{\mathcal{S}_i} \mathrm{w}(\boldsymbol{\xi}_{ij})(\tilde{\nabla}\boldsymbol{v}_i\cdot\boldsymbol{\xi}_{ij}-\boldsymbol{v}_{ij})^T(\tilde{\nabla}\boldsymbol{v}_i\cdot\boldsymbol{\xi}_{ij}-\boldsymbol{v}_{ij})\mathrm{d}V_j \tag{3.4}$$

$$\mathbf{K}_i = \int_{\mathcal{S}_i} \mathrm{w}(\boldsymbol{\xi}_{ij})\boldsymbol{\xi}_{ij}\otimes\boldsymbol{\xi}_{ij}\mathrm{d}V_j \tag{3.5}$$

It should be noted that the NOM can construct the nonlocal strong form by employing the energy functional in the traditional local manner.

The total Lagrange energy functional for linear elastic solid of the overall system can be expressed as

$$L(\dot{\boldsymbol{v}},\boldsymbol{v}) = \int_\Omega \frac{1}{2}\rho\dot{\boldsymbol{v}}\cdot\dot{\boldsymbol{v}}dV - \int_\Omega \psi(\boldsymbol{\sigma},\boldsymbol{\varepsilon}(\nabla\boldsymbol{v}))dV + \int_\Omega \mathbf{b}\cdot\boldsymbol{v}dV + \int_{\partial\Omega}\mathbf{f}\cdot\boldsymbol{v}dS \tag{3.6}$$

with $\dot{\boldsymbol{v}} = \frac{\partial\boldsymbol{v}}{\partial t}$, $\psi(\boldsymbol{\sigma},\boldsymbol{\varepsilon}(\nabla\boldsymbol{v}))$ denotes strain energy density, ρ denotes the density of the solid, $\mathbf{b}$ denotes the body force density and $\mathbf{f}$ denotes the external traction force.

Replacing the local gradient operator $\nabla\boldsymbol{v}$ with the nonlocal gradient operator $\tilde{\nabla}\boldsymbol{v}$ in Eq.3.6, we obtain

$$L(\dot{\boldsymbol{v}},\boldsymbol{v}) = \int_\Omega \frac{1}{2}\rho\dot{\boldsymbol{v}}\cdot\dot{\boldsymbol{v}}dV - \int_\Omega \psi(\boldsymbol{\sigma},\boldsymbol{\varepsilon}(\tilde{\nabla}\boldsymbol{v}))dV + \int_\Omega \mathbf{b}\cdot\boldsymbol{v}dV + \int_{\partial\Omega}\mathbf{f}\cdot\boldsymbol{v}dS \tag{3.7}$$

The external work in time $[t_1,t_2]$ can be shown as $W^{ext} = \int_{t_1}^{t_2}\int_{\partial\Omega}\mathbf{f}\cdot\boldsymbol{v}dSdt$. The integral of the Lagrangian L between two instants of time t_1 and t_2 is $\mathcal{L} = \int_{t_1}^{t_2} L(\dot{\boldsymbol{v}},\boldsymbol{v})dt$. Applying

the variation principle, we have

$$
\begin{aligned}
\delta\mathcal{L} &= \int_{t_1}^{t_2}\int_{\Omega}[\rho\dot{\boldsymbol{v}}\cdot\delta\dot{\boldsymbol{v}} - \frac{\partial\psi(\boldsymbol{\sigma},\boldsymbol{\varepsilon}(\tilde{\nabla}\boldsymbol{v}))}{\partial\boldsymbol{\varepsilon}} : \tilde{\nabla}\delta\boldsymbol{v} + \mathbf{b}\delta\boldsymbol{v}]\mathrm{d}V\mathrm{d}t + \int_{t_1}^{t_2}\int_{\partial\Omega}\mathbf{f}\cdot\delta\boldsymbol{v}dSdt \\
&= \int_{t_1}^{t_2}\int_{\Omega}[-\rho_i\ddot{\boldsymbol{v}}_i\cdot\delta\boldsymbol{v}_i - \boldsymbol{\sigma}_i : \tilde{\nabla}\delta\boldsymbol{v}_i + \mathbf{b}_i\delta\boldsymbol{v}_i]\mathrm{d}V_i\mathrm{d}t + \int_{t_1}^{t_2}\int_{\partial\Omega}\mathbf{f}\cdot\delta\boldsymbol{v}_i dS_i dt \\
&= \int_{t_1}^{t_2}\int_{\Omega}\Big(-\rho_i\ddot{\boldsymbol{v}}_i\cdot\delta\boldsymbol{v}_i - \boldsymbol{\sigma}_i : \big(\int_{\mathcal{S}_i}\mathrm{w}(\boldsymbol{\xi}_{ij})\delta\boldsymbol{v}_{ij}\otimes\boldsymbol{\xi}_{ij} + \mathbf{b}_i\delta\boldsymbol{v}_i\Big)\mathrm{d}V_i\mathrm{d}t \\
&\quad + \int_{t_1}^{t_2}\int_{\partial\Omega}\mathbf{f}\cdot\delta\boldsymbol{v}_i dS_i dt \\
&= \int_{t_1}^{t_2}\int_{\Omega}\Big(-\rho_i\ddot{\boldsymbol{v}}_i\cdot\delta\boldsymbol{v}_i - \int_{\mathcal{S}_i}\mathrm{w}(\boldsymbol{\xi}_{ij})\boldsymbol{\sigma}_i\boldsymbol{K}_i^{-1}\boldsymbol{\xi}_{ij}\cdot\delta\boldsymbol{v}_{ij}\mathrm{d}V_j\big) + \mathbf{b}_i\delta\boldsymbol{v}_i\Big)\mathrm{d}V_i\mathrm{d}t \\
&\quad + \int_{t_1}^{t_2}\int_{\partial\Omega}\mathbf{f}\cdot\delta\boldsymbol{v}_i dS_i dt \\
&= \int_{t_1}^{t_2}\int_{\Omega}\Big(-\rho_i\ddot{\boldsymbol{v}}_i\cdot\delta\boldsymbol{v}_i - \big(\int_{\mathcal{S}_i'}\mathrm{w}(\boldsymbol{\xi}_{ji})\boldsymbol{\sigma}_j\boldsymbol{K}_j^{-1}\boldsymbol{\xi}_{ji}\cdot\delta\boldsymbol{v}_i\mathrm{d}V_j - \int_{\mathcal{S}_i}\mathrm{w}(\boldsymbol{\xi}_{ij})\boldsymbol{\sigma}_i\boldsymbol{K}_i^{-1}\boldsymbol{\xi}_{ij}\cdot\delta\boldsymbol{v}_i\mathrm{d}V_j\big) \\
&\quad + \mathbf{b}_i\delta\boldsymbol{v}_i\Big)\mathrm{d}V_i\mathrm{d}t + \int_{t_1}^{t_2}\int_{\partial\Omega}\mathbf{f}\cdot\delta\boldsymbol{v}_i dS_i dt
\end{aligned}
$$

with $\boldsymbol{\sigma}$ is the Cauchy stress, and the boundary condition $\delta\boldsymbol{v}(t_1) = 0$, $\delta\boldsymbol{v}(t_2) = 0$ is considered in the above derivation.

For any $\delta\boldsymbol{v}$, the first-order variation $\delta\mathcal{L} = 0$ leads to

$$
\int_{\mathcal{S}_i}\mathrm{w}(\boldsymbol{\xi}_{ij})\boldsymbol{\sigma}_i\boldsymbol{K}_i^{-1}\boldsymbol{\xi}_{ij}\mathrm{d}V_j - \int_{\mathcal{S}_i'}\mathrm{w}(\boldsymbol{\xi}_{ji})\boldsymbol{\sigma}_j\boldsymbol{K}_j^{-1}\boldsymbol{\xi}_{ji}\mathrm{d}V_j + \mathbf{b}_i = \rho_i\ddot{\boldsymbol{v}}_i \quad \forall\boldsymbol{x}_i\in\Omega \tag{3.8}
$$

For linear elastic solid, the relationship between nonlocal and local form can be shown as

$$
\nabla\cdot\boldsymbol{\sigma}_i \overset{\text{Local - Nonlocal}}{\underset{\text{Nonlocal - Local}}{\rightleftharpoons}} \int_{\mathcal{S}_i}\mathrm{w}(\boldsymbol{\xi}_{ij})\boldsymbol{\sigma}_i\boldsymbol{K}_i^{-1}\boldsymbol{\xi}_{ij}\mathrm{d}V_j - \int_{\mathcal{S}_i'}\mathrm{w}(\boldsymbol{\xi}_{ji})\boldsymbol{\sigma}_j\boldsymbol{K}_j^{-1}\boldsymbol{\xi}_{ji}\mathrm{d}V_j \tag{3.9}
$$

The nonlocal dynamic formulation for linear elasticity solid is expressed in Eq.3.8. The nonlocal formulation is variationally consistent, and dual-support follows naturally from the variational principle. Nevertheless, Eq.3.8 suffers from the zero energy mode [Pian and Chen, 1983, Vignjevic et al., 2000, Yaghoobi and Chorzepa, 2017], we introduce the so-called operator energy functional to achieve the linear field of the field and avoid numerical instabilities, which is described in the next section.

3.3 Operator energy functional of linear elasticity solid

The operator energy functional can be construct according to the nonlocal gradient operator $\tilde{\nabla}\boldsymbol{v}$, it can be expressed as

$$\mathcal{F}(\boldsymbol{v}) = \int_{\Omega} \mathcal{F}_i^{hg} \mathrm{d}V_i = \frac{p^{hg}}{2m_{\mathbf{K}_i}} \int_{\Omega}\int_{\mathcal{S}_i} \mathrm{w}(\boldsymbol{\xi}_{ij})(\tilde{\nabla}\boldsymbol{v}_i\boldsymbol{\xi}_{ij} - \boldsymbol{v}_{ij})^T(\tilde{\nabla}\boldsymbol{v}_i\boldsymbol{\xi}_{ij} - \boldsymbol{v}_{ij})\mathrm{d}V_j\mathrm{d}V_i \tag{3.10}$$

The first-order variation of $\mathcal{F}(\boldsymbol{v})$ leads to

$$\begin{aligned}
\delta\mathcal{F}(\boldsymbol{v}) &= \frac{p^{hg}}{m_{\mathbf{K}_i}} \int_{\Omega}\int_{\mathcal{S}_i} \mathrm{w}(\boldsymbol{\xi}_{ij})(\tilde{\nabla}\boldsymbol{v}_i\boldsymbol{\xi}_{ij} - \boldsymbol{v}_{ij})^T(\tilde{\nabla}\delta\boldsymbol{v}_i\boldsymbol{\xi}_{ij} - \delta\boldsymbol{v}_{ij})\mathrm{d}V_j\mathrm{d}V_i \\
&= \frac{p^{hg}}{m_{\mathbf{K}_i}} \int_{\Omega}\int_{\mathcal{S}_i} \Big(\mathrm{w}(\boldsymbol{\xi}_{ij})(\tilde{\nabla}\boldsymbol{v}_i\boldsymbol{\xi}_{ij} - \boldsymbol{v}_{ij})^T\tilde{\nabla}\delta\boldsymbol{v}_i\boldsymbol{\xi}_{ij} - \mathrm{w}(\boldsymbol{\xi}_{ij})(\tilde{\nabla}\boldsymbol{v}_i\boldsymbol{\xi}_{ij} - \boldsymbol{v}_{ij})^T\delta\boldsymbol{v}_{ij}\Big)\mathrm{d}V_j\mathrm{d}V_i \\
&= \frac{p^{hg}}{m_{\mathbf{K}_i}} \int_{\Omega}\int_{\mathcal{S}_i} \Big(\mathrm{w}(\boldsymbol{\xi}_{ij})(\tilde{\nabla}\boldsymbol{v}_i\boldsymbol{\xi}_{ij} - \boldsymbol{v}_{ij}) \otimes \boldsymbol{\xi}_{ij}\mathrm{d}V_j : \tilde{\nabla}\delta\boldsymbol{v}_i - \mathrm{w}(\boldsymbol{\xi}_{ij})(\tilde{\nabla}\boldsymbol{v}_i\boldsymbol{\xi}_{ij} - \boldsymbol{v}_{ij})^T\delta\boldsymbol{v}_{ij}\mathrm{d}V_j\Big)\mathrm{d}V_i \\
&= \frac{p^{hg}}{m_{\mathbf{K}_i}} \int_{\Omega} \Big(\tilde{\nabla}\boldsymbol{v}_i \int_{\mathcal{S}_i} \mathrm{w}(\boldsymbol{\xi}_{ij})\boldsymbol{\xi}_{ij} \otimes \boldsymbol{\xi}_{ij}\mathrm{d}V_j - \int_{\mathcal{S}_i} \mathrm{w}(\boldsymbol{\xi}_{ij})\boldsymbol{v}_{ij} \otimes \boldsymbol{\xi}_{ij}\mathrm{d}V_j\mathrm{d}V_i\Big) : \delta\tilde{\nabla}\boldsymbol{v}_i\mathrm{d}V_i \\
&- \frac{p^{hg}}{m_{\mathbf{K}_i}} \int_{\Omega}\int_{\mathcal{S}_i} \mathrm{w}(\boldsymbol{\xi}_{ij})(\tilde{\nabla}\boldsymbol{v}_i\boldsymbol{\xi}_{ij} - \boldsymbol{v}_{ij})^T\delta\boldsymbol{v}_{ij}\mathrm{d}V_j\mathrm{d}V_i \\
&= \frac{p^{hg}}{m_{\mathbf{K}_i}} \int_{\Omega}\int_{\mathcal{S}_i} \mathrm{w}(\boldsymbol{\xi}_{ij})(\boldsymbol{v}_{ij} - \tilde{\nabla}\boldsymbol{v}_i\boldsymbol{\xi}_{ij})^T(\delta\boldsymbol{v}_j - \delta\boldsymbol{v}_i)\mathrm{d}V_j\mathrm{d}V_i \\
&= \int_{\Omega} \Big(\int_{\mathcal{S}_i'} \frac{p^{hg}}{m_{\mathbf{K}_j}} \mathrm{w}(\boldsymbol{\xi}_{ji})(\boldsymbol{v}_{ji} - \tilde{\nabla}\boldsymbol{v}_j\boldsymbol{\xi}_{ji})\mathrm{d}V_j - \int_{\mathcal{S}_i} \frac{p^{hg}}{m_{\mathbf{K}_i}} \mathrm{w}(\boldsymbol{\xi}_{ij})(\boldsymbol{v}_{ij} - \tilde{\nabla}\boldsymbol{v}_i\boldsymbol{\xi}_{ij})\mathrm{d}V_j\Big)\delta\boldsymbol{v}_i\mathrm{d}V_i
\end{aligned} \tag{3.11}$$

Hence, the bond internal force caused by operator energy functional can be shown as

$$\int_{\mathcal{S}_i'} \frac{p^{hg}}{m_{\mathbf{K}_j}} \mathrm{w}(\boldsymbol{\xi}_{ji})(\boldsymbol{v}_{ji} - \tilde{\nabla}\boldsymbol{v}_j\boldsymbol{\xi}_{ji})\mathrm{d}V_j - \int_{\mathcal{S}_i} \frac{p^{hg}}{m_{\mathbf{K}_i}} \mathrm{w}(\boldsymbol{\xi}_{ij})(\boldsymbol{v}_{ij} - \tilde{\nabla}\boldsymbol{v}_i\boldsymbol{\xi}_{ij})\mathrm{d}V_j \tag{3.12}$$

where $\frac{p^{hg}}{m_{\mathbf{K}_i}} \mathrm{w}(\boldsymbol{\xi}_{ij})(\boldsymbol{v}_{ij} - \tilde{\nabla}\boldsymbol{v}_i\boldsymbol{\xi}_{ij})$ is the zero energy internal force for vector $\boldsymbol{\xi}_{ij}$.

For linear elastic solid, the nonlocal form and local form enhanced by operator functional can be rewritten as

$$\begin{aligned}
\nabla\cdot\boldsymbol{\sigma} \overset{\text{Local - Nonlocal}}{\underset{\text{Nonlocal - Local}}{\rightleftharpoons}} &\int_{\mathcal{S}_i} (\mathrm{w}(\boldsymbol{\xi}_{ij})\boldsymbol{\sigma}_i \cdot \boldsymbol{K}_i^{-1}\boldsymbol{\xi}_{ij} + \frac{p^{hg}}{m_{\mathbf{K}_i}} \mathrm{w}(\boldsymbol{\xi}_{ij})(\boldsymbol{v}_{ij} - \tilde{\nabla}\boldsymbol{v}_i\boldsymbol{\xi}_{ij}))\mathrm{d}V_j \\
&- \int_{\mathcal{S}_i'} (\mathrm{w}(\boldsymbol{\xi}_{ji})\boldsymbol{\sigma}_j \cdot \boldsymbol{K}_j^{-1}\boldsymbol{\xi}_{ji} + \frac{p^{hg}}{m_{\mathbf{K}_j}} \mathrm{w}(\boldsymbol{\xi}_{ji})(\boldsymbol{v}_{ji} - \tilde{\nabla}\boldsymbol{v}_j\boldsymbol{\xi}_{ji}))\mathrm{d}V_j
\end{aligned} \tag{3.13}$$

3.4 Numerical implementation

The solid domain Ω is discretized into N points occupying a volume ΔV_i:

$$\Omega = \sum_{i=1}^{N} \Delta V_i, \tag{3.14}$$

where N denotes the number of points, ΔV_i is the volume associated with point $\mathbf{x}_i$.

For each point, the support is denoted by

$$\mathcal{S}_i = \{i, j_1, j_2, ..., j_{n_i}\}, \tag{3.15}$$

where $j_1, ..., j_k, ..., j_{n_i}$ are the global indexes of neighbors of point $\mathbf{x}_i$, n_i is the number of neighbors in support $\mathcal{S}_i$. The bond force between points are computed by

$$\begin{aligned}
\boldsymbol{Q}_{ij} &= [\mathbb{w}(\boldsymbol{\xi}_{ij})\boldsymbol{\sigma}_i \cdot \boldsymbol{K}_i^{-1}\boldsymbol{\xi}_{ij} + \frac{p^{hg}}{m_{\mathbf{K}_i}}\mathbb{w}(\boldsymbol{\xi}_{ij})(\boldsymbol{v}_{ij} - \tilde{\nabla}\boldsymbol{v}_i\boldsymbol{\xi}_{ij})]\Delta V_i \Delta V_j \\
\boldsymbol{Q}_{ji} &= [\mathbb{w}(\boldsymbol{\xi}_{ji})\boldsymbol{\sigma}_j \cdot \boldsymbol{K}_j^{-1}\boldsymbol{\xi}_{ji} + \frac{p^{hg}}{m_{\mathbf{K}_j}}\mathbb{w}(\boldsymbol{\xi}_{ji})(\boldsymbol{v}_{ji} - \tilde{\nabla}\boldsymbol{v}_j\boldsymbol{\xi}_{ji})]\Delta V_i \Delta V_j
\end{aligned} \tag{3.16}$$

with $\mathbb{w}(\boldsymbol{\xi}_{ij}) = 1/|\boldsymbol{\xi}_{ij}|^2$.

Finally, we get the force of point $\mathbf{x}_i$ as

$$\mathbf{P}_i = \sum_{j \in \mathcal{S}_i} \boldsymbol{Q}_{ij} - \sum_{j \in \mathcal{S}_i'} \boldsymbol{Q}_{ji} \tag{3.17}$$

In discrete form, Newton's equation of motion is expressed as

$$\boldsymbol{F}_i - \boldsymbol{P}_i = \mathbb{M}_i \ddot{\boldsymbol{v}}_i(t), \tag{3.18}$$

where t denotes the time, $v_i(t)$ denotes the ensemble of the position vector of point $\mathbf{x}_i$, $\boldsymbol{F}_i$ is the external force vector and $\boldsymbol{P}_i$ denotes the internal force vector; $\mathbb{M}_i$ refers to the mass of the point.

In this chapter, the velocity and displacement is updated via the Verlet-Velocity scheme [Verlet, 1967]and can be shown as follows

$$\begin{aligned}
\boldsymbol{v}_i(t + \Delta t) &= \boldsymbol{v}_i(t) + \dot{\boldsymbol{v}}_i(t)\Delta t + \frac{1}{2\mathbb{M}_i}[\boldsymbol{F}_i(t) - \boldsymbol{P}_i(t)]\Delta t^2 \\
\dot{\boldsymbol{v}}_i(t + \Delta t) &= \dot{\boldsymbol{v}}_i(t) + \frac{1}{2\mathbb{M}_i}\Big([\boldsymbol{F}_i(t) - \boldsymbol{P}_i(t)] + [\boldsymbol{F}_i(t + \Delta t) - \boldsymbol{P}_i(t + \Delta t]\Big)\Delta t
\end{aligned} \tag{3.19}$$

The main implementation process of explicit NOM for the dynamic analysis of liner elasticity solid can be summarized as follows:

1. **Discretization of the solution domain and initialization**
   (i) Create geometry and discrete the solution domain.
   (ii) Initialize the bond force of $\boldsymbol{P}_i = 0$ and assign values to the corresponding parameters: Young's modulus E, Poisson's ratio ν, Density ρ , Number of neighbors for each point etc.

2. **Calculate shape tensor**
   (i) For each point, calculate first-order shape tensor $\mathbf{K}_i$.
   (ii) For each point, calculate the inverse of the shape tensor $\mathbf{K}_i^{-1}$.

3. **Calculate deformation tensor**
   For each point, calculate deformation tensor $\overline{\mathbf{F}_i} = \int_{\mathcal{S}_i} \mathrm{w}(\boldsymbol{\xi}_{ij}) \boldsymbol{Y}_i(\boldsymbol{\xi}_{ij}) \otimes \boldsymbol{\xi}_{ij} \mathrm{d}V_j \cdot \mathbf{K}_i^{-1}$. with $\boldsymbol{Y}_i(\boldsymbol{\xi}_{ij}) := \boldsymbol{v}(\mathbf{x}_j, t) - \boldsymbol{v}(\mathbf{x}_i, t)$ is the current bond vector for bond $\boldsymbol{\xi}_{ij}$.

4. **Calculate the linear elasticity solid constitutive model**
   (i) For each point, calculate the linear elasticity solid strain $\boldsymbol{\varepsilon}_i$ by solving $\boldsymbol{\varepsilon}_i = \frac{1}{2}(\overline{\mathbf{F}_i} + \overline{\mathbf{F}_i}^T) - \mathbf{I}$.
   (ii) For each point, calculate the Cauchy stress tensor $\boldsymbol{\sigma}_i$ in terms of the linear strain tensor assuming Hooke's law at different conditions by solving follow equations:

$$\begin{cases} ①. \quad \boldsymbol{\sigma}_i = \dfrac{E}{1-\nu^2}\big(\nu \,\mathrm{tr}\boldsymbol{\varepsilon}_i \,\mathbf{I}_{2\times 2} + (1-\nu)\boldsymbol{\varepsilon}_i\big) & \text{Plane stress} \\ ②. \quad \boldsymbol{\sigma}_i = \dfrac{E}{(1+\nu)(1-2\nu)}\big(\nu \,\mathrm{tr}\boldsymbol{\varepsilon}_i \,\mathbf{I}_{2\times 2} + (1-2\nu)\boldsymbol{\varepsilon}_i\big) & \text{Plane strain} \\ ③. \quad \boldsymbol{\sigma}_i = \dfrac{E}{(1+\nu)(1-2\nu)}\big(\nu \,\mathrm{tr}\boldsymbol{\varepsilon}_i \,\mathbf{I}_{3\times 3} + (1-2\nu)\boldsymbol{\varepsilon}_i\big) & \text{3D} \end{cases} \tag{3.20}$$

5. **Calculate the elasticity solid internal bond force between points**
   For each neighbor point $j \in \mathcal{S}_i$, calculate the nonlocal operate $\tilde{\nabla}\boldsymbol{v}_i$, calculate internal bond forces between points $\boldsymbol{Q}_{ij}, \boldsymbol{Q}_{ji}$ by solving Eq.3.16 and add $\boldsymbol{Q}_{ij}$ to $\boldsymbol{P}_i$ and add $-\boldsymbol{Q}_{ij}$ to $\boldsymbol{P}_j$.

6. **Applying the boundary conditions to solution**
   (i) Apply the external force $\boldsymbol{F}_i$ and displacement boundary conditions to the specified points, according to Newton's second law $\boldsymbol{F}_i - \boldsymbol{P}_i = \mathbb{M}_i \ddot{\boldsymbol{v}}_i(t)$, calculate each point's acceleration $\ddot{\boldsymbol{v}}_i$.
   (ii) Update each point's velocity and displacement through the Verlet-Velocity scheme.

3.5 Numerical examples

In this section, we explore the application of explicit NOM to solve dynamic elasticity solid problems. The implementation of explicit NOM has been carried out using the

environment of Mathematica [Wolfram, 1999]. Several numerical examples are provided to show the explicit NOM's capabilities.

3.5.1 Convergence of explicit NOM: free vibration of slender beam

To demonstrate the convergence of explicit NOM, we consider the slender beam-free vibration problem in this section. The slender beam with dimensions of $1 \times 0.1m^2$. The parameters for slender beam are $E = 30$GPa, $\nu = 0$, $\rho = 3000$ kg/m^3. Plane stress conditions are assumed in this test. The slender beam is discretized into 1111, 1764, and 4221 points with Δx=0.01, 0.008, and 0.005 m, respective, where Δx denotes the spacing of the points. Based on our numerical experience, eight points closest to the target point are selected to construct the target point's support.

The initial displacement field applied to the slender beam is mathematical described by the follows

$$u(x,y) = 0.001e^{[-100(x-0.5)^2]}, v(x,y) = 0, \quad x \in [0,1], y \in [0,0.1] \tag{3.21}$$

where u and v denote the displacement in the x and y directions, respectively.

As shown in Fig.3.2 and 3.3, the displacement field evolves in the same way under different discretizations. With the evolution of time, good agreements can be seen between the different discretizations. The displacement is independent of the discretizations in explicit NOM.

3.5.2 Cantilever beam under shear load

In order to demonstrate the correctness of explicit NOM, we consider a 2D cantilever beam with pure shear traction force. Geometry and boundary conditions are shown in Fig.3.4(a). The problem is solved by the explicit NOM and Abaqus standard. Plane stress conditions are assumed in this test. The beam is discretized into 3131 points with $\Delta x = 0.01$m, as shown in Fig.3.4(b). Eight points closest to the target point are selected to construct the target point's support domain. The parameters for material are $E = 30$GPa, $\nu = 0.33$, $\rho = 2400$ kg/m^3. The shear traction force $F = 1 \times 10^{-3}$MPa. In order to obtain the static solution, a damping coefficient α is adopted. The damping force for point $\mathbf{x}_i$ is calculated by $\mathbf{f}_i^{damp} = -\alpha \dot{\boldsymbol{v}}_i$.

As shown in Fig.3.5, good agreements can be seen between the explicit NOM method numerical results and ABAQUS results.

(a) $\Delta x = 0.01m, t = 6.32 \times 10^{-5}s$

(b) $\Delta x = 0.01m, t = 1.26 \times 10^{-4}s$

(c) $\Delta x = 0.01m, t = 3.16 \times 10^{-4}s$

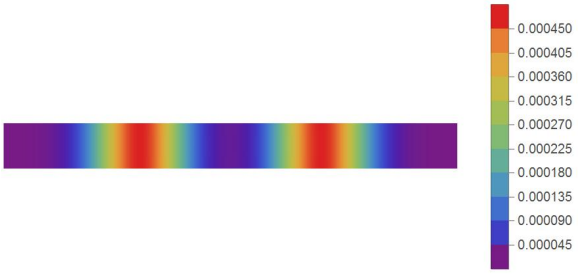

(d) $\Delta x = 0.008m, t = 6.32 \times 10^{-5}s$

(e) $\Delta x = 0.008m, t = 1.26 \times 10^{-4}s$

(f) $\Delta x = 0.008m, t = 3.16 \times 10^{-4}s$

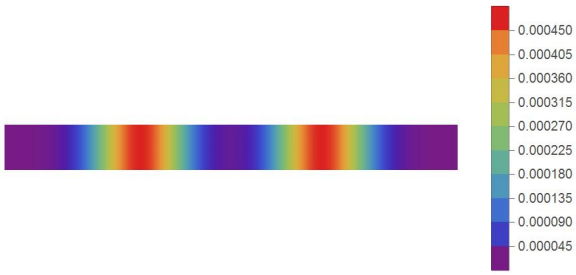

(g) $\Delta x = 0.005m, t = 6.32 \times 10^{-5}s$

(h) $\Delta x = 0.005m, t = 1.26 \times 10^{-4}s$

(i) $\Delta x = 0.005m, t = 3.16 \times 10^{-4}s$

Figure 3.2: Displacement field in x direction evolution process of free vibration of slender beam test at different discretizations and times.

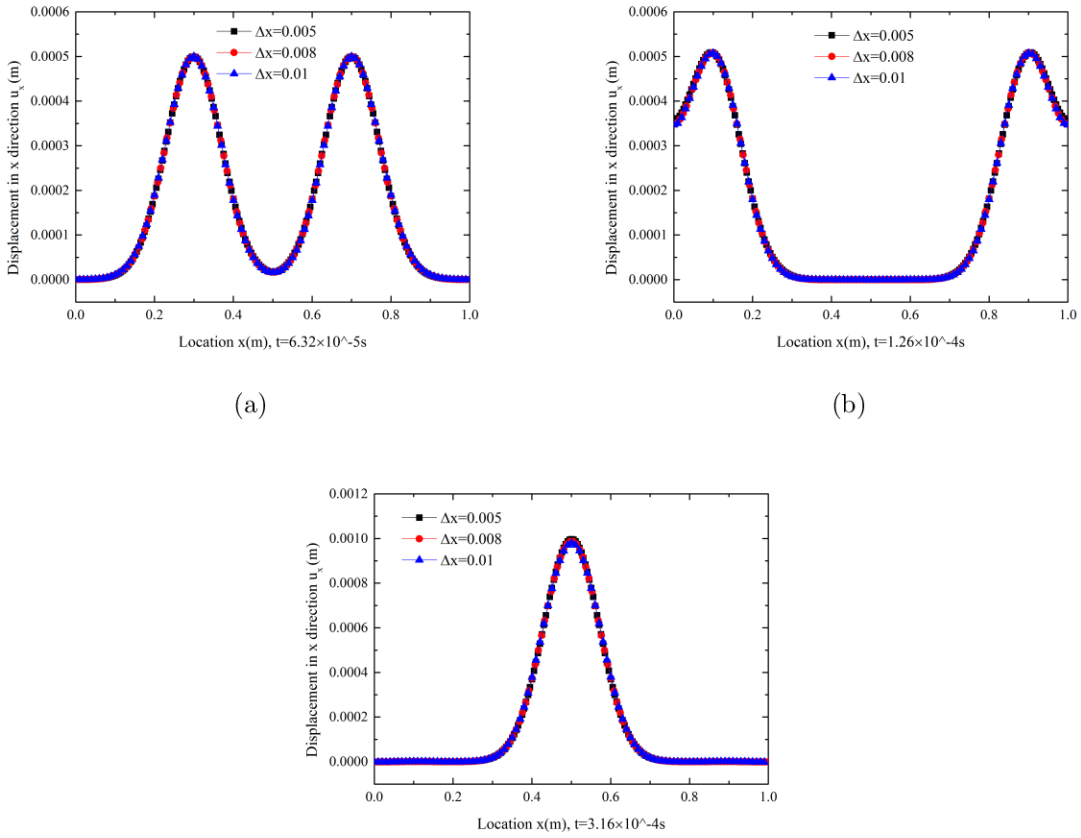

Figure 3.3: Displacement field for points in y=0.05 at different discretizations and times.

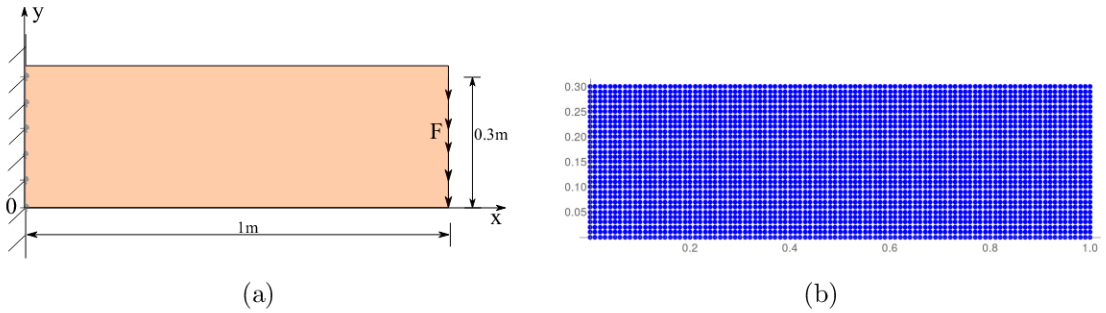

Figure 3.4: (a). Set up of the cantilever beam; (b) The discretization of cantilever beam($\Delta x = 0.01$m).

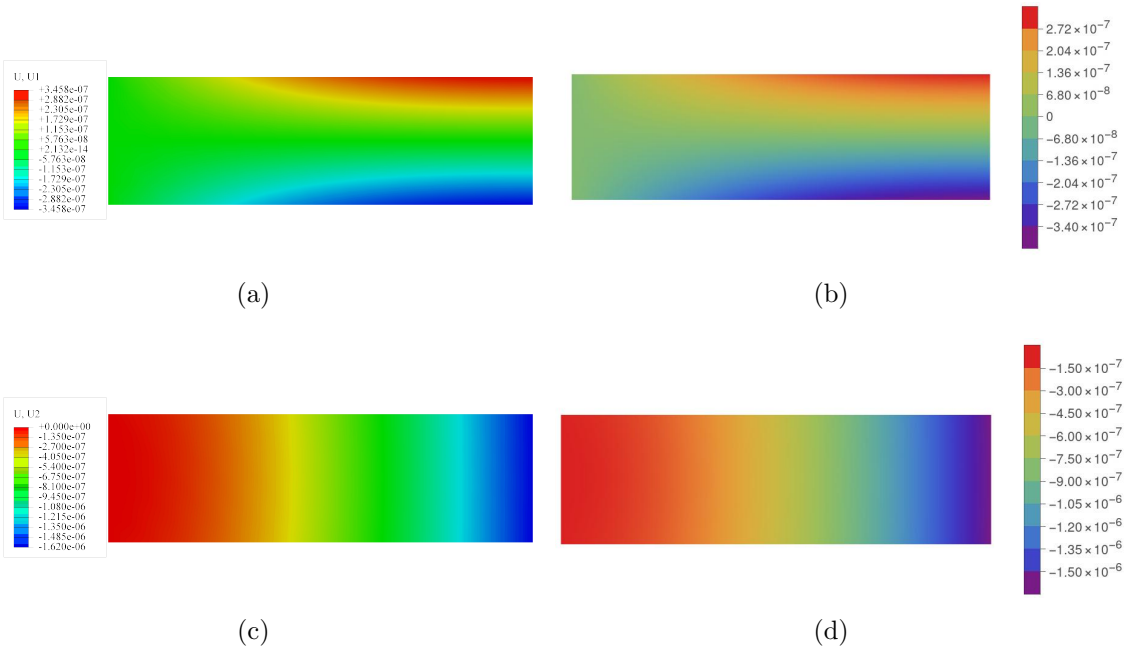

Figure 3.5: Displacement fields of the cantilever beam: (a) u_x of the ABAQUS model; (b) u_x of the NOM explicit model; (c)u_y of the ABAQUS model; (d) u_y of the NOM explicit model.

3.5.3 2D plate with holes subjected to uniform load

Consider a 2D plate with five holes subjected to the uniform load, as shown in Fig.3.6(a). The material parameters are: $E = 45\text{GPa}$, $\nu = 0.33$ and $\rho = 3000$ kg/m^3. The problem is solved by the explicit NOM and Abaqus standard. Plane strain conditions are assumed in this test. The plate is discretized into 15249 points with $\Delta x = 1/150\text{m}$, as shown in Fig.3.6(b). Eight points closest to the target point are selected to construct the target point's support domain. The upper boundary of the plate is subjected to a vertical load of $P = 1\text{MPa}$, while the bottom boundary remains stationary.

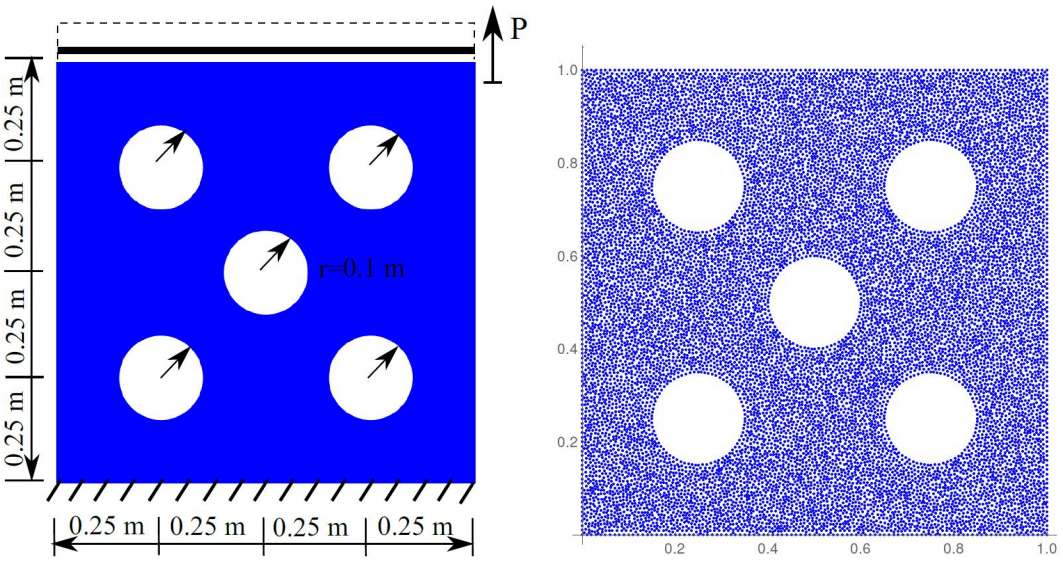

(a) (b)

Figure 3.6: (a). Set up of the plate with holes; (b) The discretization of plate with holes ($\Delta x = 1/150\text{m}$).

As shown in Fig.3.7, good agreements can be seen between the explicit nonlocal operator method numerical results and ABAQUS results.

3.5.4 Large deformation of 3D solid subjected to rectangle line load

In the last example, we present the capability of explicit NOM to model 3D large deformation problems. The solid with dimensions of $1 \times 0.1 \times 0.1m^3$ is discretized into 12221 points. The support of each point consists of 16 nearest neighbor points. A rectangle line load $P = 1\text{MPa}$ is applied to the right boundary of the solid while the left boundary is total fixed. The solid material parameters are $E = 30\text{GPa}$, $\nu = 0.33$ and $\rho = 3000$ kg/m^3. The deformation of 3D solid at different times in a cycle is depicted in Fig.3.8.

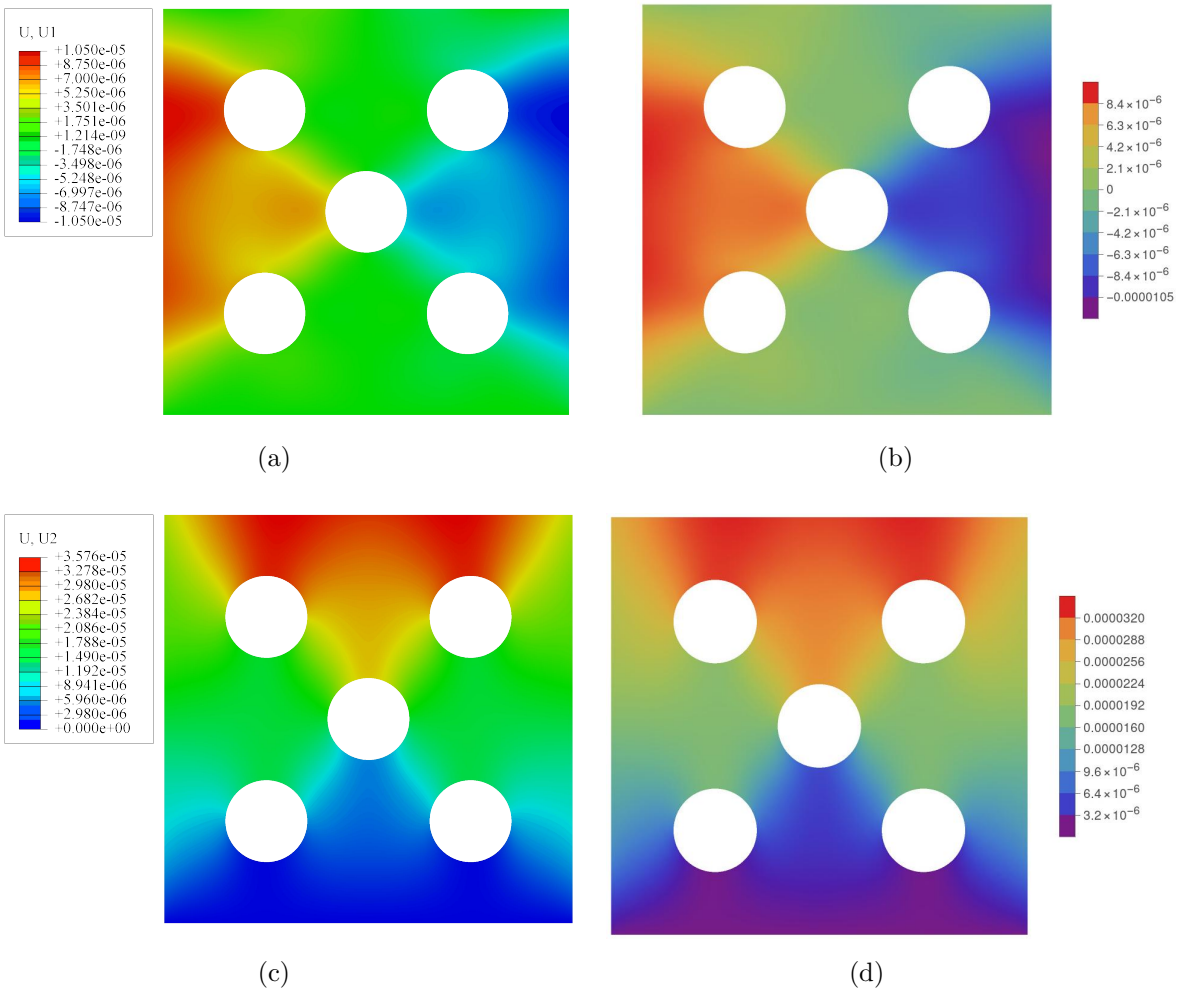

Figure 3.7: Displacement fields of the plate with holes; (a) u_x of the ABAQUS model; (b) u_x of the NOM explicit model; (c)u_y of the ABAQUS model; (d) u_y of the NOM explicit model.

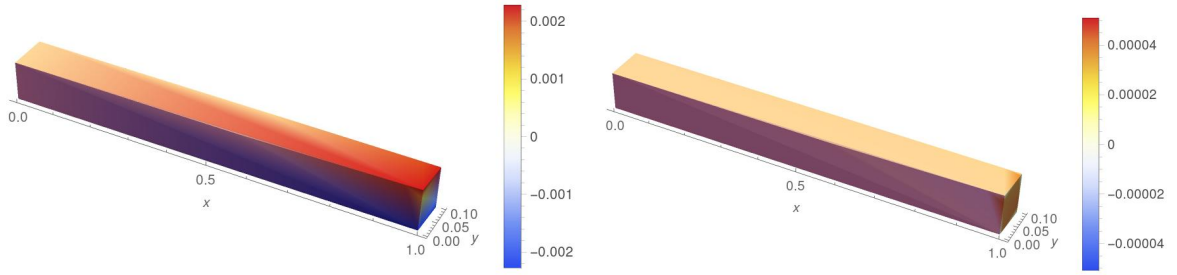

(a) $u_x, t = 2.5 \times 10^{-4} s$

(b) $u_y, t = 2.5 \times 10^{-4} s$

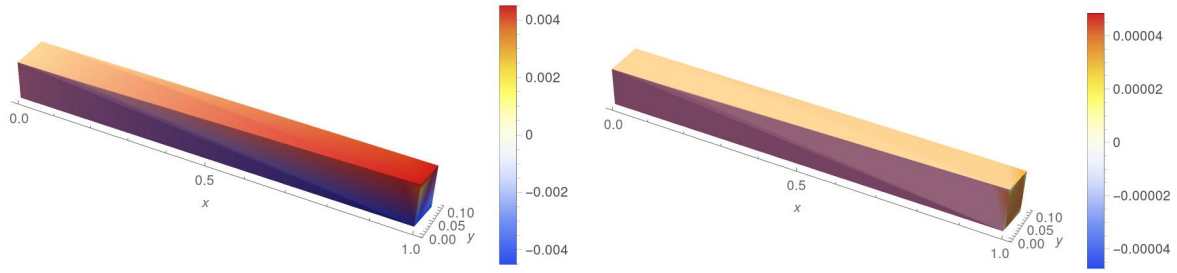

(c) $u_x, t = 5.0 \times 10^{-4} s$

(d) $u_y, t = 5.0 \times 10^{-5} s$

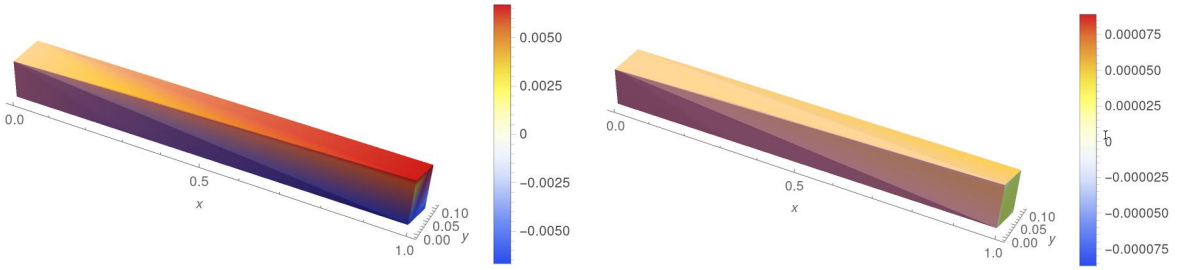

(e) $u_x, t = 7.5 \times 10^{-4} s$

(f) $u_y, t = 7.5 \times 10^{-4} s$

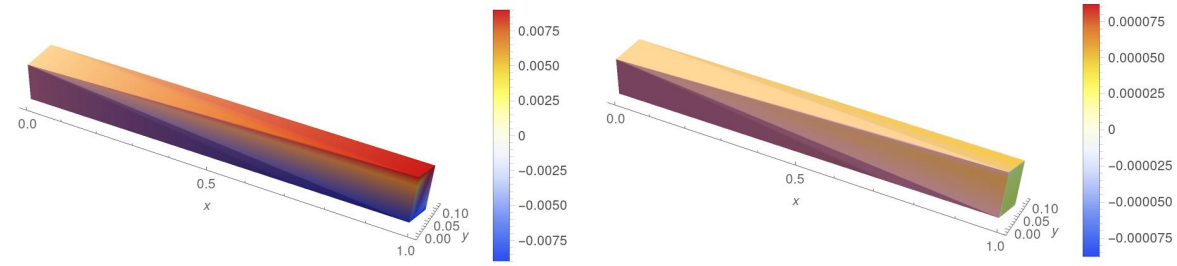

(g) $u_x, t = 1.0 \times 10^{-3} s$

(h) $t = 1.0 \times 10^{-3} s$

Figure 3.8: Displacement field in x and y directions evolution process of 3D solid at different times in a cycle.

3.6 Conclusions

In this chapter, we elaborated on the implementation progress of explicit NOM and a nonlocal dynamic elasticity solid formulation based on explicit NOM is also proposed. The nonlocal dynamic governing equation for elasticity solid is derived. The nonlocal operator energy functional is also derived and the relationship between local and nonlocal formulations is interpreted. Based on the dual property of the dual-support in NOM, the nonlocal dynamic governing equation is obtained with ease. We start from the energy form of the problem, by inserting the nonlocal expression of the gradient operator into the energy form. In the numerical simulation part, several numerical cases are presented to verify the accurateness of the nonlocal dynamic elasticity solid formulation in different conditions, and good agreement is observed between numerical simulation results and ABAQUS results.

Chapter 4

Nonlocal dynamic Kirchhoff plate formulation based on nonlocal operator method

This chapter is based on the journal paper 'Nonlocal dynamic Kirchhoff plate formulation based on nonlocal operator method' published in EWCO by my first author. The contribution of this paper is summarized as follows:

Yongzheng Zhang

- Conceptualization
- Research state of the art
- Investigation
- Formal analysis
- Methodology
- Software/Programming
- Data curation
- Data analysis
- Validation
- Visualization
- Writing original manuscript draft

Huilong Ren

- Conceptualization

- Writing review and editing

Timon Rabczuk

- Conceptualization
- Mentoring the research progress
- Writing review and editing

4.1 General

As a common engineering structure, plate/shell is widely used in civil engineering, aerospace and other fields. The mechanical analysis of rectangular thin plates has always been one of the research focuses of scholars and engineers. The governing equation of the Kirchhoff plate bending problem is a fourth-order partial differential equation whose deflection is an independent variable. The numerical method for developing this problem has a wide scientific significance for solving plate/shell problems.

The analysis of Kirchhoff plate bending problems poses challenges to 'classical' finite element formulations [Areias and Rabczuk, 2013, Amiri et al., 2014, Nguyen-Thanh et al., 2015, Areias et al., 2016b, Nguyen-Thanh et al., 2017], which are only C^0 continuous. However, the Kirchhoff plate problem is a fourth-order partial differential equation which requires a C^1 formulation if weak form based methods such as FEM are employed. An efficient alternative are so-called meshless methods as many of them are higher-order continuous. The approximation function of the meshless method [CA, 1978, Zhang et al., 2001, Chen et al., 2004, Roque et al., 2015, Roque and Martins, 2015, Greco et al., 2017] represented by the Element-free Galerkin method EFG [Krysl and Belytschko, 1995, 1996, Noguchi et al., 2000, Ivannikov et al., 2014] is highly smooth, that is, and the high-order continuity is satisfied, meantime the meshless method is easy to form high-order. The approximate function has significant advantages to the numerical solutions for higher-order partial-differential equations.

Rabczuk [Rabczuk et al., 2007b] devised a meshfree method for thin shell analysis for finite strains and arbitrary evolving cracks exploiting the higher-order continuity of the EFG shape functions and avoiding any rotational degrees of freedom. Mohammed et al.[Al-Tholaia and Al-Gahtani, 2015, Hussein Al-Tholaia and Al-Gahtani, 2016] presented a meshless method to analyze the mechanical response of elastic thin plates. However, since meshless shape functions are commonly rational functions, more integration points are needed to evaluate the weak form. For example, Brebbia [CA, 1978] employed 6×6 quadrature points, which significantly reduces the computational efficiency. An interesting alternative to meshless methods is isogeometric analysis (IGA) [Hughes et al., 2005, Cottrell et al., 2009], which also fulfills the higher-order continuity requirement needed for

thin plate analysis. This method takes advantage of NURBS/B-Spline basis functions, which are commonly used in computer-aided-design (CAD) to describe the geometries. IGA has been successfully applied to the analysis of plates and shells for instance in [Kiendl et al., 2009, Benson et al., 2010, Thai et al., 2015, Riffnaller-Schiefer et al., 2016, Li et al., 2019]. As CAD geometries are surface representations, they are particularly suited for plates and shells. One difficulty occurs for multi-patch geometries, which are still difficult to deal with.

In this chapter, we take advantage of nonlocal theories as suggested for instance in nonlocal continuum field theories with various physical fields [Eringen, 2002], peridynamics (PD) [Silling, 2000], nonlocal plasticity, (nonlocal) damage mechanics [Bažant and Jirásek, 2002] and nonlocal vector calculus [Gunzburger and Lehoucq, 2010]. Nonlocal operator method (NOM) [Rabczuk et al., 2019, Ren et al., 2020b] is a nonlocal numerical method for solving partial differential equations. The method is based on so-called differential operators. In contrast to finite elements, the NOM only needs neighboring points to develop nonlocal derivatives. Similar to the machine learning approach [Samaniego et al., 2020], it can solve PDEs directly instead of the need of shape functions, which plays an equivalent role as the derivatives of the shape functions in the meshless methods or the FEM. And therefore the complexity of the nonlocal operator method is significantly reduced. The nonlocal strong form can be derived by a variational derivation on the functional defined by nonlocal operators. This chapter presents a nonlocal operator method to predict the dynamic response of Kirchhoff plates exploiting the higher-order continuity of the NOM.

The remainder of this chapter is organized as follows: We derive the nonlocal Hessian operator for Kirchhoff plates in Section 4.2. In Section 4.3, we derive the nonlocal dynamic Kirchhoff plate formulation by a variational formulation. Section 4.4 presents details about the numerical implementation before we demonstrate the performance of the formulation through several benchmark problems in Section 4.5. We conclude the chapter in Section 4.6.

4.2 Derivation of nonlocal Hessian operator for Kirchhoff plate

We consider a Kirchhoff plate occupying a domain $\mathbf{\Omega}$ as illustrated in Fig.4.1. Let us denote the spatial coordinates with $\mathbf{x}_i$, $\boldsymbol{\xi}_{ij} := \mathbf{x}_j - \mathbf{x}_i$ is relative position vector from $\mathbf{x}_i$ to $\mathbf{x}_j$; $w_i := w(\mathbf{x}_i, t)$ and $w_j := w(\mathbf{x}_j, t)$ are the displacement value for $\mathbf{x}_i$ and $\mathbf{x}_j$, respectively; the relative displacement area for the spatial vector $\boldsymbol{\xi}_{ij}$ is $w_{ij} := w_j - w_i$.

The higher-order nonlocal operator $\tilde{\partial}_\alpha w_i$ for the scalar field w in support $\mathcal{S}_i$ can be

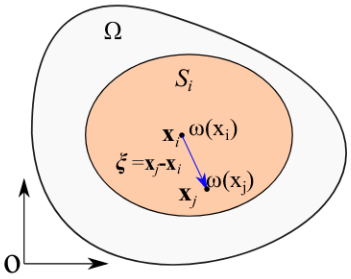

Figure 4.1: Domain and notation

expressed as [Ren et al., 2020a]

$$\tilde{\partial}_\alpha w_i := \int_{\mathcal{S}_i} \phi(\boldsymbol{\xi}_{ij}) w_{ij} \mathbf{s}_{ij} dV_j \cdot \Big(\int_{\mathcal{S}_i} \phi(\boldsymbol{\xi}_{ij}) \mathbf{s}_{ij} \mathbf{s}_{ij}^T dV_j \Big)^{-1} \tag{4.1}$$

where $\phi(\boldsymbol{\xi}_{ij})$ represents the weight function, $\boldsymbol{\xi}_{ij}$ represents relative position vector. $\mathbf{s}_{ij}$ represent the list of polynomials. For example, the polynomials and the higher-order nonlocal operator in 2D with maximal second order derivatives are $\mathbf{s}_{ij} = (x_{ij}, y_{ij}, x_{ij}^2/2, x_{ij}y_{ij}, y_{ij}^2/2)^T$ and $\tilde{\partial}_\alpha w_i = (\frac{\partial w_i}{\partial x}, \frac{\partial w_i}{\partial y}, \frac{\partial^2 w_i}{\partial x^2}, \frac{\partial^2 w_i}{\partial xy}, \frac{\partial^2 w_i}{\partial y^2})^T$.

Using nodal integration, the higher-order nonlocal operator and it's variation for a vector field w in discrete forms are

$$\tilde{\partial}_\alpha w_i = \sum_{j \in \mathcal{S}_i} \phi(\boldsymbol{\xi}_{ij}) w_{ij} \mathbf{s}_{ij} \Delta V_j \cdot \Big(\sum_{j \in \mathcal{S}_i} \phi(\boldsymbol{\xi}_{ij}) \mathbf{s}_{ij} \mathbf{s}_{ij}^T \Delta V_j \Big)^{-1} \tag{4.2}$$

$$\tilde{\partial}_\alpha \delta w_i = \sum_{j \in \mathcal{S}_i} \phi(\boldsymbol{\xi}_{ij}) (\delta w_j - \delta w_i) \boldsymbol{\xi}_{ij} \Delta V_j \cdot \Big(\sum_{j \in \mathcal{S}_i} \phi(\boldsymbol{\xi}_{ij}) \mathbf{s}_{ij} \mathbf{s}_{ij}^T \Delta V_j \Big)^{-1} \tag{4.3}$$

We use a penalty energy functional to obtain the linear field of the scalar field to eliminate zero energy modes. The higher-order operator energy functional for a scalar field w at a point $\mathbf{x}_i$ is defined as

$$\mathcal{F}_i^{hg} = \frac{\alpha_w}{2m_i} \int_{\mathcal{S}_i} \phi(\boldsymbol{\xi}_{ij}) \big(\mathbf{s}_{ij}^T \tilde{\partial}_\alpha w_i - w_{ij} \big)^2 dV_j \tag{4.4}$$

where $m_i (= \int_{\mathcal{S}_i} \phi(\boldsymbol{\xi}_{ij}) \boldsymbol{\xi}_{ij} \otimes \boldsymbol{\xi}_{ij} dV_j)$ is the normalization coefficient and α_w is the penalty coefficient. The nonuniform aspect of the deformation is defined as $\mathbf{s}_{ij}^T \tilde{\partial}_\alpha w_i - w_{ij}$, and the stability of the NOM is greatly enhanced while $\mathbf{s}_{ij}^T \tilde{\partial}_\alpha w_i - w_{ij}$ is enforced explicitly.

To devise the nonlocal Hessian operator in 2D, let us define first the vector $\boldsymbol{\xi}_{ij} = (x_{ij}, y_{ij})^T$. It can be shown that the second order shape tensor for point $\mathbf{x}_i$ is computed by [Ren et al., 2020b]

$$\mathbf{K}_{2i} = \int_{\mathcal{S}_i} \phi(\boldsymbol{\xi}_{ij}) \boldsymbol{\xi}_{ij} \otimes \boldsymbol{\xi}_{ij} dV_j = \int_{\mathcal{S}_i} \phi(\boldsymbol{\xi}_{ij}) \begin{bmatrix} x_{ij}^2 & x_{ij}y_{ij} \\ x_{ij}y_{ij} & y_{ij}^2 \end{bmatrix} dV_j \tag{4.5}$$

and the third order shape tensor for point $\mathbf{x}_i$ by

$$\begin{aligned}\mathbf{K}_{3i} &= \int_{\mathcal{S}_i} \phi(\boldsymbol{\xi}_{ij})\boldsymbol{\xi}_{ij}^3 dV_j \\ &= \Big(\int_{\mathcal{S}_i} \phi(\boldsymbol{\xi}_{ij}) x_{ij} \begin{bmatrix} x_{ij}^2 & x_{ij}y_{ij} \\ x_{ij}y_{ij} & y_{ij}^2 \end{bmatrix} dV_j, \int_{\mathcal{S}_i} \phi(\boldsymbol{\xi}_{ij}) y_{ij} \begin{bmatrix} x_{ij}^2 & x_{ij}y_{ij} \\ x_{ij}y_{ij} & y_{ij}^2 \end{bmatrix} dV_j \Big) \\ &= \Big(\int_{\mathcal{S}_i} \phi(\boldsymbol{\xi}_{ij}) \begin{bmatrix} x_{ij}^3 & x_{ij}^2y_{ij} \\ x_{ij}^2y_{ij} & x_{ij}y_{ij}^2 \end{bmatrix} dV_j, \int_{\mathcal{S}_i} \phi(\boldsymbol{\xi}_{ij}) \begin{bmatrix} x_{ij}^2y_{ij} & x_{ij}y_{ij}^2 \\ x_{ij}y_{ij}^2 & y_{ij}^3 \end{bmatrix} dV_j \Big) = (\mathbf{K}_{3i}^x, \mathbf{K}_{3i}^y) \end{aligned} \tag{4.6}$$

with $\boldsymbol{\xi}_{ij}^n := \underbrace{\boldsymbol{\xi}_{ij} \otimes \boldsymbol{\xi}_{ij} \otimes \cdots \otimes \boldsymbol{\xi}_{ij}}_{\text{n terms}}$.

which finally leads to

$$\mathbf{K}_{3i}\mathbf{K}_{2i}^{-1}\boldsymbol{\xi}_{ij} = (\mathbf{K}_{3i}^x\mathbf{K}_{2i}^{-1}\boldsymbol{\xi}_{ij}, \mathbf{K}_{3i}^y\mathbf{K}_{2i}^{-1}\boldsymbol{\xi}_{ij}). \tag{4.7}$$

The fourth-order shape tensor for point $\mathbf{x}_i$ is computed by

$$\begin{aligned}\mathbf{K}_{4i} &= \int_{\mathcal{S}_i} \phi(\boldsymbol{\xi}_{ij})\boldsymbol{\xi}_{ij}^4 dV_j \\ &= \int_{\mathcal{S}_i} \phi(\boldsymbol{\xi}_{ij}) \begin{bmatrix} x_{ij}^2 \begin{bmatrix} x_{ij}^2 & x_{ij}y_{ij} \\ x_{ij}y_{ij} & y_{ij}^2 \end{bmatrix} & x_{ij}y_{ij} \begin{bmatrix} x_{ij}^2 & x_{ij}y_{ij} \\ x_{ij}y_{ij} & y_{ij}^2 \end{bmatrix} \\ y_{ij}x_{ij} \begin{bmatrix} x_{ij}^2 & x_{ij}y_{ij} \\ x_{ij}y_{ij} & y_{ij}^2 \end{bmatrix} & y_{ij}^2 \begin{bmatrix} x_{ij}^2 & x_{ij}y_{ij} \\ x_{ij}y_{ij} & y_{ij}^2 \end{bmatrix} \end{bmatrix} dV_j \\ &= \int_{\mathcal{S}_i} \phi(\boldsymbol{\xi}_{ij}) \begin{bmatrix} \begin{bmatrix} x_{ij}^4 & x_{ij}^3y_{ij} \\ x_{ij}^3y_{ij} & x_{ij}^2y_{ij}^2 \end{bmatrix} & \begin{bmatrix} x_{ij}^3y_{ij} & x_{ij}^2y_{ij}^2 \\ x_{ij}^2y_{ij}^2 & x_{ij}y_{ij}^3 \end{bmatrix} \\ \begin{bmatrix} x_{ij}^3y_{ij} & x_{ij}^2y_{ij}^2 \\ x_{ij}^2y_{ij}^2 & x_{ij}y_{ij}^3 \end{bmatrix} & \begin{bmatrix} x_{ij}^2y_{ij}^2 & x_{ij}y_{ij}^3 \\ x_{ij}y_{ij}^3 & y_{ij}^4 \end{bmatrix} \end{bmatrix} dV_j = \begin{bmatrix} \mathbf{K}_{4i}^{xx} & \mathbf{K}_{4i}^{xy} \\ \mathbf{K}_{4i}^{yx} & \mathbf{K}_{4i}^{yy} \end{bmatrix} \end{aligned} \tag{4.8}$$

The second-order Taylor series extension for a scalar field w is given as

$$w_j = w_i + \nabla w_i \cdot \boldsymbol{\xi}_{ij} + \frac{1}{2!}\nabla^T\nabla w_i : \boldsymbol{\xi}_{ij} \otimes \boldsymbol{\xi}_{ij} + O(\mid \boldsymbol{\xi}_{ij} \mid^3) \tag{4.9}$$

so that we obtain

$$w_{ij} = \nabla w_i \cdot \boldsymbol{\xi}_{ij} + \frac{1}{2}\nabla^T\nabla w_i : \boldsymbol{\xi}_{ij} \otimes \boldsymbol{\xi}_{ij} + O(\mid \boldsymbol{\xi}_{ij} \mid^3) \tag{4.10}$$

which finally results in the following Hessian nonlocal operator

$$\frac{1}{2}\nabla^T\nabla w_i : \boldsymbol{\xi}_{ij} \otimes \boldsymbol{\xi}_{ij} = w_{ij} - \nabla w_i \cdot \boldsymbol{\xi}_{ij} \tag{4.11}$$

and

$$\frac{1}{2}\nabla^T\nabla w_i : \int_{\mathcal{S}_i} \phi(\boldsymbol{\xi}_{ij})\boldsymbol{\xi}_{ij}^4 dV_j = \int_{\mathcal{S}_i} \phi(\boldsymbol{\xi}_{ij})(w_{ij}\boldsymbol{\xi}_{ij} \otimes \boldsymbol{\xi}_{ij} - \nabla w_i \cdot \boldsymbol{\xi}_{ij}^3) dV_j. \tag{4.12}$$

The weighted tensor $\frac{1}{2}\nabla^T\nabla w : \mathbf{K}_{4i}$ can be simplified to

$$\begin{aligned}
&\frac{1}{2}\nabla^T\nabla w_i : \mathbf{K}_{4i} = \int_{\mathcal{S}_i} \phi(\boldsymbol{\xi}_{ij})(w_{ij}\boldsymbol{\xi}_{ij} \otimes \boldsymbol{\xi}_{ij} - \nabla w_i \cdot \boldsymbol{\xi}_{ij}^3) dV_j \\
&= \int_{\mathcal{S}_i} \phi(\boldsymbol{\xi}_{ij}) w_{ij}\boldsymbol{\xi}_{ij} \otimes \boldsymbol{\xi}_{ij} dV_j - \nabla w_i \cdot \int_{\mathcal{S}_i} \phi(\boldsymbol{\xi}_{ij})\boldsymbol{\xi}_{ij}^3 dV_j \\
&= \int_{\mathcal{S}_i} \phi(\boldsymbol{\xi}_{ij}) w_{ij}\boldsymbol{\xi}_{ij} \otimes \boldsymbol{\xi}_{ij} dV_j - \int_{\mathcal{S}_i} \phi(\boldsymbol{\xi}_{ij}) w_{ij}\boldsymbol{\xi}_{ij} dV_j \cdot \Big(\int_{\mathcal{S}_i} \phi(\boldsymbol{\xi}_{ij})\boldsymbol{\xi}_{ij} \otimes \boldsymbol{\xi}_{ij} \mathrm{d}V_j \Big)^{-1} \mathbf{K}_{3i} \\
&= \int_{\mathcal{S}_i} \phi(\boldsymbol{\xi}_{ij}) w_{ij}\boldsymbol{\xi}_{ij} \otimes \boldsymbol{\xi}_{ij} dV_j - \int_{\mathcal{S}_i} \phi(\boldsymbol{\xi}_{ij}) w_{ij}\boldsymbol{\xi}_{ij} dV_j \cdot \mathbf{K}_{2i}^{-1}\mathbf{K}_{3i} \\
&= \int_{\mathcal{S}_i} \phi(\boldsymbol{\xi}_{ij}) w_{ij}(\boldsymbol{\xi}_{ij} \otimes \boldsymbol{\xi}_{ij} - \mathbf{K}_{3i}\mathbf{K}_{2i}^{-1}\boldsymbol{\xi}_{ij}) dV_j.
\end{aligned} \tag{4.13}$$

Note that the rank of $\mathbf{K}_{4i}$ is 3 and the 2D nonlocal Hessian operator has only three independent variables where $\frac{\partial^2 \delta w_i}{\partial x \partial y} = \frac{\partial^2 \delta w_i}{\partial y \partial x}$, let $\mathbf{K}_{4i}^{-1}$ as the pseudo-inverse of $\mathbf{K}_{4i}$ in this study.

For the scalar field w, the 2D nonlocal Hessian operator for point $\mathbf{x}_i$ can be written in matrix form as

$$\tilde{\nabla}^T\tilde{\nabla} w_i = \begin{bmatrix} \frac{\partial^2 w_i}{\partial x^2} & \frac{\partial^2 w_i}{\partial x \partial y} \\ \frac{\partial^2 w_i}{\partial y \partial x} & \frac{\partial^2 w_i}{\partial y^2}. \end{bmatrix} \tag{4.14}$$

We let $\mathbf{K}_{3i}^x\mathbf{K}_{2i}^{-1}, \mathbf{K}_{3i}^y\mathbf{K}_{2i}^{-1}$ and the pseudo-inverse of $\mathbf{K}_{4i}$ be explicitly written as

$$\mathbf{K}_{3i}^x\mathbf{K}_{2i}^{-1} = \begin{bmatrix} a_{11} & a_{12} \\ a_{12} & a_{22} \end{bmatrix}; \mathbf{K}_{3i}^y\mathbf{K}_{2i}^{-1} = \begin{bmatrix} b_{11} & b_{12} \\ b_{12} & b_{22} \end{bmatrix} \tag{4.15}$$

$$\mathbf{K}_{4i}^{-1} = \begin{bmatrix} \begin{bmatrix} c_1 & c_2 \\ c_2 & c_3 \end{bmatrix} & \begin{bmatrix} c_2 & c_3 \\ c_3 & c_4 \end{bmatrix} \\ \begin{bmatrix} c_2 & c_3 \\ c_3 & c_4 \end{bmatrix} & \begin{bmatrix} c_3 & c_4 \\ c_4 & c_5 \end{bmatrix} \end{bmatrix} \tag{4.16}$$

To facilitate the calculation $\mathbf{K}_{4i}^{-1}$, we convert $\mathbf{K}_{4i}$ to a 3×3 matrix yielding

$$\begin{bmatrix} c_1 & c_2 & c_3 \\ c_2 & c_3 & c_4 \\ c_3 & c_4 & c_5 \end{bmatrix}^{-1} = \int_{\mathcal{S}_i} \phi(\boldsymbol{\xi}_{ij}) \begin{bmatrix} x_{ij}^4 & x_{ij}^3 y & x_{ij}^2 y_{ij}^2 \\ x_{ij}^3 y_{ij} & x_{ij}^2 y_{ij}^2 & x_{ij} y_{ij}^3 \\ x_{ij}^2 y_{ij}^2 & x_{ij} y_{ij}^3 & y_{ij}^4 \end{bmatrix} dV_j \tag{4.17}$$

Since $\boldsymbol{\xi}_{ij} \otimes \boldsymbol{\xi}_{ij} - \mathbf{K}_{3i}\mathbf{K}_{2i}^{-1}\boldsymbol{\xi}_{ij}$ is a matrix $\mathbf{Q}_{2\times 2}$ with the terms $Q_{12} = Q_{21}$. Remove the repeated terms in matrix $\mathbf{Q}$, and the remain terms Q_{11}, Q_{12}, Q_{22} in matrix $\mathbf{Q}$ can be reconstituted a vector $\mathbf{L}_{3\times 1} = (Q_{11}, Q_{12}, Q_{22})^T$. Then Eq.4.13 can be rewritten as

$$\int_{\mathcal{S}_i} \phi(\boldsymbol{\xi}_{ij}) \begin{bmatrix} x_{ij}^4 & x_{ij}^3 y & x_{ij}^2 y_{ij}^2 \\ x_{ij}^3 y_{ij} & x_{ij}^2 y_{ij}^2 & x_{ij} y_{ij}^3 \\ x_{ij}^2 y_{ij}^2 & x_{ij} y_{ij}^3 & y_{ij}^4 \end{bmatrix} dV_j \begin{bmatrix} \frac{\partial^2 w_i}{\partial x^2} \\ \frac{\partial^2 w_i}{\partial x \partial y} \\ \frac{\partial^2 w_i}{\partial y^2} \end{bmatrix} = \int_{\mathcal{S}_i} \phi(\boldsymbol{\xi}_{ij}) w_{ij} \mathbf{L}_i dV_j \tag{4.18}$$

Finally, $\left(\boldsymbol{\xi}_{ij} \otimes \boldsymbol{\xi}_{ij} - \mathbf{K}_{3i}\mathbf{K}_{2i}^{-1}\boldsymbol{\xi}_{ij}\right) : \mathbf{K}_{4i}^{-1}$ can be obtained by reconstituting terms in Eq.4.18 and can be expressed as

$$\left(\boldsymbol{\xi}_{ij} \otimes \boldsymbol{\xi}_{ij} - \mathbf{K}_{3i}\mathbf{K}_{2i}^{-1}\boldsymbol{\xi}_{ij}\right) : \mathbf{K}_{4i}^{-1} = \begin{bmatrix} e_{i11} & e_{i12} \\ e_{i21} & e_{i22} \end{bmatrix} \tag{4.19}$$

where

$$\begin{aligned}
e_{i11} &= c_1(x_{ij}^2 - a_{11}x_{ij} - a_{12}y_{ij}) + c_2(x_{ij}y_{ij} - a_{12}x_{ij} - a_{22}y_{ij}) + c_3(y_{ij}^2 - b_{12}x_{ij} - b_{22}y_{ij}) \\
e_{i12} &= e_{i21} = c_2(x_{ij}^2 - a_{11}x_{ij} - a_{12}y_{ij}) + c_3(-a_{12}x_{ij} - a_{22}y_{ij} + x_{ij}y_{ij}) + c_4(y_{ij}^2 - b_{12}x_{ij} - b_{22}y_{ij}) \\
e_{i22} &= c_3(x_{ij}^2 - a_{11}x_{ij} - a_{12}y_{ij}) + c_4(-a_{12}x_{ij} - a_{22}y_{ij} + x_{ij}y_{ij}) + c_5(y_{ij}^2 - b_{12}x_{ij} - b_{22}y_{ij}).
\end{aligned}$$

The explicit form of the nonlocal Hessian operator in 2D can finally be expressed by

$$\tilde{\nabla}^T \tilde{\nabla} w_i = 2 \int_{\mathcal{S}_i} \phi(\boldsymbol{\xi}_{ij}) w_{ij} \begin{bmatrix} e_{i11} & e_{i12} \\ e_{i21} & e_{i22} \end{bmatrix} dV_j \tag{4.20}$$

Note that $e_{i11}, e_{i12}, e_{i22}$ are calculated for each neighbor in the support domain. As a result, the variation of nonlocal Hessian operator can be obtained in explicit form as

$$\tilde{\nabla}^T \tilde{\nabla} \delta w_i = 2 \int_{\mathcal{S}_i} \phi(\boldsymbol{\xi}_{ij})(\delta w_j - \delta w_i) \begin{bmatrix} e_{i11} & e_{i12} \\ e_{i21} & e_{i22} \end{bmatrix} dV_j. \tag{4.21}$$

4.3 Derivation of nonlocal dynamic Kirchhoff plate formulation

4.3.1 Classical elastic plate theory

Kirchhoff plate theory assumes that the normal stress in the thickness direction can be ignored and the normal of the midplane of the plate remains normal after deformation. Hence, all stresses and strains can be expressed by the deflection w of the midplane of

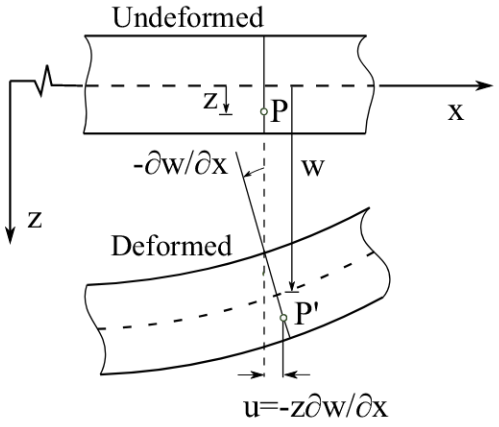

Figure 4.2: Deformed configuration of a Kirchhoff plate in bending.

the plate. Considering the plate element shown in Fig.4.2, the in-plane displacements u and v can, therefore, be expressed in terms of the first derivatives of w, i.e.

$$u(x,y,z) = -z\frac{\partial w}{\partial x};\ v(x,y,z) = -z\frac{\partial w}{\partial y};\ w(x,y,z) \simeq w(x,y,0) \cong w(x,y). \tag{4.22}$$

The strain resultant $\boldsymbol{\kappa}$ can be obtained by

$$\boldsymbol{\kappa} = \left[\kappa_x, \kappa_y, \kappa_{xy}\right]^T = \left[-\tfrac{\partial^2 w}{\partial x^2}, -\tfrac{\partial^2 w}{\partial y^2}, -\tfrac{2\partial^2 w}{\partial x \partial y}\right]^T \tag{4.23}$$

where κ_x and κ_y indicates the curvature of the midplane of the plate in the x- and y-direction while κ_{xy} refers to the torsion, respectively.

The stress resultants of the Kirchhoff plate are given by

$$\mathbf{M} = \left[M_x, M_y, M_{xy}\right]^T \tag{4.24}$$

where M_x and M_y are the bending moment per unit length around the y- and negative x-axes, respectively, while $M_{xy}(= M_{yx})$ is the torque per unit length.

With a linear stress distribution in the z-direction and assuming a thickness of t, the stresses can be computed by

$$\sigma_x = \frac{12M_x}{t^3}z; \sigma_y = \frac{12M_y}{t^3}z; \tau_{xy} = \tau_{yx} = \frac{12M_{xy}}{t^3}z \tag{4.25}$$

The Cauchy stress tensor can also be expressed in terms of the linear strain tensor assuming Hooke's law:

$$\sigma = \frac{E}{1-\nu^2}\big(\nu\,\mathrm{tr}\varepsilon\,\mathbf{I}_{2\times 2} + (1-\nu)\varepsilon\big) \tag{4.26}$$

with

$$\varepsilon = \begin{bmatrix} \varepsilon_{11} & \varepsilon_{12} \\ \varepsilon_{21} & \varepsilon_{22} \end{bmatrix}$$

Finally, the constitutive model can be formulated in terms of the stress and strain resultants by

$$\mathbf{M} = \mathbf{D}_{plate}\boldsymbol{\kappa} \tag{4.27}$$

where $\mathbf{D}_{plate}$ is the constitutive matrix defined as

$$\mathbf{D}_{plate} = \frac{Et^3}{12(1-\nu^2)} \begin{bmatrix} 1 & \nu & 0 \\ \nu & 1 & 0 \\ 0 & 0 & \frac{1-\nu}{2} \end{bmatrix} = D_0 \begin{bmatrix} 1 & \nu & 0 \\ \nu & 1 & 0 \\ 0 & 0 & \frac{1-\nu}{2} \end{bmatrix} \tag{4.28}$$

where $D_0 = \frac{Et^3}{12(1-\nu^2)}$ is the Kirchhoff plate's bending stiffness, such that Eq.(4.27) can be rewritten as

$$\overline{\mathbf{M}} = \begin{bmatrix} M_x & M_{xy} \\ M_{yx} & M_y \end{bmatrix} = D_0\big(\nu \,\mathrm{tr}\overline{\boldsymbol{\kappa}}\, \boldsymbol{I}_{2\times 2} + (1-\nu)\overline{\boldsymbol{\kappa}}\big) \tag{4.29}$$

$$\overline{\boldsymbol{\kappa}} = \nabla^T\nabla w = \begin{bmatrix} \frac{\partial^2 w}{\partial x^2} & \frac{\partial^2 w}{\partial x \partial y} \\ \frac{\partial^2 w}{\partial y \partial x} & \frac{\partial^2 w}{\partial y^2} \end{bmatrix} \tag{4.30}$$

4.3.2 Nonlocal dynamic Kirchhoff plate formulation

The total Lagrange energy functional for the Kirchhoff plate can be expressed as

$$\begin{aligned} L(\dot{w}, w) &= \int_\Omega \frac{1}{2}\rho\dot{w}^2 \mathrm{d}\Omega - \int_\Omega (\frac{1}{2}\overline{\mathbf{M}} : \overline{\boldsymbol{\kappa}} - q_z w)\mathrm{d}\Omega - \int_{\partial\Omega} \overline{M_n}\frac{\partial w}{\partial n} dS \\ &= \int_\Omega \frac{1}{2}\rho\dot{w}^2 \mathrm{d}\Omega - \int_\Omega (\frac{1}{2}\overline{\mathbf{M}} : \nabla^T\nabla w - q_z w)\mathrm{d}\Omega - \int_{\partial\Omega} \overline{M_n}\frac{\partial w}{\partial n} dS \end{aligned} \tag{4.31}$$

with $\dot{w} = \frac{\partial w}{\partial t}$; ρ is the density of the plate and q_z a distributed load in the z-direction. Replacing the local Hessian $\nabla^T\nabla w$ with the nonlocal Hessian $\tilde{\nabla}^T\tilde{\nabla} w$ in Eq.4.31, we obtain

$$L(\dot{w}, w) = \int_\Omega \frac{1}{2}\rho\dot{w}^2 \mathrm{d}\Omega - \int_\Omega (\frac{1}{2}\overline{\mathbf{M}} : \tilde{\nabla}^T\tilde{\nabla} w - q_z w)\mathrm{d}\Omega - \int_{\partial\Omega} \overline{M_n}\frac{\partial w}{\partial n} dS \tag{4.32}$$

The integral of the Lagrangian L between two time steps t_1 and t_2 is $\digamma = \int_{t_1}^{t_2} L(\dot{w}, w)dt$. According to the principle of least action, we can write

$$\digamma = \int_{t_1}^{t_2}\int_{\Omega}\frac{1}{2}\rho\dot{w}^2\mathrm{d}\Omega\mathrm{d}t - \int_{t_1}^{t_2}\int_{\Omega}(\frac{1}{2}\overline{\mathbf{M}}:\tilde{\nabla}^T\tilde{\nabla}w - q_z w)d\Omega\mathrm{d}t - \int_{t_1}^{t_2}\int_{\partial\Omega}\overline{M_n}\frac{\partial w}{\partial n}dS\mathrm{d}t \tag{4.33}$$

Omitting the external work term $\int_{t_1}^{t_2}\int_{\partial\Omega}\overline{M_n}\frac{\partial w}{\partial n}dS\mathrm{d}t$, the first variation of $\delta\digamma$ leads to

$$\begin{aligned}
\delta\digamma &= \int_{t_1}^{t_2}\int_{\Omega}(\rho\dot{w}\cdot\delta\dot{w} - \overline{\mathbf{M}}:\tilde{\nabla}^T\tilde{\nabla}\delta w + q_z\delta w)\mathrm{d}\Omega\mathrm{d}t \\
&= \int_{t_1}^{t_2}\int_{\Omega}(-\rho_i\ddot{w}_i\cdot\delta w_i - \overline{\mathbf{M}_i}:\tilde{\nabla}^T\tilde{\nabla}\delta w_i + q_z\delta w_i)\mathrm{d}\Omega_i\mathrm{d}t \\
&= \int_{t_1}^{t_2}\int_{\Omega}\big(-\rho_i\ddot{w}_i\cdot\delta w_i - \overline{\mathbf{M}_i}:[2\int_{\mathcal{S}_i}\phi(\boldsymbol{\xi}_{ij})(\delta w_{ij}(\boldsymbol{\xi}_{ij}\otimes\boldsymbol{\xi}_{ij} - \mathbf{K}_{3i}\mathbf{K}_{2i}^{-1}\boldsymbol{\xi}_{ij})dV_j:\mathbf{K}_{4i}^{-1}] \\
&\quad + q_z\delta w_i\big)\mathrm{d}\Omega_i\mathrm{d}t \\
&= \int_{t_1}^{t_2}\int_{\Omega}\big(-\rho_i\ddot{w}_i\cdot\delta w_i - 2\int_{\mathcal{S}_i}\overline{\mathbf{M}_i}\phi(\boldsymbol{\xi}_{ij})(\delta w_j - \delta w_i)(\boldsymbol{\xi}_{ij}\otimes\boldsymbol{\xi}_{ij} - \mathbf{K}_{3i}\mathbf{K}_{2i}^{-1}\boldsymbol{\xi}_{ij})dV_j:\mathbf{K}_{4i}^{-1} \\
&\quad + q_z\delta w_i\big)\mathrm{d}\Omega_i\mathrm{d}t \\
&= \int_{t_1}^{t_2}\int_{\Omega}\Big(-\rho_i\ddot{w}_i\cdot\delta w_i - 2\{\int_{\mathcal{S}_i'}[\overline{\mathbf{M}_j}\phi(\boldsymbol{\xi}_{ji})\delta w_i(\boldsymbol{\xi}_{ji}\otimes\boldsymbol{\xi}_{ji} - \mathbf{K}_{3i}\mathbf{K}_{2i}^{-1}\boldsymbol{\xi}_{ji}):\mathbf{K}_{4i}^{-1}]dV_j - \\
&\quad \int_{\mathcal{S}_i}[\overline{\mathbf{M}_i}\phi(\boldsymbol{\xi}_{ij})\delta w_i(\boldsymbol{\xi}_{ij}\otimes\boldsymbol{\xi}_{ij} - \mathbf{K}_{3j}\mathbf{K}_{2j}^{-1}\boldsymbol{\xi}_{ij}):\mathbf{K}_{4j}^{-1}]dV_j\} + q_z\delta w_i\Big)\mathrm{d}\Omega_i\mathrm{d}t
\end{aligned}$$

where the boundary condition $\delta w(t_1) = 0$, $\delta w(t_2) = 0$ is considered in the above derivation. According to Hamilton's principle, for any δw_i, the first variation of the functional $\digamma$ should be zero, which leads to

$$\begin{aligned}
&2\int_{\mathcal{S}_i}\overline{\mathbf{M}_i}\phi(\boldsymbol{\xi}_{ij})(\boldsymbol{\xi}_{ij}\otimes\boldsymbol{\xi}_{ij} - \mathbf{K}_{3i}\mathbf{K}_{2i}^{-1}\boldsymbol{\xi}_{ij}):\mathbf{K}_{4i}^{-1}dV_j - \\
&2\int_{\mathcal{S}_i'}\overline{\mathbf{M}_j}\phi(\boldsymbol{\xi}_{ji})(\boldsymbol{\xi}_{ji}\otimes\boldsymbol{\xi}_{ji} - \mathbf{K}_{3j}\mathbf{K}_{2j}^{-1}\boldsymbol{\xi}_{ji}):\mathbf{K}_{4j}^{-1}dV_j + q_z = \rho_i\ddot{w}_i\ \ \forall\mathbf{x}_i\in\Omega
\end{aligned} \tag{4.34}$$

The nonlocal form is correlated to the local form by

$$\begin{aligned}
\nabla^T\nabla:\overline{\mathbf{M}_i} \underset{\text{Nonlocal}\to\text{Local}}{\overset{\text{Local}\to\text{Nonlocal}}{\rightleftharpoons}} &2\int_{\mathcal{S}_i}\overline{\mathbf{M}_i}\phi(\boldsymbol{\xi}_{ij})(\boldsymbol{\xi}_{ij}\otimes\boldsymbol{\xi}_{ij} - \mathbf{K}_{3i}\mathbf{K}_{2i}^{-1}\boldsymbol{\xi}_{ij}):\mathbf{K}_{4i}^{-1}dV_j - \\
&2\int_{\mathcal{S}_i'}\overline{\mathbf{M}_j}\phi(\boldsymbol{\xi}_{ji})(\boldsymbol{\xi}_{ji}\otimes\boldsymbol{\xi}_{ji} - \mathbf{K}_{3j}\mathbf{K}_{2j}^{-1}\boldsymbol{\xi}_{ji}):\mathbf{K}_{4j}^{-1}dV_j
\end{aligned} \tag{4.35}$$

According to Eq.4.20, we devise the explicit form of $\tilde{\nabla}^T\tilde{\nabla}:\overline{\mathbf{M}_i}$

$$\tilde{\nabla}^T\tilde{\nabla}:\overline{\mathbf{M}_i} = 2\int_{\mathcal{S}_i}\phi(\boldsymbol{\xi}_{ij})\overline{\mathbf{M}_i}\cdot\begin{bmatrix}e_{i11} & e_{i12}\\ e_{i21} & e_{i22}\end{bmatrix}dV_j - 2\int_{\mathcal{S}_i'}\phi(\boldsymbol{\xi}_{ji})\overline{\mathbf{M}_j}\cdot\begin{bmatrix}e_{j11} & e_{j12}\\ e_{j21} & e_{j22}\end{bmatrix}dV_j \tag{4.36}$$

As Eq.4.34 suffers from zero energy modes, we introduce the so-called nonlocal operator energy functional, which is described in the next section.

4.3.3 Operator energy functional

For the Kirchhoff plate, the maximal order of partial derivatives in Eq.4.34 is two, hence we select the second order of nonlocal operators in Eq.4.4. The operator energy functional for second order nonlocal operators of a scalar field w for point $\mathbf{x}_i$ can be expressed as

$$\mathcal{F}_i^{hg} = \frac{\alpha_w}{2m_i}\int_{\mathcal{S}_i}\phi(\boldsymbol{\xi}_{ij})\big(\mathbf{s}_{ij}^T\tilde{\partial}_\alpha w_i - w_{ij}\big)^2 dV_j \tag{4.37}$$

where $\mathbf{s}_{ij} = (x_{ij}, y_{ij}, x_{ij}^2/2, x_{ij}y_{ij}, y_{ij}^2/2)^T$, $\tilde{\partial}_\alpha w_i = (\frac{\partial w_i}{\partial x}, \frac{\partial w_i}{\partial y}, \frac{\partial^2 w_i}{\partial x^2}, \frac{\partial^2 w_i}{\partial xy}, \frac{\partial^2 w_i}{\partial y^2})^T$.

The first variation of $\mathcal{F}_i^{hg}$ is

$$\begin{aligned}
\delta\mathcal{F}_i^{hg} =& \frac{\alpha_w}{m_i}\int_{\mathcal{S}_i}\phi(\boldsymbol{\xi}_{ij})\big(\mathbf{s}_{ij}^T\tilde{\partial}_\alpha w_i - w_{ij}\big)^T\big(\tilde{\partial}_\alpha\delta w_i\mathbf{s}_{ij}^T - \delta w_{ij}\big)dV_j\\
=& \frac{\alpha_w}{m_i}\int_{\mathcal{S}_i}\phi(\boldsymbol{\xi}_{ij})\big(\mathbf{s}_{ij}^T\tilde{\partial}_\alpha w_i - w_{ij}\big)^T\tilde{\partial}_\alpha\delta w_i\mathbf{s}_{ij}^T dV_j - \frac{\alpha_w}{m_i}\int_{\mathcal{S}_i}\phi(\boldsymbol{\xi}_{ij})\big(\mathbf{s}_{ij}^T\tilde{\partial}_\alpha w_i - w_{ij}\big)^T\delta w_{ij}dV_j\\
=& \frac{\alpha_w}{m_i}\int_{\mathcal{S}_i}\phi(\boldsymbol{\xi}_{ij})\big(\mathbf{s}_{ij}^T\tilde{\partial}_\alpha w_i - w_{ij}\big)\mathbf{s}_{ij}^T dV_j\cdot\tilde{\partial}_\alpha\delta w_i - \frac{\alpha_w}{m_i}\int_{\mathcal{S}_i}\phi(\boldsymbol{\xi}_{ij})\big(\mathbf{s}_{ij}^T\tilde{\partial}_\alpha w_i - w_{ij}\big)^T\delta w_{ij}dV_j\\
=& \frac{\alpha_w}{m_i}\bigg(\tilde{\partial}_\alpha w_i\int_{\mathcal{S}_i}\phi(\boldsymbol{\xi}_{ij})\mathbf{s}_{ij}\mathbf{s}_{ij}^T dV_j - \int_{\mathcal{S}_i}\phi(\boldsymbol{\xi}_{ij})w_{ij}\mathbf{s}_{ij}^T dV_j\bigg)\cdot\tilde{\partial}_\alpha\delta w_i -\\
& \frac{\alpha_w}{m_i}\int_{\mathcal{S}_i}\phi(\boldsymbol{\xi}_{ij})\big(\mathbf{s}_{ij}^T\tilde{\partial}_\alpha w_i - w_{ij}\big)^T\delta w_{ij}dV_j\\
=& \frac{\alpha_w}{m_i}\bigg(\int_{\mathcal{S}_i}\phi(\boldsymbol{\xi}_{ij})w_{ij}\mathbf{s}_{ij}^T dV_j - \int_{\mathcal{S}_i}\phi(\boldsymbol{\xi}_{ij})w_{ij}\mathbf{s}_{ij}^T dV_j\bigg)\cdot\tilde{\partial}_\alpha\delta w_i -\\
& \frac{\alpha_w}{m_i}\int_{\mathcal{S}_i}\phi(\boldsymbol{\xi}_{ij})\big(\mathbf{s}_{ij}^T\tilde{\partial}_\alpha w_i - w_{ij}\big)^T\delta w_{ij}dV_j\\
=& \frac{\alpha_w}{m_i}\int_{\mathcal{S}_i}\phi(\boldsymbol{\xi}_{ij})\big(w_{ij} - \mathbf{s}_{ij}^T\tilde{\partial}_\alpha w_i\big)^T(\delta w_j - \delta w_i)dV_j
\end{aligned}\tag{4.38}$$

Taking the variation of $\int_\Omega\mathcal{F}_i^{hg}dV_i$ yields

$$\begin{aligned}
&\int_\Omega\mathcal{F}_i^{hg}dV_i = \int_\Omega\frac{\alpha_w}{m_i}\int_{\mathcal{S}_i}\phi(\boldsymbol{\xi}_{ij})\big(w_{ij} - \mathbf{s}_{ij}^T\tilde{\partial}_\alpha w_i\big)^T(\delta w_j - \delta w_i)dV_j dV_i\\
&= \int_\Omega\Big(\int_{\mathcal{S}_i'}\frac{\alpha_w}{m_j}\phi(\boldsymbol{\xi}_{ji})(w_{ji} - \tilde{\partial}_\alpha w_j\mathbf{s}_{ji}^T)dV_j - \int_{\mathcal{S}_i}\frac{\alpha_w}{m_i}\phi(\boldsymbol{\xi}_{ij})(w_{ij} - \tilde{\partial}_\alpha w_i\mathbf{s}_{ij}^T)dV_j\Big)\delta w_i dV_i
\end{aligned}\tag{4.39}$$

For the scalar field w, the internal force due to the operator energy functional is given by

$$\int_{\mathcal{S}_i'} \boldsymbol{f}_{ji} dV_j - \int_{\mathcal{S}_i} \boldsymbol{f}_{ij} dV_j \tag{4.40}$$

where $\boldsymbol{f}_{ij} = \frac{\alpha_w}{m_i}\phi(\boldsymbol{\xi}_{ij})(w_{ij} - \tilde{\partial}_\alpha w_i \, \mathbf{s}_{ij}^T)$ indicates the zero energy internal force. Finally, the correspondence between local and nonlocal formulation and the operator functional enhanced governing equation of Kirchhoff plate can be expressed as

$$\begin{aligned}\tilde{\nabla}^T\tilde{\nabla} : \overline{\mathbf{M}_i} \underset{\text{Nonlocal}\to\text{Local}}{\overset{\text{Local}\to\text{Nonlocal}}{\rightleftharpoons}} \int_{\mathcal{S}_i} \Big(2\phi(\boldsymbol{\xi}_{ij})\overline{\mathbf{M}_i} \cdot \begin{bmatrix} e_{i11} & e_{i12} \\ e_{i21} & e_{i22} \end{bmatrix} + \boldsymbol{f}_{ij}\Big) dV_j - \\ \int_{\mathcal{S}_i'} \Big(2\phi(\boldsymbol{\xi}_{ji})\overline{\mathbf{M}_j} \cdot \begin{bmatrix} e_{j11} & e_{j12} \\ e_{j21} & e_{j22} \end{bmatrix} + \boldsymbol{f}_{ji}\Big) dV_j\end{aligned} \tag{4.41}$$

$$\begin{aligned}&\int_{\mathcal{S}_i} \Big(2\phi(\boldsymbol{\xi}_{ij})\overline{\mathbf{M}_i} \cdot \begin{bmatrix} e_{i11} & e_{i12} \\ e_{i21} & e_{i22} \end{bmatrix} + \frac{\alpha_w}{m_i}\phi(\boldsymbol{\xi}_{ij})(w_{ij} - \tilde{\partial}_\alpha w_i \, \mathbf{s}_{ij}^T)\Big) dV_j - \\ &\int_{\mathcal{S}_i'} \Big(2\phi(\boldsymbol{\xi}_{ji})\overline{\mathbf{M}_j} \cdot \begin{bmatrix} e_{j11} & e_{j12} \\ e_{j21} & e_{j22} \end{bmatrix} + \frac{\alpha_w}{m_j}\phi(\boldsymbol{\xi}_{ji})(w_{ji} - \tilde{\partial}_\alpha w_j \mathbf{s}_{ji}^T)\Big) dV_j + q_z = \rho_i \ddot{w}_i \;\; \forall \mathbf{x}_i \in \Omega\end{aligned} \tag{4.42}$$

4.3.4 Kirchhoff plate boundary conditions

Let us consider the boundary conditions shown in Fig.4.3, which can be classified into:

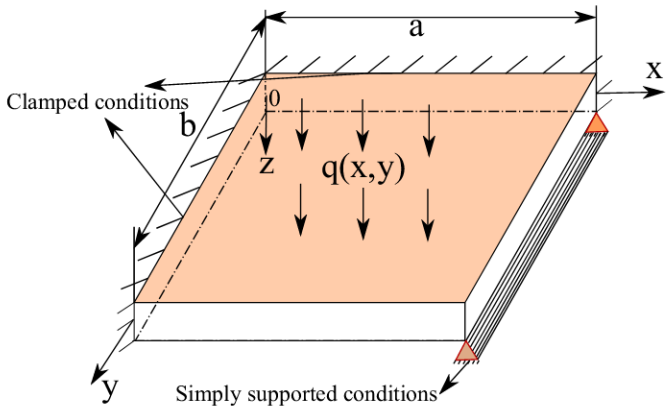

Figure 4.3: The Kirchhoff plate bending problem's boundary conditions.

1. Clamped boundary conditions, where the deflection and the slope of the mid-plane is zero. The positioning shift $\overline{w}$ and the section rotation $\overline{\theta}$ are both zero. The boundary conditions are in the direction parallel to the y-axes (as $x = 0$ clamped boundary):

$$w|_{x=0} = 0;\ \frac{\partial w}{\partial x}|_{x=0} = 0 \tag{4.43}$$

Parallel to the x-axes (as $y = 0$ clamped boundary), the Kirchhoff plate boundary conditions is

$$w|_{y=0} = 0;\ \frac{\partial w}{\partial y}|_{y=0} = 0 \tag{4.44}$$

2. Simply supported Kirchhoff plate boundary conditions where the plate is free to rotate about a line but prevented from deflecting. The positioning shift $\overline{w}$ and moment $\overline{M_n}$ value is zero: parallel to the $y-$ axes (as $x = a$ simply supported boundary), the boundary conditions is

$$w|_{x=a} = 0;\ M_x|_{x=a} = -D_0(\frac{\partial^2 w}{\partial x^2} + \nu\frac{\partial^2 w}{\partial y^2})_{x=a} = 0 \tag{4.45}$$

and Eq.4.45 can be written as

$$w|_{x=a} = 0;\ M_x|_{x=a} = -D_0\frac{\partial^2 w}{\partial x^2}|_{x=a} = 0 \tag{4.46}$$

Similarly, parallel to the $x-$ axes (as $y = b$ simply supported boundary), the boundary conditions is

$$w|_{y=b} = 0;\ M_y|_{y=b} = -D_0(\nu\frac{\partial^2 w}{\partial x^2} + \frac{\partial^2 w}{\partial y^2})_{y=b} = -D_0\frac{\partial^2 w}{\partial y^2}|_{y=b} = 0 \tag{4.47}$$

4.4 Numerical implementation

The domain Ω is decomposed into N points occupying a volume ΔV_i:

$$\Omega = \sum_{i=1}^{N} \Delta V_i, \tag{4.48}$$

For each point, the support is denoted by

$$\mathcal{S}_i = \{i, j_1, j_2, ..., j_{n_i}\}, \tag{4.49}$$

where $j_1, ..., j_k, ..., j_{n_i}$ are the global indices of the neighbors of point $\mathbf{x}_i$ and n_i represents the number of neighbors in support domain $\mathcal{S}_i$. The out-of-plane transversal force between

points are computed by

$$\begin{aligned}
\boldsymbol{T}_{ij} &= \big(2\overline{\mathbf{M}_i}\phi(\boldsymbol{\xi}_{ij})(\boldsymbol{\xi}_{ij}\otimes\boldsymbol{\xi}_{ij} - \mathbf{K}_{3i}\mathbf{K}_{2i}^{-1}\boldsymbol{\xi}_{ij}) : \mathbf{K}_{4i}^{-1} + \boldsymbol{f}_{ij}\big)\Delta V_i\Delta V_j \\
&= \Big(2\phi(\boldsymbol{\xi}_{ij})\overline{\mathbf{M}_i}\cdot\begin{bmatrix} e_{i11} & e_{i12} \\ e_{i21} & e_{i22}\end{bmatrix} + \frac{\alpha_w}{m_i}\phi(\boldsymbol{\xi}_{ij})(w_{ij} - \tilde{\partial}_\alpha w_i\,\mathbf{s}_{ij}^T)\Big)\Delta V_i\Delta V_j \\
\boldsymbol{T}_{ji} &= \big(2\overline{\mathbf{M}_j}\phi(\boldsymbol{\xi}_{ji})(\boldsymbol{\xi}_{ji}\otimes\boldsymbol{\xi}_{ji} - \mathbf{K}_{3j}\mathbf{K}_{2j}^{-1}\boldsymbol{\xi}_{ji}) : \mathbf{K}_{4j}^{-1} + \boldsymbol{f}_{ji}\big)\Delta V_i\Delta V_j \\
&= \Big(2\phi(\boldsymbol{\xi}_{ji})\overline{\mathbf{M}_j}\cdot\begin{bmatrix} e_{j11} & e_{j12} \\ e_{j21} & e_{j22}\end{bmatrix} + \frac{\alpha_w}{m_j}\phi(\boldsymbol{\xi}_{ji})(w_{ji} - \tilde{\partial}_\alpha w_j\mathbf{s}_{ji}^T)\Big)\Delta V_i\Delta V_j
\end{aligned} \tag{4.50}$$

Finally, we get the internal force $\mathbf{P}_{ij}$ between points as

$$\mathbf{P}_{ij} = \sum_{j\in\mathcal{S}_i}\boldsymbol{T}_{ij} - \sum_{j\in\mathcal{S}_i'}\boldsymbol{T}_{ji} \tag{4.51}$$

So that in discrete form, Newton's equation of motion is expressed as

$$\boldsymbol{F}_i - \boldsymbol{P}_i = \mathbb{M}_i\ddot{w}_i(t), \tag{4.52}$$

where t is the time, $w_i(t) = \big(w_1(t),\ldots,w_N(t)\big)$ is the ensemble of the position vector of N points, $\boldsymbol{F}_i$ is the external force vector and $\boldsymbol{P}_i$ denotes the internal force vector; $\mathbb{M}_i$ refers to the mass of the point. In this chapter, the velocity and displacement is updated via the Verlet-Velocity scheme [Verlet, 1967]:

$$\begin{aligned}
w_i(t+\Delta t) &= w_i(t) + \dot{w}_i(t)\Delta t + \frac{1}{2\mathbb{M}_i}[\boldsymbol{F}_i(t) - \boldsymbol{P}_i(t)]\Delta t^2 \\
\dot{w}_i(t+\Delta t) &= \dot{w}_i(t) + \frac{1}{2\mathbb{M}_i}\Big([\boldsymbol{F}_i(t) - \boldsymbol{P}_i(t)] + [\boldsymbol{F}_i(t+\Delta t) - \boldsymbol{P}_i(t+\Delta t]\Big)\Delta t
\end{aligned} \tag{4.53}$$

For reasons of stability, we applied a damping term to each point

$$\boldsymbol{F}_i^s = -c\dot{w}_i \tag{4.54}$$

$\boldsymbol{F}_i^s$ representing the damping force for each point, $\dot{w}_i$ represents the velocity (vector) of the point, and c is a damping coefficient.

The main implementation process of higher-order explicit NOM for the dynamic analysis of Kirchhoff plate can be summarized as follows :

1. **Discretization of the solution domain and initialization**
   (i) Create geometry and discretize the solution domain.
   (ii) Initialize the bond force of $\boldsymbol{P}_i = 0$ and assign values to the corresponding parameters: Young's modulus E, Poisson's ratio ν, Density ρ , Number of neighbors for each point etc.

2. **Calculate shape tensor**
   (i) For each point, calculate second, third and forth order shape tensor $\mathbf{K}_{2i}, \mathbf{K}_{3i}, \mathbf{K}_{4i}$ by solving problem Eqs.4.5-4.8.
   (ii) Calculate the inverse (pseudo-inverse) of the shape tensor $\mathbf{K}_{2i}^{-1}$, $\mathbf{K}_{3i}^{y}\mathbf{K}_{2i}^{-1}$, $\mathbf{K}_{3i}^{y}\mathbf{K}_{2i}^{-1}$,$\mathbf{K}_{4i}^{-1}$.

3. **Calculate the nonlocal Hessian operator**
   For each point, calculate the nonlocal Hessian operator $\tilde{\nabla}^T\tilde{\nabla}w_i$ by solving Eqs.4.14-4.20.

4. **Calculate the Kirchhoff plate constitutive model**
   (i) Calculate Kirchhoff plate's bending stiffness and strain resultant $D_0, \overline{\boldsymbol{\kappa}}$ by solving Eq.4.28 and Eq.4.30.
   (ii) Calculate Kirchhoff plate constitutive model by solving Eq.4.29.

5. **Calculate the Kirchhoff plate internal bond force between points**
   For each neighbor point $j \in \mathcal{S}_i$, calculate $\boldsymbol{T}_{ij}, \boldsymbol{T}_{ji}, \boldsymbol{P}_{ij}$ by solving Eqs.4.50 - 4.51 and add $\boldsymbol{P}_{ij}$ to $\boldsymbol{P}_i$ and add $-\boldsymbol{P}_{ij}$ to $\boldsymbol{P}_j$.

6. **Applying the boundary conditions to solution**
   (i) Apply the external force $\boldsymbol{F}_i$, damping force $\boldsymbol{F}_i^s$ and displacement boundary conditions to the specified points, according to Newton's second law $\boldsymbol{F}_i - \boldsymbol{P}_i + \boldsymbol{F}_i^s = \mathbb{M}_i\ddot{w}_i(t)$, calculate each point's acceleration $\ddot{w}_i$.
   (ii) Update each point's velocity and displacement through the Verlet-Velocity scheme.

4.5 Numerical examples

The proposed nonlocal dynamic Kirchhoff plate formulation is implemented in Wolfram Mathematica. After verifying the accuracy of the nonlocal Hessian operator, several benchmark problems are studied and compared to results obtained by ABAQUS using the S4R plate/shell element [Hibbett et al., 1998].

4.5.1 Verification of nonlocal Hessian operator

Let us consider a simply supported square Kirchhoff plate with a width of $a_0 = 10$m and thickness t=0.01m. The plate is subjected to a uniform pressure of $q_z = 100N/m^2$. Young's modulus and Poisson's ratio are E=30GPa and ν=0.3, respectively. The number of neighbors of each point is set to $n = 24$. To test the accuracy of the nonlocal Hessian operator, we assume $\Upsilon = 1, 3$ (see Eq.4.55). The analytical solution of this problem is

given in [Timoshenko and Woinowsky-Krieger, 1959], i.e.

$$w = \frac{4q_0{a_0}^4}{\pi^5 D_0}\sum_{\Upsilon=1,3,\ldots}^{\infty}\frac{1}{\Upsilon^5}\Big(1-\frac{\alpha_\Upsilon\tanh\alpha_\Upsilon+2}{2\cosh\alpha_\Upsilon}\cosh\frac{2\alpha_\Upsilon y}{a_0}+\frac{\alpha_\Upsilon}{2\cosh\alpha_\Upsilon}\frac{2y}{a_0}\sinh\frac{2\alpha_\Upsilon y}{a_0}\Big)\sin\frac{\Upsilon\pi x}{a_0} \tag{4.55}$$

with $\alpha_\Upsilon = \frac{\Upsilon\pi}{2}$.

We employ the quintic spline function as weight function

$$\phi(\boldsymbol{\xi}) = \alpha_d\Big((1-\xi/h)_+^5 - 6(\frac{2}{3}-\xi/h)_+^5 + 15(\frac{1}{3}-\xi/h)_+^5\Big) \tag{4.56}$$

with $\xi = \|\boldsymbol{\xi}\|$, h is the maximum length of support, α_d= ($3^5/40$, $3^7 7/478\pi$, $3^7/40\pi$) with different dimensional space d and $x_+ = \max(0, x)$.

To accurately represent the relative error of the operator, we consider points at $y = 0$. Figs.4.5-4.6 show the deflection curve of the numerical simulation ($\frac{\partial^2 w}{\partial x^2}, \frac{\partial^2 w}{\partial x \partial y}, \frac{\partial^2 w}{\partial y^2}$) compared to the analytical solution. We also check the error in the L2-norm given by

$$\|w\|_{L2} = \sqrt{\frac{\sum_j (w_j - w_j^{exact})\cdot(w_j - w_j^{exact})\Delta V_j}{\sum_j w_j^{exact}\cdot w_j^{exact}\Delta V_j}} \tag{4.57}$$

which is shown in Fig.4.4.

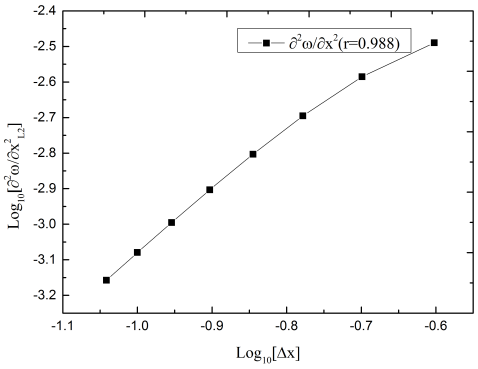

Figure 4.4: The L2-norm's convergence for $\frac{\partial^2 w}{\partial x^2}$.

4.5.2 Nonlocal dynamic Kirchhoff plate formulation with simply supported boundary condition

We now focus on a simply supported square Kirchhoff plate with a width of a_0 = 1m and thickness t=0.01m. Young's modulus and Poisson's ratio are E=200GPa and ν=0.3,

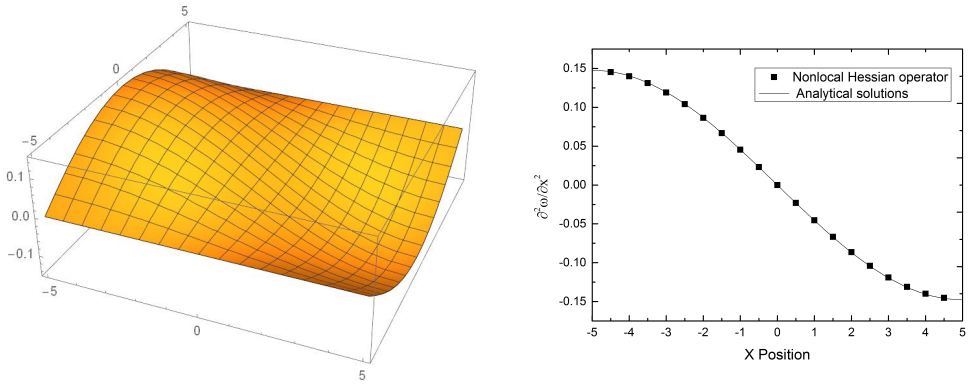

(a)

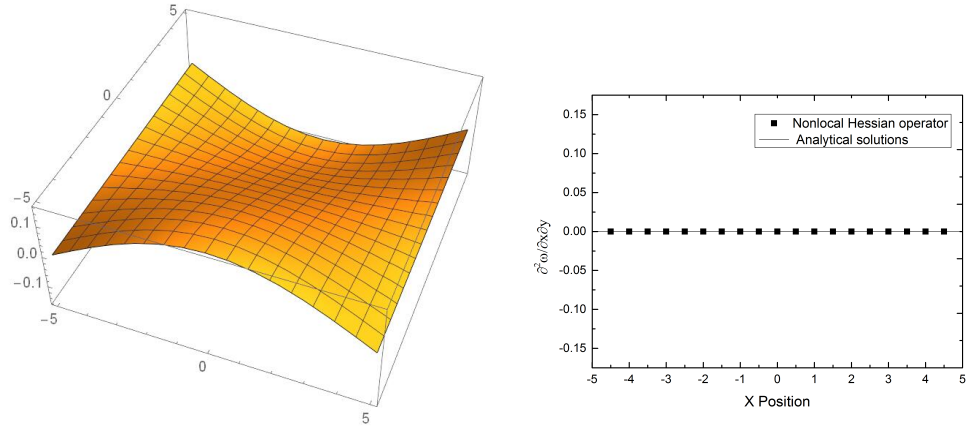

(b)

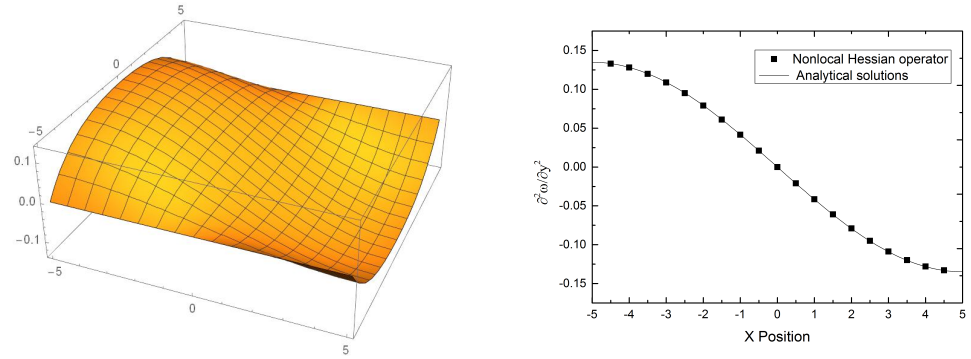

(c)

Figure 4.5: Deflection curve of analytical solutions and relative error(y=0).(a)Contour of the deflection $\frac{\partial^2 w}{\partial x^2}$ for Υ=1; (b) Contour of the deflection $\frac{\partial^2 w}{\partial x \partial y}$ for Υ=1;(c)Contour of the deflection $\frac{\partial^2 w}{\partial y^2}$ for Υ=1.

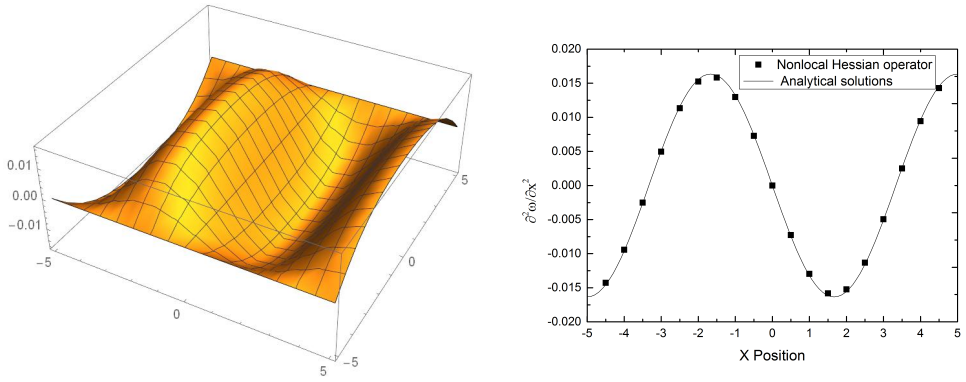

(a)

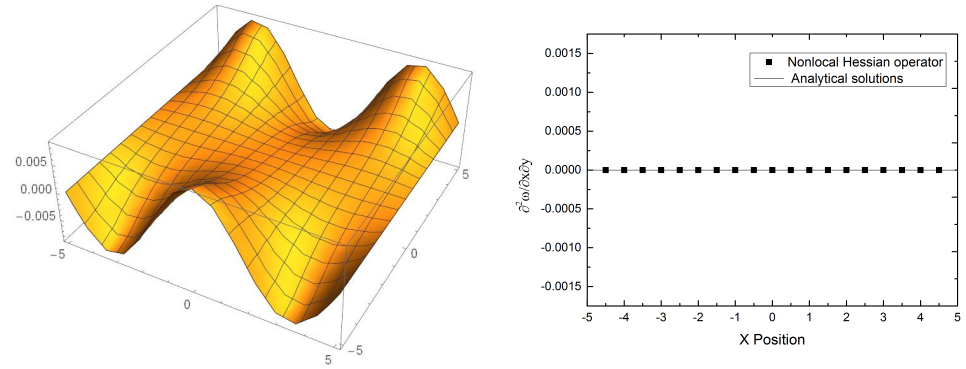

(b)

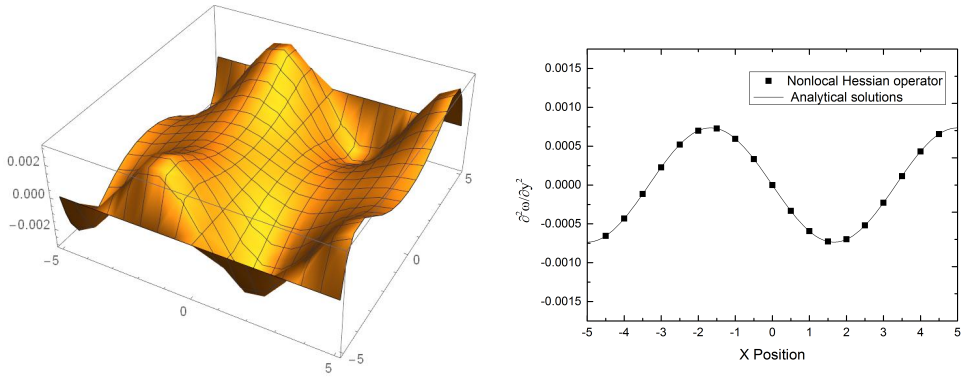

(c)

Figure 4.6: Deflection curve of analytical solutions and relative error(y=0).(a)Contour of the deflection $\frac{\partial^2 w}{\partial x^2}$ for Υ=3; (b) Contour of the deflection $\frac{\partial^2 w}{\partial x \partial y}$ for Υ=3;(c)Contour of the deflection $\frac{\partial^2 w}{\partial y^2}$ for Υ=3.

respectively. The plate density ρ =3000 Kg/m^3. A uniform pressure of $q_z = 100N/m^2$ is applied to the plate. The number of neighbors in the domain of influence of each point is set to $n = 24$. The distance between points is selected as Δx=0.01 m leading to 10201 points. For the ABAQUS model - as a comparison - we discretized the plate into 100×100 elements using the same input parameters.

Simply supported boundary conditions are assumed:

$$w(x,0) = w(x,1) = w(0,y) = w(1,y) = 0 \quad x, y \in [0,1] \tag{4.58}$$

Contour plots of the deflection can be found in Figs.4.7 and Fig.4.8, respectively. The figures show good agreement between the ABAQUS results and NOM results.

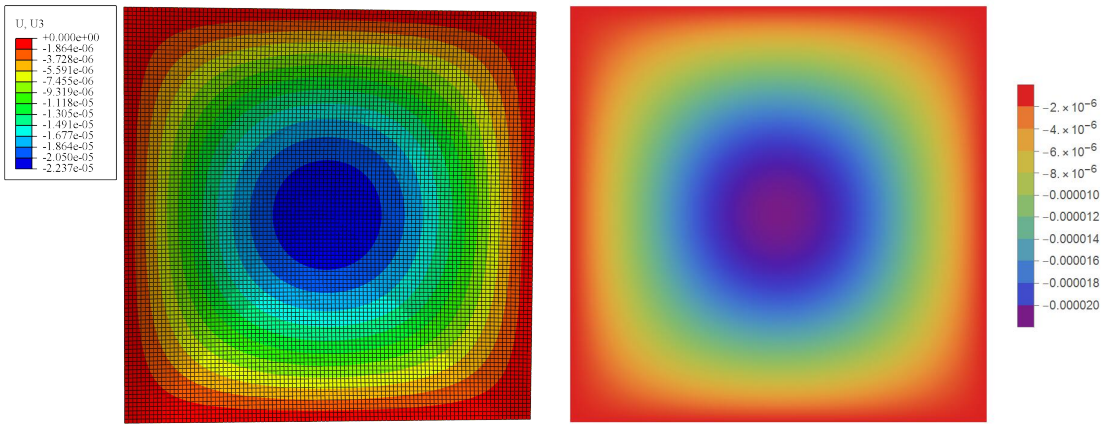

(a) (b)

Figure 4.7: Comparison of the deflection contour under uniform pressure load (a) ABAQUS (b)Nonlocal operator method.

4.5.3 Nonlocal dynamic Kirchhoff plate formulation with clamped boundary condition

Next, a plate using clamped boundary conditions is studied. The geometry and the parameters of the previous section are adopted. The clamped boundary conditions are given by

$$\begin{aligned} &w(x,0) = w(x,1) = w(0,y) = w(1,y) = 0 \\ &\frac{\partial w(0,y)}{\partial x} = \frac{\partial w(1,y)}{\partial x} = \frac{\partial w(x,0)}{\partial y} = \frac{\partial w(x,1)}{\partial y} = 0 \quad x, y \in [0,1] \end{aligned} \tag{4.59}$$

Contour plots of the deflection are illustrated in Figs.4.9 and 4.10, respectively. The figures show good agreement between the ABAQUS results and NOM results.

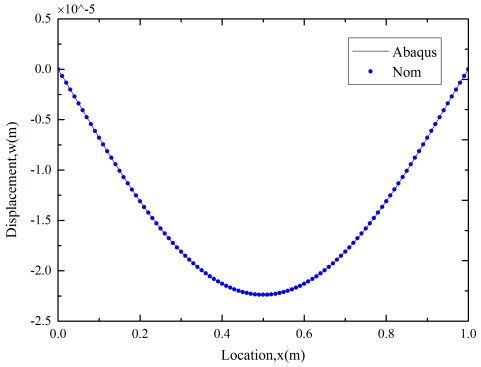

Figure 4.8: Comparison of the deflection for nodes in $y = 0.5$ under uniform pressure load.

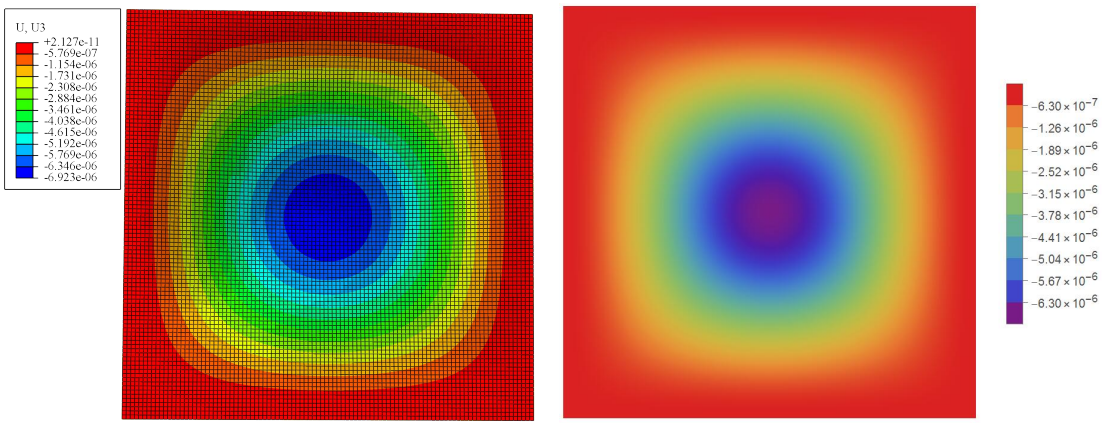

(a) (b)

Figure 4.9: Comparison of the deflection contour under uniform pressure load (a) ABAQUS (b)nonlocal operator method.

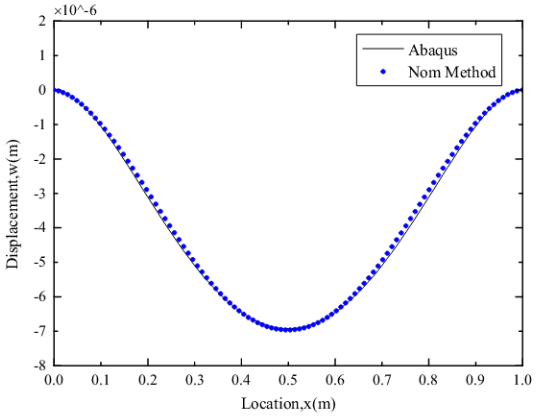

Figure 4.10: Comparison of the deflection for nodes in $y = 0.5$ under uniform pressure load.

4.5.4 Transient test of nonlocal dynamic Kirchhoff plate formulation with simply supported boundary condition

The last example is a simply supported plate where the damping is omitted. A uniform pressure of $q_z = 100N/m^2$ is applied to the plate and the neighbors assigned to each point is set to $n = 30$. All other parameters are adopted from the previous example. Fig.4.11 shows the deflection field at different times. The figures show good agreement between the ABAQUS results and NOM results. One possible reason for the slight difference is the algorithm and nonlocal effect of the current formulation.

4.6 Conclusions

In this chapter, a nonlocal dynamic Kirchhoff plate formulation based on a nonlocal operator method is proposed. Therefore, we derived the explicit form of the nonlocal Hessian operator taking advantage of a second order Taylor series expansion. The nonlocal operator energy functional is also derived and the relationship between local and nonlocal formulations is interpreted. In the numerical simulation section, we first verify the accuracy of the nonlocal Hessian operator for the Kirchhoff plate and compare it to analytical solutions. Subsequently, the nonlocal dynamic Kirchhoff plate formulation with different types of boundary conditions (clamped and simply supported) is studied and compared to simulations obtained by ABAQUS.

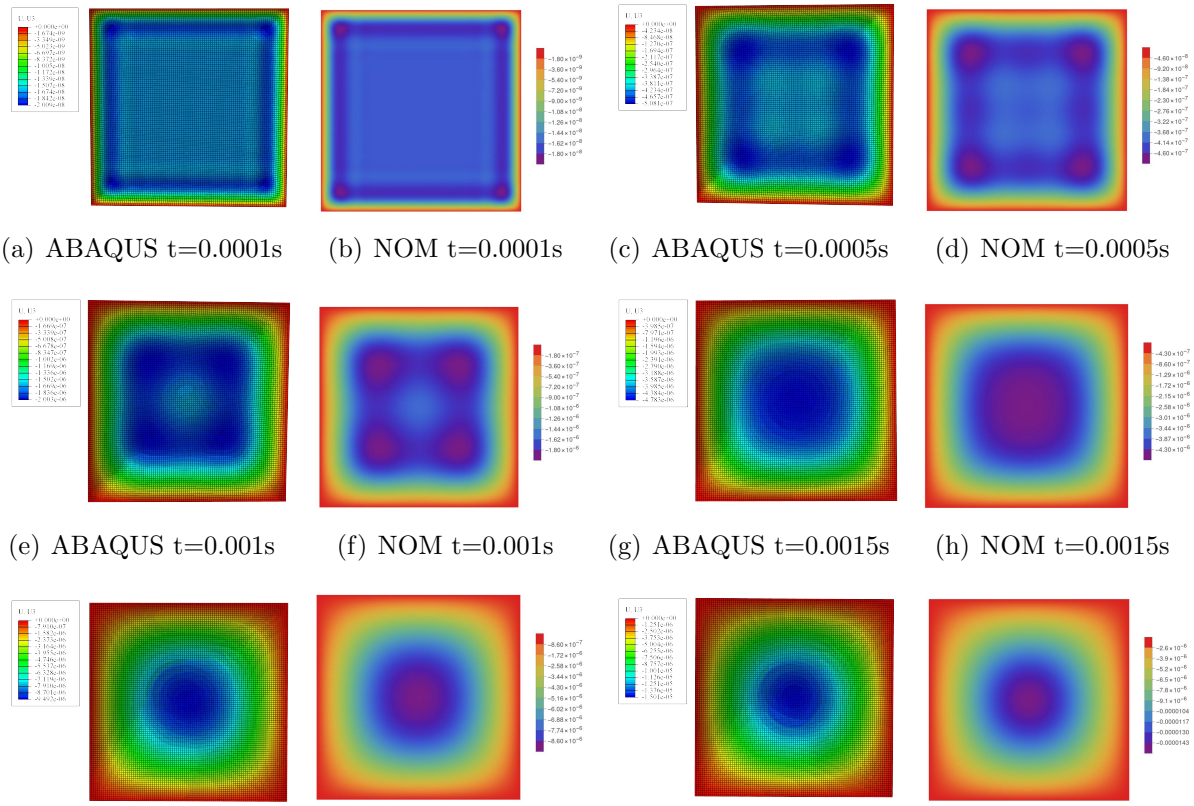

(a) ABAQUS t=0.0001s (b) NOM t=0.0001s (c) ABAQUS t=0.0005s (d) NOM t=0.0005s

(e) ABAQUS t=0.001s (f) NOM t=0.001s (g) ABAQUS t=0.0015s (h) NOM t=0.0015s

(i) ABAQUS at t=0.002s (j) NOM at t=0.002s (k) ABAQUS t=0.0025s (l) NOM t=0.0025s

Figure 4.11: The evolution the deflection contour using ABAQUS and nonlocal operator method at different time

Chapter 5

Quasi-static and dynamic fracture modelling by the nonlocal operator method

This chapter is based on the journal paper 'Quasi-static and dynamic fracture modeling by the nonlocal operator method' published in EABE by my first author. The contribution of this paper is summarized as follows:

Yongzheng Zhang

- Conceptualization
- Research state of the art
- Investigation
- Formal analysis
- Methodology
- Software/Programming
- Data curation
- Data analysis
- Validation
- Visualization
- Writing original manuscript draft

Huilong Ren

- Conceptualization

- Methodology
- Programming
- Writing review and editing

Pedro Areias

- Writing review and editing

Xiaoying Zhuang

- Conceptualization
- Writing review and editing

Timon Rabczuk

- Conceptualization
- Mentoring the research progress
- Writing review and editing

5.1 General

Modeling and predicting of material failure is of major importance in engineering applications [Anderson, 2017]. Numerical methods play an important role for such problems. They can be categorized into discrete and continuous approaches to fracture. In the discrete approach, discontinuities in the displacement field are introduced. Among the typical discrete approaches are the extended finite element method (XFEM) [Moës et al., 1999, Belytschko et al., 2001], phantom node method [Song et al., 2006], cracking particles method (CPM) [Rabczuk and Belytschko, 2004], cohesive elements [Ortiz and Pandolfi, 1999, Zhou and Molinari, 2004], peridynamics (PD) [Silling et al., 2007] or dual-horzon peridynamics (DH-PD) [Ren et al., 2016, 2017], element erosion methods [Belytschko and Lin, 1987, Johnson and Stryk, 1987] and certain meshless approaches such as the weighted reproducing kernel collocation method (RKCM) [Yang et al., 2017, Yang and Hsin, 2019]. XFEM is based on a so-called local partition of unity method and introduces additional degrees of freedom in order to allow crack growth without (or minimal) remeshing. It models the crack as continuous surface and therefore requires crack tracking algorithms and specific criteria to introduce the discontinuity in the displacement field. It is well suited for problems with a moderate number of cracks but becomes increasingly tedious for applications with a large amount of cracks and complex crack patterns such as crack interactions or crack branching. The phantom node method [Song et al., 2006] shares some similarities with XFEM but avoids additional degrees of freedom. Instead

it is based on overlapping elements which facilitates the implementation but narrows its application. There are also a few discrete crack approaches which avoid a representation of the crack surface and associated crack tracking algorithms. Classical representatives are PD and the CPM. PD replaces the divergence term in the equation of motion with an integral form that is related to a bond force. Hence, it can treat the continuum in the same way as a discontinuum. One issue is the integration of complex constitutive models, especially for coupled problems.

Continuous approaches to fracture smear the crack over a certain region without introducing strong discontinuities in the displacement field. In addition, continuous approaches to fracture do not require complex track cracking algorithms and are much easier to implement compared to discrete approaches. A classical representatives of continuous approaches to fracture is the phase field approach [Karma et al., 2001, Miehe et al., 2010b]. The phase field model can be considered as an extension of the classical Griffith fracture principle, which has meanwhile been applied to countless problems. In recent years, many scholars have developed phase field models and successfully solve many multi-physical field problems. Miehe et al.[Miehe et al., 2010a] developed a phase model for structural reliability analyses of piezoelectric solids. Hesch et al.[Hesch and Weinberg, 2014] introduced a phase field method for finite deformations based on a multiplicative split to account for the different behavior of fracture in tension and compression. Miehe et al.[Miehe et al., 2015] presented a phase field model for finite strain thermo-plasticity. Mauthe et al. [Mauthe and Miehe, 2017] proposed a phase field approach for fracture in porous media. Samaniego et al. [Samaniego et al., 2021] modelled shear bands with phase fields.

In this chapter, we present a phase field model for fracture within the NOM. We provide two different implementations, i.e. a nonlocal implicit phase field model and nonlocal explicit phase field model; the former is suited for static while the latter one for dynamic fracture. A staggered algorithm is employed where the displacement field and phase field are solved separately. Decoupling the phase field from the mechanical field guarantees the convexity of the underlying potentials. Compared with the implicit algorithms, explicit algorithms can be easier parallelized, which has not been pursued though in this manuscript. A sub-step scheme is employed to model dynamic fracture by an explicit NOM, which reduces the phase field residual adaptively and achieves a rate-independent nonlocal explicit phase field model.

The remainder of this chapter is structured as follows: In Section 5.2, we review the NOM. Section 5.3 provides a brief overview of the phase field model. In Section 5.4, we construct the operator energy functionals for the displacement and phase field in implicit and explicit form. Subsequently, we describe the numerical implementation of the phase field model using the nonlocal operator method in Section 5.5. Section 5.6 presents several benchmark problems before we conclude the chapter in Section 5.7.

5.2 Outline of phase field model for fracture

Let us consider an isotropic elastic solid $\Omega \subset \mathbb{R}^d (d \in \{1, 2, 3\})$ as shown in Fig.5.1, which is subjected to body forces $\boldsymbol{b}(\boldsymbol{x}, t) : \Omega \times [0, T] \rightarrow \mathbb{R}^d$ and traction $\boldsymbol{f}(\boldsymbol{x}, t) : \partial\Omega_{\boldsymbol{f}} \times [0, T] \rightarrow \mathbb{R}^d$ with external boundary $\partial\Omega \subset \mathbb{R}^{d-1}$ and prescribed displacement boundary condition $\boldsymbol{u}(\boldsymbol{x}, t) : \partial\Omega_{\boldsymbol{u}} \times [0, T] \rightarrow \mathbb{R}^d$, where $\partial\Omega_{\boldsymbol{f}}, \partial\Omega_{\boldsymbol{u}}$ denotes the traction and displacement boundaries, respectively and with $\partial\Omega_{\boldsymbol{f}} \subseteq \partial\Omega, \partial\Omega_{\boldsymbol{u}} \subseteq \partial\Omega, \partial\Omega_{\boldsymbol{f}} \cap \partial\Omega_{\boldsymbol{u}} = \emptyset, \partial\Omega_{\boldsymbol{f}} \cup \partial\Omega_{\boldsymbol{u}} = \partial\Omega$; d represents the dimension.

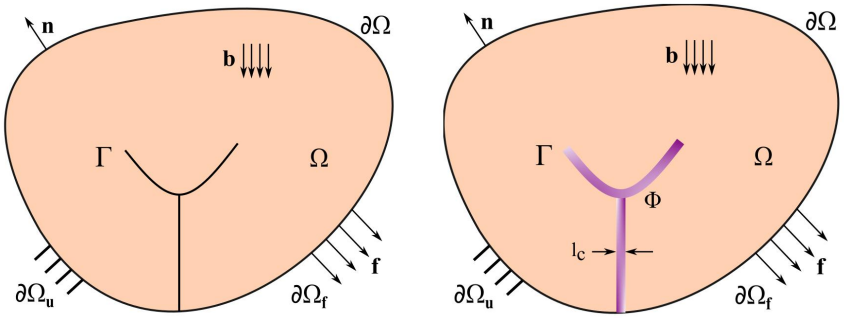

Figure 5.1: Phase field representation of fracture modeling

5.2.1 Variational formulation and regularization of elastic brittle fracture

According to Bourdin and Miehe [Bourdin et al., 2008, Miehe et al., 2010b], the energy functional for a phase field approach to fracture can be expressed by

$$\Pi(\boldsymbol{u}, \phi, \Lambda) = \int_\Omega G_c \Lambda(\phi, \nabla\phi) \mathrm{d}\Omega + \int_\Omega \psi_{\mathrm{e}}(\boldsymbol{\varepsilon}(\mathbf{u}), \phi) \mathrm{d}\Omega - \int_\Omega \mathbf{b} \cdot \boldsymbol{u} \mathrm{d}\Omega - \int_{\partial\Omega_f} \boldsymbol{f} \cdot \boldsymbol{u} \mathrm{d}S$$
$$\Lambda(\phi, \nabla\phi) = \frac{\phi^2}{2l_0} + \frac{l_0}{2} \nabla\phi \cdot \nabla\phi \tag{5.1}$$

where G_c represent critical energy release rate. The crack surface density per unit volume of the solid is denoted by $\Lambda(\phi)$; l_0 is a length scale parameter that is related to the crack width. When $l_0 \rightarrow 0$, then Γ approaches to a strong discontinuity. The displacement field and elastic energy density are denoted by $\mathbf{u}$ and ψ_{e}, respectively; $\phi(\boldsymbol{x}, t) \in [0, 1]$ is the phase field which smears out the crack surface over a certain domain. In [Miehe et al., 2010b], $\phi(\boldsymbol{x}, t) = 0$ refers to an intact material while $\phi(\boldsymbol{x}, t) = 1$ indicates a completely cracked body.

To guarantee that fracture only occurs under tension, the elastic energy is decomposed into tensile and compressive components [Bourdin et al., 2008]. The strain tensor $\boldsymbol{\varepsilon}$ can be split by the following eigen-decomposition

$$\boldsymbol{\varepsilon}_+ = \sum_{\mathrm{a}=1}^{\mathbb{b}} \langle \varepsilon_{\mathrm{a}} \rangle_+ \mathbf{n}_{\mathrm{a}} \otimes \mathbf{n}_{\mathrm{a}}, \boldsymbol{\varepsilon}_- = \sum_{\mathrm{a}=1}^{\mathbb{b}} \langle \varepsilon_{\mathrm{a}} \rangle_- \mathbf{n}_{\mathrm{a}} \otimes \mathbf{n}_{\mathrm{a}} \tag{5.2}$$

where the tensile and compressive parts of the strain tensor are $\boldsymbol{\varepsilon}_+$ and $\boldsymbol{\varepsilon}_-$, respectively. The principal strain is ε_{a} and its direction is $\mathbf{n}_{\mathrm{a}}$. The associated elastic energy density $\psi_{\boldsymbol{\varepsilon}}(\boldsymbol{\varepsilon})$ is expressed as

$$\begin{aligned} \psi_{\mathbb{e}}(\boldsymbol{\varepsilon}, \phi) &= [(1-\phi)^2 + \kappa_0]\psi_{\mathbb{e}}^+(\boldsymbol{\varepsilon}) + \psi_{\mathbb{e}}^-(\boldsymbol{\varepsilon}) \\ \psi_{\mathbb{e}}^+(\boldsymbol{\varepsilon}) &= \frac{\lambda}{2}\langle tr(\boldsymbol{\varepsilon})\rangle_+^2 + \mu tr(\boldsymbol{\varepsilon}_+)^2 \\ \psi_{\mathbb{e}}^-(\boldsymbol{\varepsilon}, \phi) &= \frac{\lambda}{2}\langle tr(\boldsymbol{\varepsilon})\rangle_-^2 + \mu tr(\boldsymbol{\varepsilon}_-)^2 \end{aligned} \tag{5.3}$$

where κ_0 ($\kappa_0 > 0$ and $\kappa_0 \ll 1$) is a small positive factor that circumvents full degradation of the positive projection of the elastic energy density, λ, μ are the Lamé parameters.

5.2.2 Governing equations

Now, the potential functional can be expressed as

$$\begin{aligned} \Pi(\boldsymbol{u}, \phi) = &\underbrace{\int_\Omega \frac{G_c}{2}\left(\frac{\phi^2}{l_0} + l_0 \nabla\phi \cdot \nabla\phi\right)\mathrm{d}\Omega + \int_\Omega [(1-\phi)^2 + \kappa_0]\psi_{\mathbb{e}}^+(\boldsymbol{\varepsilon}) + \psi_{\mathbb{e}}^-(\boldsymbol{\varepsilon})\mathrm{d}\Omega}_{W_{int}} \\ &\underbrace{- \int_\Omega \mathbf{b} \cdot \boldsymbol{u}\mathrm{d}\Omega - \int_{\partial\Omega_f} \boldsymbol{f} \cdot \boldsymbol{u}\mathrm{d}S}_{W_{ext}} \end{aligned} \tag{5.4}$$

where W_{int} is the internal energy and W_{ext} the external work. The Lagrange energy functional is written as

$$L = \frac{1}{2}\int_\Omega \rho \dot{\boldsymbol{u}} \cdot \dot{\boldsymbol{u}}\mathrm{d}\Omega - \Pi(\boldsymbol{u}, \phi) \tag{5.5}$$

According to Hamilton's principle, the first-order variation of the energy functional L should be zero, i.e. $\delta L = 0$ yielding

$$\begin{aligned} \nabla \cdot \boldsymbol{\sigma} + \mathbf{b} = \rho\ddot{\boldsymbol{u}} \quad & in \quad \Omega \\ [2l_0\psi_{\mathbb{e}}^+ + G_c]\phi - G_c l_0^2 \nabla^2\phi = 2l_0\psi_{\mathbb{e}}^+ \quad & in \quad \Omega \\ \boldsymbol{\sigma} \cdot \boldsymbol{n}^* = \boldsymbol{f} \quad & on \quad \partial\Omega_f \\ \nabla\phi \cdot \boldsymbol{n}^* = 0 \quad & on \quad \partial\Omega_f \end{aligned} \tag{5.6}$$

where $\boldsymbol{n}^*$ is outward pointing normal on $\partial\Omega_f$ and $\boldsymbol{\sigma}$ indicates the Cauchy stress tensor. The strong form can then be derived easily from the weak form yielding

$$\begin{aligned}\boldsymbol{\sigma} = \frac{\partial \psi_{\mathbb{e}}(\boldsymbol{\varepsilon},\phi)}{\partial \boldsymbol{\varepsilon}} &= [(1-\phi)^2+\kappa_0]\frac{\partial \psi_{\mathbb{e}}^+(\boldsymbol{\varepsilon})}{\partial \boldsymbol{\varepsilon}} + \frac{\partial \psi_{\mathbb{e}}^-(\boldsymbol{\varepsilon})}{\partial \boldsymbol{\varepsilon}} \\ &= [(1-\phi)^2+\kappa_0][\lambda\langle tr(\boldsymbol{\varepsilon})\rangle_+ \boldsymbol{I} + 2\mu\boldsymbol{\varepsilon}_+] + \lambda\langle tr(\boldsymbol{\varepsilon})\rangle_- \boldsymbol{I} + 2\mu\boldsymbol{\varepsilon}_- \end{aligned} \tag{5.7}$$

where $\boldsymbol{I}$ is the second-order identity tensor. To ensure the phase field increases monotonically [Miehe et al., 2010b], the local history field of the strain $H(\boldsymbol{x},\mathbb{t})$ is employed:

$$H(\boldsymbol{x},\mathbb{t}) = \max_{\mathbb{s}\in[0,\mathbb{t}]} \psi_{\mathbb{e}}^+(\boldsymbol{\varepsilon}(\boldsymbol{x},\mathbb{s})) \tag{5.8}$$

Replacing $\psi_{\mathbb{e}}^+$ with $H(\boldsymbol{x},\mathbb{t})$ in Eq.5.6 leads to

$$\begin{aligned} \nabla\cdot\boldsymbol{\sigma} + \mathbf{b} = \rho\ddot{\boldsymbol{u}} \quad & in \quad \Omega \\ [2l_0 H + G_c]\phi - G_c l_0^2 \nabla^2\phi = 2l_0 H \quad & in \quad \Omega \\ \boldsymbol{\sigma}\cdot\boldsymbol{n}^* = \boldsymbol{f} \quad & on \quad \partial\Omega_f \\ \nabla\phi\cdot\boldsymbol{n}^* = 0 \quad & on \quad \partial\Omega_f \end{aligned} \tag{5.9}$$

5.3 Construction of the operator energy functional in implicit form and explicit form

The nonlocal operator method (NOM) will suffer from zero energy modes when using nodal integration. Therefore, we add a penalty energy functional.

5.3.1 Implicit form operator energy functional

Using nodal integration in Eq.3.4 results in

$$\begin{aligned}\mathcal{F}_i^{hg} &= \frac{\mu}{2m_{\mathbf{K}_i}}\int_{\mathcal{S}_i} w(\boldsymbol{\xi}_{ij})\Big([(u_j-u_i)-\nabla u_i\cdot\boldsymbol{\xi}_{ij}]^2 + [(v_j-v_i)-\nabla v_i\cdot\boldsymbol{\xi}_{ij}]^2 \\ &+ [(w_j-w_i)-\nabla w_i\cdot\boldsymbol{\xi}_{ij}]^2\Big)\mathrm{d}V_j \\ &= \frac{\mu}{2m_{\mathbf{K}_i}}\Big(\sum_{j\in\mathcal{S}_i} w(\boldsymbol{\xi}_{ij})\Big((u_j-u_i)^2+(v_j-v_i)^2+(w_j-w_i)^2\Big)\Delta V_j - \nabla\otimes\mathbf{u}_i : \nabla\otimes\mathbf{u}_i\cdot\mathbf{K}_i\Big)\end{aligned} \tag{5.10}$$

with $\nabla u_i = [\frac{\partial u}{\partial x},\frac{\partial u}{\partial y},\frac{\partial u}{\partial z}]^T$, $\nabla\otimes\mathbf{u}_i = \begin{bmatrix}\frac{\partial u}{\partial x} & \frac{\partial u}{\partial y} & \frac{\partial u}{\partial z}\\ \frac{\partial v}{\partial x} & \frac{\partial v}{\partial y} & \frac{\partial v}{\partial z}\\ \frac{\partial w}{\partial x} & \frac{\partial w}{\partial y} & \frac{\partial w}{\partial z}\end{bmatrix}$, $\mathbf{K}_i = \begin{bmatrix}k_{11} & k_{12} & k_{13}\\ k_{12} & k_{22} & k_{23}\\ k_{13} & k_{23} & k_{33}\end{bmatrix}$.

It should be noted that the shape tensor $\mathbf{K}_i$ is involved in $\nabla \otimes \mathbf{u}_i : \nabla \otimes \mathbf{u}_i \cdot \mathbf{K}_i$ and the zero energy functional is valid in any dimension. Denoting

$$\begin{aligned} \mathrm{d}\mathscr{U}_i &= (\frac{\partial u_i}{\partial x}, \frac{\partial u_i}{\partial y}, \frac{\partial u_i}{\partial z}, \frac{\partial v_i}{\partial x}, \frac{\partial v_i}{\partial y}, \frac{\partial v_i}{\partial z}, \frac{\partial w_i}{\partial x}, \frac{\partial w_i}{\partial y}, \frac{\partial w_i}{\partial z})^T \\ \mathscr{U}_i &= (u_i, v_i, w_i, u_{j1}, v_{j1}, w_{j1} \cdots u_{jn}, v_{jn}, w_{jn})^T \end{aligned} \tag{5.11}$$

Eq.5.10 can be rewritten as

$$\begin{aligned} \mathcal{F}_i^{hg} &= \frac{\mu}{2m_{\mathbf{K}_i}} \Bigg(\sum_{j \in \mathcal{S}_i} w(\boldsymbol{\xi}_{ij}) \Big((u_j - u_i)^2 + (v_j - v_i)^2 + (w_j - w_i)^2 \Big) \Delta V_j \\ &\quad - \nabla \otimes \mathbf{u}_i : \nabla \otimes \mathbf{u}_i \cdot \mathbf{K}_i \Bigg) \\ &= \frac{\mu}{2m_{\mathbf{K}_i}} \Big(\mathscr{U}_i{}^T \begin{bmatrix} \sum_{j \in \mathcal{S}_i} \mathbf{I}_j & -\mathbf{I}_{j1} & \cdots & -\mathbf{I}_{j_n} \\ -\mathbf{I}_{j1} & \mathbf{I}_{j1} & \mathbf{0} & \mathbf{0} \\ \vdots & \mathbf{0} & \ddots & \mathbf{0} \\ -\mathbf{I}_{j_n} & \mathbf{0} & \mathbf{0} & \mathbf{I}_{j_n} \end{bmatrix} \mathscr{U}_i - \mathrm{d}\mathscr{U}_i{}^T \begin{bmatrix} \mathbf{K}_i & 0 & 0 \\ 0 & \mathbf{K}_i & 0 \\ 0 & 0 & \mathbf{K}_i \end{bmatrix} \mathrm{d}\mathscr{U}_i \Big) \\ &= \frac{\mu}{2m_{\mathbf{K}_i}} \Big(\mathscr{U}_i{}^T \begin{bmatrix} \sum_{j \in \mathcal{S}_i} \mathbf{I}_j & -\mathbf{I}_{j1} & \cdots & -\mathbf{I}_{j_n} \\ -\mathbf{I}_{j1} & \mathbf{I}_{j1} & \mathbf{0} & \mathbf{0} \\ \vdots & \mathbf{0} & \ddots & \mathbf{0} \\ -\mathbf{I}_{j_n} & \mathbf{0} & \mathbf{0} & \mathbf{I}_{j_n} \end{bmatrix} \mathscr{U}_i - \mathscr{U}_i{}^T \mathscr{B}_i{}^T \begin{bmatrix} \mathbf{K}_i & 0 & 0 \\ 0 & \mathbf{K}_i & 0 \\ 0 & 0 & \mathbf{K}_i \end{bmatrix} \mathscr{B}_i \mathscr{U}_i \Big) \\ &= \frac{\mu}{2m_{\mathbf{K}_i}} \mathscr{U}_i{}^T \Big(\begin{bmatrix} \sum_{j \in \mathcal{S}_i} \mathbf{I}_j & -\mathbf{I}_{j1} & \cdots & -\mathbf{I}_{j_n} \\ -\mathbf{I}_{j1} & \mathbf{I}_{j1} & \mathbf{0} & \mathbf{0} \\ \vdots & \mathbf{0} & \ddots & \mathbf{0} \\ -\mathbf{I}_{j_n} & \mathbf{0} & \mathbf{0} & \mathbf{I}_{j_n} \end{bmatrix} - \mathscr{B}_i{}^T \begin{bmatrix} \mathbf{K}_i & 0 & 0 \\ 0 & \mathbf{K}_i & 0 \\ 0 & 0 & \mathbf{K}_i \end{bmatrix} \mathscr{B}_i \Big) \mathscr{U}_i \end{aligned} \tag{5.12}$$

with $\mathbf{I}_j = w(\boldsymbol{\xi}_{ij}) \Delta V_j (1,1,1) \otimes (1,1,1)^T$.

$$\mathscr{K}_i^{hg} = \partial_{\mathscr{U}_i \mathscr{U}_i} \mathcal{F}_i^{hg} = \frac{\mu}{m_{\mathbf{K}_i}} \Bigg(\begin{bmatrix} \sum_{j \in \mathcal{S}_i} \mathbf{I}_j & -\mathbf{I}_{j1} & \cdots & -\mathbf{I}_{j_n} \\ -\mathbf{I}_{j1} & \mathbf{I}_{j1} & \mathbf{0} & \mathbf{0} \\ \vdots & \mathbf{0} & \ddots & \mathbf{0} \\ -\mathbf{I}_{j_n} & \mathbf{0} & \mathbf{0} & \mathbf{I}_{j_n} \end{bmatrix} - \mathscr{B}_i{}^T \begin{bmatrix} \mathbf{K}_i & 0 & 0 \\ 0 & \mathbf{K}_i & 0 \\ 0 & 0 & \mathbf{K}_i \end{bmatrix} \mathscr{B}_i \Bigg) \tag{5.13}$$

The hourglass tangent stiffness matrix can be computed accordingly by

$$\overset{hg}{\mathscr{K}_i} = \sum_{j \in \mathcal{S}_i} \partial_{\mathscr{U}_i \mathscr{U}_i} \mathcal{F}_i^{hg} \Delta V_j = \sum_{j \in \mathcal{S}_i} \mathscr{K}_i^{hg} \Delta V_j \tag{5.14}$$

5.3.2 Explicit form operator energy functional

Taking advantage of the first variation $\int_\Omega \mathcal{F}_i^{\mathbf{u}} \mathrm{d}V_i$, the operator energy functional in Eq.3.4 can be written as

$$
\begin{aligned}
&\int_\Omega \delta\mathcal{F}_i^{\mathbf{u}} \mathrm{d}V_i = \frac{\mu}{m_{\mathbf{K}_i}} \int_\Omega \int_{\mathcal{S}_i} w(\boldsymbol{\xi}_{ij})(\tilde{\nabla}\mathbf{u}_i\boldsymbol{\xi}_{ij} - \mathbf{u}_{ij})^T(\tilde{\nabla}\delta\mathbf{u}_i\boldsymbol{\xi}_{ij} - \delta\mathbf{u}_{ij})\mathrm{d}V_j\mathrm{d}V_i \\
&= \frac{\mu}{m_{\mathbf{K}_i}} \int_\Omega \int_{\mathcal{S}_i} w(\boldsymbol{\xi}_{ij})(\tilde{\nabla}\mathbf{u}_i\boldsymbol{\xi}_{ij} - \mathbf{u}_{ij})^T\tilde{\nabla}\delta\mathbf{u}_i\boldsymbol{\xi}_{ij}\mathrm{d}V_j - \frac{\mu}{m_{\mathbf{K}_i}} \int_{\mathcal{S}_i} w(\boldsymbol{\xi}_{ij})(\tilde{\nabla}\mathbf{u}_i\boldsymbol{\xi}_{ij} - \mathbf{u}_{ij})^T\delta\mathbf{u}_{ij}\mathrm{d}V_j\mathrm{d}V_i \\
&= \frac{\mu}{m_{\mathbf{K}_i}} \Big(\tilde{\nabla}\mathbf{u}_i \int_\Omega \int_{\mathcal{S}_i} w(\mathbf{x}_{ij})\boldsymbol{\xi}_{ij} \otimes \boldsymbol{\xi}_{ij}\mathrm{d}V_j - \int_{\mathcal{S}_i} w(\boldsymbol{\xi}_{ij})\mathbf{u}_{ij} \otimes \boldsymbol{\xi}_{ij}\mathrm{d}V_j\mathrm{d}V_i\Big) : \delta\tilde{\nabla}\mathbf{u}_i \\
&- \frac{\mu}{m_{\mathbf{K}_i}} \int_\Omega \int_{\mathcal{S}_i} w(\boldsymbol{\xi}_{ij})(\tilde{\nabla}\mathbf{u}_i\boldsymbol{\xi}_{ij} - \mathbf{u}_{ij})^T\delta\mathbf{u}_{ij}\mathrm{d}V_j\mathrm{d}V_i \\
&= \frac{\mu}{m_{\mathbf{K}_i}} \int_\Omega \int_{\mathcal{S}_i} w(\boldsymbol{\xi}_{ij})(\mathbf{u}_{ij} - \tilde{\nabla}\mathbf{u}_i\boldsymbol{\xi}_{ij})^T(\delta\mathbf{u}_j - \delta\mathbf{u}_i)\mathrm{d}V_j\mathrm{d}V_i \\
&= \int_\Omega \int_{\mathcal{S}_i'} \frac{\mu}{m_{\mathbf{K}_j}} w(\boldsymbol{\xi}_{ji})(\mathbf{u}_{ji} - \tilde{\nabla}\mathbf{u}_j\boldsymbol{\xi}_{ji})\mathrm{d}V_j\mathrm{d}V_i - \int_{\mathcal{S}_i} \frac{\mu}{m_{\mathbf{K}_i}} w(\boldsymbol{\xi}_{ij})(\mathbf{u}_{ij} - \tilde{\nabla}\mathbf{u}_i\boldsymbol{\xi}_{ij})\delta\mathbf{u}_i\mathrm{d}V_j\mathrm{d}V_i
\end{aligned}
\tag{5.15}
$$

The arbitrariness of the test functions, $\delta\boldsymbol{u}_i$, $\int_\Omega \delta\mathcal{F}_i^{\mathbf{u}}\mathrm{d}V_i = 0$, leads to

$$
\int_{\mathcal{S}_i'} \frac{\mu}{m_{\mathbf{K}_j}} w(\boldsymbol{\xi}_{ji})(\mathbf{u}_{ji} - \tilde{\nabla}\mathbf{u}_j\boldsymbol{\xi}_{ji})\mathrm{d}V_j - \int_{\mathcal{S}_i} \frac{\mu}{m_{\mathbf{K}_i}} w(\boldsymbol{\xi}_{ij})(\mathbf{u}_{ij} - \tilde{\nabla}\mathbf{u}_i\boldsymbol{\xi}_{ij})\delta\mathbf{u}_i\mathrm{d}V_j = 0 \quad \forall\mathbf{u}_i \in \Omega \tag{5.16}
$$

and it can be shown that

$$
\int_{\mathcal{S}_i'} \boldsymbol{h}_{ji}^{\mathbf{u}}\mathrm{d}V_j - \int_{\mathcal{S}_i} \boldsymbol{h}_{ij}^{\mathbf{u}}\mathrm{d}V_j \tag{5.17}
$$

where $\boldsymbol{h}_{ij}^{\mathbf{u}} = \frac{\mu}{m_{\mathbf{K}_i}} w(\boldsymbol{\xi}_{ij})(\mathbf{u}_{ij} - \tilde{\nabla}\mathbf{u}_i\boldsymbol{\xi}_{ij})$ is the zero energy internal force for vector $\mathbf{u}_{ij}$.

Similarly, we obtain the internal force caused by the operator energy functional for the phase field:

$$
\int_{\mathcal{S}_i'} \boldsymbol{h}_{ji}^{\phi}\mathrm{d}V_j - \int_{\mathcal{S}_i} \boldsymbol{h}_{ij}^{\phi}\mathrm{d}V_j \tag{5.18}
$$

where $\boldsymbol{h}_{ij}^{\phi} = \frac{\mu}{m_{\mathbf{K}_i}} w(\boldsymbol{\xi}_{ij})(\phi_{ij} - \tilde{\nabla}\phi_i\boldsymbol{\xi}_{ij})$ is the zero energy internal force for ϕ_i.

5.4 Numerical implementation of nonlocal phase field model by using NOM

5.4.1 Implicit nonlocal phase field model

It can be shown that the weak form of Eq.5.9 is given by

$$\begin{aligned}&\int_\Omega G_c(\frac{1}{l_0}\phi\delta\phi + l_0\nabla\phi\cdot\nabla\delta\phi)\mathrm{d}\Omega + \int_\Omega -2(1-\phi)\delta\phi H\mathrm{d}\Omega = 0\\&\int_\Omega -\boldsymbol{\sigma}:\delta\boldsymbol{\varepsilon}\mathrm{d}\Omega + \int_\Omega \mathbf{b}\cdot\delta\boldsymbol{u}\mathrm{d}\Omega + \int_{\partial\Omega_f}\boldsymbol{f}\cdot\delta\boldsymbol{u}\mathrm{d}S = 0\end{aligned} \tag{5.19}$$

which is the basis for the implicit NOM. The continuous support $\mathcal{S}_i$ at point i is defined by

$$N_i = \{j_1, .., j_k, .., j_n\} \tag{5.20}$$

where $j_1, .., j_k, .., j_n$ are the global indices of particle i's neighbors. The nonlocal operator for displacement $\tilde{\nabla}\boldsymbol{u}_i$, $\tilde{\nabla}\delta\boldsymbol{u}_i$ and phase field $\tilde{\nabla}\phi_i$, $\tilde{\nabla}\delta\phi_i$ in discrete form can be written as

$$\tilde{\nabla}\boldsymbol{u}_i \simeq \sum_{j\in\mathcal{S}_i} w(\boldsymbol{\xi}_{ij})(\boldsymbol{u}_j - \boldsymbol{u}_i)\otimes(\mathbf{K}_i^{-1}\boldsymbol{\xi}_{ij})\Delta V_j = \mathscr{B}_i^{\boldsymbol{u}}\cdot\tilde{\boldsymbol{u}}_i \tag{5.21}$$

$$\tilde{\nabla}\delta\boldsymbol{u}_i \simeq \sum_{j\in\mathcal{S}_i} w(\boldsymbol{\xi}_{ij})(\delta\boldsymbol{u}_j - \delta\boldsymbol{u}_i)\otimes(\mathbf{K}_i^{-1}\boldsymbol{\xi}_{ij})\Delta V_j = \mathscr{B}_i^{\boldsymbol{u}}\cdot\delta\tilde{\boldsymbol{u}}_i \tag{5.22}$$

$$\tilde{\nabla}\phi_i \simeq \sum_{j\in\mathcal{S}_i} w(\boldsymbol{\xi}_{ij})(\phi_j - \phi_i)(\mathbf{K}_i^{-1}\boldsymbol{\xi}_{ij})\Delta V_j = \mathscr{B}_i^{\phi}\cdot\tilde{\phi}_i \tag{5.23}$$

$$\tilde{\nabla}\delta\phi_i \simeq \sum_{j\in\mathcal{S}_i} w(\boldsymbol{\xi}_{ij})(\delta\phi_j - \delta\phi_i)(\mathbf{K}_i^{-1}\boldsymbol{\xi}_{ij})\Delta V_j = \mathscr{B}_i^{\phi}\cdot\delta\tilde{\phi}_i \tag{5.24}$$

$\tilde{\boldsymbol{u}}_i(=\mathbf{u}_i, \mathbf{u}_{j_1}, .., \mathbf{u}_{j_k}, .., \mathbf{u}_{j_n})$ representing the variation of the displacement in the i's support $\mathcal{S}_i$, $\tilde{\phi}_i(=\phi_i, \phi_{j_1}, .., \phi_{j_k}, .., \phi_{j_n})$ contains all the variations of the phase field in support $\mathcal{S}_i$. ΔV_j is the volume of neighbor point j, $\mathscr{B}_i^{\boldsymbol{u}}$ and $\mathscr{B}_i^{\phi}$ refer to the coefficient matrices:

$$\mathscr{B}_i^{\boldsymbol{u}} = \begin{bmatrix} -\sum_{j\in\mathcal{S}_i}\xi_{x_j} & 0 & 0 & \xi_{x_{j1}} & 0 & 0 & \cdots & \xi_{x_{jn}} & 0 & 0 \\ 0 & -\sum_{j\in\mathcal{S}_i}\xi_{y_j} & 0 & 0 & \xi_{y_{j1}} & 0 & \cdots & 0 & \xi_{y_{jn}} & 0 \\ 0 & 0 & -\sum_{j\in\mathcal{S}_i}\xi_{z_j} & 0 & 0 & \xi_{z_{j1}} & \cdots & 0 & 0 & \xi_{z_{jn}} \\ -\sum_{j\in\mathcal{S}_i}\xi_{x_j} & 0 & 0 & \xi_{x_{j1}} & 0 & 0 & \cdots & \xi_{x_{jn}} & 0 & 0 \\ 0 & -\sum_{j\in\mathcal{S}_i}\xi_{y_j} & 0 & 0 & \xi_{y_{j1}} & 0 & \cdots & 0 & \xi_{y_{jn}} & 0 \\ 0 & 0 & -\sum_{j\in\mathcal{S}_i}\xi_{z_j} & 0 & 0 & \xi_{z_{j1}} & \cdots & 0 & 0 & \xi_{z_{jn}} \\ -\sum_{j\in\mathcal{S}_i}\xi_{x_j} & 0 & 0 & \xi_{x_{j1}} & 0 & 0 & \cdots & \xi_{x_{jn}} & 0 & 0 \\ 0 & -\sum_{j\in\mathcal{S}_i}\xi_{y_j} & 0 & 0 & \xi_{y_{j1}} & 0 & \cdots & 0 & \xi_{y_{jn}} & 0 \\ 0 & 0 & -\sum_{j\in\mathcal{S}_i}\xi_{z_j} & 0 & 0 & \xi_{z_{j1}} & \cdots & 0 & 0 & \xi_{z_{jn}} \end{bmatrix},$$

$$\mathscr{B}_i^{\phi} = \begin{bmatrix} -\sum_{j=1}^{N_i}\xi_{x_j} & \xi_{x_{j1}} & \cdots & \xi_{x_{jn}} \\ -\sum_{j=1}^{N_i}\xi_{y_j} & \xi_{y_{j1}} & \cdots & \xi_{y_{jn}} \\ -\sum_{j=1}^{N_i}\xi_{z_j} & \xi_{z_{j1}} & \cdots & \xi_{z_{jn}} \end{bmatrix} \tag{5.25}$$

In order to obtain the elasticity matrix, we need to transform the matrix form of $\boldsymbol{\sigma}$ and $\boldsymbol{\varepsilon}$ into vector form. In Voigt notation, they read

$$\boldsymbol{\sigma}_{ij} = \begin{bmatrix} \sigma_{11} & \sigma_{12} & \sigma_{13} \\ \sigma_{21} & \sigma_{22} & \sigma_{23} \\ \sigma_{31} & \sigma_{32} & \sigma_{33} \end{bmatrix} \overset{Voigt}{\longrightarrow} \{\boldsymbol{\sigma}_{ij}\} = \begin{bmatrix} \sigma_{11} \\ \sigma_{22} \\ \sigma_{33} \\ \sigma_{23} \\ \sigma_{31} \\ \sigma_{12} \end{bmatrix}, \boldsymbol{\varepsilon}_{kl} = \begin{bmatrix} \varepsilon_{11} & \varepsilon_{12} & \varepsilon_{13} \\ \varepsilon_{21} & \varepsilon_{22} & \varepsilon_{23} \\ \varepsilon_{31} & \varepsilon_{32} & \varepsilon_{33} \end{bmatrix} \overset{Voigt}{\longrightarrow} \{\boldsymbol{\varepsilon}_{kl}\} = \begin{bmatrix} \varepsilon_{11} \\ \varepsilon_{22} \\ \varepsilon_{33} \\ 2\varepsilon_{23} \\ 2\varepsilon_{31} \\ 2\varepsilon_{12} \end{bmatrix} \tag{5.26}$$

$$\{\boldsymbol{\sigma}_{ij}\} = \mathbf{D}_{ijkl}\{\boldsymbol{\varepsilon}_{kl}\} \longrightarrow \begin{bmatrix} \sigma_{11} \\ \sigma_{22} \\ \sigma_{33} \\ \sigma_{23} \\ \sigma_{31} \\ \sigma_{12} \end{bmatrix} = \begin{bmatrix} D_{1111} & D_{1122} & D_{1133} & D_{1112} & D_{1123} & D_{1113} \\ D_{2211} & D_{2222} & D_{2233} & D_{2212} & D_{2223} & D_{2213} \\ D_{3311} & D_{3322} & D_{3333} & D_{3312} & D_{3323} & D_{3313} \\ D_{1211} & D_{1222} & D_{1233} & D_{1212} & D_{1223} & D_{1213} \\ D_{2311} & D_{2322} & D_{2333} & D_{2312} & D_{2323} & D_{2313} \\ D_{1311} & D_{1322} & D_{1333} & D_{1312} & D_{1323} & D_{1313} \end{bmatrix} \begin{bmatrix} \varepsilon_{11} \\ \varepsilon_{22} \\ \varepsilon_{33} \\ 2\varepsilon_{23} \\ 2\varepsilon_{31} \\ 2\varepsilon_{12} \end{bmatrix} \tag{5.27}$$

$$\begin{aligned} \{\boldsymbol{\varepsilon}_{kl}\} &= [\frac{\partial \boldsymbol{u}_i}{\partial x}, \frac{\partial \boldsymbol{v}_i}{\partial y}, \frac{\partial \boldsymbol{w}_i}{\partial z}, \frac{\partial \boldsymbol{w}_i}{\partial y} + \frac{\partial \boldsymbol{v}_i}{\partial z}, \frac{\partial \boldsymbol{w}_i}{\partial x} + \frac{\partial \boldsymbol{u}_i}{\partial z}, \frac{\partial \boldsymbol{u}_i}{\partial y} + \frac{\partial \boldsymbol{v}_i}{\partial x}]^T = \tilde{\mathscr{B}}_i^{\boldsymbol{u}} \cdot \{\tilde{\boldsymbol{u}}_i\} \\ \delta\{\boldsymbol{\varepsilon}_{kl}\} &= \tilde{\mathscr{B}}_i^{\boldsymbol{u}} \cdot \delta\{\tilde{\boldsymbol{u}}_i\} \end{aligned} \tag{5.28}$$

$$\tilde{\mathscr{B}}_i^{\boldsymbol{u}} = \begin{bmatrix} -\sum_{j\in\mathcal{S}_i}\xi_{x_j} & 0 & 0 & \xi_{x_{j1}} & 0 & 0 & \cdots & \xi_{x_{jn}} & 0 & 0 \\ 0 & -\sum_{j\in\mathcal{S}_i}\xi_{y_j} & 0 & 0 & \xi_{y_{j1}} & 0 & \cdots & 0 & \xi_{y_{jn}} & 0 \\ 0 & 0 & -\sum_{j\in\mathcal{S}_i}\xi_{z_j} & 0 & 0 & \xi_{z_{j1}} & \cdots & 0 & 0 & \xi_{z_{jn}} \\ 0 & -\sum_{j\in\mathcal{S}_i}\xi_{y_j} & -\sum_{j\in\mathcal{S}_i}\xi_{z_j} & 0 & \xi_{y_{j1}} & \xi_{z_{j1}} & \cdots & 0 & \xi_{y_{jn}} & \xi_{z_{jn}} \\ -\sum_{j\in\mathcal{S}_i}\xi_{x_j} & 0 & -\sum_{j\in\mathcal{S}_i}\xi_{z_j} & \xi_{x_{j1}} & 0 & \xi_{z_{j1}} & \cdots & \xi_{x_{jn}} & 0 & \xi_{z_{jn}} \\ -\sum_{j\in\mathcal{S}_i}\xi_{x_j} & -\sum_{j\in\mathcal{S}_i}\xi_{y_j} & 0 & \xi_{x_{j1}} & \xi_{y_{j1}} & 0 & \cdots & \xi_{x_{jn}} & \xi_{y_{jn}} & 0 \end{bmatrix} \tag{5.29}$$

such that Eq.5.19 becomes

$$\begin{aligned} &\sum_{j\in\mathcal{S}_i}\left(G_c l_0[\mathscr{B}_i^{\phi}]^T\cdot\mathscr{B}_i^{\phi}\cdot\tilde{\phi}_i + [G_c\frac{1}{l_0}\tilde{\phi}_i - 2(\mathbf{1}-\tilde{\phi}_i)H]\right)\Delta V_j = 0 \\ &\sum_{j\in\mathcal{S}_i} -[\tilde{\mathscr{B}}_i^{\boldsymbol{u}}]^T\mathbf{D}_{ijkl}\{\boldsymbol{\varepsilon}_i\}\Delta V_j + \sum_{j\in\mathcal{S}_i}\mathbf{b}_i\mathbf{1}\Delta V_j + \sum_{j\in\partial\Omega_{f_i}}\boldsymbol{f}_i\mathbf{1}\Delta S_j = 0 \end{aligned} \tag{5.30}$$

where $\mathbf{1} = [1, 0, \cdots, 0, 0]^T$ is a (n_i+1)-dimensional column vector. Finally, we obtain the i-th point residual of the overall systems

$$\begin{aligned} \boldsymbol{R}_i^{\boldsymbol{u}} &= \boldsymbol{F}_i^{\boldsymbol{u},ext} - \boldsymbol{F}_i^{\boldsymbol{u},int} \\ &= \underbrace{\sum_{j\in\mathcal{S}_i}\boldsymbol{f}_i\Delta S_j + \sum_{j\in\mathcal{S}_i}\mathbf{b}_i\Delta V_j}_{\boldsymbol{F}_i^{\boldsymbol{u},ext}} - \sum_{j\in\mathcal{S}_i}[\tilde{\mathscr{B}}_i^{\boldsymbol{u}}]^T\mathbf{D}_{ijkl}\{\boldsymbol{\varepsilon}_i\}\Delta V_j \end{aligned} \tag{5.31}$$

$$\begin{aligned} R_i^{\phi} &= -F_i^{\phi,int} \\ &= \sum_{j\in\mathcal{S}_i}\left(G_c l_0[\mathscr{B}_i^{\phi}]^T\cdot\mathscr{B}_i^{\phi}\cdot\tilde{\phi}_i + [G_c\frac{1}{l_0}\tilde{\phi}_i - 2(\mathbf{1}-\tilde{\phi}_i)H]\right)\Delta V_j \end{aligned} \tag{5.32}$$

where $\boldsymbol{F}_i^{\boldsymbol{u},int}$ and $\boldsymbol{F}_i^{\boldsymbol{u},ext}$ are the internal force and external force, respectively; $F_i^{\phi,int}$ is the internal force corresponding to the phase field. The asscoiated tangent stiffness matrices can be obtained from the internal forces:

$$\mathscr{K}_i^{\boldsymbol{u}} = \frac{\partial\boldsymbol{F}_i^{\boldsymbol{u},int}}{\partial\tilde{\boldsymbol{u}}_i} = \sum_{j\in\mathcal{S}_i}[\tilde{\mathscr{B}}_i^{\boldsymbol{u}}]^T\mathbf{D}_{ijkl}\tilde{\mathscr{B}}_i^{\boldsymbol{u}}\Delta V_j \tag{5.33}$$

$$\mathscr{K}_i^{\phi} = \frac{\partial F_i^{\phi,int}}{\partial\tilde{\phi}_i} = \sum_{j\in\mathcal{S}_i}\left([\mathscr{B}_i^{\phi}]^T G_c l_0\mathscr{B}_i^{\phi} + (\frac{G_c}{l_0}+2H)\mathbf{1}\otimes\mathbf{1}^T\right)\Delta V_j \tag{5.34}$$

where $\mathbf{D}_{ijkl}$ is the elasticity matrix obtained by an eigen-decomposition algorithm for the fourth-order isotropic tensor [Miehe et al., 2010b]

$$\mathbf{D}_{ijkl} = \frac{\partial\{\boldsymbol{\sigma}_{ij}\}}{\partial\{\boldsymbol{\varepsilon}_{kl}\}} = \frac{\partial}{\partial\{\boldsymbol{\varepsilon}_{kl}\}}\left([(1-\phi)^2+\kappa_0]\boldsymbol{\sigma}_{ij}^{+} + \boldsymbol{\sigma}_{ij}^{-}\right) = [(1-\phi)^2+\kappa_0]\mathbf{D}_{ijkl}^{+} + \mathbf{D}_{ijkl}^{-} \tag{5.35}$$

The strain energy and the Cauchy stress based on this eigen-decomposition method is expressed as

$$\psi_{\mathbb{e}}^{\pm}(\boldsymbol{\varepsilon}) = \lambda\langle\hat{\varepsilon_1}+\hat{\varepsilon_2}+\hat{\varepsilon_3}\rangle_{\pm}^2/2 + \mu(\langle\hat{\varepsilon_1}\rangle_{\pm}^2 + \langle\hat{\varepsilon_2}\rangle_{\pm}^2 + \langle\hat{\varepsilon_3}\rangle_{\pm}^2) \tag{5.36}$$

$$\begin{aligned}\boldsymbol{\sigma}^{\pm} &= \frac{\partial\psi_{\mathbb{e}}^{\pm}}{\partial\boldsymbol{\varepsilon}} \\ &= \lambda\langle\hat{\varepsilon_1}+\hat{\varepsilon_2}+\hat{\varepsilon_3}\rangle_{\pm} I_{3\times3} + 2\mu(\langle\hat{\varepsilon_1}\rangle_{\pm}\hat{\boldsymbol{n}}_1\otimes\hat{\boldsymbol{n}}_1 + \langle\hat{\varepsilon_2}\rangle_{\pm}\hat{\boldsymbol{n}}_2\otimes\hat{\boldsymbol{n}}_2 + \langle\hat{\varepsilon_3}\rangle_{\pm}\hat{\boldsymbol{n}}_3\otimes\hat{\boldsymbol{n}}_3)\end{aligned} \tag{5.37}$$

where $\boldsymbol{\varepsilon} = \frac{1}{2}(\tilde{\nabla}\boldsymbol{u} + \tilde{\nabla}\boldsymbol{u}^T)$, $\langle\hat{\varepsilon}\rangle_{\pm} := (\hat{\varepsilon} \pm |\hat{\varepsilon}|)/2$, $I_{3\times3}$ is the identity matrix, $\hat{\boldsymbol{n}}_1, \hat{\boldsymbol{n}}_2, \hat{\boldsymbol{n}}_3$ are eigenvectors of the principal strains $\hat{\varepsilon_1}, \hat{\varepsilon_2}, \hat{\varepsilon_3}$ of $\boldsymbol{\varepsilon}(= \sum_{i=1}^{3}\hat{\varepsilon_i}\hat{\boldsymbol{n}}_i\otimes\hat{\boldsymbol{n}}_i)$, λ, μ represent the Lamé constants, which are related to the Young's modulus and Poisson's ratio:

$$\begin{cases}\lambda = \dfrac{E\nu}{(1+\nu)(1-2\nu)} \\ \mu = \dfrac{E}{2(1+\nu)}\end{cases} \tag{5.38}$$

Finally, we can transform Eq.5.33 to

$$\mathscr{K}_i^{\boldsymbol{u}} = \sum_{j\in\mathcal{S}_i}[\tilde{\mathscr{B}}_i^{\boldsymbol{u}}]^T\Big([(1-\phi)^2+\kappa_0]\mathbf{D}_{ijkl}^{+} + \mathbf{D}_{ijkl}^{-}\Big)\tilde{\mathscr{B}}_i^{\boldsymbol{u}}\Delta V_j \tag{5.39}$$

However, Eq.5.19 suffers from zero energy modes. Therefore, a penalty force should be added yielding

$$\begin{aligned}\mathbb{K}_i^{\boldsymbol{u}} = \sum_{j\in\mathcal{S}_i}\Bigg([\tilde{\mathscr{B}}_i^{\boldsymbol{u}}]^T\Big([(1-\phi)^2+\kappa_0]\mathbf{D}_{ijkl}^{+} + \mathbf{D}_{ijkl}^{-}\Big)\tilde{\mathscr{B}}_i^{\boldsymbol{u}} + \frac{\mu}{m_{\mathbf{K}_i}}\Bigg(&\begin{bmatrix}\sum_{j\in\mathcal{S}_i}\mathbf{I}_j & -\mathbf{I}_{j1} & \cdots & -\mathbf{I}_{j_n} \\ -\mathbf{I}_{j1} & \mathbf{I}_{j1} & \mathbf{0} & \mathbf{0} \\ \vdots & \mathbf{0} & \ddots & \mathbf{0} \\ -\mathbf{I}_{j_n} & \mathbf{0} & \mathbf{0} & \mathbf{I}_{j_n}\end{bmatrix} \\ &- [\mathscr{B}_i^{\boldsymbol{u}}]^T\cdot\begin{bmatrix}\mathbf{K}_i & 0 & 0 \\ 0 & \mathbf{K}_i & 0 \\ 0 & 0 & \mathbf{K}_i\end{bmatrix}\cdot[\mathscr{B}_i^{\boldsymbol{u}}]^T\Bigg)\Bigg)\Delta V_j\end{aligned} \tag{5.40}$$

$$\begin{aligned}\mathbb{K}_i^{\phi} = \sum_{j\in\mathcal{S}_i}\Bigg([\mathscr{B}_i^{\phi}]^T G_c l_0 \mathscr{B}_i^{\phi} + \Big(\frac{G_c}{l_0}+2H\Big)\mathbf{1}\otimes\mathbf{1}^T + \frac{\mu}{m_{\mathbf{K}_i}}\Bigg(&\begin{bmatrix}\sum_{j\in\mathcal{S}_i}\mathbf{I}_j & -\mathbf{I}_{j1} & \cdots & -\mathbf{I}_{j_n} \\ -\mathbf{I}_{j1} & \mathbf{I}_{j1} & \mathbf{0} & \mathbf{0} \\ \vdots & \mathbf{0} & \ddots & \mathbf{0} \\ -\mathbf{I}_{j_n} & \mathbf{0} & \mathbf{0} & \mathbf{I}_{j_n}\end{bmatrix} \\ &- [\mathscr{B}_i^{\phi}]^T\cdot\begin{bmatrix}\mathbf{K}_i & 0 & 0 \\ 0 & \mathbf{K}_i & 0 \\ 0 & 0 & \mathbf{K}_i\end{bmatrix}\cdot[\mathscr{B}_i^{\phi}]^T\Bigg)\Bigg)\Delta V_j\end{aligned} \tag{5.41}$$

5.4.2 The staggered method

For the implicit nonlocal phase field model, a staggered update scheme is adopted [Bourdin et al., 2000, Bourdin, 2007, Liu et al., 2016], where the displacement, strain history functional and phase field are updated separately. We use the Newton-Raphson method to iteratively obtain the solution between different load steps. First, the phase field is solved for a fixed displacement field. The key steps of the staggered scheme can be summarized as follows:

①. Initialization
Initialize the displacement $\mathbf{u}_0 = 0$, phase field $\phi_0 = 0$, and the local history field of strain $H_0 = 0$. For each field, the solution is obtained for increments of the primary fields from the iteration number i to i + 1.
②. Calculate maximum strain-history functional.
Calculate the history field according to the maximum reference energy

$$H = \begin{cases} \psi_0^+(\nabla \boldsymbol{u}) & if\ \psi_0^+(\nabla \boldsymbol{u}) > H_n \\ H_n & else \end{cases} \tag{5.42}$$

③. Phase field problem: update the phase field
Calculate the phase field $\phi_{i+1} = \phi_i - (\mathbb{K}_i^{\phi})^{-1} F_i^{\phi,int}$ by solving Eq.5.32 and Eq.5.41.
When $\frac{\|\Delta\phi_{i+1}\|}{\|\sum_{k=1}^{i+1}\Delta\phi_i\|} \leq \mathrm{Tol}\,(\mathrm{Tol} = 10^{-6})$, the iteration is stopped.
④. Displacement field problem: update the displacement field
(i) Calculate $\mathbf{D}_{ijkl}$ according to an eigen-decomposition algorithm for fourth-order isotropic tensor by solving Eq.5.35.
(ii) Calculate the displacement field $\mathbf{u}_{i+1} = \mathbf{u}_i - (\mathbb{K}_i^{\mathbf{u}})^{-1} F_i^{\mathbf{u},int}$ by solving Eq.5.31 and Eq.5.40.
(iii) When $\frac{\|\Delta\mathbf{u}_{i+1}\|}{\|\sum_{k=1}^{i+1}\Delta\mathbf{u}_i\|} \leq \mathrm{Tol}\,(\mathrm{Tol} = 10^{-6})$,the iteration is stopped.

5.4.3 Explicit nonlocal phase field model for solving dynamic problems

The explicit NOM depends on the strong form of the governing equations given by

$$\nabla \cdot \boldsymbol{\sigma} + \mathbf{b} = \rho \ddot{\boldsymbol{u}} \tag{5.43}$$

$$\phi - l_0^2 \nabla^2 \phi = 0 \tag{5.44}$$

For the i-th particle's support and dual-support, we can easily to obtain the relationships

in discrete form

$$\tilde{\nabla}\cdot\boldsymbol{\sigma}_i=\sum_{j\in\mathcal{S}_i}w(\boldsymbol{\xi}_{ij})\boldsymbol{\sigma}_i\boldsymbol{K}_i^{-1}\boldsymbol{\xi}_{ij}\Delta V_j-\sum_{j\in\mathcal{S}_i'}w(\boldsymbol{\xi}_{ji})\boldsymbol{\sigma}_j\boldsymbol{K}_j^{-1}\boldsymbol{\xi}_{ji}\Delta V_j \tag{5.45}$$

$$\tilde{\nabla}^2\phi_i=\sum_{j\in\mathcal{S}_i}w(\boldsymbol{\xi}_{ij})\tilde{\nabla}\phi_i\boldsymbol{K}_i^{-1}\boldsymbol{\xi}_{ij}\Delta V_j-\sum_{j\in\mathcal{S}_i'}w(\boldsymbol{\xi}_{ji})\tilde{\nabla}\phi_j\boldsymbol{K}_j^{-1}\boldsymbol{\xi}_{ji}\Delta V_j \tag{5.46}$$

$$\tilde{\nabla}\mathbf{u}_i=\sum_{j\in\mathcal{S}_i}w(\boldsymbol{\xi}_{ij})\mathbf{u}_i\boldsymbol{K}_i^{-1}\boldsymbol{\xi}_{ij}\Delta V_j-\sum_{j\in\mathcal{S}_i'}w(\boldsymbol{\xi}_{ji})\mathbf{u}_j\boldsymbol{K}_j^{-1}\boldsymbol{\xi}_{ji}\Delta V_j \tag{5.47}$$

$$\tilde{\nabla}\phi_i=\sum_{j\in\mathcal{S}_i}w(\boldsymbol{\xi}_{ij})\phi_i\boldsymbol{K}_i^{-1}\boldsymbol{\xi}_{ij}\Delta V_j-\sum_{j\in\mathcal{S}_i'}w(\boldsymbol{\xi}_{ji})\phi_j\boldsymbol{K}_j^{-1}\boldsymbol{\xi}_{ji}\Delta V_j \tag{5.48}$$

Hence, Eq.5.44 can be transformed into nonlocal form as follows

$$\sum_{j\in\mathcal{S}_i}w(\boldsymbol{\xi}_{ij})\boldsymbol{\sigma}_i\boldsymbol{K}_i^{-1}\boldsymbol{\xi}_{ij}\Delta V_j-\sum_{j\in\mathcal{S}_i'}w(\boldsymbol{\xi}_{ji})\boldsymbol{\sigma}_j\boldsymbol{K}_j^{-1}\boldsymbol{\xi}_{ji}\Delta V_j+\boldsymbol{b}_i=\rho_i\ddot{\boldsymbol{u}}_i \tag{5.49}$$

$$\phi_i-l_0^2\Big(\sum_{j\in\mathcal{S}_i}w(\boldsymbol{\xi}_{ij})\tilde{\nabla}\phi_i\boldsymbol{K}_i^{-1}\boldsymbol{\xi}_{ij}\Delta V_j+\sum_{j\in\mathcal{S}_i'}w(\boldsymbol{\xi}_{ji})\tilde{\nabla}\phi_j\boldsymbol{K}_j^{-1}\boldsymbol{\xi}_{ji}\Delta V_j\Big)=0 \tag{5.50}$$

As Eq.5.49 and Eq.5.50 suffer from zero energy modes, a penalty force from the nonlocal operator functional is added leading to

$$\sum_{j\in\mathcal{S}_i}(w(\boldsymbol{\xi}_{ij})\boldsymbol{\sigma}_i\boldsymbol{K}_i^{-1}\boldsymbol{\xi}_{ij}+\boldsymbol{h}_{ij}^{\mathbf{u}})\Delta V_j-\sum_{j\in\mathcal{S}_i'}(w(\boldsymbol{\xi}_{ji})\boldsymbol{\sigma}_j\boldsymbol{K}_j^{-1}\boldsymbol{\xi}_{ji}+\boldsymbol{h}_{ij}^{\mathbf{u}})\Delta V_j+\boldsymbol{b}_i=\rho_i\ddot{\boldsymbol{u}}_i \tag{5.51}$$

$$\phi_i-l_0^2\Big(\sum_{j\in\mathcal{S}_i}(w(\boldsymbol{\xi}_{ij})\tilde{\nabla}\phi_i\boldsymbol{K}_i^{-1}\boldsymbol{\xi}_{ij}+\boldsymbol{h}_{ij}^{\phi})\Delta V_j+\sum_{j\in\mathcal{S}_i'}(w(\boldsymbol{\xi}_{ji})\tilde{\nabla}\phi_j\boldsymbol{K}_j^{-1}\boldsymbol{\xi}_{ji}+\boldsymbol{h}_{ij}^{\phi})\Delta V_j\Big)=0 \tag{5.52}$$

Comparing Eq.5.44 with Eq.5.52, the modified correspondence between the local and nonlocal form is

$$\tilde{\nabla}^2\phi_i\ \underset{\text{Nonlocal}\to\text{Local}}{\overset{\text{Local}\to\text{Nonlocal}}{\rightleftharpoons}}\ \sum_{j\in\mathcal{S}_i}(w(\boldsymbol{\xi}_{ij})\tilde{\nabla}\phi_i\boldsymbol{K}_i^{-1}\boldsymbol{\xi}_{ij}+\boldsymbol{h}_{ij}^{\phi})\Delta V_j+\sum_{j\in\mathcal{S}_i'}(w(\boldsymbol{\xi}_{ji})\tilde{\nabla}\phi_j\boldsymbol{K}_j^{-1}\boldsymbol{\xi}_{ji}+\boldsymbol{h}_{ij}^{\phi})\Delta V_j \tag{5.53}$$

The bond force for displacement $\mathbf{u}_{ij}$, phase field ϕ_{ij} at the i-th particle's support and dual-support can be calculated by follows

$$\boldsymbol{f}_{ij}^{\mathbf{u}}=\Big(w(\boldsymbol{\xi}_{ij})\boldsymbol{\sigma}_i\cdot\boldsymbol{K}_i^{-1}\boldsymbol{\xi}_{ij}+(1-\phi_i)\frac{\mu}{m_{\mathbf{K}_i}}w(\boldsymbol{\xi}_{ij})(\mathbf{u}_{ij}-\tilde{\nabla}\mathbf{u}_i\boldsymbol{\xi}_{ij})\Big)\Delta V_i\Delta V_j \tag{5.54}$$

$$\boldsymbol{f}_{ij}^{\phi}=\Big(w(\boldsymbol{\xi}_{ij})\tilde{\nabla}\phi_i\cdot\boldsymbol{K}_i^{-1}\boldsymbol{\xi}_{ij}+\frac{\mu}{m_{\mathbf{K}_i}}w(\boldsymbol{\xi}_{ij})(\phi_{ij}-\tilde{\nabla}\phi_i\boldsymbol{\xi}_{ij})\Big)\Delta V_i\Delta V_j \tag{5.55}$$

with $\boldsymbol{\sigma}_i=[(1-\phi)^2+\kappa_0]\boldsymbol{\sigma}_i^{+}+\boldsymbol{\sigma}_i^{-}$, which can be calculated by $\boldsymbol{\varepsilon}_i$ eigenvalue decomposition, as shown in Eq.5.37. According to Newton's third law, $\boldsymbol{f}_{ij}^{\mathbf{u}}$ has a direct action on the i's particle and $-\boldsymbol{f}_{ij}^{\mathbf{u}}$ to the j's particle, Similarly, $\boldsymbol{f}_{ij}^{\phi}$ has a direct action on the i's particle and $-\boldsymbol{f}_{ij}^{\phi}$ to the j's particle.

5.4.4 Sub-step phase field increment method

For the evolution of the phase field $\phi(\bar{\boldsymbol{X}}, \mathbb{t})$, we took advantage of a generalized formula [Miehe et al., 2015]:

$$\underbrace{\widetilde{\eta}\dot{\phi}(\bar{\boldsymbol{X}}, \mathbb{t})}_{evolution} = \underbrace{(1-\phi(\bar{\boldsymbol{X}}, \mathbb{t}))\mathcal{H}(\bar{\boldsymbol{X}}, \mathbb{t})}_{driving\,force} - \underbrace{(\phi(\bar{\boldsymbol{X}}, \mathbb{t}) - l^2\Delta\phi(\bar{\boldsymbol{X}}, \mathbb{t}))}_{geometric\,resistance}, \tag{5.56}$$

$$\mathcal{H}(\bar{\boldsymbol{X}}, \mathbb{t}) = \max_{\mathbb{s}\in[0,\mathbb{t}]} \tilde{\mathcal{D}}(state(\bar{\boldsymbol{X}}, \mathbb{s})) \tag{5.57}$$

where $\widetilde{\eta} \geq 0$ is the crack propagation viscosity. When $\widetilde{\eta} = 0$, we obtain a rate independent model. The local crack driving force is represented by $\mathcal{H}(\bar{\boldsymbol{X}}, \mathbb{t})$ and depends on the complete history at $0 \leq \mathbb{s} \leq \mathbb{t}$ of the state variables $(\bar{\boldsymbol{X}}, \mathbb{t})$ which are correlated to the solid's bulk reaction. $\tilde{\mathcal{D}}(state(\bar{\boldsymbol{X}}, \mathbb{t}))$ is the crack state function, at crack state $\tilde{\mathcal{D}}|_{state}^{unbroken} = 0$ and $\tilde{\mathcal{D}}|_{state}^{broken} = \infty$. Miehe et al.[Miehe et al., 2015] suggested three failure criteria:

①. Strain criterion with and without threshold

$$\tilde{\mathcal{D}} = \begin{cases} \dfrac{2\tilde{\psi}(\boldsymbol{\varepsilon})}{G_c/l_0} & \text{without threshold} \\ \langle \dfrac{\tilde{\psi}(\boldsymbol{\varepsilon})}{\psi_c} - 1 \rangle & \text{with threshold} \end{cases} \tag{5.58}$$

where $\tilde{\psi}(\boldsymbol{\varepsilon})(= \frac{E}{2}\varepsilon^2)$ denotes the effective part of the energy of the undamaged material, ψ_c denotes the specific crack energy per unit volume, $\psi_c = \frac{E}{2}\varepsilon_c^2$ with $\varepsilon_c = \sqrt{\frac{G_c/l_0}{3E}}$.

②. Stress criteria with and without threshold

$$\tilde{\mathcal{D}} = \begin{cases} \dfrac{2\tilde{\psi}^*(\boldsymbol{\sigma}^*)}{G_c/l_0} & \text{without threshold} \\ \langle \dfrac{\tilde{\psi}^*(\boldsymbol{\sigma}^*)}{\psi_c^*} - 1 \rangle & \text{with threshold} \end{cases} \tag{5.59}$$

where $\tilde{\psi}^*(\boldsymbol{\sigma}^*)(= \frac{\tilde{\sigma}^2}{2E})$ refers to the effective energy of the undamaged material, $\boldsymbol{\sigma}^*(= \boldsymbol{\sigma}/(1-\phi)^2)$ denotes the effective part of the Cauchy stress tensor and $\psi_c^* = \frac{\sigma_c^2}{2E}$ with $\sigma_c = \frac{9}{16}E\varepsilon_c$.

③. A principal tensile stress criterion with threshold

$$\tilde{\mathcal{D}} = \zeta\langle \sum_{i=1}^{3} (\frac{\langle \sigma_i^* \rangle}{\sigma_c})^2 - 1 \rangle \tag{5.60}$$

where $\zeta(\zeta > 0, \zeta \neq 1)$ is a dimensionless parameter. σ_c is the critical fracture stress, $\tilde{\boldsymbol{\sigma}} = \tilde{\boldsymbol{\sigma}}^+ + \tilde{\boldsymbol{\sigma}}^-, \tilde{\boldsymbol{\sigma}}^+ := \sum_{i=1}^{3}\langle\sigma_i\rangle_+ \boldsymbol{n}_i \otimes \boldsymbol{n}_i$. This criterion can be applied to general nonlinear and potentially anisotropic elasticity.

For all criteria, we can conveniently obtain the yielding driving forces independent of the length scale l_0. However, Eq. 5.56 is associated with the material viscosity $\widetilde{\eta}$. A sub-step phase field increment method is used in this analysis. The key term is to replace the phase field rate in Eq.5.56 with a phase field increment. The modified formulation can be written in discrete form as

$$\begin{cases} \Delta\phi_i = \dfrac{1}{n_\phi}\langle \Phi_i \rangle_+ \\ \Phi_i = (1-\phi_i)\mathcal{H}_i - (\phi_i - l_0^2\tilde{\nabla}^2\phi_i) \end{cases} \tag{5.61}$$

where Φ_i is the phase field residual, n_ϕ indicates the phase field mobility to control the increment of ϕ_i, $\Delta\phi_i$ is the phase field increment at each sub-step. Eq.5.61 is robust and provides flexibility in the solution algorithm. The sub-step scheme can also reduce adaptively the residual Φ_i. By substituting Eq.5.53 and Eq.5.55 into Eq.5.61, the phase field residual Φ_i can be rewritten as

$$\begin{aligned} \Phi_i &= (1-\phi_i)\mathcal{H}_i - \phi_i + l_0^2\Big(\sum_{j\in\mathcal{S}_i}(w(\boldsymbol{\xi}_{ij})\tilde{\nabla}\phi_i\boldsymbol{K}_i^{-1}\boldsymbol{\xi}_{ij} + \boldsymbol{h}_{ij}^{\phi})\Delta V_j \\ &\quad + \sum_{j\in\mathcal{S}_i'}(w(\boldsymbol{\xi}_{ji})\tilde{\nabla}\phi_j\boldsymbol{K}_j^{-1}\boldsymbol{\xi}_{ji} + \boldsymbol{h}_{ij}^{\phi})\Delta V_j\Big) \\ &= (1-\phi_i)\mathcal{H}_i - \phi_i + l_0^2\frac{\boldsymbol{f}_i^{\phi}}{\Delta V_i} \end{aligned} \tag{5.62}$$

The main steps of the sub-step update scheme procedure can be summarized as follows:

①. Initialization

Initialize the bond force of the displacement field $\boldsymbol{f}_{ij}^{\mathbf{u}} = 0$, the bond force of phase field $\boldsymbol{f}_{ij}^{\phi} = 0$ and the local crack driving force $\mathcal{H}_0 = 0$.

②. Compute crack driving force

For each particle, compute $\mathcal{H}(\bar{\boldsymbol{X}}, \mathbb{t})$ by solving problem Eq.5.57 - Eq.5.60.

③. Phase field problem: update the phase field with sub-steps

(i) For each particle, compute $\tilde{\nabla}\phi_i$, phase field residual Φ_i and phase field increment at each sub-step $\Delta\phi_i$ by solving Eq.5.48, Eq.5.61 and Eq.5.62.

(ii) Update $\phi_i = \phi_i + \Delta\phi_i$ until $L^\infty(\Phi_i) < 1.0 \times 10^{-3}$.

④. Displacement field problem: update the displacement field

(i) For each particle, compute $\tilde{\nabla}\mathbf{u}_i$, strain energy $\psi_{\mathbb{e}}^{\pm}$ and Cauchy stresses $\boldsymbol{\sigma}_i$ by solving Eq.5.36, Eq.5.37 and Eq.5.47.

(ii) For each neighbor particle $j \in \mathcal{S}_i$, compute $\boldsymbol{f}_{ij}^{\mathbf{u}}$ and add $\boldsymbol{f}_{ij}^{\mathbf{u}}$ to $\boldsymbol{f}_i^{\mathbf{u}}$ and add $-\boldsymbol{f}_{ij}^{\mathbf{u}}$ to $\boldsymbol{f}_j^{\mathbf{u}}$.

(iii) According to Newton's second law $\boldsymbol{F}_i - \boldsymbol{f}_i^{\mathbf{u}} = M_i \boldsymbol{a}_i$, compute each particle's acceleration $\boldsymbol{a}_i$, M_i being the mass of the particle i, $\boldsymbol{F}_i$ denotes the external load and $\boldsymbol{f}_i^{\mathbf{u}}$ the internal bond force.
(iv) Update each particle's velocity and displacement through the explicit time integration scheme [Verlet, 1967]:

$$\begin{cases} \text{(a). Compute } \boldsymbol{v}_i(\mathbb{t} + \dfrac{\Delta\mathbb{t}}{2}) = \boldsymbol{v}_i(\mathbb{t}) + \dfrac{\Delta\mathbb{t}}{2M}(\boldsymbol{F}^i - \boldsymbol{f}^i) \\ \text{(b). Compute } \boldsymbol{u}_i(\mathbb{t} + \Delta\mathbb{t}) = \boldsymbol{u}_i(\mathbb{t}) + \boldsymbol{v}_i(\mathbb{t} + \dfrac{1}{2}\Delta\mathbb{t})\Delta\mathbb{t} \\ \text{(c). Derive } \boldsymbol{a}_i(\mathbb{t} + \Delta\mathbb{t}) \text{ by using } \boldsymbol{u}_i(\mathbb{t} + \Delta\mathbb{t}) \\ \text{(d). Compute } \boldsymbol{v}_i(\mathbb{t} + \Delta\mathbb{t}) = \boldsymbol{v}_i(\mathbb{t} + \dfrac{1}{2}\Delta\mathbb{t}) + \dfrac{\Delta\mathbb{t}}{2M}(\boldsymbol{F}^{i+1} - \boldsymbol{f}^{i+1}) \end{cases} \tag{5.63}$$

where $\Delta\mathbb{t}$ indicates the time step, $\boldsymbol{v}_i, \boldsymbol{u}_i$ is each particle's velocity and displacement, respectively.

5.5 Numerical examples

Several benchmark problems are investigated in this section to demonstrate the feasibility of the proposed nonlocal phase field algorithm. We also studied the influence of the length scale parameter l_0, the critical energy release G_c and time step Δt on the results.

5.5.1 Square plate with a single notched edge test

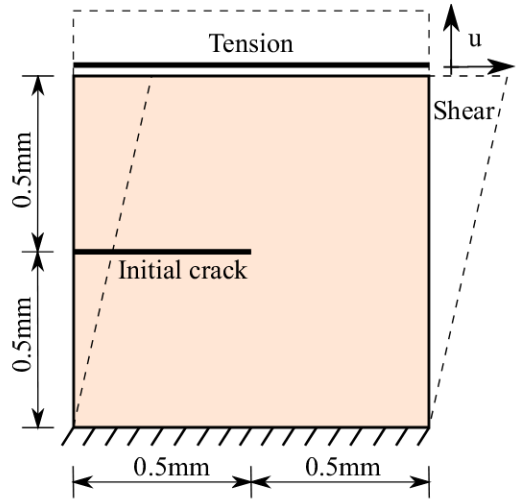

Figure 5.2: Geometry and boundary conditions.

Let us consider a single notched square plate subjected to static tensile and shear loading. Fig.5.2 depicts the setup including boundary conditions. The plate parameters are: $E = 2.1 \times 10^5$MPa , $\nu = 0.3$, the strain energy release rate is $G_c = 2.7 \times 10^{-3}$ kN/mm and we assume plane strain conditions. In order to produce the initial crack, we deleted the particles closest to the initial crack and selected the eight points closest to the target point to construct the target point's support domain. The single-edge notched square plate is discretized with 40401 and 10201 particles, respectively. The phase field length scale parameter is set to $l_0 = 0.015$ mm and $l_0 = 0.0375$ mm, respectively. In the shear test, the single edge notched square plate is discretized into 40401 particles and the phase field length scale parameter is set to $l_0 = 0.015$ mm. To prevent the singularity, $\kappa_0 = 1 \times 10^{-6}$ is chosen. A small vertical displacement increment $\Delta \boldsymbol{u} = 1 \times 10^{-5}$ mm is applied to the upper boundary of the plate while the bottom boundary is fixed.

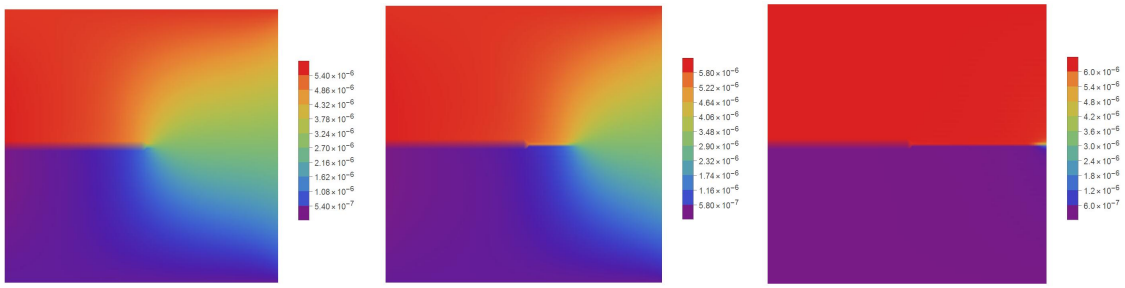

(a) $\mathbf{u} = 5.6 \times 10^{-3}$mm (b) $\mathbf{u} = 6.1 \times 10^{-3}$mm (c) $\mathbf{u} = 6.6 \times 10^{-3}$mm

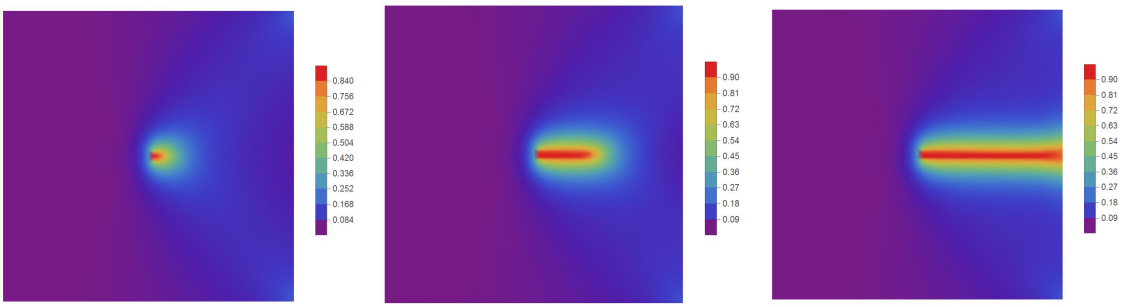

(d) $\mathbf{u} = 5.6 \times 10^{-3}$mm (e) $\mathbf{u} = 6.1 \times 10^{-3}$mm (f) $\mathbf{u} = 6.6 \times 10^{-3}$mm

Figure 5.3: Displacement field (a-c) and phase field (d-f) evolution process for $l_0 = 0.0375$ mm in tension test.

Fig.5.3 shows the crack patterns at various displacements for $l_0 = 0.0375$ mm and Fig.5.4 depicts the reaction force-displacement curves in tension test. Fig.5.5 shows the crack patterns at various displacements for $l_0 = 0.0375$ mm and Fig.5.6 depicts the reaction force-displacement curves in shear test. When using a staggered scheme, the rate at which the crack evolves is delayed in comparison to a completely monolithic scheme, which agrees well with the literature [Miehe et al., 2010a]. As expected, with a smaller length scale parameter l_0, the crack becomes less diffused. The load-deflection curves of the

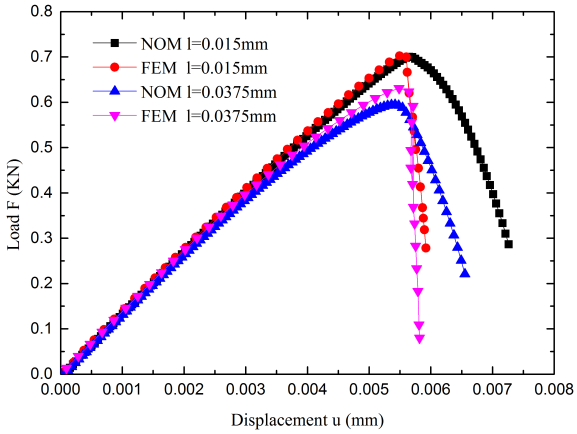

Figure 5.4: Reaction force-displacement curves in tension test.

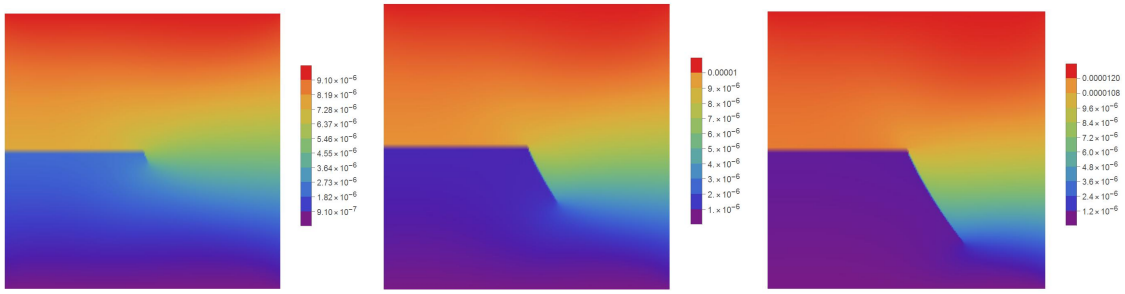

(a) $\mathbf{u} = 1.0 \times 10^{-2}$mm (b) $\mathbf{u} = 1.2 \times 10^{-2}$mm (c) $\mathbf{u} = 1.4 \times 10^{-2}$mm

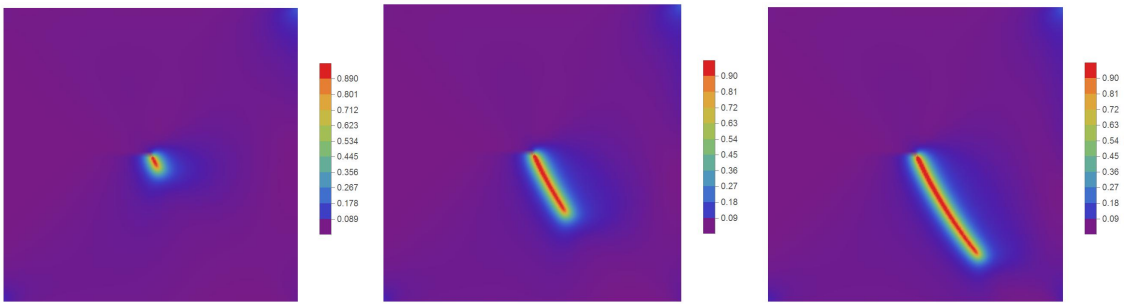

(d) $\mathbf{u} = 1.0 \times 10^{-2}$mm (e) $\mathbf{u} = 1.2 \times 10^{-2}$mm (f) $\mathbf{u} = 1.4 \times 10^{-2}$mm

Figure 5.5: Displacement field (a-c) and phase field (d-f) evolution process for $l_0 = 0.015$ mm in shear test.

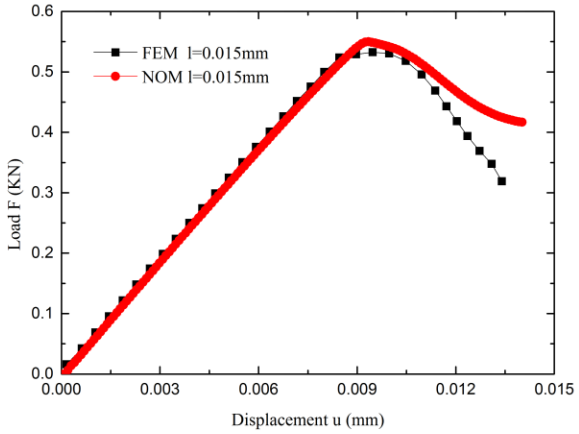

Figure 5.6: Reaction force-displacement curves in shear test.

implicit NOM agrees well with FEM results. Slight differences appear at postlocalization where FEM exhibits a sharper decay compared to the NOM. In the NOM, particles near the crack tip still have a small bond force due to their support and dual-support, which explains the 'more ductile' postlocaliaztion behaviour.

5.5.2 Initial crack rectangular plate of dynamic crack branching test

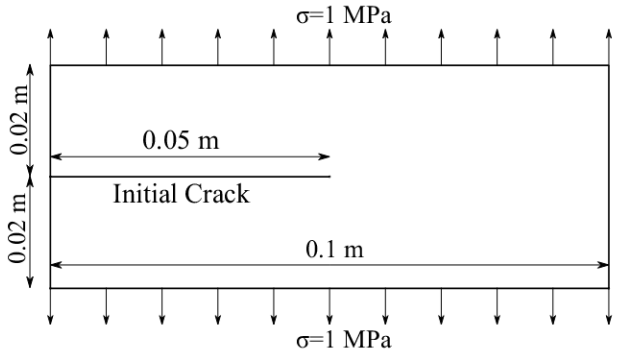

Figure 5.7: Geometry and boundary conditions.

We now investigate an initial crack plate subjected to dynamically uni-axial load as shown in Fig.5.7, which is a standard benchmark test for dynamic fracture [Xu and Needleman, 1994, Belytschko et al., 2003, Rabczuk and Belytschko, 2004, **?**, Ren et al., 2016]. Plane strain conditions are assumed. The material constants are: $E = 3.2 \times 10^4$MPa, $\nu = 0.2$, $\rho = 2450$ kg/mm^3, $G_c = 3 \times 10^{-6}$ kN/mm. The corresponding Rayleigh wave speed is v_R= 2125 m/s of this plate. The initial crack rectangular plate is discretized with 64561

particles with $\Delta x = 0.25$ mm. Note that we received nearly indistinguishable results when further refining the discretization. The length scale parameter is $l = 0.5\text{mm}(l = 2\Delta x)$. We tested three different time steps 0.01 μs, 0.025 μs and 0.05 μs, respectively.

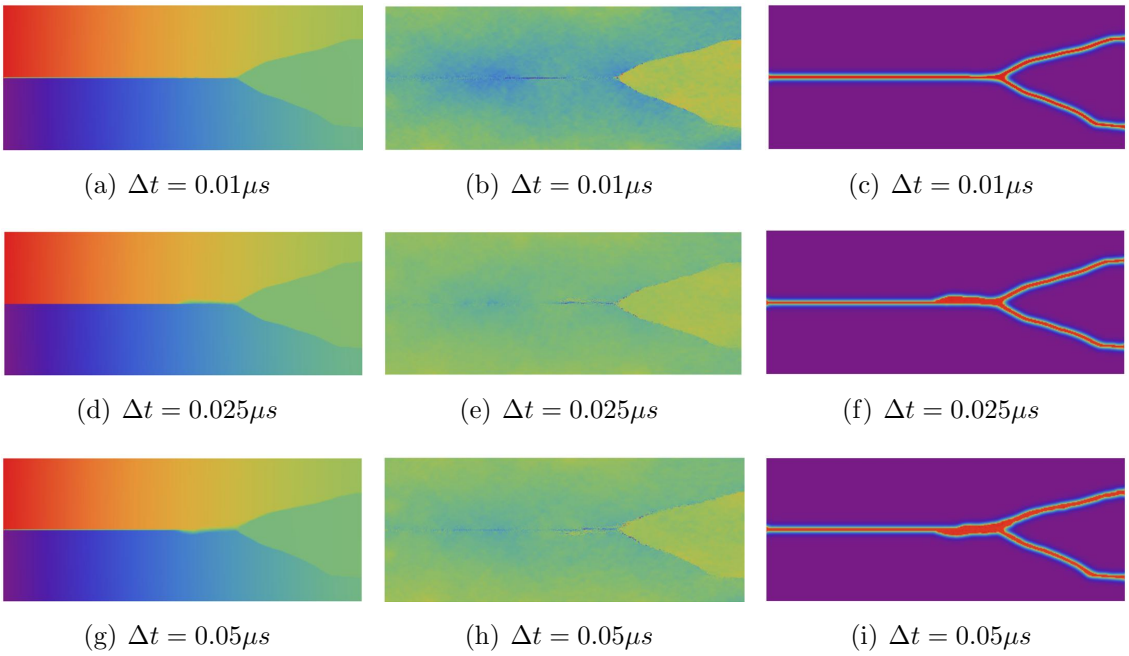

(a) $\Delta t = 0.01\mu s$ (b) $\Delta t = 0.01\mu s$ (c) $\Delta t = 0.01\mu s$

(d) $\Delta t = 0.025\mu s$ (e) $\Delta t = 0.025\mu s$ (f) $\Delta t = 0.025\mu s$

(g) $\Delta t = 0.05\mu s$ (h) $\Delta t = 0.05\mu s$ (i) $\Delta t = 0.05\mu s$

Figure 5.8: Displacement field (a,d,g), velocity field (b,e,h) and phase field (c,f,i) evolution process of dynamic crack branching tests at 90 μs for various time steps.

The displacement field, velocity field and crack propagation evolution process for different time steps at 90 μs is shown in Fig.5.8. The branching angle is in good agreement with reported results from the literature [Borden et al., 2012, Schlüter et al., 2014, Nguyen and Wu, 2018]. The potential reason for crack propagation doesn't look symmetrical with respect to the horizontal central axis is the nonlocal effect. The elastic strain energy and phase field energy curves for various time steps are shown in Fig.5.9. The phase field energy, strain energy and kinetic energy are computed by

$$E_{\boldsymbol{\phi}} = \int_{\Omega} (\frac{\phi^2}{2l} + \frac{l}{2}\nabla\phi \cdot \nabla\phi)\mathrm{d}\Omega, \tag{5.64}$$

$$E_{\boldsymbol{\varepsilon}} = \int_{\Omega} [(1-\phi)^2 + \kappa_0]\psi_{\mathrm{e}}^{+}(\boldsymbol{\varepsilon}(\nabla \boldsymbol{u})) + \psi_{\mathrm{e}}^{-}(\boldsymbol{\varepsilon}(\nabla \boldsymbol{u}))\mathrm{d}\Omega, \tag{5.65}$$

$$K(\boldsymbol{v}) = \int_{\Omega} \frac{1}{2}\rho \boldsymbol{v} \cdot \boldsymbol{v}\mathrm{d}\Omega, \tag{5.66}$$

where $\boldsymbol{v}$ denotes the velocity, ρ denotes the density.

Fig.5.10 shows the crack tip velocity for different time steps. The velocities are less than $0.6v_R$, which agrees well with experimental findings [Sharon and Fineberg, 1999] and other phase field simulations [Borden et al., 2012].

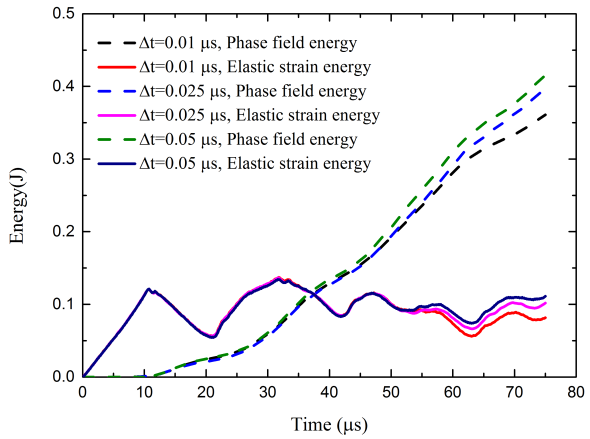

Figure 5.9: Energy of the dynamic crack branching tests for various time steps.

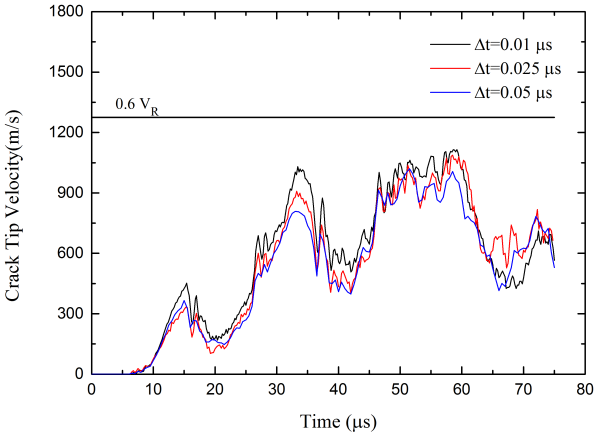

Figure 5.10: Crack tip velocity of dynamic crack branching tests for various time steps.

Let us show the effect of G_c next. We adopted a time step of 0.05 μs. Fig.5.11 shows that similar crack patterns occur. For the smallest value of G_c (such as $G_c = 5J/m^2$), multiple crack branching occurs, which seems reasonable as it is known that crack starts to branch when a certain crack speed is reached and the crack speed is inverse proportional to the critical energy release rate, which is confirmed in Fig. 5.12.

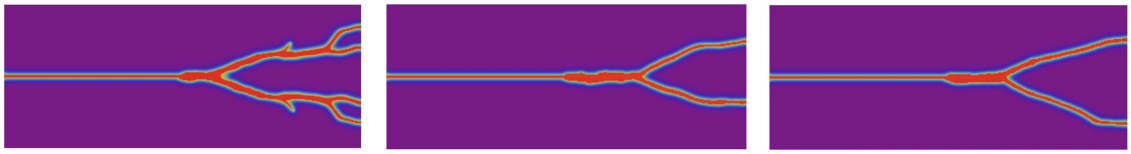

(a) $G_c = 0.5J/m^2$, $t = 52.5\mu s$ (b) $G_c = 1.5J/m^2$, $t = 67.5\mu s$ (c) $G_c = 3J/m^2$, $t = 90.0\mu s$

Figure 5.11: Phase field of dynamic crack branching tests for different G_c.

Fig.5.13 shows the elastic strain energy and phase field energy curves of the dynamic crack branching tests for various G_c. For smaller values of G_c, the elastic strain energy has a decreasing tendency as the time passes while for larger G_c values, the elastic strain energy grows more rapidly over time. The phase field energy increases more than the elastic strain energy as time passes.

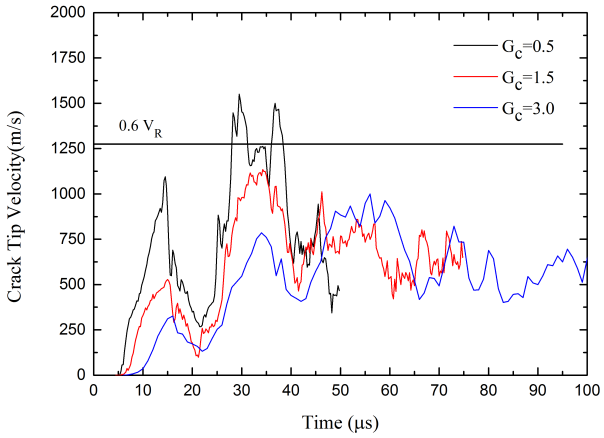

Figure 5.12: Crack tip velocity of dynamic crack branching tests for various G_c.

5.5.3 Prenotched composite structure

Let us now consider a composite plate subjected to constant velocity boundary conditions at the upper edge while the bottom boundary is fixed, see Fig.5.14. We randomly generated inclusions in the matrix according to a normal distribution and avoiding overlapping. All inclusions have the same material parameters. For the matrix we assume

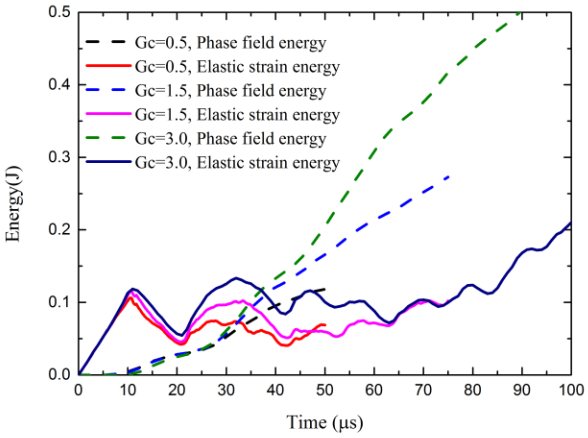

Figure 5.13: Energy of dynamic crack branching tests for various G_c.

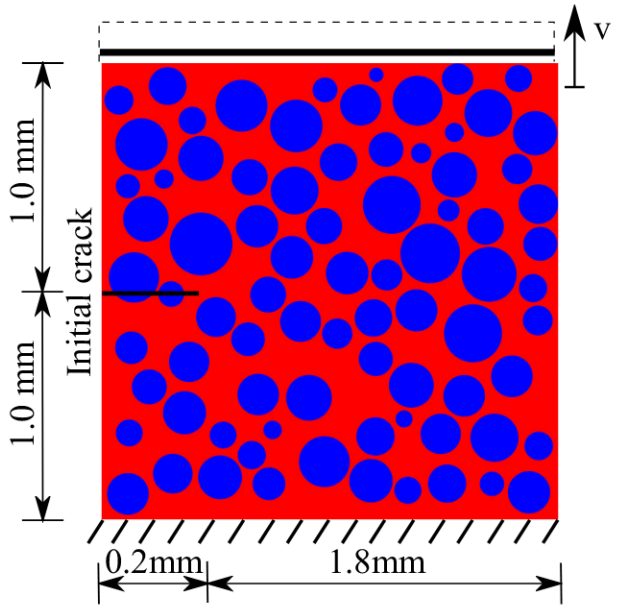

Figure 5.14: Geometry and boundary conditions of the composites plate with inclusions.

the following material parameters : $E = 72 \times 10^3$MPa ,$\nu = 0.33$, $\rho = 2400$ kg/mm^3, $G_c = 60$ J/m^2 and for the inclusions: $E = 144 \times 10^3$MPa ,$\nu = 0.33$, $\rho = 2400$ kg/mm^3, $G_c = 120$ J/m^2. We assume plane stress conditions and employ 40401 material points with point spacing of $\Delta x = 1 \times 10^{-5}$ m to discretize the specimen; finer discretizations yield very similar results. In order to produce the initial crack, we search the particles closest to the initial crack and assign a value of 1 to the phase field degrees of freedom for these particles. The phase field length scale parameter is set to $l_0 = 1.25\Delta x$. Eight neighbors are employed to construct the support domain. Four cases are studied to test the influence of the loading velocity on the crack patterns. Therefore, three different plates with N= 60, 90 and 120 inclusions, respectively, are tested; the distribution of the inclusions are shown in Fig.5.15. Velocity boundary conditions are: $v = 1.0$ m/s for Case I, II and Case III – associated to the three different microstructures – and $v = 3$ m/s for Case IV for the 'third' microstructure (Figure 5.15(c)), which is the same microstructure as for Case III.

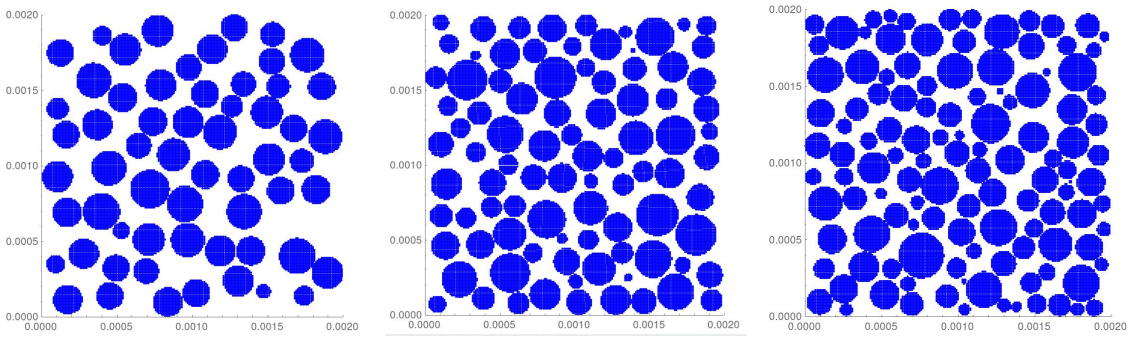

(a) N=60 (b) N=90 (c) N=120

Figure 5.15: The distribution of the inclusions of composite heterogeneous plates

The crack patterns for the four cases can be found in Fig.5.16. For cases I - III, the crack patterns are quite similar. One major crack propagates mainly around the inclusions. Crack branching is observed only for Case II. When increasing the crack speed, crack branching becomes more pronounced which agrees well with experimental observations, crack branching is also observed in Case IV and the crack propagates through the inclusions more easier. Fig.5.17 shows the elastic strain energy, kinetic energy and phase field energy curves of the dynamic crack branching tests for Case IV. The slope of phase field energy at time t =1.0-1.25 μs is larger than that in t = 0.75-1 μs, which is consistent with the propagation speed of the crack.

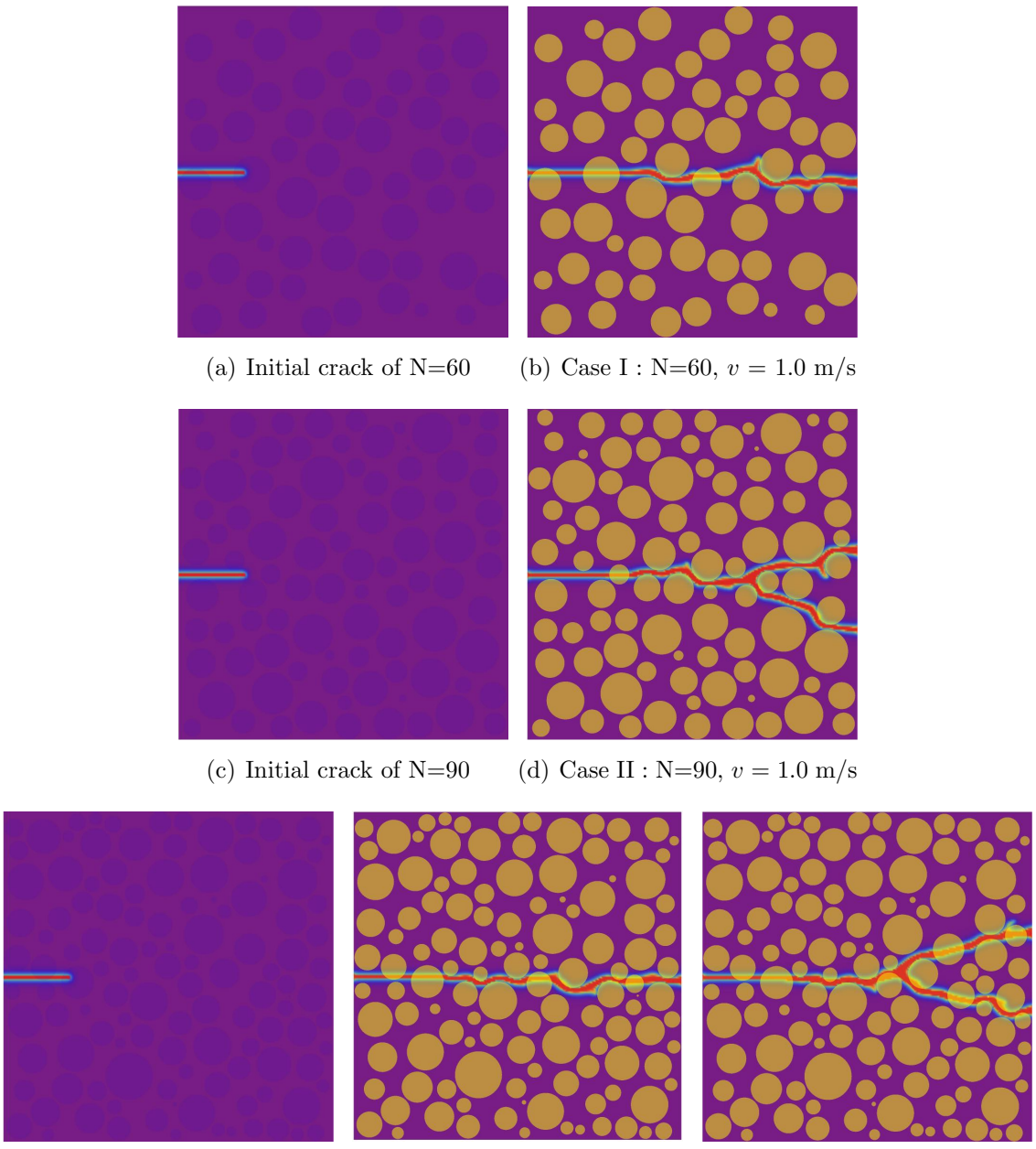

(a) Initial crack of N=60 (b) Case I : N=60, $v = 1.0$ m/s

(c) Initial crack of N=90 (d) Case II : N=90, $v = 1.0$ m/s

(e) Initial crack of N=120 (f) Case III : N=120, $v = 1.0$ m/s (g) Case IV : N=120, $v = 3.0$ m/s

Figure 5.16: The crack patterns in composite heterogeneous plates.

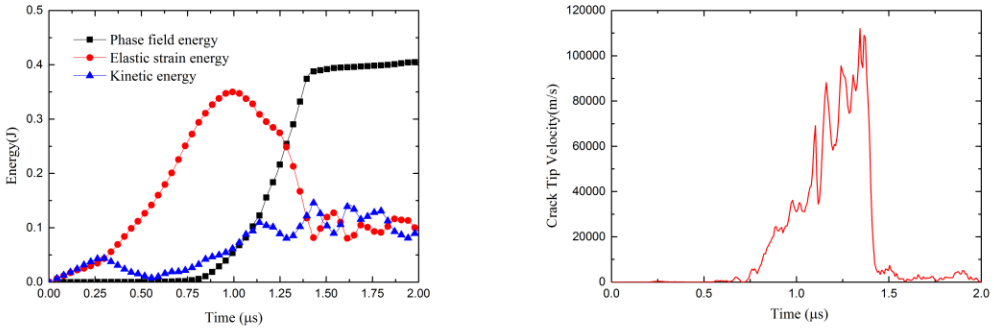

(a) (b)

Figure 5.17: Energy and crack tip velocity of Case IV

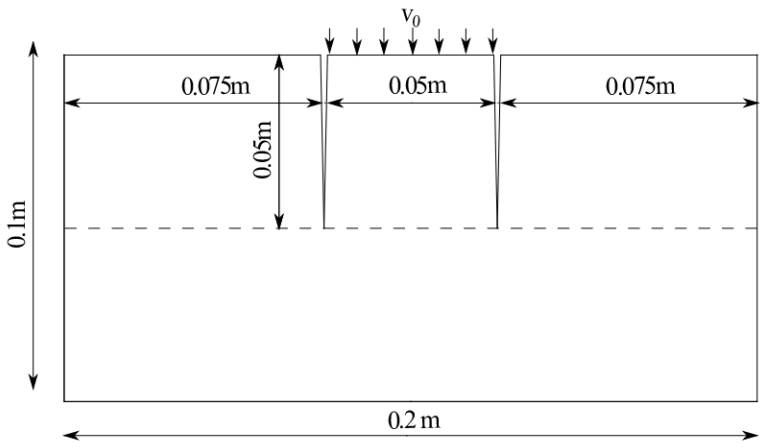

Figure 5.18: Geometry and boundary conditions of the Kalthoff-Winkler plate.

5.5.4 Kalthoff-Winkler experiment of dynamic shear loading

Finally, we apply NOM to the classical Kalthoff-Winkler experiment [Kalthoff and Winkler, 1988, Li et al., 2002, Belytschko et al., 2003, Song et al., 2006, Rabczuk et al., 2007a, Nguyen and Wu, 2018]. The geometrical setup and the loading conditions are depicted in Fig.5.18. The material parameters are: $E = 1.9 \times 10^5$ MPa, $\nu = 0.30, \rho =$ 8000 kg/mm^3, $G_c = 2.213 \times 10^4$ J/m^2, which yields a Rayleigh wave speed of v_R= 2803 m/s. Kalthoff et al. [Kalthoff and Winkler, 1988] found that the failure is brittle for low impact velocities while it turns into a ductile failure at a certain impact velocity is exceeded. Here, we focus only on brittle fracture and low impact velocities as a more complicated constitutive model is required to capture the failure transition from brittle-to-ductile, which is out of the scope of this manuscript. Instead of modeling the impactor and the associated contact, the impact is –commonly– modelled through the following boundary conditions:

$$v = \begin{cases} \dfrac{t}{t_1} v_y & \text{if } t \leq t_1 \\ v_y & \text{else} \end{cases} \tag{5.67}$$

with $t_1 = 1\mu s$. We furthermore assume the initial crack is traction-free. The plate is discretized with 321201 particles with Δx=0.25 mm, and each particle has eight neighbors. The length scale parameter is set to $l_0 = 0.375mm (l_0 = 1.5\Delta x)$. In order to model the initial crack, the neighbor list in the support of associated particles is modified. We test two different time steps, i.e. $\Delta t = 0.02\mu$s and $\Delta t = 0.04\mu$s. Fig.5.19 and Fig.5.20 depict the displacement field, velocity field and phase field for these cases. The crack angle with respect to the vertical axis is around 68°, which matches well the experiments [Kalthoff, 2000]. The crack speed – illustrated in Fig. 5.21 – does not depend on the time step and agrees well with other results from the literature [Borden et al., 2012]. The same applies to the different energy time histories, see Figure 5.22.

We also simulated the Kalthoff Winkler experiment in 3D; the thickness of the plate is 0.02 m. For sake of reducing the computational cost, we exploited symmetry condition as shown in Fig.5.23. The plate is discretized with 1447209 paiticles and the initial crack is again tractionfree. The same material parameters are employed. Fig.5.24 depicts the evolution of the crack path and displacement at an impact velocity of $v = 16.5$ m/s. The agreement to the Kalthoff Winkler experiment is excellent.

5.6 Conclusions

This chapter presents an implicit and explicit phase field model within the framework of the NOM. The coupled system for the implicit phase field model is solved using a staggered method and the Newton Raphson method. The explicit phase field model

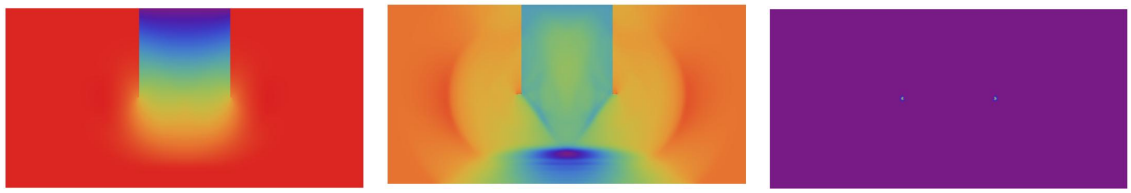

(a) $v_y = 16.5m/s, t = 24\mu s$ (b) $v_y = 16.5m/s, t = 24\mu s$ (c) $v_y = 16.5m/s, t = 24\mu s$

(d) $v_y = 16.5m/s, t = 54\mu s$ (e) $v_y = 16.5m/s, t = 54\mu s$ (f) $v_y = 16.5m/s, t = 54\mu s$

(g) $v_y = 16.5m/s, t = 90\mu s$ (h) $v_y = 16.5m/s, t = 90\mu s$ (i) $v_y = 16.5m/s, t = 90\mu s$

Figure 5.19: Displacement field (a,d,g), velocity field (b,e,h) and phase field (c,f,i) of dynamic shear Kalthoff experiment for time step $\Delta t = 0.04\mu$s at various time.

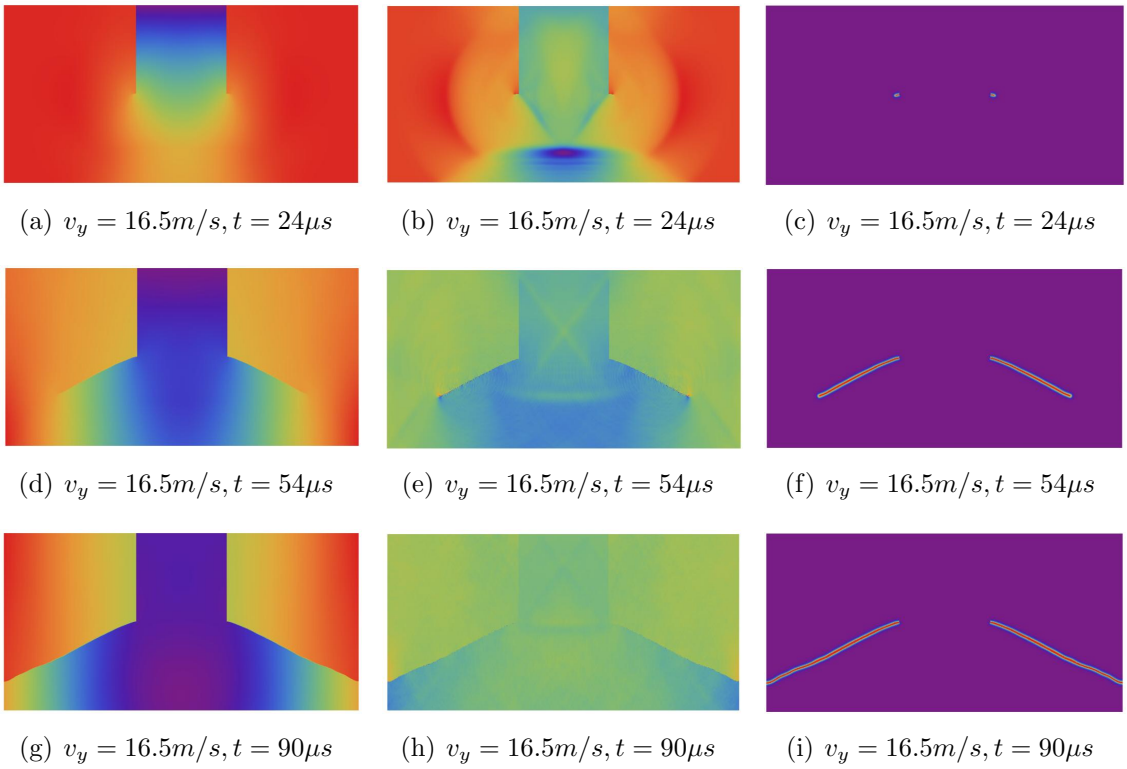

(a) $v_y = 16.5m/s, t = 24\mu s$ (b) $v_y = 16.5m/s, t = 24\mu s$ (c) $v_y = 16.5m/s, t = 24\mu s$

(d) $v_y = 16.5m/s, t = 54\mu s$ (e) $v_y = 16.5m/s, t = 54\mu s$ (f) $v_y = 16.5m/s, t = 54\mu s$

(g) $v_y = 16.5m/s, t = 90\mu s$ (h) $v_y = 16.5m/s, t = 90\mu s$ (i) $v_y = 16.5m/s, t = 90\mu s$

Figure 5.20: Displacement field (a,d,g), velocity field (b,e,h) and phase field (c,f,i) of dynamic shear Kalthoff experiment for time step $\Delta t = 0.02\mu$s at various time.

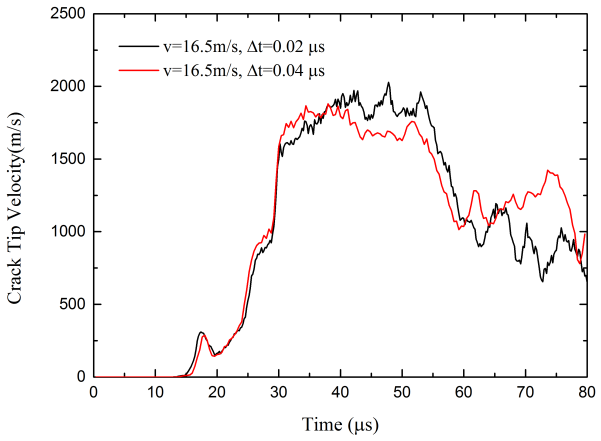

Figure 5.21: Crack tip velocity of the dynamic shear Kalthoff experiment for various time steps.

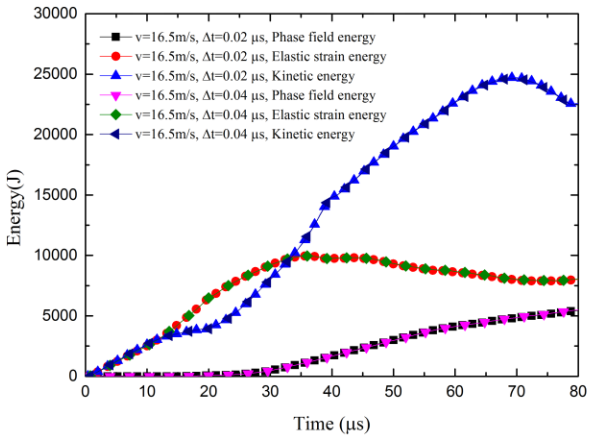

Figure 5.22: Energy of the Kalthoff experiment for various time steps.

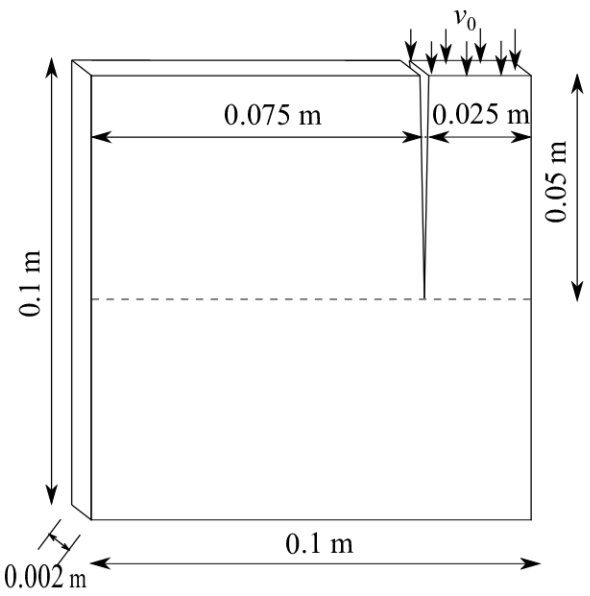

Figure 5.23: Geometry and boundary symmetry conditions of the Kalthoff-Winkler plate.

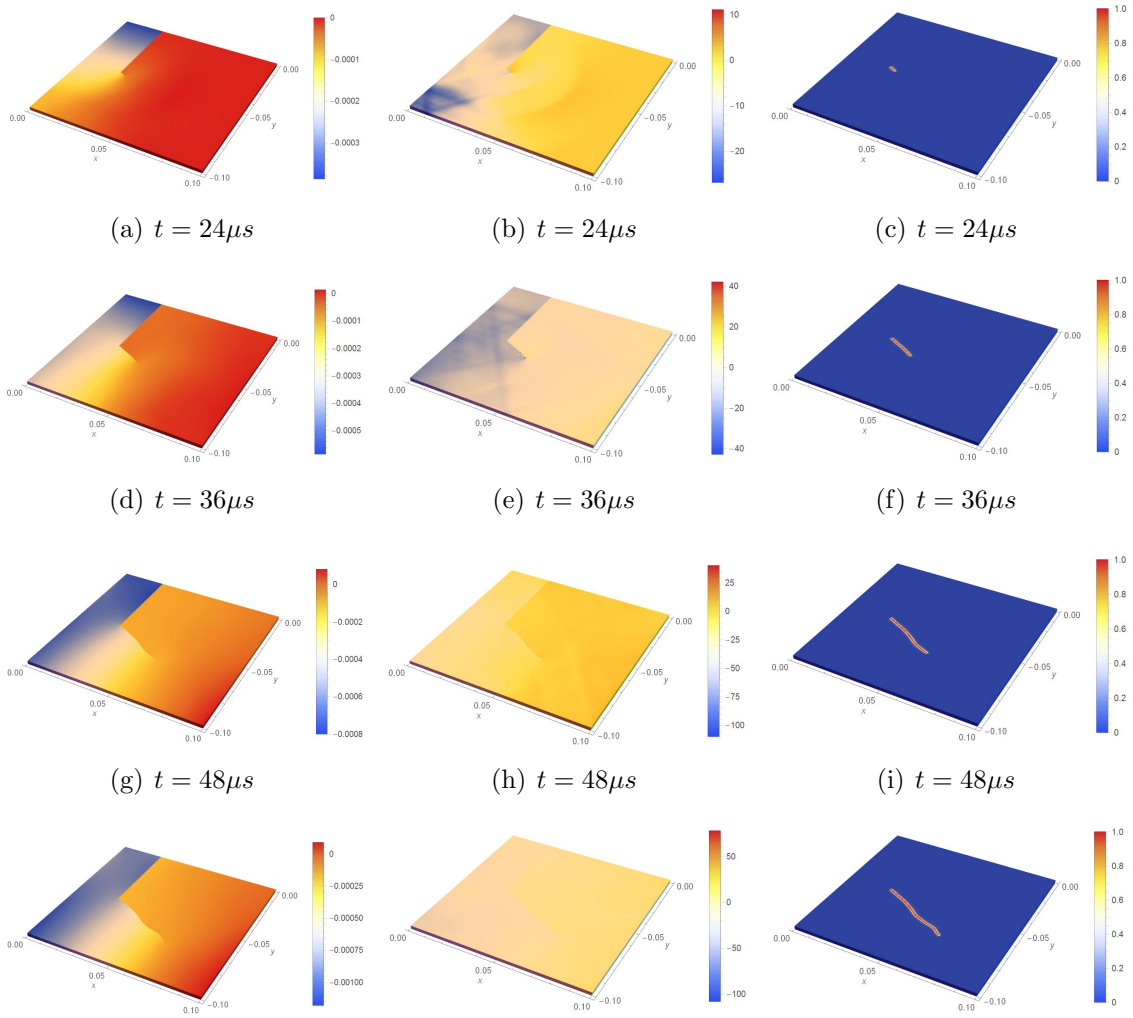

(a) $t = 24\mu s$ (b) $t = 24\mu s$ (c) $t = 24\mu s$

(d) $t = 36\mu s$ (e) $t = 36\mu s$ (f) $t = 36\mu s$

(g) $t = 48\mu s$ (h) $t = 48\mu s$ (i) $t = 48\mu s$

(j) $t = 60\mu s$ (k) $t = 60\mu s$ (l) $t = 60\mu s$

Figure 5.24: Displacement, velocity and phase field of the 3D Kalthoff experiment for $v = 16.5$ m/s at various time.

employs an explicit time integration algorithm for the mechanical field and an adaptive sub-step scheme is adopted. The phase field sub-step scheme based on different damage criteria can reduce the phase field residual adaptively and achieve a rate-independent phase field model. The advantage of the presented approach is its ease in implementation. Several numerical examples demonstrate the performance of the approach. They include a prenotched specimen under shear and tensile loading and two classical dynamic fracture benchmark problems. In the first case, we show the influence of several factors including the critical energy release rate on the final fracture pattern. The smaller the critical energy release rate, the more crack branches occur which agrees well with experimental data and also intuition as the critical energy release rate is inverse proportional to the crack speed, which in turn drives the crack branching.

Chapter 6

Discussion and conclusions

In this chapter, we present a discussion of the results and general conclusions of this dissertation. We also outline future research directions that continue the NOM that developed in this dissertation.

6.1 Discussion

In the second chapter, we presented the implementation procedure of first/higher-order implicit NOM. The performance of first/higher-order NOM results is demonstrated compared with the corresponding analytical solutions or the results of the FEM commercial software. Similar to the FEM and messless method, NOM can establish the operator energy functional and tangent stiffness matrix by some matrix multiplications. However, unlike FEM and the messless method, NOM can derive differential operators directly without employing shape functions. Hence, the complexity of the NOM is significantly reduced. The NOM requires only the definition of the energy, for a given energy functional, the nonlocal operators can be established automatically by the highest order of partial derivative and dimensions. Support, dual-support, nonlocal differential operators, and operator energy functional are the fundamental components of NOM. Several numerical examples illustrate the method's high performance and capabilities.

In the third chapter, we elaborated on the implementation progress of explicit NOM. Based on the dual property of the dual-support in NOM, the nonlocal dynamic governing equation is obtained with ease. We start from the energy form of the problem, by inserting the nonlocal expression of the gradient operator into the energy form. In the numerical simulation section, several numerical cases are presented to verify the accuracy of the nonlocal dynamic elasticity solid formulation in different conditions, and good agreement is observed between numerical simulation results and ABAQUS results.

In the fourth chapter, we proposed a nonlocal dynamic Kirchhoff plate formulation based on NOM. In the numerical simulation section, we first verify the accuracy of the nonlocal Hessian operator for the Kirchhoff plate and compare it to analytical solutions. Subsequently, the nonlocal dynamic Kirchhoff plate formulation with different types of boundary conditions (clamped and simply supported) is studied and compared to simulations obtained by ABAQUS. Good agreement is observed between numerical simulation results and ABAQUS results.

In the last chapter, we presented a quasi-static and dynamic fracture modeling within the framework of the NOM. The coupled system for the implicit phase field model is solved using a staggered method and the Newton Raphson method. The explicit phase field model employs an explicit time integration algorithm for the mechanical field and an adaptive sub-step scheme is adopted. The phase field sub-step scheme based on different damage criteria can reduce the phase field residual adaptively and achieve a rate-independent phase field model. The advantage of the presented approach is its ease in implementation as – in contrast to many other methods such as FEM – it does not require any shape functions. Several numerical examples demonstrate the performance of the approach. They include a pre-notched specimen under shear and tensile loading and two classical dynamic fracture benchmark problems, i.e., a crack branching problem and the Kalthoff-Winkler impact problem. In the first case, we show the influence of several factors including the critical energy release rate on the final fracture pattern. The smaller the critical energy release rate, the more crack branches occur which agrees well with experimental data and also intuition as the critical energy release rate is inverse proportional to the crack speed, which in turn drives the crack branching.

Nevertheless, there are still some limitations in nonlocal quasi-static and dynamic fracture modeling. For example, this modeling might not capture local behavior detailed enough, due to the nonlocal effects, it also makes a method computationally more expensive, and this modeling can't model fluid flow through the crack explicitly. These drawbacks will be fully studied and improved in future work.

6.2 Conclusions

The primary contribution of this dissertation was devoted to the implementation, development, and application of NOM. NOM is based on nonlocal theory and employs the nonlocal operators of integral form to replace the local partial differential operators of different orders. Thus nonlocal operator method applies a uniform model to the mechanical behaviors from continuity to non-continuity and microscopic to macroscopic. In this disseration, NOM can be classified as first-order NOM and higher-order NOM. The first-order NOM is based on common nonlocal operators such as gradient, curl, and

divergence. These nonlocal operators employ the first-order of TSE and can be used directly to solve many problems using the usual FEM. The operator energy function is also introduced to eliminate the zero-energy model. The first-order NOM is appropriate for C^0 continuity problems such as solid mechanics and phase-field fracture models. The higher-order NOM generalizes the first-order NOM by employing a higher-order TSE. Higher-order TSE can provide arbitrary order partial derivatives in any dimension. These higher-order derivatives are appropriate for higher-order partial derivative physical issues such as plate theory and strain gradient solid mechanics. Higher-order NOM considerably improves NOM's capacity to solve more complex issues.

6.3 Outlook

Although NOM has been used to solve various PDEs issues, the majority of the problems that have been addressed are limited to continuous problems. NOM is a generic numerical method with a robust theoretical foundation. NOM's implementation is somewhat similar to that of FEM. As a result, NOM has the ability to solve a wide range of engineering problems. Other potential NOM applications still remain, future NOM applications can be suggested as shown in Table 6.1.

Table 6.1: Outlook of NOM

Future NOM applications
• Material nonlinearities including plasticity, viscoelasticity and viscoplasticity.
• Multi-physics problems (coupled thermo-mechanical, electro-mechanical, electro-chemical problems to name a few) exploiting the ease in implementation.
• Plate and shell problems, especially higher-order theories or theories of thin plate/shell analysis exploiting the higher-order continuity of NOM. When NOM is applied to a curvilinear coordinate system, it is also viable to handle shell problems.
• Higher order gradient (elastoplasticity) problems exploiting the higher-order continuity of NOM
• Finite strain and/or large deformation problems exploiting the 'meshfree character' of NOM.
• The wave propagation analysis of gradient elasticity problems and studying – in this context – interesting phenomena like size, surface and nonlocal effects.
• Modeling of discontinuities as they occur in fracture/crack propagation in solids, fluid-structure interaction or fluid mechanics such as two-phase flow.
• Higher-order PDEs on stationary and evolving surface exploiting the higher-order continuity of NOM including its ease in implementation.

Bibliography

M. M. H. Al-Tholaia and H. J. Al-Gahtani. Rbf-based meshless method for large deflection of elastic thin plates on nonlinear foundations. *Engineering Analysis with Boundary Elements*, 51:146–155, 2015.

B. Alali, K. Liu, and M. Gunzburger. A generalized nonlocal vector calculus. *Zeitschrift für angewandte Mathematik und Physik*, 66(5):2807–2828, 2015.

N. Aluru. A point collocation method based on reproducing kernel approximations. *International Journal for Numerical Methods in Engineering*, 47(6):1083–1121, 2000.

J. Amani, E. Oterkus, P. Areias, G. Zi, T. Nguyen-Thoi, and T. Rabczuk. A non-ordinary state-based peridynamics formulation for thermoplastic fracture. *International Journal of Impact Engineering*, 87:83–94, 2016.

F. Amiri, D. Millán, Y. Shen, T. Rabczuk, and M. Arroyo. Phase-field modeling of fracture in linear thin shells. *Theoretical and Applied Fracture Mechanics*, 69:102–109, 2014.

T. L. Anderson. *Fracture mechanics: fundamentals and applications*. CRC press, 2017.

P. F. Antonietti, A. Cangiani, J. Collis, Z. Dong, E. H. Georgoulis, S. Giani, and P. Houston. Review of discontinuous galerkin finite element methods for partial differential equations on complicated domains. In *Building bridges: connections and challenges in modern approaches to numerical partial differential equations*, pages 281–310. Springer, 2016.

P. Areias and T. Rabczuk. Finite strain fracture of plates and shells with configurational forces and edge rotations. *International Journal for Numerical Methods in Engineering*, 94(12):1099–1122, 2013.

P. Areias and T. Rabczuk. Steiner-point free edge cutting of tetrahedral meshes with applications in fracture. *Finite Elements in Analysis and Design*, 132:27–41, 2017.

P. Areias, T. Rabczuk, and D. Dias-da Costa. Element-wise fracture algorithm based on rotation of edges. *Engineering Fracture Mechanics*, 110:113–137, 2013.

P. Areias, T. Rabczuk, and P. Camanho. Finite strain fracture of 2d problems with injected anisotropic softening elements. *Theoretical and Applied Fracture Mechanics*, 72:50–63, 2014.

P. Areias, M. Msekh, and T. Rabczuk. Damage and fracture algorithm using the screened poisson equation and local remeshing. *Engineering Fracture Mechanics*, 158:116–143, 2016a.

P. Areias, T. Rabczuk, and M. Msekh. Phase-field analysis of finite-strain plates and shells including element subdivision. *Computer Methods in Applied Mechanics and Engineering*, 312:322–350, 2016b.

P. Areias, J. Reinoso, P. Camanho, J. C. De Sá, and T. Rabczuk. Effective 2d and 3d crack propagation with local mesh refinement and the screened poisson equation. *Engineering Fracture Mechanics*, 189:339–360, 2018.

Y. Azdoud, F. Han, and G. Lubineau. A morphing framework to couple non-local and local anisotropic continua. *International Journal of Solids and Structures*, 50(9):1332–1341, 2013.

Y. Azdoud, F. Han, and G. Lubineau. The morphing method as a flexible tool for adaptive local/non-local simulation of static fracture. *Computational Mechanics*, 54(3):711–722, 2014.

I. Babuška and J. M. Melenk. The partition of unity method. *International journal for numerical methods in engineering*, 40(4):727–758, 1997.

I. Babuska, R. Tempone, and G. E. Zouraris. Galerkin finite element approximations of stochastic elliptic partial differential equations. *SIAM Journal on Numerical Analysis*, 42(2):800–825, 2004.

R. Ballarini, V. Diana, L. Biolzi, and S. Casolo. Bond-based peridynamic modelling of singular and nonsingular crack-tip fields. *Meccanica*, 53(14):3495–3515, 2018.

Z. P. Bažant and M. Jirásek. Nonlocal integral formulations of plasticity and damage: survey of progress. *Journal of Engineering Mechanics*, 128(11):1119–1149, 2002.

Z. P. Bažant, W. Luo, V. T. Chau, and M. A. Bessa. Wave dispersion and basic concepts of peridynamics compared to classical nonlocal damage models. *Journal of Applied Mechanics*, 83(11), 2016.

S. Bazazzadeh, A. Shojaei, M. Zaccariotto, and U. Galvanetto. Application of the peridynamic differential operator to the solution of sloshing problems in tanks. *Engineering Computations*, 2018.

T. Belytschko and J. I. Lin. A three-dimensional impact-penetration algorithm with erosion. *International Journal of Impact Engineering*, 5(1-4):111–127, 1987.

T. Belytschko, N. Moës, U. S, and P. C. Arbitrary discontinuities in finite elements. *International Journal for Numerical Methods in Engineering*, 50(4):993–1013, 2001.

T. Belytschko, H. Chen, J. Xu, and G. Zi. Dynamic crack propagation based on loss of hyperbolicity and a new discontinuous enrichment. *International Journal for Numerical Methods in Engineering*, 58(12):1873–1905, 2003.

D. Benson, Y. Bazilevs, M.-C. Hsu, and T. Hughes. Isogeometric shell analysis: the reissner–mindlin shell. *Computer Methods in Applied Mechanics and Engineering*, 199 (5-8):276–289, 2010.

K. Bertoldi, D. Bigoni, and W. Drugan. Structural interfaces in linear elasticity. part i: Nonlocality and gradient approximations. *Journal of the Mechanics and Physics of Solids*, 55(1):1–34, 2007.

T. Bode, C. Weißenfels, and P. Wriggers. Peridynamic petrov–galerkin method: a generalization of the peridynamic theory of correspondence materials. *Computer Methods in Applied Mechanics and Engineering*, 358:112636, 2020.

M. Borden, C. Verhoosel, M. Scott, T. Hughes, and C. Landis. A phase-field description of dynamic brittle fracture. *Computer Methods in Applied Mechanics and Engineering*, 217:77–95, 2012.

A. P. Boresi, K. Chong, and J. D. Lee. *Elasticity in engineering mechanics*. John Wiley & Sons, 2010.

G. Borino, B. Failla, and F. Parrinello. A symmetric nonlocal damage theory. *International Journal of Solids and Structures*, 40(13-14):3621–3645, 2003.

B. Bourdin. Numerical implementation of the variational formulation for quasi-static brittle fracture. *Interfaces and free boundaries*, 9(3):411–430, 2007.

B. Bourdin, G. A. Francfort, and J.-J. Marigo. Numerical experiments in revisited brittle fracture. *Journal of the Mechanics and Physics of Solids*, 48(4):797–826, 2000.

B. Bourdin, G. A. Francfort, and J.-J. Marigo. The variational approach to fracture. *Journal of elasticity*, 91(1-3):5–148, 2008.

M. Breitenfeld, P. Geubelle, O. Weckner, and S. Silling. Non-ordinary state-based peridynamic analysis of stationary crack problems. *Computer Methods in Applied Mechanics and Engineering*, 272:233–250, 2014.

S. N. Butt, J. J. Timothy, and G. Meschke. Wave dispersion and propagation in state-based peridynamics. *Computational Mechanics*, 60(5):725–738, 2017.

B. CA. The boundary element method for engineers, 1978.

L. A. Caffarelli and A. Vasseur. The de giorgi method for nonlocal fluid dynamics. In *Nonlinear partial differential equations*, pages 1–38. Springer, 2012.

W. Chan and H. Chen. Peridynamic bond-associated correspondence model: Wave dispersion property. *International Journal for Numerical Methods in Engineering*, 2021.

H. Chen and W. Chan. Higher-order peridynamic material correspondence models for elasticity. *Journal of Elasticity*, 142(1):135–161, 2020.

J. Chen, I. Chen, K. Chen, Y. Lee, and Y. Yeh. A meshless method for free vibration analysis of circular and rectangular clamped plates using radial basis function. *Engineering Analysis with Boundary Elements*, 28(5):535–545, 2004.

J.-S. Chen, W. K. Liu, M. C. Hillman, S.-W. Chi, Y. Lian, and M. A. Bessa. Reproducing kernel particle method for solving partial differential equations. *Encyclopedia of Computational Mechanics Second Edition*, pages 1–44, 2017.

S. R. Chowdhury, P. Roy, D. Roy, and J. Reddy. A peridynamic theory for linear elastic shells. *International Journal of Solids and Structures*, 84:110–132, 2016.

I. Cialenco, G. E. Fasshauer, and Q. Ye. Approximation of stochastic partial differential equations by a kernel-based collocation method. *International Journal of Computer Mathematics*, 89(18):2543–2561, 2012.

J. A. Cottrell, T. J. Hughes, and Y. Bazilevs. *Isogeometric analysis: toward integration of CAD and FEA*. John Wiley & Sons, 2009.

L. Dalcin, N. Collier, P. Vignal, A. Côrtes, and V. M. Calo. Petiga: A framework for high-performance isogeometric analysis. *Computer Methods in Applied Mechanics and Engineering*, 308:151–181, 2016.

C. De Falco, A. Reali, and R. Vázquez. Geopdes: a research tool for isogeometric analysis of pdes. *Advances in Engineering Software*, 42(12):1020–1034, 2011.

M. K. Deb, I. M. Babuška, and J. T. Oden. Solution of stochastic partial differential equations using galerkin finite element techniques. *Computer Methods in Applied Mechanics and Engineering*, 190(48):6359–6372, 2001.

M. Di Paola, G. Failla, and M. Zingales. Physically-based approach to the mechanics of strong non-local linear elasticity theory. *Journal of Elasticity*, 97(2):103–130, 2009.

M. Di Paola, G. Failla, and M. Zingales. The mechanically-based approach to 3d non-local linear elasticity theory: Long-range central interactions. *International Journal of Solids and Structures*, 47(18-19):2347–2358, 2010.

M. Dorduncu. Stress analysis of laminated composite beams using refined zigzag theory and peridynamic differential operator. *Composite Structures*, 218:193–203, 2019.

M. Dorduncu. Stress analysis of sandwich plates with functionally graded cores using peridynamic differential operator and refined zigzag theory. *Thin-Walled Structures*, 146:106468, 2020.

M. Dorduncu and M. K. Apalak. Elastic flexural analysis of adhesively bonded similar and dissimilar beams using refined zigzag theory and peridynamic differential operator. *International Journal of Adhesion and Adhesives*, 101:102631, 2020.

M. Dorduncu, K. Kaya, and O. F. Ergin. Peridynamic analysis of laminated composite plates based on first-order shear deformation theory. *International Journal of Applied Mechanics*, 12(03):2050031, 2020.

Q. Du, M. Gunzburger, R. B. Lehoucq, and K. Zhou. A nonlocal vector calculus, nonlocal volume-constrained problems, and nonlocal balance laws. *Mathematical Models and Methods in Applied Sciences*, 23(03):493–540, 2013.

C. A. Duarte and J. T. Oden. An hp adaptive method using clouds. *Computer methods in applied mechanics and engineering*, 139(1-4):237–262, 1996.

R. A. El-Nabulsi. Jerk in planetary systems and rotational dynamics, nonlocal motion relative to earth and nonlocal fluid dynamics in rotating earth frame. *Earth, Moon, and Planets*, 122(1):15–41, 2018.

E. Emmrich and O. Weckner. Analysis and numerical approximation of an integro-differential equation modeling non-local effects in linear elasticity. *Mathematics and mechanics of solids*, 12(4):363–384, 2007.

A. C. Eringen. Linear theory of nonlocal elasticity and dispersion of plane waves. *International Journal of Engineering Science*, 10(5):425–435, 1972a.

A. C. Eringen. On nonlocal fluid mechanics. *International Journal of Engineering Science*, 10(6):561–575, 1972b.

A. C. Eringen. Theory of nonlocal electromagnetic elastic solids. *Journal of Mathematical Physics*, 14(6):733–740, 1973.

A. C. Eringen. Theory of nonlocal elasticity and some applications. Technical report, Princeton Univ NJ Dept of Civil Engineering, 1984.

A. C. Eringen. Vistas of nonlocal continuum physics. *International journal of engineering science*, 30(10):1551–1565, 1992.

A. C. Eringen. *Nonlocal continuum field theories*. Springer Science & Business Media, 2002.

A. C. Eringen and J. Wegner. Nonlocal continuum field theories. *Appl. Mech. Rev.*, 56 (2):B20–B22, 2003.

S. A. Faghidian. Integro-differential nonlocal theory of elasticity. *International Journal of Engineering Science*, 129:96–110, 2018.

G. E. Fasshauer and Q. Ye. A kernel-based collocation method for elliptic partial differential equations with random coefficients. In *Monte Carlo and Quasi-Monte Carlo Methods 2012*, pages 331–347. Springer, 2013.

X. Feng, L. Hennings, and M. Neilan. Finite element methods for second order linear elliptic partial differential equations in non-divergence form. *Mathematics of Computation*, 86(307):2025–2051, 2017.

Y. Gao and S. Oterkus. Non-local modeling for fluid flow coupled with heat transfer by using peridynamic differential operator. *Engineering Analysis with Boundary Elements*, 105:104–121, 2019.

F. Garotta, N. Demo, M. Tezzele, M. Carraturo, A. Reali, and G. Rozza. Reduced order isogeometric analysis approach for pdes in parametrized domains. In *Quantification of Uncertainty: Improving Efficiency and Technology*, pages 153–170. Springer, 2020.

L. Gavete, F. Ureña, J. J. Benito, A. García, M. Ureña, and E. Salete. Solving second order non-linear elliptic partial differential equations using generalized finite difference method. *Journal of Computational and Applied Mathematics*, 318:378–387, 2017.

W. Gerstle, N. Sau, and S. Silling. Peridynamic modeling of concrete structures. *Nuclear engineering and design*, 237(12-13):1250–1258, 2007.

S. S. Ghorashi, N. Valizadeh, S. Mohammadi, and T. Rabczuk. T-spline based xiga for fracture analysis of orthotropic media. *Computers & Structures*, 147:138–146, 2015.

J. Grande and A. Reusken. A higher order finite element method for partial differential equations on surfaces. *SIAM Journal on Numerical Analysis*, 54(1):388–414, 2016.

F. Greco, L. Coox, F. Maurin, and W. Desmet. Nurbs-enhanced maximum-entropy schemes. *Computer Methods in Applied Mechanics and Engineering*, 317:580–597, 2017.

X. Gu, E. Madenci, and Q. Zhang. Revisit of non-ordinary state-based peridynamics. *Engineering fracture mechanics*, 190:31–52, 2018.

X. Gu, Q. Zhang, and E. Madenci. Refined bond-based peridynamics for thermal diffusion. *Engineering Computations*, 2019.

M. Gunzburger and R. B. Lehoucq. A nonlocal vector calculus with application to nonlocal boundary value problems. *Multiscale Modeling & Simulation*, 8(5):1581–1598, 2010.

E. Haghighat, A. C. Bekar, E. Madenci, and R. Juanes. A nonlocal physics-informed deep learning framework using the peridynamic differential operator. *Computer Methods in Applied Mechanics and Engineering*, 385:114012, 2021.

D. Han, Y. Zhang, Q. Wang, W. Lu, and B. Jia. The review of the bond-based peridynamics modeling. *Journal of Micromechanics and Molecular Physics*, 4(01):1830001, 2019.

N. A. Hashim, W. Coombs, C. Augarde, and G. Hattori. An implicit non-ordinary state-based peridynamics with stabilised correspondence material model for finite deformation analysis. *Computer Methods in Applied Mechanics and Engineering*, 371: 113304, 2020.

C. Hesch and K. Weinberg. Thermodynamically consistent algorithms for a finite-deformation phase-field approach to fracture. *International Journal for Numerical Methods in Engineering*, 99(12):906–924, 2014.

Hibbett, Karlsson, and Sorensen. *ABAQUS / standard: User's Manual*, volume 1. Hibbitt, Karlsson & Sorensen, 1998.

M. N. Hossain, D. Paladim, F. Vogel, and S. Bordas. Implementation of a xfem toolbox in diffpack. In *International Conference on Extended Finite Element Methods-XFEM 2013, September 11–13, 2013, Lyon, France*, 2013.

H.-Y. Hu, J.-S. Chen, and W. Hu. Error analysis of collocation method based on reproducing kernel approximation. *Numerical Methods for Partial Differential Equations*, 27(3):554–580, 2011.

T.-H. Huang, H. Wei, J.-S. Chen, and M. C. Hillman. Rkpm2d: an open-source implementation of nodally integrated reproducing kernel particle method for solving partial differential equations. *Computational particle mechanics*, 7(2):393–433, 2020.

T. J. Hughes, J. A. Cottrell, and Y. Bazilevs. Isogeometric analysis: Cad, finite elements, nurbs, exact geometry and mesh refinement. *Computer methods in applied mechanics and engineering*, 194(39-41):4135–4195, 2005.

M. M. Hussein Al-Tholaia and H. J. Al-Gahtani. Rbf-based meshless method for large deflection of elastic thin rectangular plates with boundary conditions involving free edges. *Mathematical Problems in Engineering*, 2016, 2016.

V. Ivannikov, C. Tiago, and P. Pimenta. Meshless implementation of the geometrically exact kirchhoff–love shell theory. *International Journal for Numerical Methods in Engineering*, 100(1):1–39, 2014.

Y. Jiang and J. Ma. High-order finite element methods for time-fractional partial differential equations. *Journal of Computational and Applied Mathematics*, 235(11):3285–3290, 2011.

M. Jirásek. Nonlocal damage mechanics. *Revue européenne de génie civil*, 11(7-8):993–1021, 2007.

G. R. Johnson and R. A. Stryk. Eroding interface and improved tetrahedral element algorithms for high-velocity impact computations in three dimensions. *International Journal of Impact Engineering*, 5(1-4):411–421, 1987.

J. Kalthoff and S. Winkler. Failure mode transition at high rates of shear loading. *DGM Informationsgesellschaft mbH, Impact Loading and Dynamic Behavior of Materials*, 1: 185–195, 1988.

J. F. Kalthoff. Modes of dynamic shear failure in solids. *International Journal of Fracture*, 101(1):1–31, 2000.

X. Kan, J. Yan, S. Li, and A. Zhang. On differences and comparisons of peridynamic differential operators and nonlocal differential operators. *Computational Mechanics*, pages 1–19, 2021.

A. Karma, D. Kessler, and H. Levine. Phase-field model of mode III dynamic fracture. *Physical Review Letters*, 87(4):045501, 2001.

J. Kiendl, K.-U. Bletzinger, J. Linhard, and R. Wüchner. Isogeometric shell analysis with kirchhoff–love elements. *Computer Methods in Applied Mechanics and Engineering*, 198 (49-52):3902–3914, 2009.

Y. Krongauz and T. Belytschko. A petrov-galerkin diffuse element method (pg dem) and its comparison to efg. *Computational Mechanics*, 19(4):327–333, 1997.

P. Krysl and T. Belytschko. Analysis of thin plates by the element-free galerkin method. *Computational Mechanics*, 17(1-2):26–35, 1995.

P. Krysl and T. Belytschko. Analysis of thin shells by the element-free galerkin method. *International Journal of Solids and Structures*, 33(20-22):3057–3080, 1996.

E. Larsson, V. Shcherbakov, and A. Heryudono. A least squares radial basis function partition of unity method for solving pdes. *SIAM Journal on Scientific Computing*, 39 (6):A2538–A2563, 2017.

S. Larsson and V. Thomée. *Partial differential equations with numerical methods*, volume 45. Springer, 2003.

H.-L. Lee and W.-J. Chang. Free transverse vibration of the fluid-conveying single-walled carbon nanotube using nonlocal elastic theory. *Journal of Applied Physics*, 103(2): 024302, 2008.

K. Li, D. Wu, and W. Gao. Spectral stochastic isogeometric analysis for linear stability analysis of plate. *Computer Methods in Applied Mechanics and Engineering*, 352:1–31, 2019.

S. Li, W. Liu, A. Rosakis, T. Belytschko, and W. Hao. Mesh-free galerkin simulations of dynamic shear band propagation and failure mode transition. *International Journal of solids and structures*, 39(5):1213–1240, 2002.

P. Lindsay, M. Parks, and A. Prakash. Enabling fast, stable and accurate peridynamic computations using multi-time-step integration. *Computer Methods in Applied Mechanics and Engineering*, 306:382–405, 2016.

T. Liszka. An interpolation method for an irregular net of nodes. *International Journal for Numerical Methods in Engineering*, 20(9):1599–1612, 1984.

G. Liu, Q. Li, M. Msekh, and Z. Zheng. Abaqus implementation of monolithic and staggered schemes for quasi-static and dynamic fracture phase-field model. *Computational Materials Science*, 121:35–47, 2016.

G.-R. Liu and M. B. Liu. *Smoothed particle hydrodynamics: a meshfree particle method*. World scientific, 2003.

M. Liu and G.-R. Liu. Restoring particle consistency in smoothed particle hydrodynamics. *Applied numerical mathematics*, 56(1):19–36, 2006.

W. K. Liu, S. Jun, and Y. F. Zhang. Reproducing kernel particle methods. *International journal for numerical methods in fluids*, 20(8-9):1081–1106, 1995.

E. Lorentz. A nonlocal damage model for plain concrete consistent with cohesive fracture. *International Journal of Fracture*, 207(2):123–159, 2017.

G. Lubineau, Y. Azdoud, F. Han, C. Rey, and A. Askari. A morphing strategy to couple non-local to local continuum mechanics. *Journal of the Mechanics and Physics of Solids*, 60(6):1088–1102, 2012.

L. B. Lucy. A numerical approach to the testing of the fission hypothesis. *The astronomical journal*, 82:1013–1024, 1977.

R. W. Macek and S. A. Silling. Peridynamics via finite element analysis. *Finite elements in analysis and design*, 43(15):1169–1178, 2007.

E. Madenci, A. Barut, and M. Futch. Peridynamic differential operator and its applications. *Computer Methods in Applied Mechanics and Engineering*, 304:408–451, 2016.

E. Madenci, M. Dorduncu, A. Barut, and M. Futch. Numerical solution of linear and nonlinear partial differential equations using the peridynamic differential operator. *Numerical Methods for Partial Differential Equations*, 33(5):1726–1753, 2017.

E. Madenci, M. Dorduncu, and X. Gu. Peridynamic least squares minimization. *Computer Methods in Applied Mechanics and Engineering*, 348:846–874, 2019a.

E. Madenci, M. Dorduncu, N. Phan, and X. Gu. Weak form of bond-associated non-ordinary state-based peridynamics free of zero energy modes with uniform or non-uniform discretization. *Engineering Fracture Mechanics*, 218:106613, 2019b.

A. Mahdavi, S.-W. Chi, and H. Zhu. A gradient reproducing kernel collocation method for high order differential equations. *Computational Mechanics*, 64(5):1421–1454, 2019.

A. Mahdavi, S.-W. Chi, and N. Kamali. Harmonic-enriched reproducing kernel approximation for highly oscillatory differential equations. *Journal of Engineering Mechanics*, 146(4):04020014, 2020.

S. Mauthe and C. Miehe. Hydraulic fracture in poro-hydro-elastic media. *Mechanics Research Communications*, 80:69–83, 2017.

J. Mehrmashhadi, M. Bahadori, and F. Bobaru. On validating peridynamic models and a phase-field model for dynamic brittle fracture in glass. *Engineering Fracture Mechanics*, 240:107355, 2020.

C. Miehe, M. Hofacker, and F. Welschinger. A phase field model for rate-independent crack propagation: Robust algorithmic implementation based on operator splits. *Computer Methods in Applied Mechanics and Engineering*, 199(45-48):2765–2778, 2010a.

C. Miehe, F. Welschinger, and M. Hofacker. Thermodynamically consistent phase-field models of fracture: Variational principles and multi-field fe implementations. *International Journal for Numerical Methods in Engineering*, 83(10):1273–1311, 2010b.

C. Miehe, L.-M. Schänzel, and H. Ulmer. Phase field modeling of fracture in multi-physics problems. Part I. Balance of crack surface and failure criteria for brittle crack propagation in thermo-elastic solids. *Computer Methods in Applied Mechanics and Engineering*, 294:449–485, 2015.

S. Mikki. Theory of electromagnetic radiation in nonlocal metamaterials—part i: Foundations. *Progress In Electromagnetics Research B*, 89:63–86, 2020a.

S. Mikki. Theory of electromagnetic radiation in nonlocal metamaterials—part ii: Applications. *Progress In Electromagnetics Research B*, 89:87–109, 2020b.

N. Moës, J. Dolbow, and T. Belytschko. A finite element method for crack growth without remeshing. *International journal for numerical methods in engineering*, 46(1):131–150, 1999.

M. Mohammadi and R. Mokhtari. A reproducing kernel method for solving a class of nonlinear systems of pdes. *Mathematical Modelling and Analysis*, 19(2):180–198, 2014.

M. Mohammadi, F. S. Zafarghandi, E. Babolian, and S. Jvadi. A local reproducing kernel method accompanied by some different edge improvement techniques: application to the burgers' equation. *Iranian Journal of Science and Technology, Transactions A: Science*, 42(2):857–871, 2018.

V. Mutnuri and S. Gopalakrishnan. A re-examination of wave dispersion and on equivalent spatial gradient of the integral in bond-based peridynamics. *Journal of Peridynamics and Nonlocal Modeling*, 2(3):243–277, 2020.

B. Nayroles, G. Touzot, and P. Villon. Generalizing the finite element method: diffuse approximation and diffuse elements. *Computational mechanics*, 10(5):307–318, 1992.

V. P. Nguyen and J.-Y. Wu. Modeling dynamic fracture of solids with a phase-field regularized cohesive zone model. *Computer Methods in Applied Mechanics and Engineering*, 340:1000–1022, 2018.

N. Nguyen-Thanh, N. Valizadeh, M. Nguyen, H. Nguyen-Xuan, X. Zhuang, P. Areias, G. Zi, Y. Bazilevs, L. De Lorenzis, and T. Rabczuk. An extended isogeometric thin shell analysis based on kirchhoff–love theory. *Computer Methods in Applied Mechanics and Engineering*, 284:265–291, 2015.

N. Nguyen-Thanh, K. Zhou, X. Zhuang, P. Areias, H. Nguyen-Xuan, Y. Bazilevs, and T. Rabczuk. Isogeometric analysis of large-deformation thin shells using rht-splines for multiple-patch coupling. *Computer Methods in Applied Mechanics and Engineering*, 316:1157–1178, 2017.

H. Noguchi, T. Kawashima, and T. Miyamura. Element free analyses of shell and spatial structures. *International Journal for Numerical Methods in Engineering*, 47(6):1215–1240, 2000.

J. O'Grady and J. Foster. Peridynamic plates and flat shells: A non-ordinary, state-based model. *International Journal of Solids and Structures*, 51(25-26):4572–4579, 2014.

M. Ortiz and A. Pandolfi. Finite-deformation irreversible cohesive elements for three-dimensional crack-propagation analysis. *International journal for numerical methods in engineering*, 44(9):1267–1282, 1999.

E. Oterkus, E. Madenci, O. Weckner, S. Silling, P. Bogert, and A. Tessler. Combined finite element and peridynamic analyses for predicting failure in a stiffened composite curved panel with a central slot. *Composite Structures*, 94(3):839–850, 2012.

T. H. Pian and D. Chen. On the suppression of zero energy deformation modes. *International Journal for Numerical Methods in Engineering*, 19(12):1741–1752, 1983.

G. Pijaudier-Cabot and Z. P. Bažant. Nonlocal damage theory. *Journal of engineering mechanics*, 113(10):1512–1533, 1987.

G. Pijaudier-Cabot, K. Haidar, and J.-F. Dubé. Non-local damage model with evolving internal length. *International journal for numerical and analytical methods in geomechanics*, 28(7-8):633–652, 2004.

Y. Z. Povstenko. The nonlocal theory of elasticity and its applications to the description of defects in solid bodies. *Journal of Mathematical Sciences*, 97(1):3840–3845, 1999.

T. Rabczuk and T. Belytschko. Cracking particles: a simplified meshfree method for arbitrary evolving cracks. *International Journal for Numerical Methods in Engineering*, 61(13):2316–2343, 2004.

T. Rabczuk and T. Belytschko. A three-dimensional large deformation meshfree method for arbitrary evolving cracks. *Computer methods in applied mechanics and engineering*, 196(29-30):2777–2799, 2007.

T. Rabczuk and H. Ren. A peridynamics formulation for quasi-static fracture and contact in rock. *Engineering Geology*, 225:42–48, 2017.

T. Rabczuk, P. Areias, and T. Belytschko. A simplified mesh-free method for shear bands with cohesive surfaces. *International Journal for Numerical Methods in Engineering*, 69(5):993–1021, 2007a.

T. Rabczuk, P. Areias, and T. Belytschko. A meshfree thin shell method for non-linear dynamic fracture. *International journal for numerical methods in engineering*, 72(5): 524–548, 2007b.

T. Rabczuk, G. Zi, S. Bordas, and H. Nguyen-Xuan. A simple and robust three-dimensional cracking-particle method without enrichment. *Computer Methods in Applied Mechanics and Engineering*, 199(37-40):2437–2455, 2010.

T. Rabczuk, H. Ren, and X. Zhuang. A nonlocal operator method for partial differential equations with application to electromagnetic waveguide problem. *Computers, Materials & Continua 59 (2019), Nr. 1*, 2019.

H. Rafii-Tabar, E. Ghavanloo, and S. A. Fazelzadeh. Nonlocal continuum-based modeling of mechanical characteristics of nanoscopic structures. *Physics Reports*, 638:1–97, 2016.

H. Ren, X. Zhuang, Y. Cai, and T. Rabczuk. Dual-horizon peridynamics. *International Journal for Numerical Methods in Engineering*, 108(12):1451–1476, 2016.

H. Ren, X. Zhuang, and T. Rabczuk. Dual-horizon peridynamics: A stable solution to varying horizons. *Computer Methods in Applied Mechanics and Engineering*, 318: 762–782, 2017.

H. Ren, X. Zhuang, and T. Rabczuk. A higher order nonlocal operator method for solving partial differential equations. *Computer Methods in Applied Mechanics and Engineering*, 367:113132, 2020a.

H. Ren, X. Zhuang, and T. Rabczuk. A nonlocal operator method for solving partial differential equations. *Computer Methods in Applied Mechanics and Engineering*, 358: 112621, 2020b.

H. Ren, X. Zhuang, and T. Rabczuk. Nonlocal operator method with numerical integration for gradient solid. *Computers & Structures*, 233:106235, 2020c.

A. Riffnaller-Schiefer, U. H. Augsdörfer, and D. W. Fellner. Isogeometric shell analysis with nurbs compatible subdivision surfaces. *Applied Mathematics and Computation*, 272:139–147, 2016.

D. Rogula. Introduction to nonlocal theory of material media. In *Nonlocal theory of material media*, pages 123–222. Springer, 1982.

C. Roque and P. Martins. Differential evolution optimization for the analysis of composite plates with radial basis collocation meshless method. *Composite Structures*, 124:317–326, 2015.

C. Roque, J. Madeira, and A. Ferreira. Multiobjective optimization for node adaptation in the analysis of composite plates using a meshless collocation method. *Engineering Analysis with Boundary Elements*, 50:109–116, 2015.

P. Roy, S. Deepu, A. Pathrikar, D. Roy, and J. Reddy. Phase field based peridynamics damage model for delamination of composite structures. *Composite Structures*, 180: 972–993, 2017.

P. Roy, A. Pathrikar, and D. Roy. Phase field–based peridynamics damage model: Applications to delamination of composite structures and inelastic response of ceramics. In *Peridynamic Modeling, Numerical Techniques, and Applications*, pages 327–354. Elsevier, 2021.

A. Safdari-Vaighani, A. Heryudono, and E. Larsson. A radial basis function partition of unity collocation method for convection–diffusion equations arising in financial applications. *Journal of Scientific Computing*, 64(2):341–367, 2015.

M. Samal, M. Seidenfuss, E. Roos, B. Dutta, and H. Kushwaha. Finite element formulation of a new nonlocal damage model. *Finite Elements in Analysis and Design*, 44 (6-7):358–371, 2008.

C. Samaniego, J. Ulloa, P. Rodríguez, G. Houzeaux, M. Vázquez, and E. Samaniego. A phase-field model for ductile fracture with shear bands: A parallel implementation. *International Journal of Mechanical Sciences*, 200:106424, 2021.

E. Samaniego, C. Anitescu, S. Goswami, V. M. Nguyen-Thanh, H. Guo, K. Hamdia, X. Zhuang, and T. Rabczuk. An energy approach to the solution of partial differential equations in computational mechanics via machine learning: Concepts, implementation and applications. *Computer Methods in Applied Mechanics and Engineering*, 362: 112790, 2020.

A. Schlüter, A. Willenbücher, C. Kuhn, and R. Müller. Phase field approximation of dynamic brittle fracture. *Computational Mechanics*, 54(5):1141–1161, 2014.

E. Sharon and J. Fineberg. Confirming the continuum theory of dynamic brittle fracture for fast cracks. *Nature*, 397(6717):333–335, 1999.

F. Shen, Q. Zhang, D. Huang, and J.-j. Zhao. Damage and failure process of concrete structure under uni-axial tension based on peridynamics modeling. *Chinese Journal of Computational Mechanics*, 30:79–83, 2013.

S. A. Silling. Reformulation of elasticity theory for discontinuities and long-range forces. *Journal of the Mechanics and Physics of Solids*, 48(1):175–209, 2000.

S. A. Silling. Linearized theory of peridynamic states. *Journal of Elasticity*, 99(1):85–111, 2010.

S. A. Silling and E. Askari. A meshfree method based on the peridynamic model of solid mechanics. *Computers & structures*, 83(17-18):1526–1535, 2005.

S. A. Silling and F. Bobaru. Peridynamic modeling of membranes and fibers. *International Journal of Non-Linear Mechanics*, 40(2-3):395–409, 2005.

S. A. Silling and R. B. Lehoucq. Convergence of peridynamics to classical elasticity theory. *Journal of Elasticity*, 93(1):13, 2008.

S. A. Silling and R. B. Lehoucq. Peridynamic theory of solid mechanics. In *Advances in applied mechanics*, volume 44, pages 73–168. Elsevier, 2010.

S. A. Silling, M. Epton, O. Weckner, J. Xu, and E. Askari. Peridynamic states and constitutive modeling. *Journal of Elasticity*, 88(2):151–184, 2007.

S. A. Silling, O. Weckner, E. Askari, and F. Bobaru. Crack nucleation in a peridynamic solid. *International Journal of Fracture*, 162(1):219–227, 2010.

J. H. Song, P. M. Areias, and T. Belytschko. A method for dynamic crack and shear band propagation with phantom nodes. *International Journal for Numerical Methods in Engineering*, 67(6):868–893, 2006.

A. Tagliabue, L. Dede, and A. Quarteroni. Isogeometric analysis and error estimates for high order partial differential equations in fluid dynamics. *Computers & Fluids*, 102: 277–303, 2014.

C. H. Thai, H. Nguyen-Xuan, S. P. A. Bordas, N. Nguyen-Thanh, and T. Rabczuk. Isogeometric analysis of laminated composite plates using the higher-order shear deformation theory. *Mechanics of Advanced Materials and Structures*, 22(6):451–469, 2015.

S. Timoshenko and J. Goodier. *Theory of elasticity (3rd edn).*, volume 412. McGraw-Hill: New York, 1970.

S. P. Timoshenko and S. Woinowsky-Krieger. *Theory of plates and shells*. McGraw-hill, 1959.

F. Ureña, L. Gavete, A. García, J. J. Benito, and A. M. Vargas. Solving second order non-linear hyperbolic pdes using generalized finite difference method (gfdm). *Journal of Computational and Applied Mathematics*, 363:1–21, 2020.

T. Van Mechelen and Z. Jacob. Nonlocal topological electromagnetic phases of matter. *Physical Review B*, 99(20):205146, 2019.

L. Verlet. Computer" experiments" on classical fluids. i. thermodynamical properties of lennard-jones molecules. *Physical review*, 159(1):98, 1967.

R. Vignjevic, J. Campbell, and L. Libersky. A treatment of zero-energy modes in the smoothed particle hydrodynamics method. *Computer methods in Applied mechanics and Engineering*, 184(1):67–85, 2000.

L. Wang, J. Xu, and J. Wang. Elastodynamics of linearized isotropic state-based peridynamic media. *Journal of Elasticity*, 137(2):157–176, 2019a.

Y. Wang, X. Zhou, and X. Xu. Numerical simulation of propagation and coalescence of flaws in rock materials under compressive loads using the extended non-ordinary state-based peridynamics. *Engineering Fracture Mechanics*, 163:248–273, 2016.

Y. Wang, X. Zhou, and M. Kou. An improved coupled thermo-mechanic bond-based peridynamic model for cracking behaviors in brittle solids subjected to thermal shocks. *European Journal of Mechanics-A/Solids*, 73:282–305, 2019b.

O. Weckner, G. Brunk, M. A. Epton, S. A. Silling, and E. Askari. Green's functions in non-local three-dimensional linear elasticity. *Proceedings of the Royal Society A: Mathematical, Physical and Engineering Sciences*, 465(2111):3463–3487, 2009.

R. A. Wildman and G. A. Gazonas. A finite difference-augmented peridynamics method for reducing wave dispersion. *International Journal of Fracture*, 190(1):39–52, 2014.

S. Wolfram. The mathematica book. *Assembly Automation*, 1999.

X. Xu and A. Needleman. Numerical simulations of fast crack growth in brittle solids. *Journal of the Mechanics and Physics of Solids*, 42(9):1397–1434, 1994.

A. Yaghoobi and M. G. Chorzepa. Higher-order approximation to suppress the zero-energy mode in non-ordinary state-based peridynamics. *Computers & Structures*, 188: 63–79, 2017.

A. Yaghoobi and M. G. Chorzepa. Formulation of symmetry boundary modeling in non-ordinary state-based peridynamics and coupling with finite element analysis. *Mathematics and Mechanics of Solids*, 23(8):1156–1176, 2018.

J. P. Yang and Y. C. Chen. Gradient enhanced localized radial basis collocation method for inverse analysis of cauchy problems. *International Journal of Applied Mechanics*, 12(9):2050106, 2020.

J. P. Yang and W.-C. Hsin. Weighted reproducing kernel collocation method based on error analysis for solving inverse elasticity problems. *Acta Mechanica*, 230(10):3477–3497, 2019.

J. P. Yang and Q. Lin. Investigation of multiply connected inverse cauchy problems by efficient weighted collocation method. *International Journal of Applied Mechanics*, 12 (01):2050012, 2020.

J. P. Yang, P.-C. Guan, and C.-M. Fan. Solving inverse laplace equation with singularity by weighted reproducing kernel collocation method. *International Journal of Applied Mechanics*, 9(05):1750065, 2017.

Z. Yang, E. Oterkus, and S. Oterkus. Peridynamic higher-order beam formulation. *Journal of Peridynamics and Nonlocal Modeling*, 3(1):67–83, 2021.

H. Y. Y. Yin and W. Hai. Damage analysis method for laminates based on peridynamic theory. *Chinese Journal of Theoretical and Applied Mechanics*, 4, 2013.

H. Yu, X. Chen, and Y. Sun. A generalized bond-based peridynamic model for quasi-brittle materials enriched with bond tension–rotation–shear coupling effects. *Computer Methods in Applied Mechanics and Engineering*, 372:113405, 2020.

Q. Zhang, S. Li, A.-M. Zhang, Y. Peng, and J. Yan. A peridynamic reissner-mindlin shell theory. *International Journal for Numerical Methods in Engineering*, 122(1):122–147, 2021.

X. Zhang, X.-H. Liu, K.-Z. Song, and M.-W. Lu. Least-squares collocation meshless method. *International Journal for Numerical Methods in Engineering*, 51(9):1089–1100, 2001.

F. Zhou and J.-F. Molinari. Dynamic crack propagation with cohesive elements: a methodology to address mesh dependency. *International Journal for Numerical Methods in Engineering*, 59(1):1–24, 2004.

X.-P. Zhou and Y.-T. Wang. Numerical simulation of crack propagation and coalescence in pre-cracked rock-like brazilian disks using the non-ordinary state-based peridynamics. *International Journal of Rock Mechanics and Mining Sciences*, 89:235–249, 2016.

X. Zhuang and C. Augarde. Aspects of the use of orthogonal basis functions in the element-free galerkin method. *International Journal for Numerical Methods in Engineering*, 81(3):366–380, 2010.

O. C. Zienkiewicz, R. L. Taylor, P. Nithiarasu, and J. Zhu. *The finite element method*, volume 3. McGraw-hill London, 1977.

Appendix A

Mathematica code for higher-order nonlocal operator method

```
FuncRK[uvw_List, uvw0_List] := Block[{El = uvw[[1, 1]], nu = uvw[[2, 1]], u01 = uvw[[3, 2]], u10 = uvw[[3, 3]],
  v01 = uvw[[4, 2]], v10 = uvw[[4, 3]], $67, $92, $93, $97, $98, $99, $101, $102, $100, $103, $133, $105,
  $124, $127, $128, $162, $180, $173, $174, $175, $176, $177, $178, $179, $192, $202, $203, $204, $205,
  $221, $181, $182, $183, $184, $185, $206, $207, $208, $209, $210, $211, $186, $187, $188, $189, $190,
  $212, $213, $214, $215, $216, $217, $223, $222, $218, $219, $220}, $67 = nu^2; $92 = -$67; $93 = 1 + $92;
 $97 = 1/$93; $98 = -nu; $99 = 1 + $98; $101 = u10 + v01; $102 = nu $101; $100 = $99 u10; $103 = $100 + $102;
 $133 = 1/$93^2; $105 = $99 v01; $124 = $105 + $102; $127 = u01 + v10; $128 = $127^2; $162 = 1/2 El $99 $97 $127;
 $180 = ($99 $97 $127)/2; $173 = 2 $97 u10 v01; $174 = 2 nu $133 u10 $103; $175 = 2 nu $133 v01 $124;
 $176 = $99 nu $133 $128; $177 = -1/2 ($97 $128); $178 = $173 + $174 + $175 + $176 + $177;
 $179 = $178/2; $192 = 1/$93^3; $202 = 2 El $99 nu $133 $127; $203 = -(El $97 $127);
 $204 = $202 + $203; $205 = $204/2; $221 = (El $99 $97)/2; $181 = $97 u10; $182 = nu $97 v01;
 $183 = $97 $103; $184 = $181 + $182 + $183; $185 = $184/2; $206 = 2 El nu $133 u10; $207 = 2 El $67 $133 v01;
 $208 = 2 El $97 v01; $209 = 2 El nu $133 $103; $210 = $206 + $207 + $208 + $209; $211 = $210/2;
 $186 = nu $97 u10; $187 = $97 v01; $188 = $97 $124; $189 = $186 + $187 + $188; $190 = $189/2;
 $212 = 2 El $67 $133 u10; $213 = 2 El $97 u10; $214 = 2 El nu $133 v01; $215 = 2 El nu $133 $124;
 $216 = $212 + $213 + $214 + $215; $217 = $216/2; $223 = El nu $97; $222 = El $97; $218 = El $99 nu $133 $127;
 $219 = -1/2 (El $97 $127); $220 = $218 + $219;
 {{1/2 ($97 u10 $103 + $97 v01 $124 + ($99 $97 $128)/2), 1/2 (2 El $97 u10 v01 + 2 El nu $133 u10 $103 + 2 El nu $133 v01 $124 + El $99 nu $133 $128 - (El $97 $128)/2),
   $162, 1/2 (El $97 u10 + El nu $97 v01 + El $97 $103), 1/2 (El nu $97 u10 + El $97 v01 + El $97 $124), $162},
  {{0, $179, $180, $185, $190, $180},
   {$179, 1/2 (8 El nu $133 u10 v01 + 8 El $67 $192 u10 $103 + 2 El $133 u10 $103 + 8 El $67 $192 v01 $124 + 2 El $133 v01 $124 + 4 El $99 $67 $192 $128 +
       El $99 $133 $128 - 2 El nu $133 $128), $205, $211, $217, $205}, {$180, $220, $221, 0, 0, $221}, {$185, $211, 0, $222, $223, 0},
   {$190, $217, 0, $223, $222, 0}, {$180, $220, $221, 0, 0, $221}}}]
```

```
MultiIndex[d_, sum_] := Module[{a, b, c}, a = Subsets[Range[d + sum], {d}];
   Do[c = a[[i]];
    b = c - 1;
    b[[2 ;;]] -= c[[1 ;; -2]];
    a[[i]] = b, {i, Length[a]}]; a];
GFD0CoeffHalf[ndim_Integer, diffMax_Integer] := Module[{a, ai, iDf, iDffact, iDfsum, Py, xy, len, io},
   If[ndim < 1, Print["Error, ndim should be positive!"]; Return[]];
   xy = {x, y, z, l, m, n, o, p, q}[[1 ;; ndim]];
   a = MultiIndex[ndim, diffMax][[2 ;;]]; len = Length[a];
   iDf = ConstantArray[0, len];
   iDfsum = ConstantArray[0, len];
   iDffact = ConstantArray[0, len];
   Py = ConstantArray[0, len];
   Do[ai = a[[i]];
    iDf[[i]] = FromDigits[ai];
    iDfsum[[i]] = Total[ai];
    iDffact[[i]] = Times @@ Factorial[ai];
    Py[[i]] = Times @@ (xy^ai), {i, len}];
   io = Ordering[iDfsum];
   {iDf[[io]], iDffact[[io]], iDfsum[[io]], Py[[io]]}];

NOMPwKhg[np0_, coord_List, vol_, Nei_List, pfun_, WeiF_, hgPen_] :=
  Module[{tl, ndof, Nnode, ndim, udim, kk, np}, If[np0 < 0, np = Ceiling[Length[coord] / 1000], np = np0];
   tl = Ngroup[Length[coord], np];
   kk = ParallelTable[NOMPwKhgPart[tl[[i]], coord, vol, Nei, pfun, WeiF, hgPen], {i, np}];
   {Flatten[kk[[All, 1]], 1], Flatten[kk[[All, 2]], 1]}];
NOMPwKhgPart[nodeList_, coord_List, vol_, Nei_List, pfun_, WeiF_, hgPen_] :=
  Module[{pvol, Nnode, pwList, hgList, kp = 1, coordi, pw, khg, NeiI, hg, hi, voli = 0},
   Nnode = Length[coord];
   pwList = EmptyList[Length[nodeList]];
   hgList = EmptyList[Length[nodeList]];
   If[Length[vol] == 0, pvol = ConstantArray[vol, Nnode];];
   If[Length[vol] == Nnode, pvol = vol];
   Do[
    NeiI = Nei[[i]];
    coordi = ListMinus[coord[[NeiI]], coord[[i]]];
    voli = pvol[[NeiI]];
    hi = Norm[coordi[[-1]]];
    {pw, khg} = Khgs[coordi, pfun, WeiF, voli, hgPen, hi];
    pw = PhuToPu[pw, iDfsum, iDffact, hi];
    pwList[[kp]] = pw;
    hgList[[kp++]] = khg;
    , {i, nodeList}
   ];
   {pwList, hgList}];
```

```
Ngroup[nmax_, ngroup_] := Module[{tl = {}, i1, i2, inc}, inc = Round[nmax / ngroup];
   Do[AppendTo[tl, Range[inc (i - 1) + 1, inc i]], {i, 1, ngroup - 1}];
   AppendTo[tl, Range[inc (ngroup - 1) + 1, nmax]]; tl];
EmptyList[n_Integer] := Block[{el = {}}, Do[AppendTo[el, {}], {i, n}]; el];
ListMinus[v1_List, v0_List] := Module[{v2 = v1}, Do[v2[[i]] -= v0, {i, Length[v1]}]; v2];
PhuToPu[pw_List, iDfsum_List, iDffact_List, h_] := Module[{p = {}, i},
   p = pw;
   Do[p[[i]] *= 1. / (h^iDfsum[[i]] / iDffact[[i]]), {i, Length[pw]}]; p];
Khgs[v1_List, pfun_, wfun_, vol_List, penalty_, h_] := Module[{
    len = Length[pfun[v1[[1]], 1]],
    num = Length[v1], k, p, trH = 0, r1, p1, w1, pkp = {}, pw0, wl},
   pkp = ConstantArray[0, {num, num}];
   k = ConstantArray[0, {len, len}];
   p = ConstantArray[0, {num, len}];
   wl = Norm /@ v1;
   Do[wl[[i]] = wfun[wl[[i]], h] vol[[i]], {i, num}];
   wl *= 1.0 / Total[wl];
   Do[r1 = Norm[v1[[i]]]; w1 = wl[[i]];
    trH += w1 r1 r1;
    pkp[[i, i]] = w1;
    p1 = pfun[v1[[i]], h]; p[[i]] = w1 p1;
    k += w1 TensorProduct[p1, p1], {i, num}];
   pw0 = Inverse[k].p^T;
   pkp -= p.pw0;
   pkp *= penalty / trH;
   {pw0, pkp}];
NOMRK[np_, nodes_List, volSet_List, nonvars_List, coord_List, uvw_List, PW_List,
   KHG_List, Nei_List, idf_List, pfun_, WeiF_, FuncRK_, hgPen_] := Module[{tl, vtl, nvs,
    ndof, Nnode, ndim, udim, kk, ksp, rsp},
   {tl, vtl, nvs} = NgroupL[nodes, volSet, nonvars, np];
   kk = ParallelTable[NOMRKPartNonVars[tl[[i]], vtl[[i]], nvs[[i]], coord,
      uvw, PW, KHG, Nei, idf, pfun, WeiF, FuncRK, hgPen], {i, Length[tl]}];
   ksp = kk[[1, 1]];
   rsp = kk[[1, 2]];
   Do[ksp += kk[[i, 1]];
    rsp += kk[[i, 2]], {i, 2, Length[tl]}];
   {ksp, rsp}
  ];
```

```
NOMRKPartNonVars[nodeList_List, volSet_List, nonvars_List, coord_List, uvw_List,
   PW_List, KHG_List, Nei_List, idf2_List, pfun_, WeiF_, FuncRK_, hgPen_] :=
  Module[{pvol, Nnode, ndim, udim, ndof, Ksp, Rsp, coordi, pw, khg, nablaU,
    NeiI, NeiI2, Kst, hg, HG, hi, uvwi, duvwi, Ri, Di, Rst, Rhg, k = 1, ishgPen1 = True},
   If[Length[nonvars] ≠ Length[nodeList], Print["Error"]; Return[]];
   Nnode = Length[coord];
   ndim = Length[coord[[1]]];
   udim = Length[idf2];
   ndof = udim Nnode;
   Ksp = SparseArray[{}, {ndof, ndof}];
   Rsp = SparseArray[{}, ndof];
   If[Length[hgPen] > 0, ishgPen1 = False];
   Do[
    NeiI = Nei[[i]];
    uvwi = uvw[[Prepend[NeiI, i]]];
    {pw, khg} = {PW[[i]], KHG[[i]]};
    duvwi = pw.uvwi;
    PrependTo[duvwi, uvwi[[1]]];
    {Ri, Di} = FuncRK[duvwi^T, nonvars[[k]]];
    nablaU = UNablaU[idf2, pw];
    Rst = Ri.nablaU;
    Kst = nablaU^T.Di.nablaU;
    If[hgPen ≠ 0.,
     hg = If[ishgPen1, hgPen KhgUdim[khg, udim], KhgUdim[khg, udim, hgPen]];
     Rhg = hg.Flatten[uvwi]; Kst += hg; Rst += Rhg];
    Rst *= volSet[[k]];
    Kst *= volSet[[k]];
    k++;
    PrependTo[NeiI, i];
    NeiI2 = NeiIIndex[NeiI, udim];
    Rsp[[NeiI2]] += Rst;
    Ksp += SparseArray[Tuples[NeiI2, 2] → Flatten[Kst], {ndof, ndof}], {i, nodeList}
   ];
   {Ksp, Rsp}];
```

```
NgroupL[nodes_List, volSet_List, nonvars_List, ngroup0_] := Module[{tl = {},
    vtl = {}, nv = {}, i1, i2, inc, nmax, ngroup},
   nmax = Length[nodes];
   If[ngroup0 < 0, ngroup = Ceiling[nmax / 1000], ngroup = ngroup0];
   inc = Round[nmax / ngroup];
   Do[i1 = Range[inc (i - 1) + 1, inc i];
    AppendTo[tl, nodes[[i1]]];
    AppendTo[vtl, volSet[[i1]]];
    AppendTo[nv, nonvars[[i1]]];, {i, 1, ngroup - 1}];
   i1 = Range[inc (ngroup - 1) + 1, nmax];
   AppendTo[tl, nodes[[i1]]]; AppendTo[vtl, volSet[[i1]]];
   AppendTo[nv, nonvars[[i1]]]; {tl, vtl, nv}];
UNablaU[idf_List, pw_List] := Module[{udim = Length[idf], ulen,
    nNode = Length[pw[[1]]], nablaU = {}, kn = 1, i, j},
   ulen = Length[Flatten[idf]];
   nablaU = ConstantArray[0, {ulen, udim nNode}];
   Do[Do[If[j ≠ 1, nablaU[[kn++, i ;; -1 ;; udim]] = pw[[j - 1]],
      nablaU[[kn++, i]] = 1], {j, idf[[i]]}], {i, udim}]; nablaU];
KhgNdim[khg_, ndim_] := Module[{kn}, kn = ConstantArray[0., ndim Dimensions[khg]];
   Do[kn[[i ;; -1 ;; ndim, i ;; -1 ;; ndim]] = khg, {i, ndim}]; kn];
KhgUdim[khg_, dim_, hgList_] := Module[{kn}, kn = ConstantArray[0., dim Dimensions[khg]];
   Do[kn[[i ;; -1 ;; dim, i ;; -1 ;; dim]] = hgList[[i]] khg, {i, dim}]; kn];
NeiIIndex[NeiI_List, udim_] := Module[{n2, n3}, n2 = ConstantArray[0, udim Length[NeiI]];
   n3 = udim (NeiI - 1);
   Do[n2[[i ;; -1 ;; udim]] = n3 + i, {i, udim}];
   n2];
```